UNIVERSITAT POLITÈCNICA DE VALÈNCIA

DEPARTAMENT DE FÍSICA APLICADA

Instituto de Diseño y Fabricación para la producción Automatizado

Preparation and Characterization of SnS thin films by Chemical Spray Pyrolysis for fabrication of solar cells

Doctoral Thesis

Presented by:

Thierno SALL

Supervisor: Prof. Bernabé Marí SOUCASE

December, 2017

Preparation and Characterization of SnS thin films by Chemical Spray Pyrolysis for fabrication of solar cells

Instituto de Diseño y Fabricación para la Producción Automatizada

Departament de Física Aplicada

Universitat Politècnica de València

Doctoral Thesis

Presented by:

Thierno SALL

Supervisor: Prof. Bernabé Marí SOUCASE

December, 2017

UNIVERSITAT
POLITÈCNICA
DE VALÈNCIA

Dr. Bernabé Marí Soucase, catedrático del Departamento de Física Aplicada de la Escuela Técnica Superior de Ingeniería del Diseño de la Universidad Politècnica de València y Director del Laboratorio de Semiconductores de la UPV.

INFORMO QUE:

La presente memoria. "**Preparation and characterization of SnS thin films by Chemical Spray Pyrolysis for fabrication of solar cells"** ha Sido realizada bajo mi dirección en el Departamento de Física Aplicada de la Escuela Técnica Superior de Ingeniería del Diseño de la Universidad Politècnica de Valencia por el licenciado en Física Dr Thierno SALL, y que constituye su tesis para optar al grado de Doctor en Física.

Y para que así conste, en cumplimiento de la legislación vigente, presenta en la Universidad Politécnica de Valencia la referida Tesis Doctoral, firmado el presente informe en

Valencia a…/…/2017

Fdo.: Bernabé Marí Soucase

Catedrático del Departamento de Física Aplicada

In the name of God, the Gracious, the Merciful

1. Read: In the Name of your Lord who created.

2. Created man from a clot.

96. Surah Al-Alaq (The Clot)

I dedicate this

Thesis

To all my family

To my friends

To my teachers

To those who know me

“ Qui abandonne son foyer pour se mettre en quête du savoir suit la voie de Dieu.

L’encre de l’élève est plus sacrée que la sang du martyr ”

MAHOMET

“Who leaves his home to go in search of knowledge follows the path of God.

The ink of the student is more sacred than the blood of the martyr”

MAHOMET

“Que sale de su casa para ir en busca del conocimiento sigue el camino de Dios.

La tinta del estudiante es más sagrada que la sangre del mártir”

MAHOMET

« La démarche scientifique n'utilise pas le verbe croire; la science se contente de proposer des modèles explicatifs provisoires de la réalité; et elle est prête à les modifier dès qu'une information nouvelle apporte une contradiction [...].»

(Albert Jacquard/1925-2013/Petite philosophie à l'usage des non-philosophes/1997)

«El enfoque científico no utiliza el verbo creer; La ciencia sólo ofrece modelos explicativos temporales de la realidad; y ella está dispuesta a cambiar a medida que nueva información aporta una contradicción [...].»

(Albert Jacquard/1925-2013/Petite philosophie à l'usage des non-philosophes/1997)

«The scientific approach does not use the verb believe; science only offers temporary explanatory models of reality; and is willing to change as soon as new information brings a contradiction [...]. »

(Albert Jacquard/1925-2013/Petite philosophie à l'usage des non-philosophes/1997)

Acknowledgements

First of all and foremost, I would like to express my greatest gratitude to “ALLAH” for giving me the strength, courage and patience to complete this modest study.

I would first like to thank my supervisor Prof. Bernabé Marí SOUCASE for his trust and scientific assistance during the PhD period. My gratitude to him cannot be expressed in words. I also want to thank Prof. Miguel MOLLAR for his decisive contribution to the realization of this thesis.

This work was performed in semiconductors physics laboratory of the Universitat Politècnica de València leaded by Professor Bernabé Marí SOUCASE.

I want to thank all members of the jury, starting with its president, GARCÍA MANRIQUE, Juan Antonio and TORTOSA JORQUES, María Dolores and SAHAL, Mustapha.

I want to thank the members of the physics laboratory of semiconductors of the Universitat Politècnica de València for their hospitality and scientific assistance they have given to me over the years.

I thank my father Oumar SALL; God has removed to our affection on Sunday the 22th of December, 2013 during the “Grand Magal of Touba Day”. May God welcomes him to his Paradise and protect his family. I thank my mother for her patience and endurance.

This work would not have been the same without the influence of my entire family. I witness them here all my love. I thank my parents namely my mother, Wédji Guèye, for education and love she gave me. I witness them my trust and my love.

For All my Family

Dr. Thierno SALL

UNIVERSITAT POLITÈCNICA DE VALÈNCIA

PhD Thesis of Physics

Presented by:

Dr. Thierno SALL

Supervisor: Prof. Bernabé Marí SOUCASE

Title: Preparation and Characterization of SnS thin films by Chemical Spray Pyrolysis for fabrication of solar cells

Abstract:

Chalcopyrite semiconductors such as $CuInSe_2$, $CuInS_2$, Cu $(In,Ga)(S,Se)_2$, and SnS were used as absorbers in solar cells thanks to their high efficiencies due to their direct gap of the order of 1.5eV ($CuInS_2$) and to their large absorption coefficient which was of the order of 10^5 cm^{-1}. To improve these efficiencies and avoid the peak effect at the absorber-window interface, an intermediate gap buffer layer between the two layers, whose ideal would be 2.8eV, was required. Thus indium trisulphide (β-In_2S_3) had attracted the attention of many researchers not only because it was ecological and none of its elements was harmful to the environment but also because it could be prepared with a gap greater than 2.5eV which will recover part of the solar spectrum located in the region of the small wavelengths.

Different characterization techniques had been used to optimize the deposition parameters. So, in this study we used:

-X-ray diffraction and Raman Spectroscopy to probe the structure and quality of thin films, respectively.

-Energy Dispersion Spectroscopy (EDS) to identify elements present in thin films.

-Scanning Electron Microscope (SEM) to study the morphology.

-Atomic Force Microscope (AFM) for the study of topography - roughness.

-Transmission and Photoluminescence to study the optical properties of thin films.

β-In_2S_3 thin layers prepared by Chemical Spray Pyrolysis technique with different [S]/[In] ratios at different substrate temperatures showed polycrystalline thin films with (0 0 12) as the main peak independently of the ratio and temperature of the substrate. A decrease in the intensity of the main peak was however noted when the ratio passed from 2 to 3 for the temperature 250 °C but increased at 300 °C. The peak (109) which was low at 250 °C and 300 °C increased in intensity at temperature 350 °C and this for all ratios. Raman spectroscopy confirmed the β-In_2S_3 phase obtained by XRD for some samples analyzed and elaborated at 250 °C. Homogeneous, dense and compact films were obtained independently of substrate ratio and temperature, and the EDS analysis revealed good stoichiometry for all samples. For transmission measurements we observed that the transmittance increased significantly with the increase of the substrate temperature (350 °C).

β-In_2S_3 thin layers deposited by Chemical Spray Pyrolysis technique at different substrate temperatures (250 °C−300 °C−350 °C) showed well crystallized thin films with (0 0 12) as preferred direction perpendicular to the plane containing the surface of glass substrate. SEM images showed dense, uniform, well-covered layers that adhered well to glass substrates and no crack and no void space were noted for all substrate temperatures. Microanalysis X confirmed the presence of In and S elements with good stoichiometry after vacuum annealing for 30 minutes. Raman spectroscopy analysis confirmed β-In_2S_3 phase with more prominent modes after vacuum annealing. We also noted a reduction in the gap energies after annealing for layers prepared at temperatures of 250 °C and 350 °C while for those prepared at 300 °C the energy of the gap remains stable.

Indium trisulfide (β-In_2S_3) thin layers were synthesized with and without alcohol in the bidistilled solvent. (0 0 12) was obtained as the main peak with a maximum intensity at the substrate temperature of 300 °C as shown by X-ray diffraction. We also noted (107) peak

only in the non-alcoholic prepared samples. Dense and compact homogeneous layers which adhered well to the glass substrate and without void, for films prepared with 5% alcohol, were obtained on the SEM images while for those prepared with bidistilled water, we observed some cracks. Layers had nearly the same roughness independently of the solvent but larger grain sizes were revealed by the AFM micrographs for the alcohol-free layers. Thin films produced with alcohol had higher transmission than those obtained without alcohol.

Tin sulfide, SnS, thin films were prepared by Chemical Spray Pyrolysis (CSP) technique on glass substrates at different substrate temperatures and with different molar ratio of precursors in the spray solution.

Tin mono-sulfide (SnS) thin films must be deposited onto glass substrate with [S]/[Sn] ratio equal to one (1) and substrate temperature equal to 350 °C to obtained dense, well-covered, and homogeneous films without pinholes and cracks. Distance between nozzle to substrate was kept to 25cm, sprayed volume 5mL, air pressure 0.7bar and spray rate 1.5 mL/min.

Films doped with Silver (Ag) and Aluminum (Al) are all orthorhombic structure with (111) as main peak. The intensity of main peak increased when the percentage of dopant element increased in the initial solution without any secondary phase for Al-doping films and with Ag_8SnS_6 and Ag for Ag-doping ones. SEM and AFM analysis showed that Ag-doping element had no effect in the morphology and the topography while Al-doping affected the surface morphology with “fishing net” like morphology with lots of holes for samples doped from 3% to 7%. EDS highlighted an increase of Ag in films when the its amount increased in the solution with S/Sn≈0.98 near to 1 at 5% of Ag-doping percentage where as for Al-doping EDS highlighted improvement of stoichiometry with an increase of Al percentage atomic in films when Al concentration increased in the initial solution with S/Sn≈0.99 at 10%. Electrical and energy band gap measurement showed a decrease of resistivity when Ag and Al percentages increased in the solution to reach relatively low resistivity of 108Ω.cm and 170Ω.cm at 10% for both, and an increase of energy band gap when the Ag and Al-doping elements increased in the solution with 1.66eV and 1.70eV for SnS doped with Ag and SnS doped with Al, respectively.

SnS thin films doped with iron (Fe^{2+}), XRD analysis revealed polycristalline samples with (111) as main peak with $SnFe_2S_4$ as secondary phase justifying the decrease of (111) intensity with the increase of Fe-doping concentration.

Morphology change came at 5% and 7% corresponding to more compact and denser films. Enhancement of stoichiometry could be noted from 3% to 7% given by EDS.

Band gap energy of films increased with Fe-doping from 1.50eV (pristine) to 1.77eV (5%) and resistivity varied with doping percentage and reached high value of 362.78 Ω.cm at 7%.

Spray pyrolyzed SnS thin films doped with indium were studied using various optical and electrical techniques. Structural analysis shows that all films crystallize in orthorhombic structure with (111) as a preferential direction without secondary phases. Doping of SnS layers with indium results in better morphology with increased grain size. Absorption measurements indicate dominant direct transition with energy decreasing from around 1.7 eV to 1.5 eV with increased indium supply. Apart from direct transition, an indirect one, of energy of around 1.05 eV, independent on indium doping was identified. The photoluminescence study revealed two donors to acceptor transitions between two deep defect levels and one shallower with energy of around 90 meV. The observed transitions did not depend significantly on In concentration. The conductivity measurements reveal thermal activation of conductivity with energy decreasing from around 165 meV to 145 meV with increased In content.

Finally, we were investigated the J-V characteristics of FTO/CdS/SnS, FTO/ZnO/CdS/SnS, FTO/ZnO:Al/CdS/SnS, FTO/ZnO:Al/SnS and FTO/In_2S_3/SnS solar cells and we found that efficiencies are very low due probably to the recombination at the junction, grain boundaries, etc.

Thierno SALL

Universitat Politècnica de València

December, 2017

Contents

Chapter I: Generalities on Photovoltaic Cells

1. The Sun, an Inexhaustible Energy Source 26
   1.1. Main Features 26
   1.2. Emissions of the Sun 27
   1.3. Constant illumination 28
2. Semiconductors 29
   2.1. Different types of semiconductor 29
   2.2. Band Structure 30
   2.3. Intrinsic Semiconductor 31
   2.4. Extrinsic Semiconductor 32
3. Structure of Solar Cells based on thin films 35
   3.1. Substrate and the "Super Substrate" configurations 35
   3.2. Different layers of thin films solar cell 36
   3.2.1. Absorber layer 36
   3.2.2. Buffer layer 37
   3.2.3. Transparent Conductive Oxide layer (TCO) 37
   3.2.4. Back Contact 38
   3.2.5. Substratum 38
   3.2.6. Anti-Reflection Layer (ARL) 38
   3.2.7. Top grid 39
4. Principle of solar cell operation 40
   4.1. Introduction 40
   4.2. Electrical characteristics 40
      4.2.1. The ideal solar cell 40
      4.2.2. Solar cell characteristics in Practice 42
      4.2.3. Quantum Efficiency and Spectral Response 42
   4.3. Typical solar cell structures 44
      4.3.1. The p-n junction 44
5. Industrial Application 47

6. Conclusion 48
References 48

Chapter II: State of Art

1. In_2S_3 Thin Films Review 50
1.1. Introduction 50
1.2. In_2S_3 thin films properties 50
1.2.1. Crystallographic structure 50
1.2.2. Phases in the In-S system 51
1.2.3. Optical properties 52
1.2.4. Electrical properties 53
1.2.5. Morphological properties 54
1.2.6. Technical synthesis of In_2S_3 thin films 54
1.2.7. Industrial Application 55
2. SnS Thin Films Review 56
2.1. Introduction 56
2.2. SnS thin films proprieties 56
2.2.1. Crystallographic structure 56
2.2.2. Phase Diagram of the Sn-S System 57
2.2.3. Optical properties 58
2.2.4. Electrical properties 58
2.2.5. Morphological properties 59
3. CdS Thin Films properties 59
3.1. Introduction 59
3.2. CdS thin films properties 60
3.2.1. Crystallographic structure 60
3.2.2. Optical properties 61
3.2.3. Electrical properties 61
3.2.4. Morphological properties 61
4. ZnO Thin Films properties 62
4.1. Introduction 62

4.2. ZnO thin films properties 62
4.2.1. Crystallographic structure 62
4.2.2. Optical properties 64
4.2.3. Electrical properties 64
4.2.4. Morphological properties 65
5. SnS-Based Thin-Film Solar Cells 66
5.1. Introduction 66
5.2. Previous Works on SnS-based cells 66
6. Conclusion 67
References 68

Chapter III: Experimental and Characterization Techniques

1. Development techniques of thin film 74
1.1. Introduction 74
1.2. Chemical Spray Pyrolysis technique 74
1.2.1. Operating principle of Chemical Spray Pyrolysis 74
1.2.2. Experimental device 76
1.3. Definition of a thin layer 78
1.4. The different types of crystalline growth 79
1.5. Surface Tension 80
1.5.1. Introduction 80
1.5.2. Some observations 80
1.5.3. Surface tension 81
1.5.4. Surface tension of some liquids 82
1.5.5. Wetting 84
1.6. Conclusion 85
2. Characterization Techniques 85
2.1. X-ray diffraction 85
2.1.1. Rigaku Ultima IV 87
2.2. Raman Spectroscopy 88
2.2.1. Historical 88

2.2.2. Raman Spectroscopy Principle 88
2.2.3. The advantages and disadvantages of Raman Spectroscopy 90
2.2.4. Working method of Raman Spectrometer Principle 91
2.3. Scanning Electron Microscopy (SEM) 93
2.3.1. Introduction 93
2.3.2. Scanning Electronic Microscope Principle (SEM) 95
2.3.3. Energy Dispersion X-ray Spectroscopy (EDS) 97
2.4. Atomic Force Microscopy (AFM) 98
2.4.1. Introduction 98
2.4.2. Device Description 98
2.4.3. Working Principle of Atomic Force Microscopy (AFM) 99
2.4.4. Working mode of Atomic Force Microscope 100
2.4.4.1. Contact mode operating 100
2.4.4.2. Working non-contact mode 101
2.5. Photoluminescence (PL) 101
2.5.1. Introduction 101
2.5.2. Definition 102
2.5.3. Theory of photoluminescence 102
2.6. Transmittance and Absorbance measurement 105
2.6.1. Absorbance 105
2.6.2. Transmittance 108
2.6.3. Experimental apparatus 108
2.7. Heat treatment 109
2.7.1. Working Principle of the Oven 109
2.8. Four Point Probe Resistivity measurements 111
2.8.1. Introduction 111
2.8.2. Principle of the technique of 4 points 111
2.9. Capacitance-Voltage measurements 112
2.9.1. Introduction 112
2.9.2. Semiconductor in solution 113
3. Conclusion 114

References 114

Chapter IV: Results and Discussion

A-Optimization of deposition parameters of In_2S_3 Thin Films 117
1. [S]/[In] Ratio Effect at Different Substrate Temperatures 117
1.1. Introduction 117
1.2. Results and discussion 117
1.2.1. X-ray diffraction analysis 117
1.2.2. Raman Spectroscopy analysis 120
1.2.3. Morphological analysis by SEM 121
1.2.4. EDS analysis 121
1.2.5. Optical Characterization 123
1.3. Conclusion 126
2. Indium Trisulfide (In_2S_3) elaborated at Different Substrate Temperatures 127
2.1. Introduction 127
2.2. Experimental conditions for the preparation of thin layers of In_2S_3 by the Chemical Spray Pyrolysis method 127
2.2.1. Preparation of glass substrates 127
2.2.2. Elaboration of thin layers of indium trisulphide (In_2S_3) 128
2.3. Results and Discussions 128
2.3.1. X-ray diffraction analysis 128
2.3.2. Morphological analysis by SEM 130
2.3.3. Analysis by X-ray Energy Dispersion Spectroscopy (EDS).......... 131
2.3.4. Optical properties characterization 132
2.3.5. Analysis by Photoluminescence (PL) 134
2.3.6. Raman Spectroscopy analysis 135
2.4. Conclusion 136
3. β-In_2S_3 deposited by Chemical Spray Pyrolysis Method from Bi-Distilled Water Solvent and Alcohol Solvent 136
3.1. Introduction 136
3.2. Experimental details 137

3.3. Results and Discussions 137
3.3.1. X-ray diffraction analysis 137
3.3.2. Morphological analysis by SEM 139
3.3.3. Topographic analysis by AFM 140
3.3.4. Energy Dispersion X-ray Spectroscopy analysis (EDS) 142
3.3.5. Optical Properties of In_2S_3 Thin Films 143
3.4. Conclusion 145
B-Optimization of deposition parameters of SnS Thin Films 146
1-Effect of [S]/[Sn] ratios 146
1.1. Experimental details 146
1.2. Results and Discussion 147
1.2.1. X-ray diffraction 147
1.2.2. Raman Spectroscopy 148
1.2.3. Surface Morphology measured by SEM 148
1.2.4. Surface Topography measured by AFM 149
1.2.5. Energy Dispersive Spectroscopy analysis (EDS) 150
1.2.6. Optical properties 151
1.3. Conclusion 153
2. Effect of substrate temperature 153
2.1. Experimental Details 153
2.2. Results and Discussion 154
2.2.1. X-ray diffraction (XRD) analysis 154
2.2.2. Raman Spectroscopy analysis 156
2.2.3. Scanning Electron Microscopy analysis 157
2.2.4. Atomic Force Microscopy analysis 158
2.2.5. Energy-Dispersive X-ray Spectroscopy measurements 159
2.2.6. Electrical measurements 160
2.2.7. Optical analysis 161
2.3. Conclusion 162
3-Effect of substrate nature 163
3.1. Experimental 163

3.2. Results and Discussion 163
3.2.1. XRD analysis 163
3.2.2. Raman Spectroscopy analysis 164
3.2.3. SEM analysis and EDS measurements 165
3.2.4. Atomic Force Microscopy (AFM) analysis 167
3.2.5. Optical analysis 168
3.3. Conclusion 169
C-Effect of doping on the physical and chemical properties of SnS thin films 170
1- Introduction 170
2. SnS thin films doped with silver (Ag^{+}) 170
2.1. Experimental details 170
2.2. Results and Discussions 170
2.2.1. X-ray diffraction (XRD) analysis 170
2.2.2. Scanning Electron Microscopy (SEM) analysis 172
2.2.3. Electrical properties 174
2.2.4. Electrochemical analysis: Mott-Schottky plots 174
2.2.5. Optical properties 175
2.3. Conclusion 177
3. SnS thin films doped with aluminum (Al^{3+}) 177
3.1. Experimental details 177
3.2. Results and Discussion 177
3.2.1. X-ray diffraction (XRD) analysis 178
3.2.2. Surface Morphology and Composition analysis 179
3.2.3. Electrical properties 181
3.2.4. Mott-Schottky plots 182
3.2.5. Optical properties 183
3.3. Conclusion 185
4. SnS thin films doped with Iron (Fe^{2+}) 185
4.1. Experimental Procedure 185
4.2. Results and Discussion 186
4.2.1. X-ray diffraction analysis 186

4.2.2. Morphological properties and Microanalysis 187
4.2.3. Optical properties 188
4.2.4. Electrical properties.. 190
4.2.5. Electrochemical analysis: Mott-Schottky plots............................. 191
4.3. Conclusion.. 192
5. SnS thin films doped with Indium (In^{3+}).. 193
5.1. Thin film preparation 193
5.2. Results and Discussion.. 193
5.2.1. X-ray diffraction analysis.. 193
5.2.2. Atomic Force Microscopy analysis... 194
5.2.3. Optical Absorption 195
5.2.4. Photoluminescence.. 197
5.2.5. Conductivity measurements 199
5.3. Conclusion.. 200
D. CdS, ZnO and ZnO:Al Thin Films... 201
1. Introduction 201
2. CdS Thin Films 201
2.1. Structural Investigation of CdS Thin Films 201
2.2. Morphology and Microanalysis of CdS Thin Films 202
2.3. Electrical analysis of CdS Thin Films.. 203
2.4. Optical property of CdS Thin Film 203
3. ZnO Thin Films... 204
3.1. Structural Investigation of CdS Thin Films 204
3.2. Morphology and Microanalysis of ZnO Thin Films.......................... 204
3.3. Electrical analysis of ZnO Thin Films 205
3.4. Optical property of ZnO Thin Film.. 206
4. ZnO:Al Thin Films.. 206
4.1. Structural Investigation of ZnO-Al doped Thin Films 206
4.2. Morphology and Microanalysis of ZnO-Al doped Thin Films........... 207
4.3. Electrical analysis of ZnO-Al doped Thin Films............................... 208
4.4. Optical property of ZnO-Al doped Thin Film 208

5. Conclusion 209
References 210

Chapter V: SnS-based Solar Cells

1. Introduction 214
2. Experimental Procedure 214
3. J-V characteristics of cells 214
4. Result and Discussion 215
5. Conclusion 218

Chapter VI: General Conclusion

1. General Conclusion 219

List of Symbols and Acronyms

ALCVD	Atomic Layer Chemical Vapor Deposition
AFM	Atomic Force Microscopy
AM	Air Mass
ALD	Atomic Layer Deposition
ARL	Anti-Reflection Layer
Å	Angström
A	Absorbance
C	Capacitance
CVD	Chemical Vapor Deposition
CSP	Chemical Spray Pyrolysis
CBD	Chemical Bath Deposition
$CS(NH_2)_2$	Thiourea
°C	Celsius degree
CZST	Cu_2ZnSnS_4
CIS	$CuInS_2$
CIGS	$CuIn_{1-x}Ga_x$(S and/or Se)$_2$
D	Crystallite Size (Scherrer's Formula)
d	Interreticular Distance
EQE(λ)	External Quantum Efficiency
IQE(λ)	Internal Quantum Efficiency
Eg	Band gap energy
E_f	Fermi level
EDS	Energy Dispersive Spectroscopy

ENSCP	Ecole Nationale Supérieure de Chimie de Paris
FESEM	Field Emission Electron Microscopy
FTO	Fluor Tin Oxide
FF	Fill Factor
°F	Farad
g	Gravity acceleration-9.8m/s^2
HZB	Helmholtz-Zentrum Berlin
H_2O	Bi-Distilled water
HNO_3	Nitric acid
IR	Infrared
$InCl_3$	Indium Chloride
ILGAR	Ion Layer Gas Reaction
IPE	Institut fur Physikalische Elektronik, Uni Stuttgart
ITO	Indium Tin Oxide
I_m	Maximum current
I_o	Saturation current
I_{ph}	Photon flux incident
I_{sc}	Short circuit current
JCPDS	Joint Comity on Powder Diffraction Standards
K	Kelvin degree
K_B	Boltzmann's constant
mm	Millimeter
mbar	Millibar
m_c^*	Effective mass of electrons
m_v^*	Effective mass of holes
MOCD	Metal Organic Chemical Deposition

nm	Nanometer
N	Newton (force unity)
N_C	Effective Density of States Electrons
N_V	Effective Density of States Holes
NREL	National Renewable Energy Laboratory
PL	Photoluminescence
PVD	Physical Vapor Deposition
P_{max}	Power maximum
P_{ideal}	Power ideal
π	Pi number
q	Elementary charge
R_s	Serie Resistance
R_{sh}	Parallel Resistance
SR(λ)	Spectral Response
SEM	Scanning Electron Microscopy
%	Percentage
λ	Wavelength
µm	Micrometer
(hkl)	Interreticular plans
β	Full Width at Half Maximum (FWHM)
Θ	Bragg angle
T%	Transmittance
T	Temperature
TCO	Transparent Conductive Oxide
h	Plank Constant

ν	Photon's frequency
UV	Ultraviolet
V_m	Maximum voltage
V_{oc}	Open circuit voltage
XRD	X-Ray Diffraction
ZSW	Zentrum fur Sonnenenergie−und Wassersto-Forschung

Chapter I: Generalities on Photovoltaic Cells

1. The Sun, an Inexhaustible Energy Source

1.1. Main Features

Solar energy is the energy produced by the sun through his radiation. From this, man can, by converting sunlight, produce electrical energy, photovoltaic solar energy, or heat, solar thermal energy. Clean energy, renewable and economical, the solar energy is the most equitably distributed energy on our planet unlike fossil fuels (oil, coal ...). That is why all countries of the world have access to and can benefit from it. However, due to the spherical shape of the earth, the solar radiation is not identical at all points of the globe. This is why the countries closest to the equator receive more solar energy than the countries situated to the poles. Fig. 1 shows the map of the average annual sunshine.

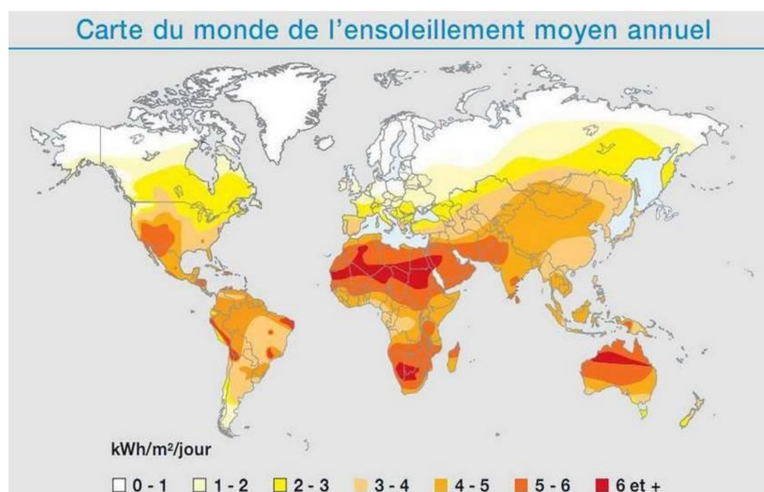

Fig. 1: Map of the average annual sunshine [1]

The sun is a star, a huge ball of gas composed primarily of 70% hydrogen, 28% helium and 2% other atoms in the universe; its radius is 696 000 km and it is placed at 150 million km from Earth. This distance is so great that the light reaches us eight seconds after being sent out with a velocity of 300 000 km/s. Its radius is 109 times that of the Earth (696 000 km) and its mass 333 000 times that of our planet. The moon is 400 times smaller than the sun,

but 400 times closer to the Earth, which explains the apparent size of two similar stars in the sky, which can realize particularly during solar eclipses. Its temperature radiation, if one compares the sun to a black body of 5700 K under the law of Stefan, gives it its yellow color. So by analyzing the color, we can easily obtain the temperature of radiation.

1.2. Emissions of the Sun

The energy emitted by the Sun is first in the form of electromagnetic radiation which together forms the solar radiation which is the only significant source of energy for the atmosphere.

Our eyes perceive only a portion of solar radiation; one located in the area said visible wavelength range from 0.40µm and 0.80µm. The sun, however, emits in a broad range of wavelengths from (in the sense of small to larger wavelengths) gamma rays (wavelengths less than 10^{-12} m) to radio waves (of lengths wave reaching 1000 m), through X-rays, ultraviolet radiation, visible radiation, infrared radiation and microwave radiation.

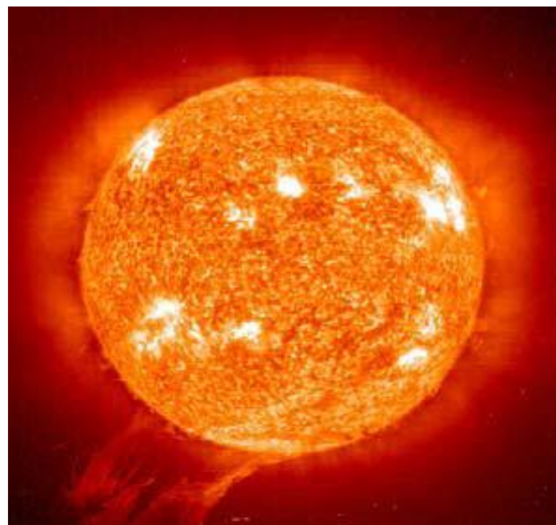

Fig. 2: Photograph of the Sun

The greater part of the solar energy is radiated in the ultraviolet, visible and near infrared: 99% of the energy outside atmosphere is between 200 nm and 4µm. At the ground, due to the absorption of solar radiation by water vapor, the spectrum is limited upwards to about 2.5µm.

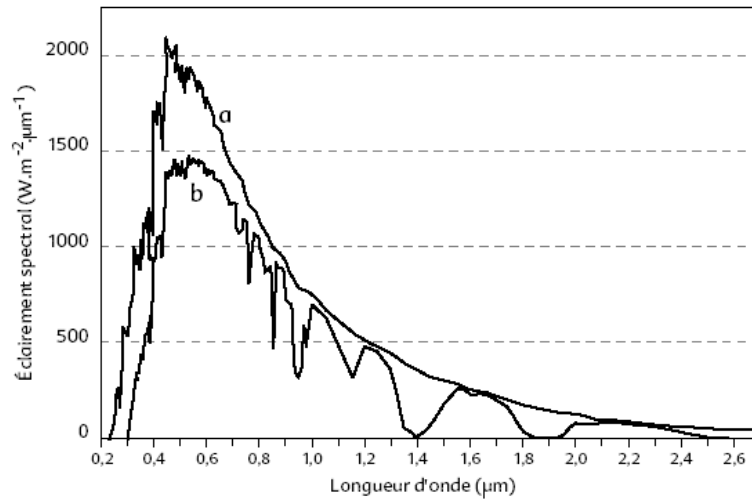

Fig. 3: Spectral density of the irradiance from direct sunlight: a) Solar radiation outside the atmosphere and b) Direct solar radiation on the ground [2]

Table 1: The irradiance of solar radiation outside the atmosphere in the various fields of wavelength [2]

Spectral region	**Wavelength (µm)**	**Irradiance ($W.m^{-2}$)**	**Percentage (%)**
Infrarouge	>70	695	50.8
Visible	0.40 à 0.70	559	40.9
UV-A	0.30 à 0.40	86	6.3
UV-B	0.28 à 0.32	21	1.5
UV-C	< 0.28	6	0.4

1.3. Constant illumination

The luminous intensity after the sun normally incident to the surface of the earth is called the solar constant. This constant is approximately valued at 1.4 KW/m^2 above the atmospheric layer and is reduced to earth to 1 KW/m^2 due to reflection and absorption of the particles present in the atmospheric layer. This loss is called "air mass" (AM). The AM0 designation corresponds to an air mass zero for light incident above our atmosphere at normal incidence. AM1 corresponds to the same light reaching the Earth's surface. The name refers to the AM1.5 air mass corresponds to light reaching at 48.2 degrees on the surface of the earth, a weaker light of the fact that the thickness of the crossing atmospheric layer is greater.

The formula AMm: $m \approx 1/\sin(A)$ with A the angle between the incidence of light rays and the horizontal to the earth.

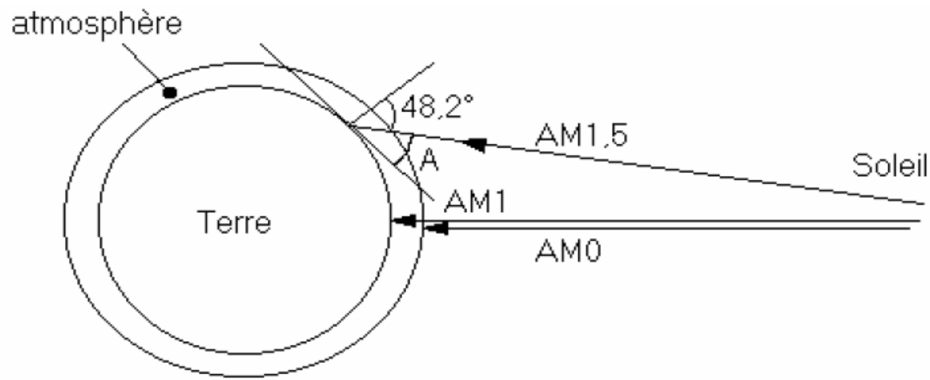

Fig. 4: Various illuminations constants [3]

2. Semiconductors

The solid exists in two states. In one state the atoms are arranged randomly, this state is called amorphous while in the other state they are arranged regularly at the nodes of a network and we said that this state is crystallized (what interests us in this study).

The electrons of an isolated atom orbiting the nucleus occupy discrete energy levels that each defines an electronic layer. In a crystal where a set of atoms is evenly distributed energy states of the electrons become bands separated by empty spaces called bandgap due to the interaction between the atoms of the crystal. The upper band is the conduction band and the lower band valence band. Electric transport occurs in the conduction band since the electrons in the valence band are bound to the nucleus.

In insulating the valence band is full while the conduction band is completely empty. So that neither an electric field nor temperature can pass an electron from the valence band to the conduction band because the gap is several electron volts (> 5eV).

In conductor there is an odd number of electrons per atom or there is an even number of electrons but with an overlap of the conduction band and the valence band. The number of electrons is proportional to the number of atoms of the metal and the gap is zero.

In semiconductor band gap is relatively small (1-3 eV) to allow an electric field or temperature to be able to move an electron from the valence band to the conduction band.

2.1. Different types of semiconductor

The semiconductors are divided into two groups: natural semiconductors such as silicon (Si) and germanium (Ge) in column IV of the periodic table of elements and compound semiconductors developed at the laboratory. We distinguish among these different groups:

Group III-V: an element of column III combined with one element of column V: InP, InSb, GaAs,...

Group III-VI: an element of column III combined with one element of column VI: In_2S_3

Group II-VI element of a column II combined with an element of Column VI: CdTe, ZnTe, ZnS, CdS...

Group IV-VI: an element of column IV combined with one element of column VI SnS_2, PbS, PbTe, SnS... ..

Group I-III-VI_2: an element of column I combined with an element of column III and an element of column VI: $CuInS_2$, $CuInSe_2$.

2.2. Band Structure

The semiconductors are classified into two groups according to their band structure:

-When the maximum of the valence band is below the minimum of the conduction band, it was a direct gap. In other words the extrema correspond to the same value of k, that is to say the same momentum p. During the transition, the electron may emit a photon whose wavelength is directly related to the energy distance (operating principle of light emitting diodes and laser diodes).

-When on the other hand the extrema are offset, it is called indirect gap. For an electron transits from the conduction band to the valence band, it takes both, a change in energy and k therefore a change in momentum. This change is made by an exchange of momentum with the lattice in the form of vibration (phonon).

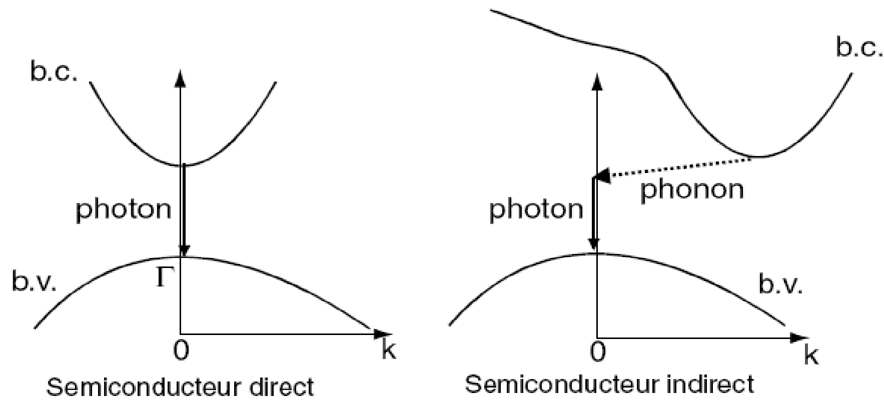

Fig. 5: The representation of the absorption of light in a direct gap and indirect gaps of semiconductors [4]

2.3. Intrinsic Semiconductor

Semiconductor is said intrinsic if the vast majority of carriers (electrons and holes) are generated by the atoms of the semiconductor. And in this case an electron receives certain energy can pass from the valence band to the conduction band. The number of holes in the valence band corresponds exactly to the number of electrons in the conduction band. Also with increasing temperature the number of electrons in the conduction band increases because the electrons that were in the valence band received enough energy to pass into the conduction band.

The filling statistical energy levels obeys to Fermi-Dirac distribution since the electrons and holes are fermions that are to say particles of half-integer spin. The probability of occupancy of an energy level E by an electron at the temperature T is given by the following formula [5]:

$$f(E) = \frac{1}{1 + \exp\left(\frac{E - E_f}{K_B T}\right)} \qquad (1)$$

K_B is Boltzmann's constant, E_f is the Fermi level, that is to say the average statistical level occupied by all of the charge carriers and whatever the temperature, probability of occupancy for this state energy is always equal to $\frac{1}{2}$, n_i the number of electrons in an intrinsic semiconductor, E_c denotes the lowest energy level of the conduction band and E_v denotes the highest energy level of the band valence.

It can be shown, from calculations on the densities of energy states that the concentration of electron n and the concentration of hole p are given by the following expressions:

$$n = N_c \exp(\frac{-(E_c - E_f)}{K_B T}) \ (2) \qquad p = N_v \exp\left(\frac{-(E_f - E_v)}{K_B T}\right) (3)$$

Where $$N_c = 2(\frac{K_B T m_c^*}{2\pi\hbar^2})^{3/2} \ (4)$$

$$N_c = 2(\frac{K_B T m_v^*}{2\pi\hbar^2})^{3/2} \ (5)$$

N_C and N_V are the effective densities of states (cm^{-3}) for electrons and holes respectively and ħ is the reduced Planck constant ($\hbar = h/2\pi$).

$$p = n = n_i \ (6)$$

$$\boldsymbol{E_i} = \boldsymbol{E_f} = \frac{\boldsymbol{(E_c - E_v)}}{\boldsymbol{2}} + \frac{\boldsymbol{3K_B T}}{\boldsymbol{4}} \ln(\frac{m_v^*}{m_c^*}) \quad \text{with} \quad m_c^* \approx m_v^* \ (7)$$

m_c^* is the effective mass of electrons

m_v^* is the effective mass of holes

Fermi level of an intrinsic semiconductor is always very close to the middle of the gap at room temperature:

$$E_f \approx \frac{E_c + E_v}{2} \quad (8)$$

The conductivity of the semiconductor depends on the number of free electrons: when this number increases the conductivity increases. Therefore, the conductivity of an intrinsic semiconductor increases with temperature.

2.4. Extrinsic Semiconductor

Semiconductor is said extrinsic when doped i.e. when a small amount of foreign atoms (impurity) is added into the semiconductor to modify its conductivity properties. Doping a semiconductor is therefore to introduce into its matrix, atoms of another material. These atoms will replace some initial atoms and thus introduce more electrons or holes.

There are two types of doping:

- n-type doping, which consists in producing an excess of electrons, which are negatively charged.

- p-type doping, which consists in producing an electron deficit, therefore an excess of holes, considered positively charged.

The impurity atom causes effects that depend on the column it occupies in the periodic table of Mendeleev, in relation to the column of the atom it replaces.

If the dopant atom belongs to the same column as the atom it replaces, they are isovalent (or isoelectric). The valence electrons of the impurity atom exactly replace the electrons of the original atom. Electrical conduction properties of the material are not changed.

If the dopant atom belongs to the previous column, it then lacks a peripheral electron to restore all the initial covalent bonds. It appears an electron deficiency, i.e. a hole. The atom inserted is called acceptor (electron), because it is able to receive an additional electron from the valence band. It is a p-type doping.

If the dopant atom belongs to the next column, it has an extra electron compared to the initial atom. The initial covalent bonds are restored, but one of the electrons is not used in those links. It is therefore in a free state of system. The atom inserted is called donor (electron). It is an n-type doping.

A single dopant atom can be both donor and acceptor: it is called amphoteric. This is for example the case of silicon (Si column IV), which is a dopant for gallium arsenide (GaAs): if the Si gets substitution of one atom of gallium (III column), it is electron donor. If it substituted an atom of arsenic of Arsenic (column V), it is acceptor.

For example for silicon we can intentionally introduce an atom of column III (Boron) or an atom from column V (Phosphorus or Arsenic). If a phosphorus atom substitutes a silicon atom, it forms four bonds with 4 silicon atoms neighbors. The thermal agitation is sufficient to release the 5th electron bound to the phosphorus atom, which subsequently will be free to move in the crystal thus increasing the number of free electrons in the conduction band and

therefore participating in the electrical conduction of the semiconductor. It is said that the silicon is doped n-type and the phosphorus atom is called donor atom.

A donor atom such as phosphorus into the silicon gives an energy level allowed in the gap (E_D). This level is located a few meV below the conduction band and low energy can pass the electrons of donor level to the conduction band. At room temperature the electrons have enough energy ($\frac{K_B T}{q} = 25.6$meV) to move from donor level to conduction band ionizing, therefore, positively donor atoms (P^+).

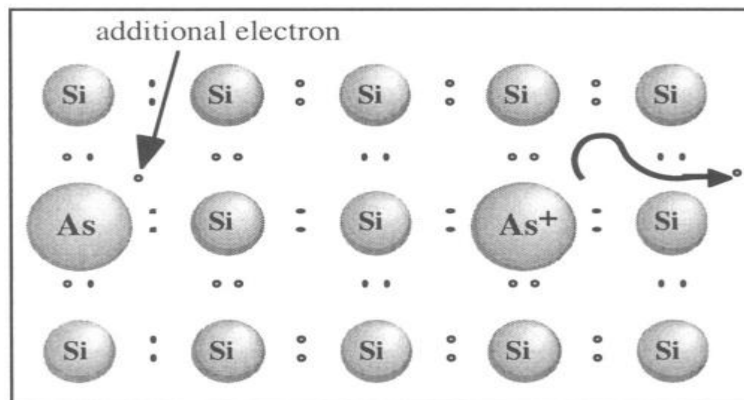

Fig. 6: Doping silicon with arsenic (n-type semiconductor) [6]

In the other hand if a silicon atom is substituted by a boron atom which has 3 electrons in its outer layer, the boron atom form three bounds with three silicon atoms and it fails to satisfy electron 4 bonds. Thus, it captures an electron creating a hole in the crystal. The hole can move in the crystal participating in the electric conduction. These boron atoms are referred to as acceptor atoms.

Similarly the introduction of boron in the silicon atom gives an energy level allowed in the gap (E_A), which is located a few meV above the valence band. At room temperature the electrons of the top of the valence band have enough energy to pass through the energy level created by the boron atoms creating holes in the valence band and ionizing negatively boron atoms (B^-).

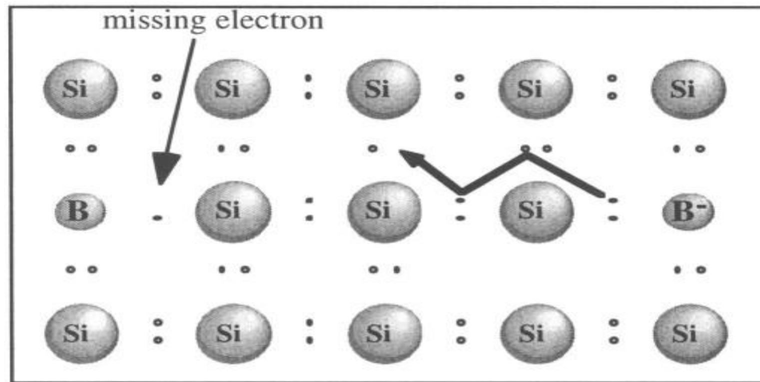

Fig. 7: Doping silicon with boron (p-type semiconductor) [7]

3. Structure of Solar Cells based on thin films

Solar cells based on thin layers are composed of several layers. Generally there is the substrate, the transparent conductive oxide (TCO), the buffer layer (n-type), the absorbent layer (p-type) and the metal contact. Each component has different physical and chemical properties that affect the performance of the entire solar cell. Each component has a crystal structure, a microstructure, a lattice parameter, an electron affinity, a diffusion coefficient etc ... different. The interfaces between the thin layers may have defects and energy states at the interfaces, recombination centers, inter-diffusions and chemical changes.

3.1. Substrate and "Super Substrate" configurations

The solar cells are thin film "substrate" configuration or "super substrate" configuration. For the "substrate" configuration, the substrate is either a metal or a glass coated with a thin metal layer which acts as a contact. The structure of the solar cell substrate configuration: Glass/Metal/TCO/absorber/buffer layer/metal contact and the cell is illuminated front side. In the "super-substrate" configuration the glass substrate is not only a support but at the same time window for illumination. In the "super-substrate" configuration, the substrate is transparent and the conductive oxide deposited on the substrate serves as contact. The structure of the solar cell "super-substrate" configuration is:

Glass/TCO/buffer layer/absorber/Contact metal and the illumination take place through the substrate side. Both configurations are commonly used.

3.2. Different layers of thin films solar cell

3.2.1. Absorber layer

This is the layer which absorbs light and converts the electromagnetic radiation into electricity. It must have the following properties:

- Ideal gap energy is of the order of 1.5eV ($CuInS_2$) and the gap is measured either by the transmittance, the photoreflectance and photoluminescence.

- Absorption coefficient of the absorber must be high to absorb almost all the energy of illumination with a thin layer (1µm). The indirect gap semiconductors typically have an absorption coefficient lower than direct gap semiconductors. The semiconductor chalcopyrite structure for the photovoltaic application, such as $CuInSe_2$ and $CuInS_2$, which have a direct gap, has a high absorption coefficient ($10^5 cm^{-1}$). A promising new layer is being studied by many laboratory namely Cu_2ZnSnS_4 (CZST). This is a layer whose constituent elements are abundant, non-toxic and whose corresponding chemicals are cheap. It has a gap of energy around 1.5eV and its absorption coefficient exceeds $10^4 cm^{-1}$.

- Diffusion length and very large life duration are needed for minority carriers to have a high efficiency. However, these conditions are very difficult to fulfill for a thin layer due to the fact that the distance that the carriers have to travel is very small for diffusion in the cell. To get a better diffusion length, eliminating defects and impurities, which lead to recombination and reduce the carrier mobility is required.

-No degeneracy should only be possible in the material, regardless of defects because it produces a short circuit.

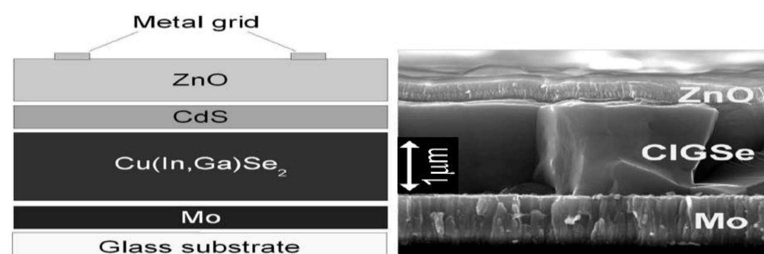

Fig. 8: Cross- section of the scanning electron microscope of a solar cell based on a thin layer of $Cu(In,Ga)Se_2$ [8]

3.2.2. Buffer layer

The buffer layers are used to form a heterojunction with the absorbent layer to provide a "soft" transition between the absorber and the transparent conductive oxide. It must allow light to reach the absorbent layer without photocurrent generation in the buffer layer. The requirements for a buffer layer are:

- Wide energy gap for better transmission in the visible range, for example, CdS (Eg = 2.4eV), CuI (Eg = 2.9eV) In_2S_3 (Eg = 2.1eV-2.9eV).

- Perfect junction is that separates the electrons and holes. This is possible if the discontinuity between the buffer layer and the absorbent layer is done without band offset for minority carriers, contrariwise it must be a large potential barrier for majority carriers. But if there is a band offset for minority carriers in the buffer layer, there could lead to peak formation (spike). A band alignment with moderate peak is rather ideal however the presence of peak means that the band offset decreases the minority carrier and the interface becomes less selective.

- Lattice mismatch at the junction is important if both layers, buffer and absorbent, are well oriented. In microcrystalline layers, the lattice mismatch varies spatially and so we will have an average lattice mismatch.

- Sufficient doping of the buffer layer is required to eliminate the generation of minority carriers (leakage) and to maintain the Fermi level away from the middle of the gap at the interface to prevent recombination.

CdS is the most studied and most widely used buffer layer, but in recent years the researchers are working to find him an alternative layer because cadmium is toxic. For example indium trisulfide (In_2S_3) is a good candidate to replace CdS.

3.2.3. Transparent Conductive Oxide layer (TCO)

The transparent conductive oxide is n-type with good electrical conductivity and high transmittance in the visible range. The conductivity of the TCO depends on the carrier concentration and mobility. The increase in carriers could lead to an improvement in the

absorption of free carriers, which reduces the transparency of the TCO in the field of wavelengths. Increase mobility by improving the crystalline properties leads to a good transparent conductive oxide. ZnO is the most used material in solar cells.

3.2.4. Back Contact

In the "super-substrate" configuration it is beneficial to use a material with a wide band gap to increase the selection of types of carriers and reduce recombination [9] interface. In the "substrate" configuration, for an ohmic contact, a metal can be used with a "work function" higher than that of the p-type layer.

3.2.5. Substratum

The substrate should be stable at the manufacturing temperature of the solar cell. It should be also adherent with the layer deposited on it. Generally a glass is used for solar cells and avoiding diffusion of substrate impurities into the deposited layer. But sometimes diffusion of impurity from the glass towards the deposited layer can have a beneficial effect [10]. For example sodium which diffused from the glass substrate to the absorbent layer improves CIGS grains and the performance of the cell [11].

3.2.6. Antireflection layer (ARL)

The antireflection layer is used to improve performance by eliminating the losses by reflection of the electromagnetic radiation from the sun. The principle of action of anti-reflection coatings is based on the interference of light beams in the thin dielectric layers. If the thickness of the dielectric layer is equal to:

$$d = \frac{(2N+1)\lambda}{4n} \quad N = 0, 1, 2, 3 \ldots \quad (9)$$

We obtain the cancellation of the beams reflected at the air/ARL and ARL/semiconductor. For high efficiency solar cells, anti-reflective layer is used (with two different dielectrics).

Various antireflective layers are used in photovoltaics: TiO_2, SiO_2, ZnS, MgF_2, SiNx, etc. [12].

3.2.7. Top grid

For the front grille, a metal layer or a stack of two layers is typically used. The first layer of the front grid must establish an ohmic contact with the window and must have a high melting point to prevent the diffusion to the cell during the operation period. Nickel is usually used for this purpose. The bottom layer should be a good electrical conductor and aluminum is often used.

Stability over time is necessary for a good solar cell. The diffusion and reaction at the interfaces must be controlled. Good adhesion between the different layers of the cell is also important. Finally, all cell materials should be cheap and abundant.

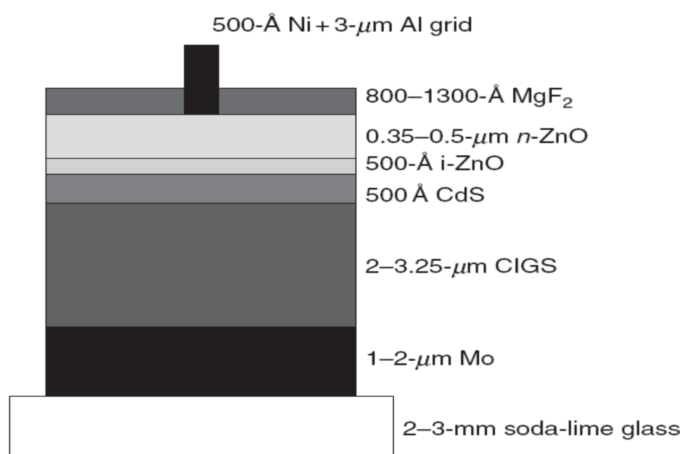

Fig. 9: Schematic diagram of high efficiency solar cell with thin layer of CIGS [13]

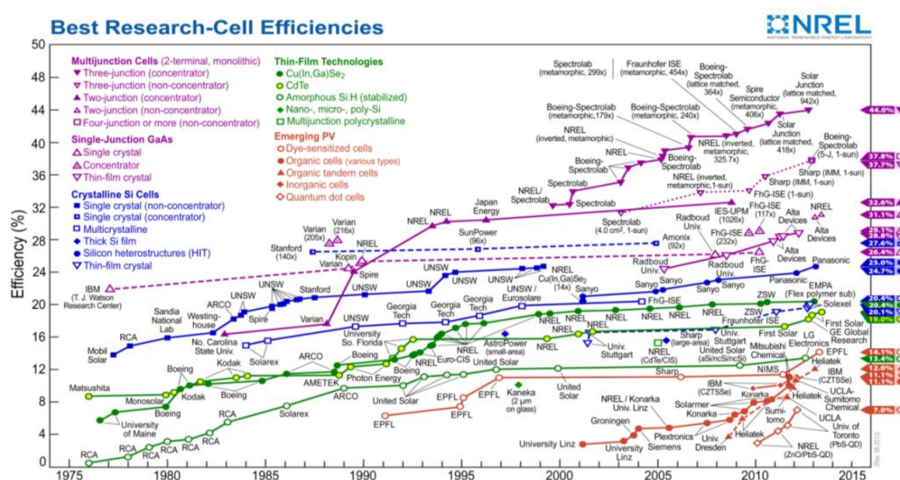

Fig. 10: Evolution record performance for different laboratory photovoltaic cell technologies. Source: NREL [14]

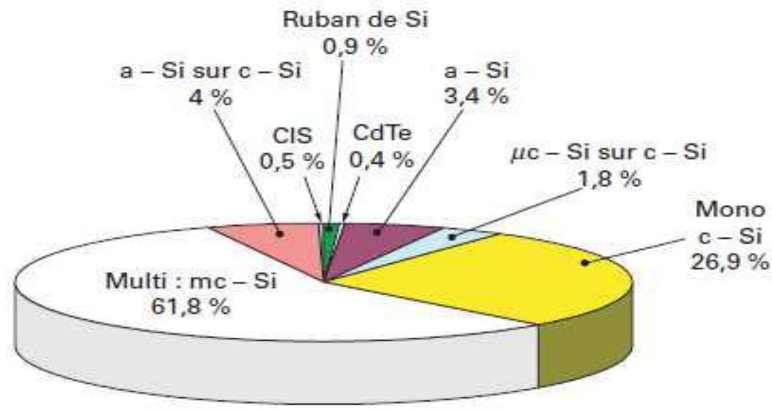

Fig. 11: Distribution of market shares of the major photovoltaic cells [15]

4. Principle of solar cell operation

4.1. Introduction

Photovoltaic energy conversion in solar cell consists to convert directly light of the sun into electricity. The absorption of light generates electron-hole pairs which are separated electron in the n-side and hole in the p-side of the structure of the device.

4.2. Electrical characteristics

4.2.1 The ideal solar cell

Current source connected in parallel with a rectifying diode represented an ideal solar cell as shown in Fig. 12. I-V characteristic is described by the follow equation:

$$\mathrm{I} = I_{ph} - I_0 \left(\exp\left(\frac{qV}{K_B T}\right) - 1 \right) \quad (10)$$

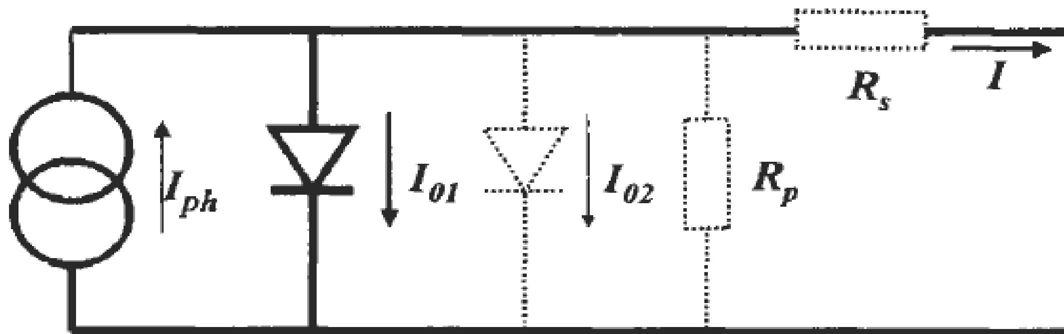

Fig. 12: The equivalent circuit of an ideal solar cell (full lines). Non-ideal components are shown by the dotted line [16]

where K_B is the Boltzmann constant, T the absolute temperature, q the electron charge, and V the terminals of the cell voltage. I_o is the saturation current which served to reminder that a

solar cell in the dark is simply a semiconductor current rectifier, or diode. I_{ph} is related to the photon flux incident on the cell.

In the ideal case, I_{sc}, short circuit current is equal to the photogenerated current I_{ph}, and V_{oc}, the open circuit voltage is given by:

$$V_{oc} = \frac{K_B T}{q} \ln(1 + \frac{I_{ph}}{I_0}) \quad (11)$$

The maximum power generated by the cell at a voltage V_m and current I_m and a fill factor FF, between 0 and 1, defines the idealism characteristic of the I-V is given by:

$$FF = \frac{V_m I_m}{V_{oc} I_{sc}} \quad (12)$$

where

$$P_{max} = V_m I_m \quad (13)$$

and

$$P_{ideal} = V_{oc} I_{sc} \quad (14)$$

4.2.2. Solar cell characteristics in Practice

In practice, I-V characteristic of solar cell differs to some extend from the ideal characteristic. A second diode with an "ideal factory of 2" is used to fit an observed curve.

The solar cell may contain series resistance (R_s) and parallel resistance (R_{sh}) leading to the follow equation:

$$I = I_{ph} - I_{01}\left[\exp\left(\frac{V + IR_s}{K_B T}\right) - 1\right] - I_{02}\left[\frac{\exp(V + IR_s)}{K_B T} - 1\right] - \frac{(V + IR_s)}{R_{sh}} \quad (15)$$

The effect of the second diode, and of then series and parallel resistances, on the I-V characteristic is shown in Fig. 13, Fig. 16 and Fig. 17, respectively.

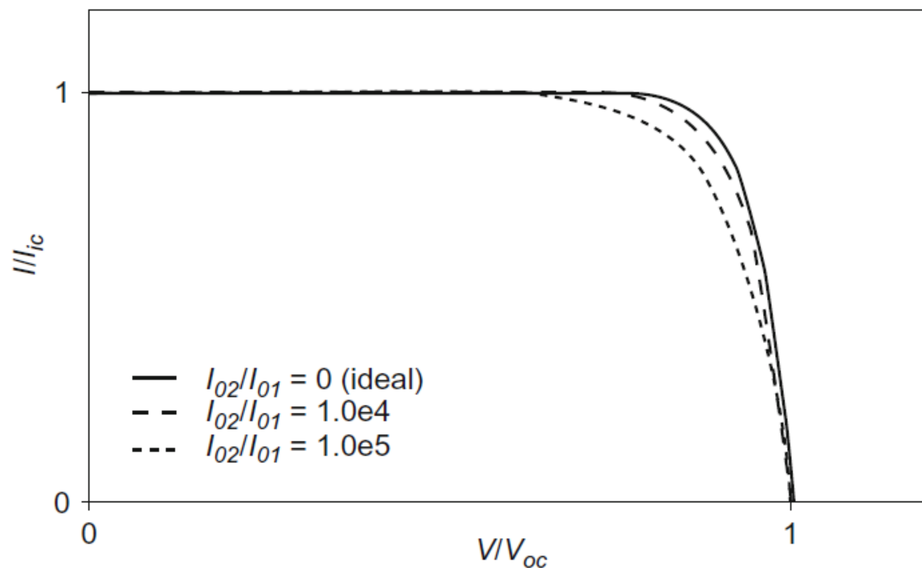

Fig. 13: I-V characteristic of the solar cell in the two diode model for three values of the ratio I_{02}/I_{01}[16]

4.2.3. The quantum efficiency and spectral response

The quantum efficiency of a solar cell is defined as the ratio of the number of electrons in the external circuit produced by an incident photon of given wavelength. Thus, one can define external and internal quantum efficiencies (denoted by EQE(λ) and IQE(λ), respectively). They differ in the treatment of photons reflected from the cell: all photons impinging on the cell surface are taken into account in the value of the EQE but only photons that are not reflected are considered in the value of IQE.

Two types of quantum efficiency of a solar cell are often considered:

- **External Quantum Efficiency (EQE)** is the ratio of the number of charge carriers collected by the solar cell to the number of photons of given energy shining on the solar cell from outside (incident photons).
- **Internal Quantum Efficiency (IQE)** is the ratio of the number of charge carriers collected by the solar cell to the number of photons of given energy that shine on the solar cell from outside and are absorbed by the cell.

The IQE is always larger than the EQE. A low IQE indicates that the active layer of the solar cell is unable to make good use of the photons. To measure the IQE, one first measures the

EQE of the solar device, then measures its transmission and reflection, and combines these data to infer the IQE.

$$\text{EQE}= \frac{Electrons/sec}{Photons/sec} \quad (16)$$

$$\text{EQE}= \frac{Current/(charge\ of\ one\ electron)}{(Total\ power\ of\ photons)/(Energy\ of\ one\ electron)} \quad (17)$$

$$\text{IQE}= \frac{Electrons/sec}{Absorbed\ photons/sec} \quad (18)$$

$$\text{IQE}= \frac{EQE}{1-Reflection-Transmission} \quad (19)$$

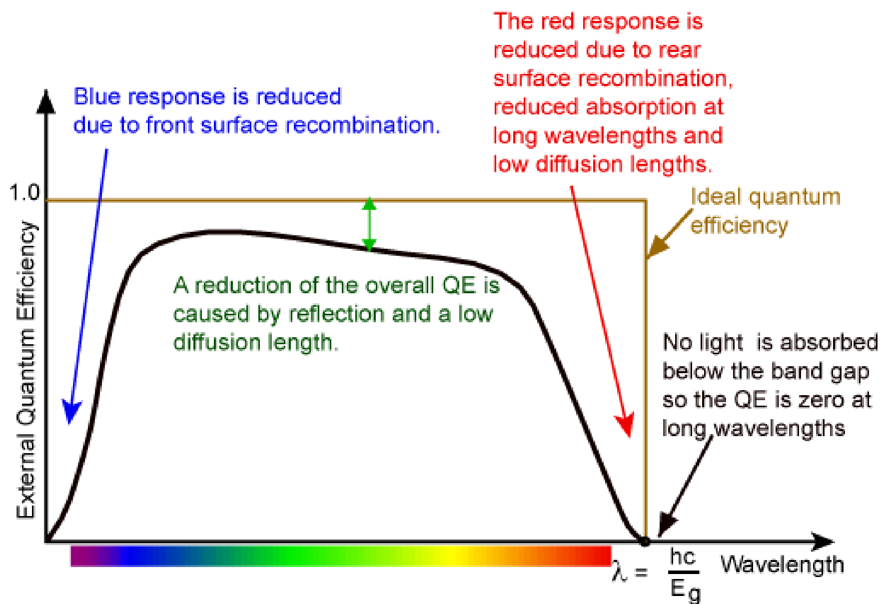

Fig. 14: Quantum efficiency of a silicon solar cell. Quantum efficiency is usually not measured much below 350 nm as the power from the AM1.5 contained in such low wavelengths is low [17].

The spectral response (denoted by SR(λ), with the units A/W) is defined as the ratio of the photocurrent generated by a solar cell under monochromatic illumination of a given wavelength, to the value of the spectral irradiance at the same wavelength. Since the number

of photons and irradiance are related, the spectral response can be written in terms of the quantum efficiency as shown in equation (20).

$$SR(\lambda) = \frac{q\lambda}{hc} QE(\lambda) = 0.808\lambda QE(\lambda) \quad (20)$$

where λ is in micrometers. Spectral response in (20) can be either internal or external, depending on which value is used for the quantum efficiency.

4.3. Typical solar cell structures

4.3.1. The p-n junction

A **p-n junction** is formed when a p-type doped portion of the semiconductor is in interface with an n-type doped portion. As a fundamental component for functions such as rectification, the p-n junction forms the basic unit of a bipolar transistor. If both the p-type and the n-type regions are of the same semiconductor material, the junction is called **homojunction.** If the junction layers are made of different semiconductor materials, it is **heterojunction.**

-Homojunction

A **homojunction** is a semiconductor interface that occurs between layers of similar semiconductor material; these materials have equal band gaps but typically have different doping. In most practical cases a homojunction occurs at the interface between an n-type (donor doped) and p-type (acceptor doped) semiconductor such as silicon, this is called p-n junction. For example: p-SnS/n-SnS.

This is not a necessary condition as the only requirement is that the same semiconductor (same band gap) is found on both sides of the junction, in contrast to a heterojunction. An n-type to n-type junction, for example, would be considered homojunction if the doping levels are different.

The different doping level will cause band bending, and depletion region will be formed at the interface.

-Heterojunction

A **heterojunction** is a semiconductor interface that formed between two semiconductors of different energy gaps, a small band gap semiconductor known as "absorber," in which optical absorption takes place and a large band gap semiconductor, known as "window," that is highly transparent to solar radiation. In the heterojunction, the front surface recombination loss is eliminated. However, interface recombination cannot be ignored. Two different kinds of configurations are possible: front-wall configuration in which photons first incident on the absorber layer, whereas they first incident on window layer in the back-wall configuration. For example: p-SnS/n-In_2S_3; p-SnS/n-CdS; p-SnS/n-ZnO etc.

-Series and shunt resistances

Solar cells generally have parasitic series and shunt resistance associated with them, as shown in Fig. 15. Both types of parasitic resistance act to reduce the fill-factor.

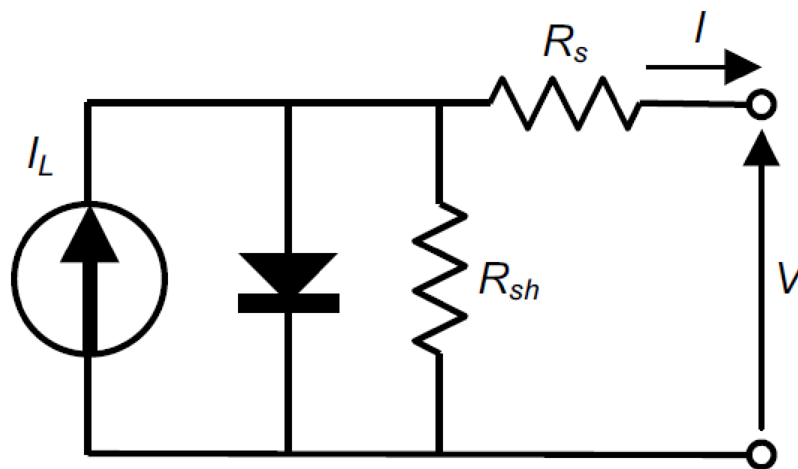

Fig. 15: Parasitic series and shunt resistances in a solar cell circuit [18]

The major contributors to the series resistance (Rs) are the bulk resistance of the semiconductor material, the metallic contacts and interconnections, carrier transport through the top diffused layer, and contact resistance between the metallic contacts and the semiconductor. The effect of series resistance is shown in Fig. 16.

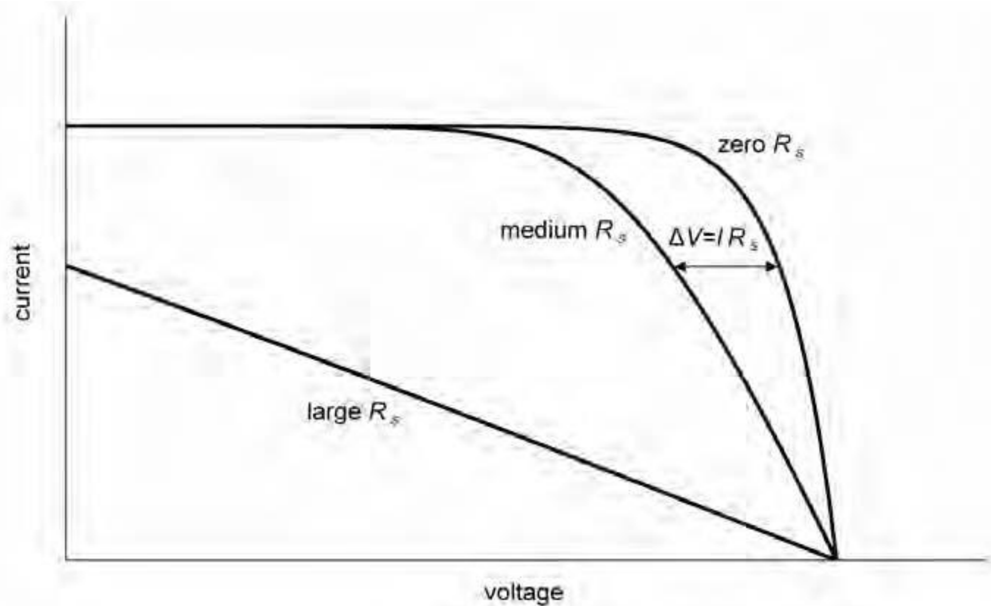

Fig. 16: The effect of series resistance on fill factor [19]

The shunt resistance (Rsh) is due to p-n junction non-idealities and impurities near the junction, which cause partial shorting of the junction, particularly near cell edges. The effect of shunt resistance is shown in Fig. 17.

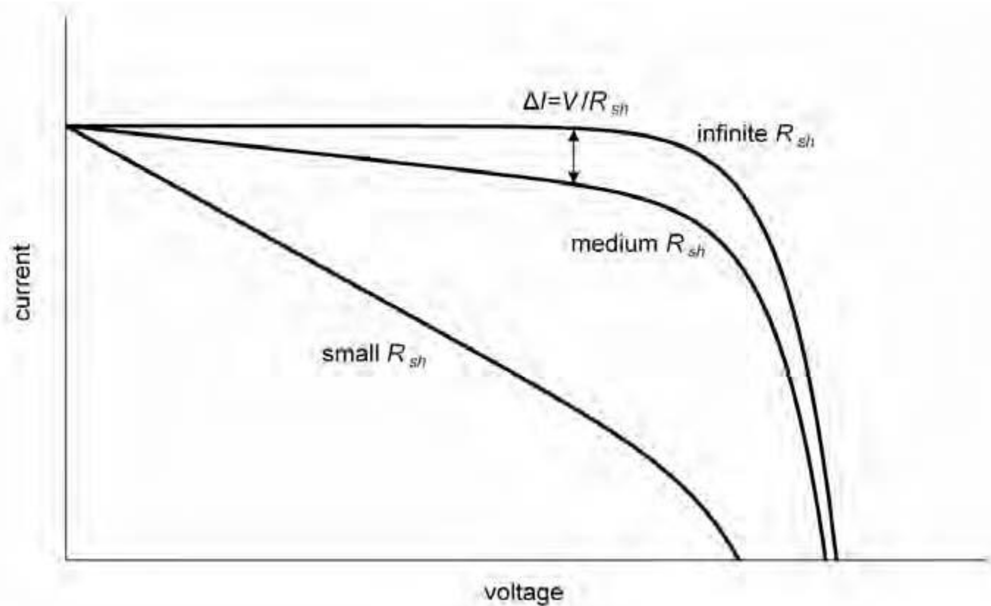

Fig. 17: The effect of shunt resistance on fill factor in a solar cell [19].

Since the fill factor determines the power output of the cell, the maximum power output is related to the series resistance, as given approximately by:

$$FF \approx FF_0(1 - r_s) \quad (21)$$

Or, empirically but more accurately

$$FF \approx FF_0(1 - 1.1r_s) + \frac{r_s}{5.4} \quad (22)$$

which is valid for $r_s \prec$ and $v_{oc} \succ 10$

$$r_s = \frac{R_s}{R_{ch}} \quad (23)$$

$$R_{ch} = \frac{V_{oc}}{I_{sc}} \quad (24)$$

5. Industrial Application

The conditions that required an alternative thin buffer layers to be used in the photovoltaic industry thin layers are:

- A high efficiency: at least comparable to that of CdS buffer layer.

- The industrial feasibility of the deposition method, a method that does not break the cycle of production, suitable for large-scale deposit and ensures reproducibility and process stability.

- The compatibility online: vacuum deposition method is preferred but more expensive which means that the research was done with other techniques such as Chemical Spray Pyrolysis.

- Stability: A long stability of cell in long-term working conditions.

6. Conclusion

As you see, facing to a major energy crisis due to a sharp increase in the world population on the one hand, the emergence of newly industrialized countries and global warming due to fossil energy sources such as oil, coal etc. in the other hand, "alternative" energy sources of such as solar, wind etc. will reduce the harmful effects of an unrestrained consumption of fossil energy sources. But the so-called renewable energies such as solar should be supported in research in order to improve their performance which is still low compared to those of fossil fuels. Indium trisulfide for example is the material used in this doctoral thesis as an

alternative buffer layer to CdS, which is a material, certainly gives good performance as a buffer layer but also it contains cadmium element that threatens environment by its toxicity.

References

[1] Document, « L'Electricité Photovoltaïque : Principe et Applications », Rapport Technique, Total Société, Edition Juin 2006.

[2] Pierre Bessemoulin et Jean Oliviéra : La météorologie huitième série-numéro 31- Septembre 2000.

[3] Benoit Brousse. Thèse de doctorat: Réalisation et caractérisation de cellules photovoltaïques organiques obtenues par dépôt physique. 2004.

[4] Jérôme Fais Introduction à la physique des semi-conducteurs-Institut de physique, université de Neuchâtel, Neuchâtel mai 2001.

[5] C. Kittel, (1972) Introduction à la physique de l'état solide, Dunod Université 630, 3ième édition, pp 367-368.

[6] Jean-Pierre et Cynthia A. Colinge. Physics of semiconductor Devices, pp.31

[7] Jean-Pierre et Cynthia A. Colinge. Physics of semiconductor Devices, pp.32

[8] P. Pistor. PhD. Formation and Electro, ic Properties of In_2S_3/Cu(In, Ga)Se_2 junctions and Related Thin Films Solar Cell. pp 7

[9] I. Konovalov. Thin Solid Films 451-452 (2004) 413

[10] D. Schock, M. Ruckh and H. W. Schock. Sol Energy Mater. Sol. Cells 41-42 (1996) 281

[11] M. Bodegard, L. Stolt and J. Hedström Proc. 12th European PVSEC (1994) 1743

[12] J. Zhao, A. Wang, P. P. Altermatt, S. R. Wenham and M. A. Green. 24% efficient perl silicon solar cell: Recent improvements in high efficiency silicon cell research. Solar En. Mat. &Sol. Cells, 1996, Vol. 41/42, pp. 87-99.

[13] S. R. Kodigala. Thin Film and Nanostructures $Cu(In_{1-x}Ga_x)Se_2$ Based Thin Film Solar Cells. Vol 35 pp. 548.

[14] Source: National Renewable Energy Lab (NREL – Kazmerski and Zweibel)

[15] J.C. Muller, Electricité photovoltaïque : filières et marchés, Technique de l'Ingénieur BE 8 579-2.

[16] Tom Markvart and Luis Castafier, "Practical Handbook of Photovoltaics: Fundamentals and Applications", British Library Cataloguing in Publication Data.

[17] https://en.wikipedia.org/wiki/Quantum_efficiency

[18] Pveducation.org

[19] S.R. Wenham, M.A. Green, M.E. Watt and R. Corkish, “APPLIED PHOTOVOLTAICS Second Edition”, First published by Earthscan in the UK and USA in 2007.

Chapter II: State of Art

1. In_2S_3 Thin Films Review

1.1. Introduction

Semiconductor compounds, III-VI, where III is In or Ga and VI is S or Se are too attractive in recent years because of their technological applications as buffer layer in solar cells. In_2S_3 (Eg>2.5eV) is used to replace the CdS in solar cells based on $Cu(In,Ga)Se_2$ [1]. It is not only used to remove cadmium which poses an environmental problem but also to enhance the transmission in the region of short wavelengths (blue). In_2S_3 is also used in other cases for preparing the $CuInS_2$ which is one of the most promising absorber layers in photovoltaic thin film.

The aim of our work is to prepare thin films of In_2S_3 by Chemical Spray Pyrolysis method and to characterize all films for use in photovoltaic solar cells as buffer layers.

1.2. In_2S_3 thin films properties

1.2.1. Crystallographic structure

In_2S_3 belongs to the III-VI family of semiconductors which are derived from semiconductor II-VI by replacing the element of column II by the element of column III. There are mainly three allotropes α, β and γ where β phase which crystallizes in quadratic form is the most stable. The hexagonal γ-In_2S_3 phase obtained at high temperature is stable above 750 °C. The β-In_2S_3 phase, which is the most stable at room temperature, has dark red color and spinel structure. The α-phase In_2S_3 cubic structure may be stable at room temperature according to the deposition method used for its development. At low temperature, α-cubic metastable phase with 5.358Å lattice parameter is formed with 70% of the indium atoms in the octahedral sites and the rest in tetra websites [2]. The α-phase passes to β-phase irreversibly at 360 °C in which 8 of the 12 tetrahedral sites are occupied by the "In" atoms and 4 vacant. All octahedral sites are occupied by atoms of "In" and we can write $In_6(In_2\square S)_{12}$ where □ are vacant sites and the parenthesis represent the tetrahedral sites [3]. A small fraction of indium atoms could leave their positions and occupy the vacant site leading to the simultaneous

existence of interstitial atoms and vacant sites resulting in a high degree of disorder in the crystal of In_2S_3 [4].

In the Table 1 are grouped structural characteristics of the main phases present in In_2S_3 layers.

Table 1: Structural characteristics of In_2S_3 allotropic phases [5]

Compound	Lattice parameters	Space groups
α-In_2S_3	a=5.358	F3m
β-In_2S_3	a=7.62 c=32.36	$I4_1$/amd
γ-In_2S_3	a=3.85 c=9.15	Pm1

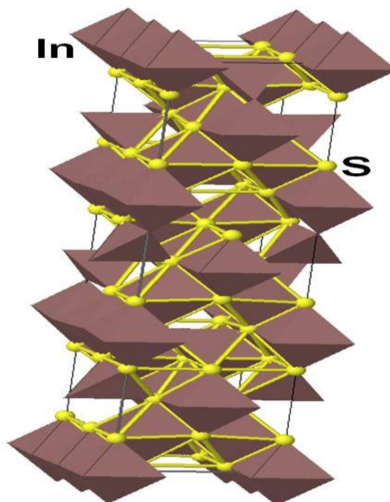

Fig. 1: Crystal structure of β-In_2S_3

1.2.2. Phases in the In-S system

The phase diagram in Fig. 2 allows us to identify the material we study in this thesis. Duffin et al [6] and Ansell et al [7] show that at thermodynamic equilibrium room temperature and atmospheric pressure there are three phases:

-InS (Orthorhombic)

-In_6S_7 (Monoclinic)

-In_2S_3 (Tetragonal / Cubic)

Gödecke et al [8] who established this diagram shows that the stable and stoichiometric In_2S_3 phase, at room temperature, is obtained up to 420 °C and has tetragonal structure. Above 420 °C, the β-In_2S_3 phase transforms into α-In_2S_3 cubic structure up to 750 °C. Between 750 °C and the melting temperature of 1090 °C, the stable tetragonal In_2S_3 γ-phase is obtained. Generally, three changes mentioned above are based on an organization of the sulfur atoms in a cubic sub-lattice.

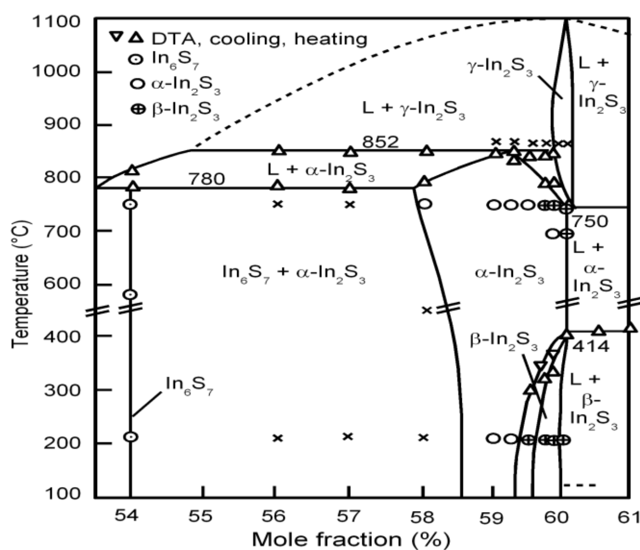

Fig. 2: Extract from the phase diagram of the In-S [8]

In α and β phases, the tetrahedral and octahedral sites are occupied by the indium atoms like in the spinel structure (e.g. $MgAl_2O_4$) however all cation sites are not completely occupied. In the γ phase, the indium atoms exclusively occupy the octahedral sites. The unoccupied sites (vacant sites) are randomly distributed over the tetrahedral sites in α-phase and the symmetry is preserved. In the β-phase, the vacant sites are ordered along the c-axis in a 4_1 helical symmetry causing a distortion of the crystal structure decreasing the symmetry resulting in the tetragonal structure.

1.2.3. Optical properties

Almost all of the II-VI compounds are semiconductor direct band gap with high absorption coefficient and emission (except $HgSe_2$ and HgTe which are semi metals). The energy gap of In_2S_3 single crystal, measured with a direct gap, is 2.0 eV at room temperature [9]. But we observe in literature a fluctuation of this energy closely related to the method of preparation. Indeed, Teny. John T. et al [10] have reported band gap energy of 2.67eV for In_2S_3 prepared

by spray pyrolysis method before annealing and after annealing at 400 °C it becomes 2.62eV due to the improvement of the crystallinity of the layer after heat treatment. R. Ranjith et al have obtained bandgap of 2.49 eV with SILAR method (2s/2w) which becomes 2.39 eV (6s/2w), which shows that the energy gap decreases when the immersion time increases [11]. Layers of In_2S_3 deposited by Atomic Layer Epitay (ALE) show an energy gap of 3.3eV, which decreases to 2.25eV after annealing [12]. Indra et al. prepared thin layer of In_2S_3 by the Chemical Bath Deposition method (CBD) with an optical gap of 2.84 eV [13]. Anita. R. Warrier et al, with the SILAR method, showed a variation of the band gap energy from 2.32eV to 2.92eV when rinsing time increases [14]. This is probably explained by the presence of oxygen in the layer. N. Barraud [15] observed an increase in the energy gap by the presence of sodium (Na) and explained this by the increase of the ionicity of the sulfur-cation bond. The shift to shorter wavelengths (blue) is explained by Kim et al as the result of excess of sulfur in the material [16]. Yoshida et al and Yasaki et al explained the expansion of the energy gap of In_2S_3 by the effect of the grain size [17].

1.2.4. Electrical properties

Studies done on In_2S_3 showed that its conductivity is still n-type, excepted one response of p-type highlighted by Becker when the nanocrystals are prepared with an excess of sulfur precursor or when InP is used as source indium. Electrical measurements on thin films prepared by the SILAR method (R.S. Man and C.D Lokhande) showed high resistivity of $1.2342.10^5$ Ω.cm [18] with a decrease of resistivity when the temperature increases confirming the semiconductor behavior material. Teny. John T. et al [10] observed that In_2S_3 layers deposited by spray are all n-type and the introduction of oxygen during annealing does not change the type of majority carriers. Kundacki M. et al [19] found high resistivity of $1.5.10^7$Ω.cm of In_2S_3 prepared by SILAR at 300K they explained by the nanocrystalline nature of film, the discontinuity of the grain boundaries and the presence of defects in the material. Bessergenev et al [20] noted that the effect of the substitution of sulfur by the oxygen in the indium trisulfide (In_2S_3) increases the conductivity. The electrical conductivity also increases with the presence of sodium (Na) in the film. When sodium is introduced into the crystal matrix, it creates a disorder by occupying certain part of the tetrahedral sites

which be explained the increase in conductivity [20]. However, N. Barreau et al noted that when the introduction of sodium exceeded certain value all the tetra sites are occupied resulting in less disorder in the material and a decrease in electrical conductivity [21]. The introduction of oxygen into the material changes the property of the grain boundaries giving as result an increase of the electrical conductivity of the layer [22].

1.2.5. Morphological properties

An excess of sulfur with respect to the stoichiometric value leads to an increase in the lattice parameters "a" and "c" [23]. B. Asenjo et al obtained a porous surface formed of spherical aggregates of micrometric of In_2S_3 prepared by electrodeposition and the annealing had no effect on the morphology [24]. Yahmadia et al observed fibrous structure with the presence of In_6S_7 secondary phase [25]. R. S. Mane and L. D. Lokhande deposited In_2S_3 thin film by SILAR, homogeneous, without cracks, and covering the whole surface of the substrate [18]. Teny. T. John et al have reported dense spray-coated layer with uniform grain sizes after annealing at 300 °C compared to as-deposited film [10]. A dense and homogeneous film was also obtained by Indra Puspitasani et al by CBD method [13]. Yoshida et al have reported large variation of the morphology with the temperature of the reaction [26].

1.2.6. Technical synthesis of In_2S_3 thin films

Panoply of techniques exists for the preparation of indium trisulfide (In_2S_3) thin films. Among them, the most used techniques are thermal evaporation [27], RF sputtering [28], Atomic Layer Deposition (ALD) [29], Metal Organic Chemical Deposition (MOCVD) [20], Chemical Spray Pyrolysis (CSP) [30], Spray Ion Layer Gas Reaction (ILGAR) [31], Spin Coating [32] and Chemical Bath Deposition (CBD) [33]. The deposition method generally has significant effect on the properties of layers and the cost of production. The chemical composition of materials depends on the deposition method used and generally when the technique requires the use of chemicals as source, residual elements are often detected in as the chore ($InCl_3$) detected in films deposited by ALD [29], Spray Pyrolysis [34] and CBD [33]. However, the techniques leading to less contamination are those of PVD (Physical Vapor Deposition) such RF sputtering and thermal evaporation.

The solar cell based on CIGS with In_2S_3 as buffer layer and prepared by CBD leads to an efficiency of 15.7%. [35]

In_2S_3 deposited by ALCVD as buffer layer leads to an efficiency of 13.5% on a small area [36]. Naghavi et al obtained with In_2S_3 and CIGS record efficiency of 16.4% using the ALCVD technology [37].

By adjusting the conditions of deposition and the thickness of In_2S_3 and $CuInS_2$ thin films prepared by Spray Pyrolysis method, Teny Theresa John et al had an efficiency of 9.5% without anti-reflection layer [38].

The record efficiencies for $Cu(In,Ga)Se_2$ with In_2S_3 as buffer layer and the best results are summarized in the Table 2.

Table 2: The efficiency obtained from CIGS absorber layer and In_2S_3 buffer layer prepared using different methods.

Deposition technique	**Research Institute**	**Efficiency (%)**	**Substrate temperature (°C)**	**Annealing (°C)**	**Référence**
ALCVD	ENSCP	16.4	220	-	[37]
CBD	ZSW	15.7[a,ls]	70	200	[39]
ILGAR	HZB	14.7*	220	-	[40]
PVD	IPE	14.8	120	200	[41]
Sputtering	ZSW	13.3	220	200	[42]
PVD	HZW	15.2*	<50	200	[43]

*Independent confirmed, [a]active area, [ls]light soaking, ENSCP: Ecole Nationale Supérieure de Chimie de Paris, ZSW: Zentrum fur Sonnenenergie-und Wassersto-Forschung, HZB: Helmholtz-Zentrum Berlin, IPE: Institut fur physikalische Elektronik, Uni Stuttgart

1.2.7. Industrial Application

The conditions required for an alternative buffer layers in order to be used in the photovoltaic industry thin films are:

- A high efficiency: at least comparable to that of CdS buffer layer.

- The industrial feasibility of the deposition method, a method that does not break the cycle of production, suitable for large-scale deposit and ensures reproducibility and stability of the process.

- The compatibility online: vacuum deposition method is preferred but more expensive which means that the research was done on other techniques such as spray pyrolysis.

- Stability: a long stability of cell in long-term working conditions.

2. SnS Thin Films Review

2.1. Introduction

SnS compound is a material used in solar cells multiple layers as absorber layer. It belongs to the IV-VI family of semiconductors of the periodic table of elements. He focused attention of many researchers because of its elements, Sn and S, which are abundant in nature, non-toxic and adequate physical properties such as its energy gap which is close to the ideal value (1.5eV), and wide absorption coefficient in order to replace absorbers as CIGS and CdTe which contain rare and toxic elements such as indium, gallium and tellurium. In addition, good quality SnS films can be fabricated at relatively low temperatures, supporting low-cost manufacturing.

2.2. SnS thin films proprieties

2.2.1. Crystallographic structure

SnS is a p-type semiconductor belonging to IV−VI compound and was first reported by the German mineralogist Herzenberg in 1932 [44]. It has an orthorhombic structure and in the structure, six S atoms surround one Sn atom in which three S atoms reside at a distance of 2.68 Å with interatomic angles of 88°100', 88°100', and 95°80'; and three additional S atoms at a distance of 3.38 Å with interaction angles of 118°, 118°, and 75° [45]. The crystallographic properties of SnS are: crystal structure−orthorhombic, lattice parameters: a = 4.32Å, b = 11.19Å, c = 3.97Å, ratio of lattice constants: a: b: c = 0.386: 1: 0.355, unit cell volume: V = 191.91Å (calculated from unit cell) [46-47]. P. K. Nair et al obtained cubic SnS thin film via two chemical routes with a lattice constant “a” of 11.587Å [48].

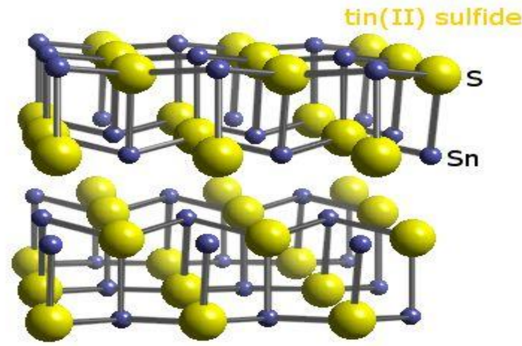

Fig. 3: Structure of SnS [49]

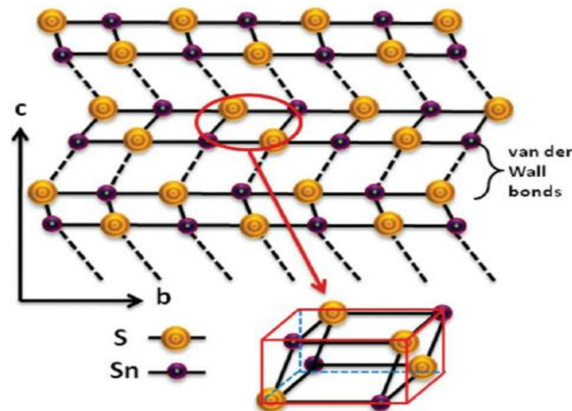

Fig. 4: Schematic of diagram of double-layered structured SnS [50]

2.2.2. Phase Diagram of the SnS System

Albers et al have presented an extensive report on the equilibrium between the solid, liquid and gaseous phases of SnS establishing the phase diagram of material forms with Sn and S as SnS [51]. This diagram is very importance since beacause it allows to understand and to know the formation domain of compounds like SnS, SnS_2, and Sn_2S_3 in terms of S: Sn ratio and temperature.

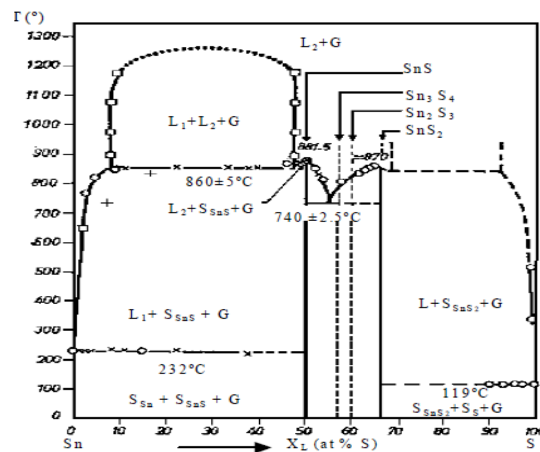

Fig. 5: Phase Diagram of the SnS System [51]

2.2.3. Optical properties

This compound has a direct bandgap near to 1.3eV [44], which is close to optimal band gap (1.5 eV) of solar cells and an indirect band gap of 1.1 eV [52] and has a high absorption coefficient ($\alpha > 10^4$ cm^{-1}) [45]. But we note in literature a fluctuation of this band gap energy closely related to the method of preparation. Indeed, B. Ghosh et al obtained band gap energy between 1.33 and 1.53eV of SnS high purity powder at substrate temperature of 250 °C and annealed at 200 °C and 300°C for two, four and six hours, and at 400 °C for two and four hours in argon ambience [53]. P. Sinsermsuksabal et al deposited SnS using Atomic Layer Deposition (ALD) at 200°C and obtained a decrease of band gap from 1.42 to 1.30 eV when the film thickness increases from 97 to 330nm [54]. Pramanick et al used Chemical Bath Deposition (CBD) to prepare n-type SnS thin films at room temperature with 1.51eV band gap energy [55]. Rodriguez et al deposited SnS by Chemical Spray Pyrolysis (CSP) technique using $SnCl_2$ and N, N-Dimethythiourea as sources of tin and sulfur, respectively and obtained a band gap of 1.70eV for films deposited at 320-396 °C [56] while Thankaraju et al obtained n-type SnS films by the same technique using $SnCl_2$ and thiourea as sources of tin and sulfur onto FTO and obtained indirect band gap of 1eV [57]. Chamberlain and Merdan obtained an indirect energy gap of 1.13 ± 0.02 eV and 1.22 ± 0.02 eV at 77K and direct energy gap of 1.43 ± 0.02 eV of single crystal specimens of p-type SnS [58].

2.2.4. Electrical properties

SnS is p-type semiconductor but some researchers convert p-type SnS into n-type by doping. Indeed, G. G. Ninan et al deposited SnS doped with copper (Cu^{2+}) using Chemical Spray Pyrolysis and obtained n-type SnS:Cu and annealing could not produce any notable effect on conductivity [59]. W. Albers et al were prepared SnS crystal by melting the components in an evacuated quartz tube at about 900 °C and obtained p-type semiconductor with a hole density between 10^{17} and 10^{18} cm^{-3} at room temperature [60]. J.S Anderson and M.C Morton measured the conductivity of stannous sulfide between ordinary temperature and 400 °C, and follow the express:

$\sigma(T)=A_1e^{-E_1/KT}+A_2^{-E_2/KT}$, where the first term, A_1, E_1 are relatively small (A_1=01-10; E_1=00.1-0.35eV), dominates the conductivity at lower temperatures, while the second term

(A_2=300-1200; E_2=ca.0.6eV) dominates the conductivity at higher temperatures. They attributed the changes in the conductivity to the stoichiometric excess of non-metal in the lattice [61].

2.2.5. Morphological properties

P. Sinsermsuksakul obtained SnS films composed by small grain with rectangular-plate shape coalescing together in films of ~90nm-thick SnS film (1000cycles). When the temperature increases from 200 to 300 °C, crystallinity of films increases with sharp crystal facets and for films deposited for 4000cycles at 120°C (~370nm) and 200 °C (~330nm) elongated platelets oriented perpendicular to the substrate surface are observed [54]. P. A. Nwafe deposited pinhole and strongly adhered SnS films to the substrate using thermal evaporation. He obtained large leaf-like grains or rice-like grains depending on the deposition conditions [62]. T. H Sajeesh prepared SnS thin films using Chemical Spray Pyrolysis with different substrate temperatures and observed smooth surface with regular spherical grains at Ts=300 °C while when Ts=375 °C sample had needle like polycristalline growth [63]. Sunil H. Chaki et al synthesized SnS thin films by Chemical Bath Deposition dip coating and SILAR techniques and obtained well uniformly covered, smooth and homogeneous films without pinholes and cracks with grain size in the nanometer (nm) range [64].

3. CdS Thin Films properties

3.1. Introduction

Cadmium sulfide (CdS) thin films belong to the II-VI family compound of periodic table of elements and having a band gap of 2.42eV. CdS polycristalline films have wide range of application especially in $CuIn_xGa_{1-x}Se_2$ and CdTe solar cells, respectively as buffer layer and window layer materials [65-66]. It is deposited by different kind of method but most effective is the Chemical Bath Deposition (CBD). Structural, optical, and electrical and morphological properties of some previous studies are illustrated in this chapter.

3.2. CdS thin films properties

3.2.1. Crystallographic structure

The CdS exhibits hexagonal and cubic structures or mixed. The former is preferable for thin film solar cell applications, despite of higher lattice mismatch of 1.2% with CIS as compared to 0.7% of cubic CdS owing to stableness [67]. Indeed, A. A Yadav et al deposited nanocrystalline cadmium sulphide thin films using Spray Pyrolysis. They observed polycristalline hexagonal structure CdS thin films with CdO as secondary phase at 300 °C. Elsewhere, they noticed that the increase in the peak intensity from 275 to 300 °C substrate temperature may be attributed to the continuous increase in film thickness [68]. M. A. Islam et al performed CdS thin films using Close Spaced Vapor Transport (CSVT), Chemical Bath Deposition (CBD) and sputtering techniques. All films have polycristalline structure with (002) as relatively highly oriented peak along "c" axis. Otherwise they observed that the number of CdS peaks found for CBD process well exceeds the peaks in films grown by CSVT and sputtering. However, peak height along the (002) plane is observed quite higher for sputtered CdS film indicating the better crystalline quality [69]. Salah Abdul-Jabbar Jassim et al study the influence of substrate temperature of CdS thin films using thermal evaporation technique for deposition. It is seen that films are polycristalline in nature with a predominant peak at 2θ=30.9° which can be assigned to CdS hexagonal plane (002). When the substrate temperature increases, the intensity of (002) peak decreases [70]. A. Ashour obtained polycristalline CdS thin films deposited by Spray Pyrolysis at various substrates temperatures (200 °C -300 °C -400 °C) with (002) as main peak with an improvement of crystallinity with temperature without formation of secondary phase [71].

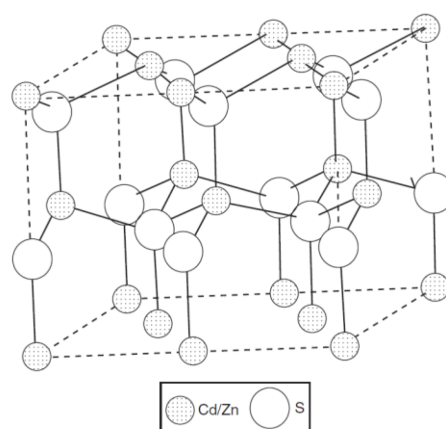

Fig. 6: Hexagonal structure of CdS.

3.2.2. Optical properties

A. A. Yadav et al observed band gap of 2.51eV at 275 °C substrate temperature and band gap increases to 2.52eV and 2.58eV for substrate temperature of 325 °C and 350 °C, respectively. They explained the higher band gap value at temperature other than 300 °C by the difference in the composition of CdS compound as observed from EDS (Energy Dispersive analysis X-ray) and smaller grain sizes [68-72]. According to M. A. Islama et al, band gaps of 2.44 eV are found for CSVT-CdS, 2.38 eV for CBD grown CdS and 2.42 eV for the films deposited by sputtering technique are founded [69]. Salah Abdul-Jabbar Jassim et al obtained the optical band gap in the range (2.3−2.43 eV) by extrapolating the linear portion of the plot $(\alpha h\nu)^2$ versus $h\nu$ at $\alpha = 0$ and they claim that those values are in good agreement with the reported ones [70-73]. A. Ashour found direct band gaps value, 2.39-2.42eV, which is in agreement with the reported value by others [71-74-75-76].

3.2.3. Electrical properties

CdS thin film is an n-type semiconductor. A. Hasnat and J. Podder study the electrical characteristic of pure CdS thin films for different thicknesses. All films showed similar temperature dependence of resistivity, i.e., a phase change occurs for all films. It can be seen that the position of the maximum resistivity i.e., phase change temperature (TP), shifts gradually towards higher temperature with increase in thickness of the film and the resistivity is found in the order of $10^{-4}\Omega$.cm at room temperature [77]. According to A. Ashour, all films exhibited semiconducting behaviors with the resistivity range of 10^{3}-10^{5} Ω.cm and the resistivity of the films was found to decrease as the substrate temperature increases due to the growth of the grain size and the improvement in film stoichiometry as indicated by the XRD pattern [71]. Referring to studies made by S. Abdul-Jabbar Jassim et al, the conductivity of the films increases, from 3.2 to 22 $(\Omega.cm)^{-1}$, with a decrease of substrate temperature due to the decrease of residual defects and the increase of crystallite size in the films; hence conductivity increases with decreasing substrate temperature [70].

3.2.4. Morphological properties

SEM (Scanning Electron Microscopy) has been proved to be a unique, convenient and versatile method to analyze surface morphology of thin film and to determine the grain size. A. A Yade et al noticed that SEM micrograph of films deposited at 300 °C was uniform,

without cracks with dense surface morphology covering entire substrate surface area with average grain size of 120nm. The elemental analysis (in at. %) of Cd (50.07%) and S (49.93%) supports the confirmation of optimized substrate temperature of 300 °C [68]. According to M. A. Islam et al, the micrographs showed that the as-deposited films are without any void, pinhole or cracks and they are covered very well the substrates. But there are some cracks observed in 400 °C-annealed films for CSVT-CdS and CBD-CdS films. EDS analysis revealed good stoichiometry of as-grown films of 49.95%-Cd and 50.05%-S for CSVT-CdS, 46.72%-Cd and 53.28%-S for CBD-CdS and 48.69%-Cd and 51.31%-S for sputtering technique [69]. S. J Ikhmayies et al prepared CdS doped with Indium (In) using Spray Pyrolysis technique and observed apparent nanocrystalline nature of films with large grains in film thickness of 500nm while large density of smaller grain and smaller density of large grain are observed in film thickness of 140nm. EDS analysis revealed 55.5 at%-S, 41.5at-Cd and 3at%-In for 140 nm-films and 46.21at%-S, 50.15at%-Cd and 36.65at%-In for 500 nm-films [78].

4. ZnO Thin Films properties

4.1. Introduction

Zinc oxide (ZnO) has attracted many scientists due to its interesting properties and the use of ZnO-based electronic and optoelectronic devices for use of ZnO as window layer in photovoltaic multilayer structures. ZnO has a band gap of 3.4eV at room temperature which corresponds to the near ultra-violet (UV) region and large exciton energy of 60meV.

4.2. ZnO thin films properties

4.2.1. Crystallographic structure

Zinc oxide is semiconductor belonging to II-VI family group. At ambient pressure and temperature, ZnO crystallizes in the wurtzite (B4 type) structure, as shown in Fig. 7. This is a hexagonal lattice, belonging to the space group $P6_3mc$, and is characterized by two interconnecting sub-lattices of Zn^{2+} and O^{2-}, such that each Zn ion is surrounded by tetrahedral of O ions, and vice-versa [79].

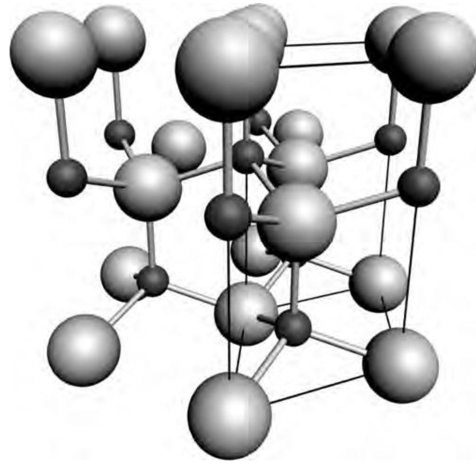

Fig. 7: The hexagonal wurtzite structure of ZnO. O atoms are shown as large white spheres, Zn atoms as smaller black spheres. One unit cell is outlined for clarity [79]

M. M. Ali prepared ZnO thin film by Chemical Bath Deposition onto glass substrates with bath temperature of 80 °C and 300 °C, 350 °C and 400 °C annealing temperatures for 12 minutes. X-ray diffraction analysis shows polycristalline and exhibit hexagonal structure with (002) as preferential c-axis orientation. 350 °C is the best annealing temperature due to the fact that it increases crystallites sizes, and decreases dislocation density and microstrain with lattice parameters of a=3.257Å and c=5.213Å which agree well with standard values [80]. M. Sahal et al prepared ZnO by sol-gel method associated with spin coating using zinc acetate dehydrate [$Zn(CH_3COO)_2).2H_2O$] as source of zinc and 2-methoxyethanol and MEA (monoethanolamine) [$NH_2C_2H_4OH$] were used as a solvent and stabilizer, respectively; [$Al(NO_3)_3.9H_2O$] was used as dopant source. No significant different were observed for the undoped and Al-doped ZnO thin films with the exception of the position of the (002) dominant peak which are located at $2\theta=34.33°$ and 34.18° [81]. W. Gao and Z. Li deposited ZnO onto glass substrates with direct current (dc) or radio frequency (rf) magnetron sputtering using Zn or ZnO target. All films exhibit (002) preferential orientation with clear peak shape and high intensity, and Al-doping decreased the intensity of (002) to a certain degree [82]. P. Kandasamy and A. Lourdusamy were deposited ZnO thin films by Chemical Spray Pyrolysis (CSP) technique using zinc acetate dihydrate solution on microscopic glass substrates by varying the precursor concentration (0.1 to 0.3 M). All diffractograms of the prepared films clean indicate the polycristalline nature of ZnO films with prominent diffraction peak from plan (002) on self-texturing phenomenon [83].

4.2.2. Optical properties

M. M. Ali obtained the band gap of ZnO films of 3.32eV (as-deposited at 80 °C), 3.12eV (at Ta =300 °C), 3.04eV (at Ta =350 °C) and 3.10eV (at Ta= 400 °C), respectively [80]. M. Sahal et al noticed a blue shit of the cut-off wavelength proportional to the Al doping amount. The calculated optical band gap of the samples varies, depending on the Al concentration, from 3.25eV for undoped ZnO films to 3.53eV for 3% of Al concentration [81]. T. Ning et al studied the optical characterization of ZnO thin films deposited by RF magnetron sputtering method onto amorphous glass substrates and found an optical forbidden band gap about 3.22-3.32eV [84]. P. Kandasamy and A. Lourdusamy observed a blue shift in band edge. The band gap increased from 2.9 to 3.20eV when the concentration was changed from 0.1 to 0.3 M and the widening band gap is attributed primarily to the Moss- Burstein shift in the semiconductor [83]. A. Maldonado et al prepared ZnO doped with chromium (Cr) by Spray Pyrolysis using a solution of zinc acetate dissolved in a mixture of deionized water, isopropyl alcohol, and acetic acid ~3:5:2 volume proportion, respectively. A high transmittance on the order of 80% is found in all films, which makes them adequate as transparent films and band-gap energy of 3.3eV was calculated from the graph of the squared absorption coefficient versus photon energy [85].

4.2.3. Electrical properties

The studies of ZnO shows that the conductivity is generally n-type but after doping with certain element it is possible to get the p-type. Indeed, S. Jeon et al studied the electrical properties of ZnO thin films deposited by Atomic Layer Deposition (ALD) at low temperatures. Stoichiometric n-type ZnO thin films were obtained with carrier concentration in the range of $10^{16}cm^{-3}$ and resistivity of 0.1-1Ω.cm. When the temperature of deposition was higher than 110 °C, high oxygen deficiencies and higher n-type carrier concentration up to 10^{20} cm^{-3} than films deposited at lower temperature were noticed [86]. M. Sahal et al remarked a drastically decrease of the resistivity when ZnO were doped with aluminum (Al) to reach a minimum resistivity of about 9Ω.cm for a dopant concentration of 2% and explained this resistivity diminution by electrons coming from the donor Al^{3+} ions incorporated substituting Zn^{2+} cation sites or in interstitial position [81-87]. Y. Aoun et al deposited ZnO thin films by Spray Pyrolysis technique and studies the electrical properties.

They found n-type ZnO with electrical resistivity in the order of 0.36Ω.cm [88]. R. Ding et al fabricated p-type ZnO thin films via magnetron sputtering and phosphorus diffusion. ZnO thin films changed from n-type to p-type by phosphorus diffusion from the n^+-Si substrate to the ZnO films and being activated thermally during deposition [89]. X. Li et al have demonstrated a possibility to dope as a p-type ZnO films using nitrogen and other group-V element. ZnO p-type films have been fabricated by Metal-Organic Chemical Vapor Deposition (MOCVD) using diethylzinc (DEZn) and nitric oxide (NO) as precursors [90].

4.2.4. Morphological properties

A. Bedia et al studied the morphology and optical properties of ZnO thin films deposited by Spray Pyrolysis onto glass substrates at various temperatures. They remarked that microstructure of films consists of many spherical grain uniformly distributed throughout the surface. Indeed, a high density of small grain were observed at low substrate temperature (350 °C) while when the substrate temperature increases up to 550 °C, the crystallinity quality of films is improved and large grain size obviously becomes larger [91]. According to W. Gao and Z. Li, the zinc oxide grain in the dc films grow mainly along c-axis to form a good columnar structure, while the rf film grow also along c-axis, the grain grew with less columnar structure and much diverse orientations. Then, surface morphology shows that the rf have denser feature (small gap between clusters) than the dc films [82]. According to A. Maldonado et al, ZnO:Cr thin films are grown at 475, 500 and 525 °C by Spray Pyrolysis. Scanning Electron Microscopy shows well-defined hexagonal slices appear for low-temperature regime and an increase in substrate temperature gives rise to less-faceted hexagons with a flake-like shape with average grain size around 500, 450 and 165x535nm, for films deposited at 475, 500 and 525 °C, respectively [85]. R. Yousefi, F. Jamali-Sheini prepared Cl-doped ZnO nanostructures in a horizontal furnace. Field Emission Scanning Electron (FESEM) image of undoped ZnO is micro-disks widely distributed of diagonals from 800nm to 4μm, with a thickness about 1μm and a perfect hexagonal geometry while Cl-doped ZnO nano-disks is very narrow (250-300nm) and have a hexagonal shape distributed of the diagonal [92].

5. SnS-Based Thin-Film Solar Cells

5.1. Introduction

One promising absorber material for low-cost thin-film solar cells is tin sulfide (SnS). SnS consists of earth abundant elements and has an indirect band gap of 1.07 eV with a high optical absorption constant of $\alpha > 10^4 cm^{-1}$ above 1.3 eV [93-94].

The theoretical efficiency for a single junction solar cell using SnS as a binary compound absorber material is predicted by Loferski to be 24% [95].

5.2. Previous Works SnS-based

G. R. Gopinath et al deposited polycristalline In_2S_3 thin films using Chemical Bath Deposition (CBD) onto SnS as absorber layer prepared by Thermally Evaporated in order to fabricate SnS/In_2S_3 solar cell structure. An open circuit voltage of 110mV, short circuit density of 1.98mA/cm^2, and full factor of 0.26 were observed for unoptimazed device that gave a solar conversion efficiency of 0.6%. The observed low efficiency might be due to the recombination of charge carriers at the interface due to lattice mismatch of a large conduction band offset at the interface because of the difference in electron affinity values of both the layers [96].

M. Patel and A. Ray fabricated sprayed-deposited M/SnS/In_2S_3/SnO:F/Glass (M= Cu, graphite) device in order to improve photovoltaic performance. A best result of V_{oc}=0.29V, J_{sc}=4.8mA/cm^2, and η=0.55% are found using copper contact [97].

C. Prastani et al synthesized SnS nanoparticles (NPs) by a colloidal route at low temperature and after were immersed in a CBD bath deposited In_2S_3 layer to form core/shell SnS/In_2S_3 nanoparticles by centrifugation and washed with ethanol. They observed dark conductivity of $2.310^{-7}(\Omega.cm)^{-1}$ and photoconductivity of $1.3\ 10^{-2}\ (\Omega.cm)^{-1}$ [98].

H. Li et al prepared CdS/SnS heterojunction for photovoltaic application evaporating SnS thin films onto CdS/ITO coated glass substrate. They observed that I-V characteristic curves of SnS/CdS heterojunctions were related with the thickness and annealing temperature of CdS buffer layer and the optimum thickness and annealing temperature of CdS buffer layer were 50nm and 350°C, respectively. The best device had V_{oc}=0.087V, J_{sc}=0.096mA/cm^2, and η=0.0025% under AM1.5 [99].

K. T. Ramakrishna Reddy et al elaborated polycristalline thin film of tin sulphide (SnS) using Spray Pyrolyis technique. Heterojunction solar cells were fabricated using sprayed SnS as absorber layer and indium doped cadmium sulphide (CdS:In) as window layer (p-SnS/n-CdS junction). The best cell had an open circuit voltage of 260mV, a short circuit current density of 9.6mA/cm^2, a fill factor of 0.53 and a conversion efficiency of 1.3%. This low value of the efficiency could be due to shunting and series resistance problems with calculated value of the series resistance approximately 23Ω [100].

A. R. Garcia-Angelmo et al fabricated stainless steel/SnS/CdS/ZnO/ZnO:Al structure solar cell and report open-circuit voltage (V_{oc}) of 0.470V, short-circuit current density (J_{sc}) of 6.2mA/cm^2, and an efficiency of 1.28% in an area of cell of 1cm^2 under standard conditions [101].

A. Schneikart et al prepared thin films solar cell with SnS as absorber layer material by thermal evaporation of SnS. ZnO:Al coated glass was used as front contact with an intrinsic ZnO buffer layer and/or CdS window layer and gold back contact. The CdS/SnS solar cell showed an open circuit voltage of 217mV, a short circuit current density of 19mA/cm^2, and a conversion efficiency of 1.6% [102].

B. Ghosh et al fabricated SnS/ZnO heterojunction for photovoltaic application using electrodeposited ZnO film onto ITO substrate. Glass/ZnO/SnS/In back contact configuration was used. They observed V_{oc} of 0.12V, J_{sc} of 39.91μA, FF of 0.33, and η of 0.003% in an area cell of 0.4cm^2 [103].

P. Sinsermsuksakul et al overcame efficiency limitation of SnS-based solar cell using p-SnS/n-Z(O,S) junction and obtained an efficiency of over 4.4%, which is more than twice as large as the highest efficiency obtained previously by solar cells using SnS absorber layer reducing inter alia recombination near the SnS-Zn(O,S) junction by inserting a few monolayers of SnO_2 between these layers [104].

6. Conclusion

We have seen in this chapter previous work done on the various materials used in this thesis, namely In_2S_3, SnS, CdS and ZnO, in order to compare them with the results obtained in Chapter IV.

References

[1] S. Spiering, D. Hariskose, M. Powalla, N. Nagahavi and D. Lincot, Thin Solid Film 431-432, (2003) 359

[2] R. Diehland and R. Nitsche, J. Cryst. Growth 20 (1973) 38

[3] R. S. Becker, T. Zheng, J. Elton and M. Saeki, Solar Energy Matter 13(1986) 97

[4] M. Rehwald, G. Harbeke, J. Phys. Chem. Solids. 26 (1965)

[5] N. Kamoun, Doctorat d'état, (2000).

[6] W. Duffin and J. Hogg, « Crystalline phases in the system In-In_2S_3, » Acta crystallografica, vol. 20, pp. 566-569, 1966

[7] H. Ansell and R. Boorman, « Phase relationships in the In-S system », Journal of the Electrochemical Society », Vol. 118, n° 1, pp. 133-136, 1971

[8] T. Gödecke and K. Schubert, « On the Phase Diagram InS_M », Zeitschrift für Metallikunde », vol. 76, pp. 358-364, May 1985.

[9] J George, K. S. Joseph, B. Prodeepetal. « Reactively evaporated films of indium sulphide ». Phys Status Solidi, App, Res 1988, 106:123.

[10] T. T. John, T. Abe and Y. Kashiwaba, « Spray pyrolyzed β-In_2S_3 thin films: Effect of post deposition annealing. Vacuum 80(2006) 870-875.

[11] R. R. Ranjith, T. T. John, C. S. Kartha, K. P. Vijayakumer, T. Abe and Y. Kashiwaba. « Post deposition annealing effect on In_2S_3 thin films deposited using SILAR technique ». Materials Science in Semiconductor Pocessing 10(2007) 49-55.

[12] E. B. Yousfi, B. Weinberger, F. Donsanti, P. Cowache and D. Lincot, thin solid films. 387 (2001) 29.

[13] I. Puspitasari, T.P Gujar, Kwang-Deog Jung, Oh-Shim Joo. « Simple Chemical method for nanoporous network of In_2S_3 platelets for buffer layer in CIS solar Cells ». Journal of Materials processsing technology 201 (2008) 775-779.

[14] A. R. Warier, T. T. John, K. P. Vijayakumar, C. S. Kartha. « Structural and optical Properties of Indium Sulfide Thin films Prepared by SILAR Technique ». The open condensed Matter Physics Journal, 2009, 2, 9-14.

[15] N. Barreau, J. C. Bernede and S. Marsillac, Journal of Crystal Gowth 241 (2002) 51.

[16] W. T. Kim and C.D. Kim, J. App. Phys. 60 (1986) 2631.

[17] Y. Yasaki, N. Csonoyama and T. Sakata, J. Electroanal. Chem 469 (1999) 215.

[18] R. S. Mane, C. D. Lokhande. « Studies on structural, optical and electrical properties of indium sulfide thin films ». Materials Chemistry Physics 78 (2002) 15-17.

[19] M. Kundakci. « The annealing effect on the structural, optical and photoelectrical properties of $CuInS_2/In_2S_3$ films ».Physioca B 406 (2011) 2953-2961.

[20] V. G Bessergenew, E. N. Ivanova, Yu. A. Kovalevskaya, S. A. Gemilov, V. Nkirichenko and S.V. Larinov, Inorg. Mater 32 (1996) 592-

[21] N. Barreau, J. C. B ernede, S. Marsillac, C. Amory and W. N. Shafarman, thin Solid Films 431-432 (2003) 326.

[22] N. Barreau, S. Marsillac, Dalbertini and J. C. Berned, Thin Solid Films 403-404 (2002) 331.

[23] W. T. Kim and C. D. Kim, J. App. Phy 60 (1986) 2631.

[24] B. Asenjo, A. M. Chaparoo, M. T. Gutierrez, J. Herrero, C. Maffiotte. « Study of the Electrodeposition of In_2S_3 thin films ». Thin Solid Films 480-481 (2005) 151-156.

[25] B. Yahmadia, N.Kamonna, R. Rennaceura, M. Mnarib, M. Dachraouib and K. Adelkrim. Thin Solid Films 473 (2005) 201.

[26] T. Yoshida, K. Yamaguchi, H. Toyoda, K. Akao, T. Sugiura and H. Minoura, NJ, 97-20 (1997) 37.

[27] A. A. El. Shazly, D. Abdelkady, H. S. Metoually, M. A.M. Segman, J. Phys. Condens. Matter 10(1998) 5943.

[28] D. Harisko et al, Proceedings of 19 the European Photovoltaic Solar Energy Conference, Paris, France (2004).

[29] T. Asikainen, M. Ritala, M. Leskela.APP. Surf. Sci. 82/83 (1994) 122.

[30] Teny Theresa John, PhD Thesis, Cochin University of Science and Technology, India (2004).

[31] N. A Allsop, A. Schonmann, A. Belaidi, H. J. muffler, B. Mertesacker, W. Bohne, E. Dtrub, J. Rohrich, M.C Lux-Steiner, C. H. Fisher, Thin Solid Films. 513 (2006) 52.

[32] Y. Yasaki, N. Sonoyama, T. Sakata, J. Electroanal. Chem. 469 (1999) 116.

[33] J. Kessler et al, Proceedings of 23rd IEEE Photovoltaic specialists Conference (19993).

[34] M. Mathew, phD Thesis, Cochin University of Science and Technology India (2009).

[35] D. Braunger, D. Hariskos, T. Watre and H.W. Schock, Sol Energy Mater. Sol Cells, 40 (1996) 97.

[36] E. B Yousfi, B. Weinberger, F. Donsanti, P. Cowache and D. Lincot, Thin Solid Films 387 (2001) 29.

[37] N. Naghavi, S. Spiering, M. Powalla, B. Cavana and D. Lincot, Prog. Photovolt : Res. App. 11 (2003) 437.

[38] T. T. John, M. Mathew, C. S. Kartha, K. P. Vijayakumar, T. Abe and Y. Kashiwaba. Solar Energy Materials Solar Cells 89 (2005) 27-36.

[39] D.Hariskos, M. Ruckh, U. Rühle, T. Walter, J. Hedström, and L. Stolt. Solar Energy Materials and Solar Cells, vol 41/42, pp. 345-353, 1996.

[40] N. Allsop, A. Schönmann, H-H Muffler, M. Bär, M. Lux-Steiner, and C-H. Fisher. Progression Photovoltaics: Research and Applications 52, vol. 13, pp. 607-616, 2005.

[41] A. Strohm, L. Eisenman, R. Gebhardt, A. Harding, T.Schlötzer, D. Abou-Ras and H. Schock, Thin Solid Films, vol. 480-481, pp. 162-167, 2005.

[42] D. Hariskos, R. Menern, E. LMotter, S. Spiering and M. Powalla. 20th European Photovoltaic Solar Conference (Barcolona, Spain), pp.1713-1716.

[43] P. Pistor, R. Caballero, D. Hariskos, V. Izquierdo-Roca, R. Wächter, S. Schorr and R. Klenk. « Quality and Stalibility of compound indium sulfide as source material for buffer layers in Cu(In, Ga)Se_2 Solar Cells », Solar Energy Materials and Solar Cells , vol .93, pp. 148-152, January 2009.

[44] Herzenberg R (1932) Rev Miner 4:33

[45] Juarez AS, Silver AT, Ortiz A (2005) Fabrication of SnS_2/SnS heterojunction thin film diodes by plasma-enhanced Chemical vapor deposition. Thin Solid Films 480–481: 452–456

[46] P. Ramdohr. "Vorkommen und Eigenschaften des Herzenbergits". In: Zeitschrift für Kristallographie 92 (1935), pp. 186–189.

[47] A. Sugaki, A. Kitakaze, and H. Kitazawa. "Synthesized tin and tin-sulfide minerals; Synthetic sulfide minerals (XIII)". In: Science Reports of the Tohoku University 16(3) (1985), pp. 199–211.

[48] P. K. Nair, A. R. Garcia-Angelmo, and M. T. S. Nair. "Cubic and orthorhombic SnS thin-film absorbers for tin sulfide solar cells", Phys. Status Solidi A 213, No. 1, (2016), pp. 170–177.

[49] https://www.webelements.com/compounds/tin/tin_sulphide.html

[50]N. Koteeswara Reddy, M. Devika & E. S. R. Gopal, "Review on Tin (II) Sulfide (SnS) Material: Synthesis, Properties, and Applications", Critical Reviews in Solid State and Materials Sciences, 0:1−40, 2015.

[51] W. Albers, C. Haas, H. J. Vink, and J. D. Wasscher. "Investigations on SnS". In: Journal of Applied Physics 32 (1961), pp. 2220–2225.

[52] http://pv.mit.edu/home/research/thin-film/

[53] B. Ghosh; R. Bhattacharje; P. Banerjee, S. Das, Applied Surface Science **257** (2011) 3670-3676

[54] Sinsermsuksakul, Prasert, thesis, "Development of Earth-Abundant Tin(II) Sulfide Thin-Film Solar Cells by Vapor Deposition", Doctoral dissertation, Harvard University, 2013.

[55] P. Pramanik, P. K Basu, S. Biswas, Thin Solid Films **150** (1987) 269-276.

[56]M. C. Rodriguez, H. Martinez, A.S. Juarez, J. C. Alvarez, A. T. Silver, M. E. Calixto, Thin Solid Films 517 (2009) 2497-2499.

[57] B. Thangaraju, P, Kaliannan, J. Physics D: Applied Physics **33** (2000) 1054-1059.

[58] J. M. Chamberlain and M. Merdan. "Infrared photoconductivity in p-SnS". In: Journal of Physics C: Solid State Physics 10 (1977), pp. L571–L574.

[59] G. G. Ninan, C. Sudha Kartha and K.P. Vijayakumar, "On the preparation for n-type SnS:Cu using chemical spray pyrolysis for photovoltaic application : Effect of annealing", Solar Energy Material and Solar Cell, 157 (2016), pp.229-233.

[60] W. Albers, C. Haas, F. van der Maesen**, "**The preparation and the electrical and optical properties of SnS crystals", Journal of Physics and Chemistry of Solids, Volume 15, Issues 3–4, October 1960, pp. 306-310

[61] J. S. Anderson and M. C. Morton. “The electrical conductivity of stannous sulphide”. In: Proceedings of the Royal Society of London. Series A. Mathematical and Physical Sciences 184 (1945), pp. 83–101.
[62] Patrick Akata Nwofe, thesis, “Deposition and Characterization of SnS Thin Films for Application in Photovoltaic Solar Cell Devices”, University of Northumbria at Newcastle, 2013.
[63] T. H. SAJEESH, thesis, “Spray Pyrolysed Tin Chalcogenide Thin Films: Optimization of optoelectronic properties of SnS for possible photovoltaic application as an absorber layer”, Cochin University of Science and Technology, May 2012.
[64] Sunil H. ChakiŽ, Mahesh D. Chaudhary, and M. P. Deshpande, “SnS thin films deposited by chemical bath deposition, dip coating and SILAR techniques”, Journal of Semiconductors, Vol. 37, No. 5, 053001-1-9
[65] T. Negami, Y. Hashimoto, and S. Nishiwaki, Sol. Energy. Mater. Sol. Cells 67, 331 (2001).
[66] M. Tsuji, T. Aramoto, H. Ohyama, T. Hibino, and K. Omura, J. Cryst. Growth 214, 1142 (2000).
[67] Subba Ramaiah Kodigala, “Thin Films and Nanostructures Cu(In1_xGax)Se2 Based Thin Film Solar Cells”, Volume 35.
[68] A.A. Yadav*, M.A. Barote, E.U. Masumdar, “Studies on nanocrystalline cadmium sulphide (CdS) thin films deposited by spray pyrolysis”, Solid State Sciences 12 (2010), pp. 1173-1177.
[69] M.A. Islama, M.S. Hossainb, M.M. Aliyub, P. Chelvanathana, Q. Hudaa, M.R. Karimc, K. Sopiana, N. Amina, “Comparison of Structural and Optical Properties of CdS Thin Films Grown by CSVT, CBD and Sputtering Techniques”, PV Asia Pacific Conference 2012, Energy Procedia 33 (2013), pp. 203 – 213.
[70] Salah Abdul-Jabbar Jassim, Abubaker A. Rashid Ali Zumaila , Gassan Abdella Ali Al Waly, “Influence of substrate temperature on the structural, optical and electrical properties of CdS thin films deposited by thermal evaporation”, Results in Physics 3 (2013), pp. 173–178.
[71] A. ASHOUR, “Physical Properties of Spray Pyrolyzed CdS Thin Films”, Turkish Journal of Physics, 27 (2003), pp. 551-558.
[72] G. Hode, A. Albu Yaran, F. Decker, P. Mutuke, “Three-dimensional quantum-size effect in chemically deposited cadmium selenide films”, Phys. Rev. B 36 (1987) 4215-4222.
[73] Sahay PP, Nath RK, Tewari S, “Optical properties of thermally evaporated CdS thin films”, Cryst. Res. Technol. 42, No. 3, pp.275 – 280.
[74] B. Su and K.L. Choy, Thin Solid Films, 359, (2000), 160.
[75] A. Ashour, N. El-Kadry and S.A. Mahmoud, Thin Solid Films, 269, (1995), 117.
[76] U. Pal, R. Silva-Gonzalez, G. Martinez-Montes, M. Gracia-Jimenez, M.A. Vidal and Sh. Torres, Thin Solid Films, 305, (1997), 345.
[77] A. Hasnat and J. Podder, “Optical and Electrical Characteristics of pure CdS thin films for different thichness”, Journal of Bangladesh Academy of Sciences, Vol. 37, No. 1, 2013, pp. 33-41.
[78]Shadia J. Ikhmayies, Hassan K. Juwhari, Riyad N. Ahmad-Bitar, “Nanocrystalline CdS:In thin films prepared by the spray-pyrolysis technique”, Journal of Luminescence 141 (2013), pp.27–32.

[79] Jagadish and S. Pearton, Zinc Oxide Bulk, Thin Films and Nanostructures, Processing, Properties, and Applications, 2006.
[80]Mohammad M. Ali, “Characterization of ZnO thin films grown by chemical bath deposition”, Journal of Basrah Researches ((Sciences)) Volume 37. Number 3 A/ 15 June ((2011)).
[81]M. Sahal, B. Hartiti, A. Ridah, M. Mollar and B. Mari, “Structure, electrical and optical of ZnO thin films deposited by sol-gel method”, Microelectronics Journal, 39 (2008) 1425-1428.
[82] Wei Gao, Zhengwei Li, “ZnO thin films produced by magnetron sputtering”, Ceramics International 30 (2004) 1155–1159.
[83]Prabakaram Kandasamy and Almalraj Lourdusamy, “Studies on zinc oxide thin films by Chemical Spray Pyrolysis technique”, International Journal of Physical Sciences, Vol9 (11), pp. 261-266, 16 June, 2014.
[84] TANG Ning, WANG JinLiang, XU HengXing, PENG HongYong & FAN Chao, “Optical characterization of ZnO thin films deposited by RF magnetron sputtering method”, Science in China Series E: Technological Sciences, vol. 52 | no. 8, Aug. 2009, pp. 2200-2203.
[85]A. Maldonado,a) M. de la L. Olvera, and R. Asomoza, “Characteristics of ZnO:Cr thin films deposited by spray pyrolysis”, Journal of Vacuum Science & Technology A, 18 (5) Sep/Oct 2000,pp. 2098-2101.
[86] Sunyeol Jeon, Seokhwan Bang, Seungjun Lee, Semyung Kwon, Wooho Jeong, Hyeongtag Jeon, Ho Jung Chang, and Hyung-Ho Park, “Structural and Electrical Properties of ZnO Thin Films Deposited by Atomic Layer Deposition at Low Temperatures”, Journal of The Electrochemical Society, 155-10-2008-pp.H738-H743.
[87] Su-Shia Lin, Jow-Lay Huang, P. Sajgalik, “The properties of heavily Al-doped ZnO films before and after annealing in the different atmosphere”, Surface & Coatings Technology 185 (2004), pp. 254 – 263.
[88] Yacine Aoun; Ž, Boubaker Benhaoua , Brahim Gasmi , and Said Benramache, “Structural, optical and electrical properties of zinc oxide thin films deposited by a spray pyrolysis technique”, Journal of Semiconductors, Vol. 36, No. 1, January 2015.
[89] Ruiqin Ding, Huiqun Zhu, Qingguang Zeng, “Fabrication of p-type ZnO thin films via magnetron sputtering and phosphorus diffusion”, Vacuum 82 (2008), pp. 510–513.
[90] X. Li, S.E. Asher, B.M. Keyes, H.R. Moutinho, J. Luther, and T. J. Coutts, “p-TYPE ZnO THIN FILMS GROWN BY MOCVD”, Prepared for the 31st IEEE Photovoltaics Specialists Conference and Exhibition Lake Buena Vista, Florida January 3–7, 2005.
[91] A. Bedia, F.Z. Bedia, M. Aillerie, N. Maloufi, B. Benyoucef, “Morphological and Optical properties of ZnO thin films prepared by spray pyrolysis on glass substrates at various temperatures for integration in solar cell”, The International Conference on Technologies and Materials for Renewable Energy, Environment and Sustainability, TMREES15, Energy Procedia 74 (2015), pp.529 – 538.

[92] Ramin Yousefi, Farid Jamali-Sheini, “Effect of chlorine ion concentration on morphology and optical properties of Cl-doped ZnO nanostructures”, Ceramics International 38 (2012), pp. 5821–5825.
[93] Vidal J, Lany S, d’Avezac M, Zunger A, Zakutayev A, Francis J and Tate J 2012 Appl. Phys. Lett. **100** 032104
[94] Reddy K T R, Reddy N K and Miles R W 2006 Sol. Energy Mater. Sol. Cells 90 3041.
[95] Loferski J J 1956 J. Appl. Phys. 27 777
[96] G. R. Gopinath and K. T. Ramakrishna Reddy, “Growth of Polycrystalline In_2S_3 Thin Films by Chemical Bath Deposition Using Acetic Acid as a Complexing Agent for Solar Cell Application”, Hindawi Publishing Corporation ISRN Condensed Matter Physics Volume 2013, Article ID 140230, 6 pages.
[97] Malkeshkumar Patel and Abhijit Ray, “Junction and Back Contact Properties of Spray-Deposited M/SnS/In_2S_3/SnO2:F/Glass (M = Cu, Graphite) Devices: Considerations to Improve Photovoltaic Performance”, Journal of ELECTRONIC MATERIALS, Vol. 44, No. 1, 2015.
[98] C. Prastani, M. Nanu, D.E. Nanu, R. E. I. Schropp and J. K. Rath, “Development of SnS/In_2S_3 core-shell nanoparticles for solar cell application”, Photovoltaic Specialists Conference (PVSC), 2013 IEEE 39th.
[99] Hongnan Li, Shuying Cheng*, Jie Zhang*, Weihui Huang, Haifang Zhou, Hongjie Jia, “Fabrication of CdS/SnS Heterojunction for Photovoltaic Application”, World Journal of Condensed Matter Physics, 2015, 5, pp.10-17.
[100] K.T. Ramakrishna Reddy, N. Koteswara Reddy, and R.W. Miles, “Photovoltaic properties of SnS based solar cell”, Solar Energy Materials & Solar Cells 90 (2006), pp. 3041–3046.
[101] A. R. Garcia-Angelmo, R. Romano-Trujillo, J. Campos-_Alvarez, O. Gomez-Daza, M. T. S. Nair, and P. K. Nair, “Thin film solar cell of SnS absorber with cubic crystalline structure”, Phys. Status Solidi A 212, No. 10, (2015), pp. 2332–2340.
[102] A Schneikart, H-J Schimper, A Klein and W Jaegermann, “Efficiency limitations of thermally evaporated thin-film SnS solar cells”, J. Phys. D: Appl. Phys. 46 (2013) 305109 (7pp).
[103] Biswajit Ghosh, Madhumita Das, Pushan Banerjee and Subrata Das, “Fabrication of the SnS/ZnO heterojunction for PV applications using electrodeposited ZnO films”, Semicond. Sci. Technol. 24 (2009) 025024 (7pp).
[104] Prasert Sinsermsuksakul, Leizhi Sun, Sang Woon Lee, Helen Hejin Park, Sang Bok Kim, Chuanxi Yang , and Roy G. Gordon, “Overcoming Efficiency Limitations of SnS-Based Solar Cells”, Adv. Energy Mater. 2014, 1400496.

Chapter III: Experimental and Characterization Techniques

1. Development techniques of thin film

1.1. Introduction

To develop thin semiconductor layers several techniques are used: CBD, electrodeposition, RF sputtering, SILAR, Spray Pyrolysis, Vacuum Evaporation etc. We chose Chemical Spray Pyrolysis to prepare thin films for its simplicity, its ease of use and cheap experimentation and it allows us to obtain good quality films on large surfaces for photovoltaic application. This deposition method was created by Chamberlin and Skarman in 1966 to deposit cadmium sulfide (CdS) thin films for photovoltaic application [1]. Today the Spray Pyrolysis is used to deposit buffer layers, absorbent layers, layers used as optical window and transparent conductive oxides.

1.2. Chemical Spray Pyrolysis technique

1.2.1. Working principle of Chemical Spray Pyrolysis

In principle Chemical Spray Pyrolysis is a simple technique where, generally, aqueous solution containing elements to be deposited via salt is sprayed onto a hot substrate. The droplets of the solution when they reach the hot surface undergoing pyrolytic decomposition and form thereby the desired compound. Other product and excess solvent evaporate. The hot substrate provides the thermal energy required for decomposition and then the recombination of the various elements to form the desired layer.

The crucial step is the control of the chemical decomposition of the precursor to form the thin layer on the substrate. In the case of an aerosol consisting of droplets, the main difficulty in Spray Pyrolysis reside in the completion of an ideal adsorption of chemical species through the substrate since this adsorption is directly related to the good solvent evaporation. If this evaporation occurs too late during the process, the precursor and solvent reach the substrate in the liquid state and then generate a spreading of the droplet: this is the situation (I). This process promotes layers which can be thicker and therefore prone to high porosities

or even cracks. If evaporation takes place too early, the chemical reaction can begin before the precursors reach the substrate. This leads to the formation of solid particles of the desired material: this corresponds to the case (IV). The resulting deposit is porous and has low adhesion to the substrate.

The case (II) and (III) are the best settings for Spray Pyrolysis deposition, since evaporation of the solvent and/or precursors take place in appropriate moment. Both cases show excellent adhesion to substrates.

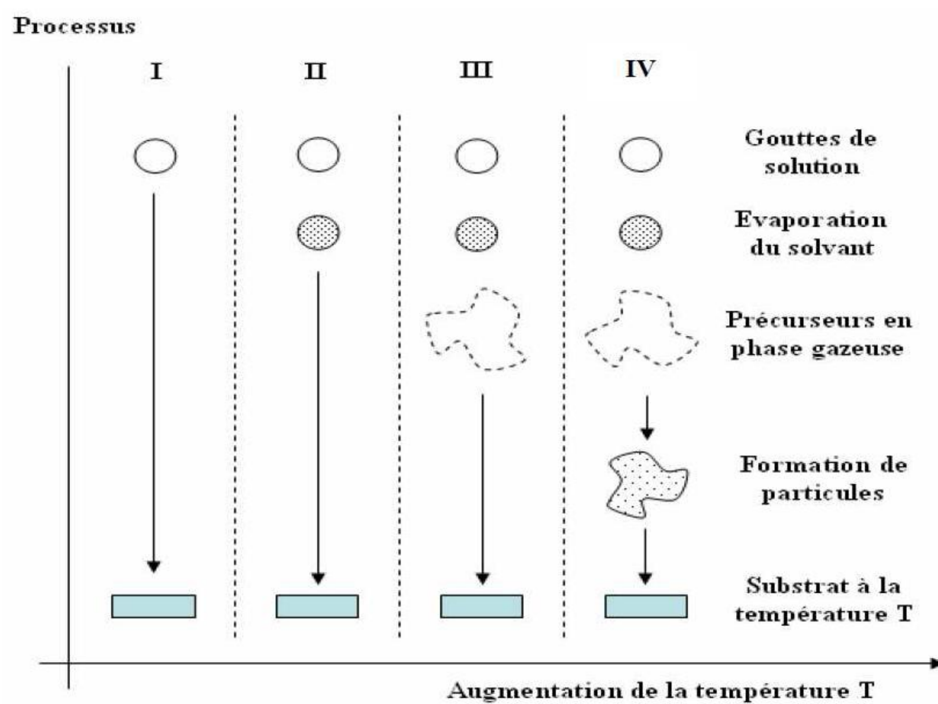

Fig. 1: Main reaction cases encountered in Spray Pyrolysis [2]

The technique has some advantages:

- The Technique is simple and cheap. The technique can be used for the deposition on large surfaces. This is a technique used at room temperature and which allows thin films of quality comparable to those of other conventional techniques.
- The Chemicals used are either inorganic or organic and are not expensive compared to pure products used in other techniques.
- The Properties of thin films can be modified by varying the ratios of the various constituents in the starting solution. However, having stoichiometry is a serious problem in some cases. To balance the deficit component caused by evaporation of the

latter during the experiment, excess product is deliberately used in the starting solution.

The technique has some drawbacks:

The limits of this deposition technique are generally the small size of the grains obtained compared to other vacuum deposition techniques. The properties of thin films obtained by the Spray Pyrolysis method are influenced by the substrate temperature, the nature of the chemicals, the concentration ratio of the different elements in the starting solution and the flow rate. Recently researchers are interested more and more in Spray Pyrolysis technique with oscillation of the substrate surface, the nozzle or both at the same time in order to obtain layers with uniform thicknesses. The substrate temperature, may be, is one of the most important parameters to obtain thin films of good quality. The structural, optical, electrical, morphological etc. properties of layers depend strongly on the nature and the substrate temperature. The composition of the initial solution, the concentration ratio, the doping elements, the type of solvent, the pH of the solution controls the properties of the deposited thin films. The flow rate, the type of carrier gas used, the heat treatment (annealing) are other parameters that also have significant effect on the properties of the deposited films.

1.2.2. Experimental Apparatus

Figure 2 shows the experimental setup used to prepare thin films studied in this research work. The equipment consists of:

-**An air compressor** directly extracted from the atmosphere. To obtain a good quality air supply, the air pipeline is provided with a series of filters and moisture traps to remove residual particles, water and oil.

-**Syringe pump** (type Creson, Burette 1S). This syringe has the advantage to produce a continuous or discontinuous flow depending on the type of deposit desired. We can also control the volume of the solution to be deposited as well as the time required for this.

-**Nozzle** with an orifice of 0.5mm of diameter and having two pipes, one for the spray solution and the other for the carrier gas. The carrier gas disperses the solution into a

multitude of fine droplets to be "conically" projected on the substrate with a determined speed.

- **Steel hotplate** size of (60 x 55 x 25mm^3), heated by five tubular resistors of 125 Watt and 50mm length placed in parallel and operating with an accuracy of $\pm$ 5 °C.

-**Thermocouples** (chromel/alumel) having a temperature range from 200 °C to 1372 °C being below the substrate ensuring the temperature change during the deposition layer.

-**Electronic system** for controlling the substrate temperature and also to fix the deposition temperature.

- Nozzle:

The solution is sprayed from the nozzle onto the heated substrate. The nozzle has two ducts, one for the spray solution and the other for the carrier gas (here, air). Gas pressure bursts into a multitude of very fine droplets of the solution onto the substrate. These droplets should not be too large to avoid the sudden cooling of the substrate surface nor too small to prevent evaporation of the solvent before reaching the substrate.

- Nozzle-substrate distance:

It is very important because it acts on the droplet size during the impact onto the substrate. It must be optimized to obtain uniformity of spraying over the entire surface.

-Flow rate:

It is an important parameter that influences the properties of thin layers formed. It influences the growth of the deposit, and good crystallinity and good morphology are generally observed when the flow rate is small.

-Temperature of the substrate:

It plays a major role in the determination of the properties of thin layers formed. It is generally observed that higher temperatures lead to thin layers of good crystallinity.

Esquema del dispositivo de la pulverización química «Spray Pirólisis»

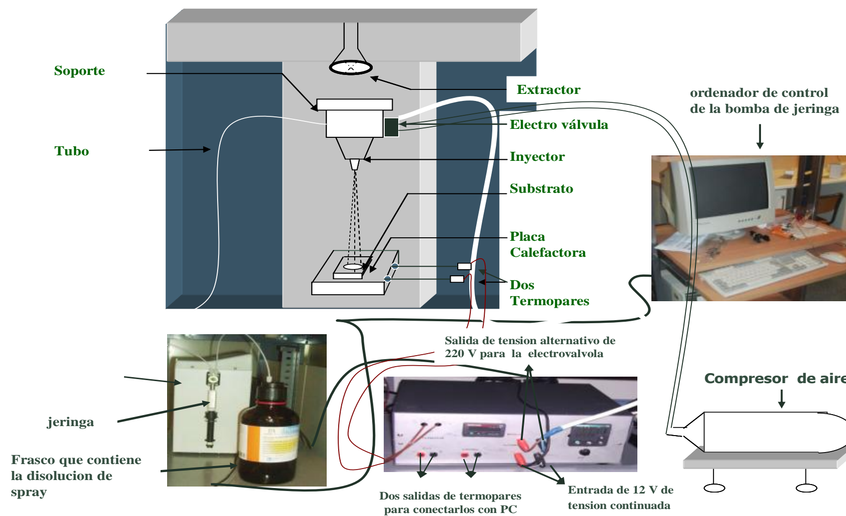

Fig. 2: Diagram of Chemical Spray Pyrolysis apparatus [3]

1.3. Definition of a thin layer

Thin layer of material is a deposit whose thickness is reduced so that it is expressed in nanometers (10-100 nm) and this small thickness causes a disturbance of physical properties [4]. The difference between solid state materials and thin films is related to the fact that we neglect the boundary effects in bulk materials properties while in thin films boundary effects are predominant. Indeed when the thickness of a material is low, the two-dimensional effects will be strong but when the thickness exceeds a threshold the material will find its bulky property [5].

Thin films are deposited on a support called substrate. Therefore, it is important to take account of the very strong influence of the substrates on the structural properties of the layer deposited thereon. And thin layer of the same material and the same thickness can have significantly different physical properties depending on whether it is deposited on a glass substrate, ITO, FTO, silicon etc.

The interest in thin layers is mainly related to the use of fewer materials relevant to the physical properties and simplicity of the technologies used in their preparation.

It easily follows from these characteristics that thin layer is anisotropic by nature [4].

1.4. The different types of crystalline growth

The three main types of crystalline growth described for the first time by Bauker and Poppa are:

- **Frank-Van der Merwe Growth Mode**: This is a layer after layer growth. In other words each mono-atomic layer begins to be deposited if the previous is completed. The energy of the deposited atoms is minimized when the substrate is completely covered. This is usually the type of growth observed for some type of metal on metal systems, for noble gas onto some metals and in the case of homo-epitaxial semiconductors.
- **Volmer-Weber Growth Mode**: In this mode of growth the formation of deposited element takes the form of three-dimensional islands. This type of growth is found in systems where the surface energy of the deposited atoms is higher than the surface energy of the atoms of the substrate. This mode of growth is observed in many metals onto insulation type systems.
- **Stranski-Krastanov Growth Mode**: Here the formation of one (or more) (s) mono-atomic (s) layer (s) on the substrate is on a FVM mode and there is islets layer growth on this. This is an intermediate mode that appears in the case of heteroepitaxial growth. A low lattice mismatch between the epitaxial material and the substrate induces a stress in the epitaxial layer deposited. The growth is primarily two-dimensional and is monolayer by monolayer, resulting in an increase of this constraint. Then, above a critical thickness, an elastic relaxation leads to 3D islands formation at the expense of deposited material.

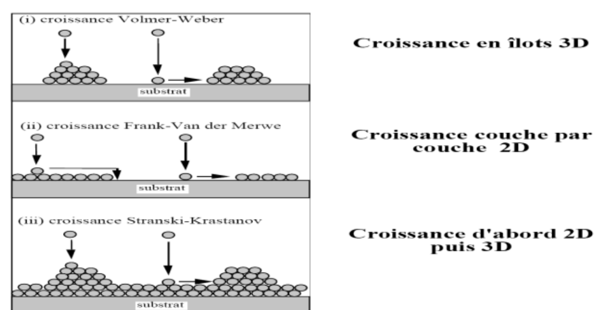

Fig. 3: Different modes of growth: (i) 3D growth by formation of island formation (Volmer-Weber) (ii), 2D growth layer by layer (Frank-Van der Merwe), (iii) 2D growth followed by 3D growth (Stranski-Krastanov)

1.5. Surface Tension

1.5.1. Introduction

We observe certain phenomena of life without paying much attention and without asking any questions about these phenomena. For example we often observe pretty round water droplets form on the stainless steel while on the wood, water appears to "spread".

Why water does not seem to spread in the same way on all surfaces?

To explain these phenomena we use what is called surface tension.

1.5.2. Some observations

-In a test tube the free water surface forms a meniscus near the edges. Fig. 8.

-Some insects (gerris) are able to move on water. Fig. 6.

-Trombone, razor blade or thin coin onto water surface does not sink. Fig. 7.

It is very difficult to accept that an object having a density greater than water cannot sink when it is placed above and yet this can happen.

The question we might ask is: How all these elements observed can float and how we can explain that the insect can remain on the surface of the water?

To answer this question we are interested more precisely in the phenomenon called surface tension.

Fig. 4: An insect (gerris) walking on the water without sinking [6]

Fig. 5: Very thin coin on water without sinking [7]

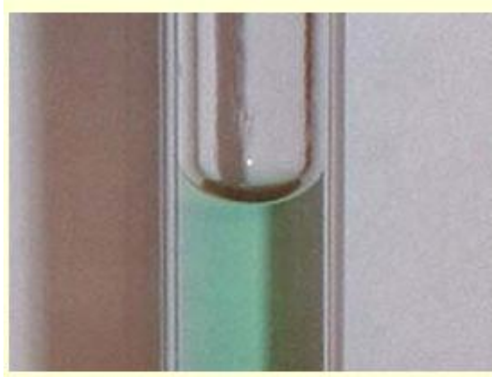

Fig. 6: Meniscus at the edges of a tube [8]

1.5.3. Surface tension

If we model the insect to a cylinder, we can understand the causes of its flotation.

Either a cylinder of mass 5g, L=10cm height and base diameter d=10mm. It is located in the Galilean supposed terrestrial reference and apply the second law of Newton.

The forces that can be applied to the insect are:

- Gravity (weight): $P = mg$

- The air thrust of Archimedes: $\pi air = -\rho.V.g$

- The thrust of Archimedes of water will not be considered because the insect is not immersed in water.

According to Newton's second law, we have:

$m.a = P + \pi$

$a = 0$, because the insect is in equilibrium when $P + \pi = 0$

But $\pi=\rho.V.g$ with $\rho=1.2kg/m^3$, $V=\pi r^2h=7.8.10^{-6}\,cm^3$, $m=5g$ and $g=10cm/s^2$

$\pi =9.3.10^{-5}N$

The weight of the insect is equal to $P = mg = 5.10^{-2}N$.

The weight of the insect is 500 times larger than the thrust of Archimedes so we can neglect π_{air} which therefore causes that the insect must sink!!! However, it is not. So there is a force which "holds" the insect and prevents it from sinking. This force is the surface tension and is denoted $F\gamma$.

Molecules within a liquid are surrounded on all sides by other molecules. It follows that the forces exerted on a molecule within the liquid compensate each other and that means that the system {molecules} is pseudo-isolated. On the other hand, it not be said the same for those who are on the surface because they do not have "neighbors" of the air side. It follows that the forces are directed inwardly of the liquid. Thus, the surface tension is a force existing at the interface between two media: it is a surface force as shown in Fig. 7.

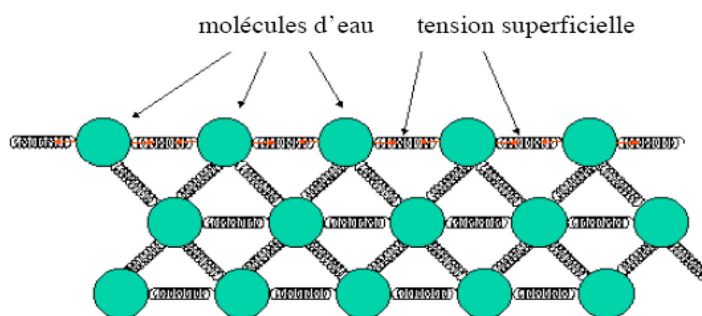

Fig. 7: Forces exerted on the molecules in and on the surface of the water [9]

1.5.4. Surface tension of some liquids

Surface tension depends on the liquid and the temperature. That of pure water is high, 72.8mN/m at 20 °C.

We will give some surface tensions of some liquid in the Table 1.

Table 1: Surface tension of some liquids

Liquid	Temperature (°C)	Surface Tension (mN/m)
Pure water	25	72.0
Methanol	25	22.45
Ethanol	25	22.38
Propan-2-ol	25	21.70
Glycerine	25	63.00
Ether	25	17.00
Ethanol (40%)+water	25	29.63
Ethanol (11.1%)+water	25	46.03

Table 2: Surface tension of water at different temperatures and in contact with air [10]

Temperature (°C)	Surface Tension (mN/m)
-8	77.0
0	75.6
15	73.5
20	72.8
25	72.0
30	71.2
40	69.6
50	67.9
60	66.2
70	64.4
80	62.6
100	58.6

The surface tension of water in contact with air decreases when the water temperature increases.

We noted also that the surface tension of water decreases when the mass percentage of propan-2-ol alcohol increase in water as shown in Table 3.

Table.3: Surface tension of water + propan-2-ol at 25 °C [11]

Mass percentage of propan-2-ol	Surface Tension (mN/m)
0	72.01
5	49.58
10	40.42
15	34.63
20	30.57
25	28.28
30	26.82
40	25.27
50	24.26
60	23.51
70	22.68
80	22.14
90	21.69
100	21.22

1.5.5. Wetting

Surface tension is the source of the form of a liquid when it is deposited on a solid surface, this is called "wetting". Figure 8 summarize this particularity.

The determining parameter is the contact angle θ between the tangent plane to the surface of the drop and the solid plan that supports the liquid drop.

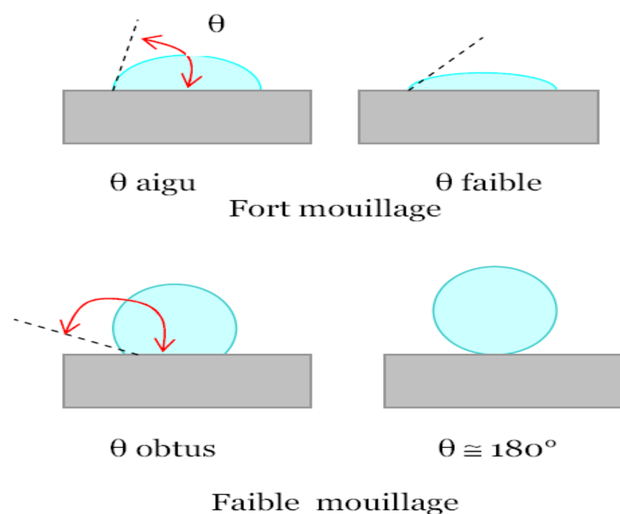

Fig. 8: Different types of wetting [12]

When θ is acute wetting is important while when θ is obtuse wetting is low. This is the case of mercury where θ = 135°. For θ = 180°, the wetting is zero and if θ = 0 wetting is perfect.

The wetting is related to the nature of the liquid, the physical nature of the medium and the condition of the surface. Helium liquid is the best wetting liquid.

1.6. Conclusion

Surface tension is a very important element to study for homogeneous, uniform and adherent thin films deposited onto glass substrate that we use in our work. This is why we used different amounts of alcohol that we added in the solvent of double distilled water in order to study the role of decrease of surface tension of water on the physico-chemical properties of layers prepared by Chemical Spray Pyrolysis.

2. Characterization Techniques

2.1. X-ray diffraction (XRD)

The X-ray diffraction (XDR) is an accurate and non-destructive technique used for the structural analysis. XRD gives lots of information such as: structure, orientation, crystallite size and the different phases of the material. Obtained diffraction peaks are compared with JCPDS file (Joint Council Powder Diffraction Standard) to obtain information on the phases, their relative abundance and the preferred orientation of crystallites. From the width of the diffraction peaks, the average crystallite size can be calculated and interplanar distance is obtained by the Bragg's formula.

$$2d\sin\theta = n\lambda \quad (1)$$

λ: wavelength of the incident radiation

d: interplanar distance determined by the nature of the material

θ: angle between the incident X-ray beam and normal planes (h k l)

n: diffraction order

To determine the diffraction conditions on (h k l) plan family, only one of the parameters θ or λ is fixed and the other variable.

The choice of the variable parameter determines two groups of X-ray diffraction methods:

θ fixed and λ variable: LAUE method.

λ fixed and θ variable: the rotating crystal method and powder method

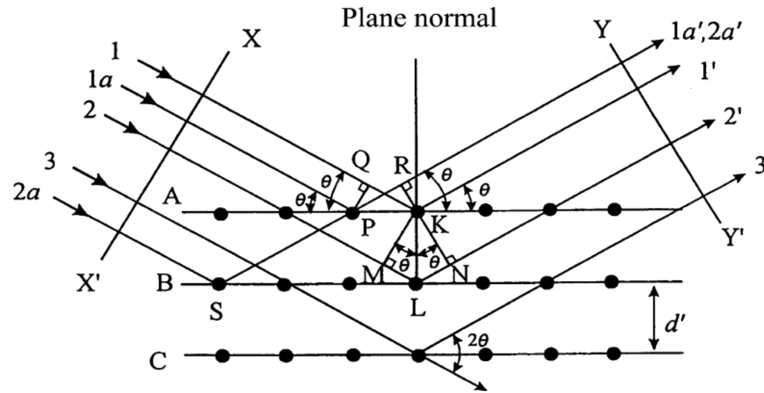

Fig. 9: Bragg's Law [13]

The correlation between the interplanar spacing and the lattice ("a" and "c" for example) parameter (s), obviously depends on the crystal structure identified by the positioning of the diffraction peaks.

For cubic system, the lattice parameter is determined from the following expression:

$$\frac{1}{d^2} = \frac{(h^2 + k^2 + l^2)}{a^2} \quad (2)$$

For hexagonal system, we have the following expression:

$$\frac{1}{d^2} = \frac{4(h^2 + k^2 + hk)}{3a^2} + \frac{l^2}{c^2} \quad (3)$$

For tetragonal system or quadratic expression is:

$$\frac{1}{d^2} = \frac{(h^2 + k^2)}{a^2} + \frac{l^2}{c^2} \quad (4)$$

For orthorhombic system, we have the following expression:

$$\frac{1}{d^2} = \frac{h^2}{a^2} + \frac{k^2}{b^2} + \frac{l^2}{c^2} \quad (5)$$

The size of the crystallites (D) can be given by the Debye-Scherrer formula:

$$D = \frac{K\lambda}{\beta \cos \theta} \quad (6)$$

K is a constant, the shape factor which is almost equal to 1 (typically 0.9)

β Full Width at Half Maximum (FWHM) generally measured in radians

θ Bragg's angle

λ wavelength of the incident beam

The diameters of real crystallites must be distributed around the value of D. We can also have a peak broadening due to the optics of the apparatus used, which makes delicate the interpretation of this average diameter when it is less than one micrometer ($\prec 1\mu m$).

The microstrain (ε) can also be calculated using equation (7) [14].

$$\varepsilon = \frac{\beta \cos\theta}{4} \quad (7)$$

The dislocation density (δ) is calculated using the Williamson and Smallman's formula [15].

$$\delta = \frac{1}{D^2} \quad (8)$$

2.1.1. Rigaku Ultima IV

X-rays radiation has property to pass through a material and be diffracted by the atoms. The technique allowed to determine the inter-spacings and ordering of atoms in the crystal lattice. As X-rays diffract in different ways according to the arrangement of atoms in the lattice, the X-ray diffraction by the material is used to find its crystallographic structure.

The "2θ" degree depends on the energy of the incident radiation and spatial distribution of atoms (crystal structure). The diffractogramme obtained after diffraction constitutes the imprint characteristic of the analysis of the crystal structure.

The measurements were made with an apparatus consisting of an X-ray tube, which emits radiation on the sample that refracts a portion of the emitted radiation to a detector system.

This technique is mainly used by geologists to identify minerals. The diffraction patterns can be obtained directly from a piece of solid or small amount of powder (powder pattern).

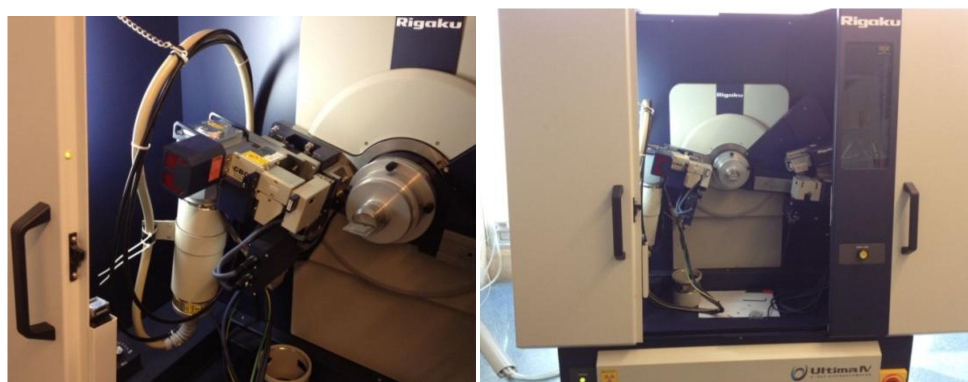

Fig. 10: Rigaku Ultima IV diffractometer, X-ray diffraction [16]

2.2. Raman Spectroscopy

2.2.1. Historical

In 1928, in India, Sir C.V. Raman was the first to be interested in inelastic light emission phenomenon. The radiation emitted by the bombarded molecules contains photons of the same frequency as the incident radiation, but also different frequencies of photons. This effect is very small - about 1 photon of 10^6 will be emitted with a wavelength slightly different from the incident wavelength. This process was then called after the name of its discoverer, and the frequency change is called Raman Effect.

2.2.2. Raman Spectroscopy Principle

When we illuminate a material by monochromatic light beam, this exciting radiation is transmitted, reflected, absorbed or scattered by the material. Among the fraction of incident photons scattered we can observe mainly three types of waves:

- Photons having the same energy as the incident photons, it is called Rayleigh scattering (elastic scattering).
- Small fraction of light (1 of 1 million) is diffused with different frequencies from those of the incident photons; it is called Raman diffusion (inelastic diffusion). Whatever the nature of the diffusion, the incident photon excites an electron in a higher-energy “virtual" state vibrational (which is not a proper state of the molecule and has a very short lifetime of $\approx 10^{-14}$ s) and then returns to a lower energy vibrational state by emitting a scattered photon.
-When the final vibrational state has higher energy than the initial state, the system earns a phonon. This energy has been ceded by the incident light, which is diffused at lower frequency$(h\nu - \Delta E)$; it is the Stokes scattering.

-But if the final vibrational state has lower energy than that of the initial state, the system lost a phonon and light is emitted at a higher frequency $(h\nu + \Delta E)$; it is anti-Stokes scattering.

According to Bose-Einstein statistics, the anti-Stokes scattering obtained from an excited state, is less probable that the Stokes diffusion, which is obtained from the basic level and experience shows that the Stokes rays are much more intense than anti-Stokes rays.

It should be noted, given the small magnitude of interatomic distances for the exciting wavelength, that Raman spectroscopy permits to study only the Brillouin zone center of vibration modes. These modes will be active in Raman, only if there is change in the polarizability of the study material (electrically coupling of monochromatic beam and atomic vibrations).

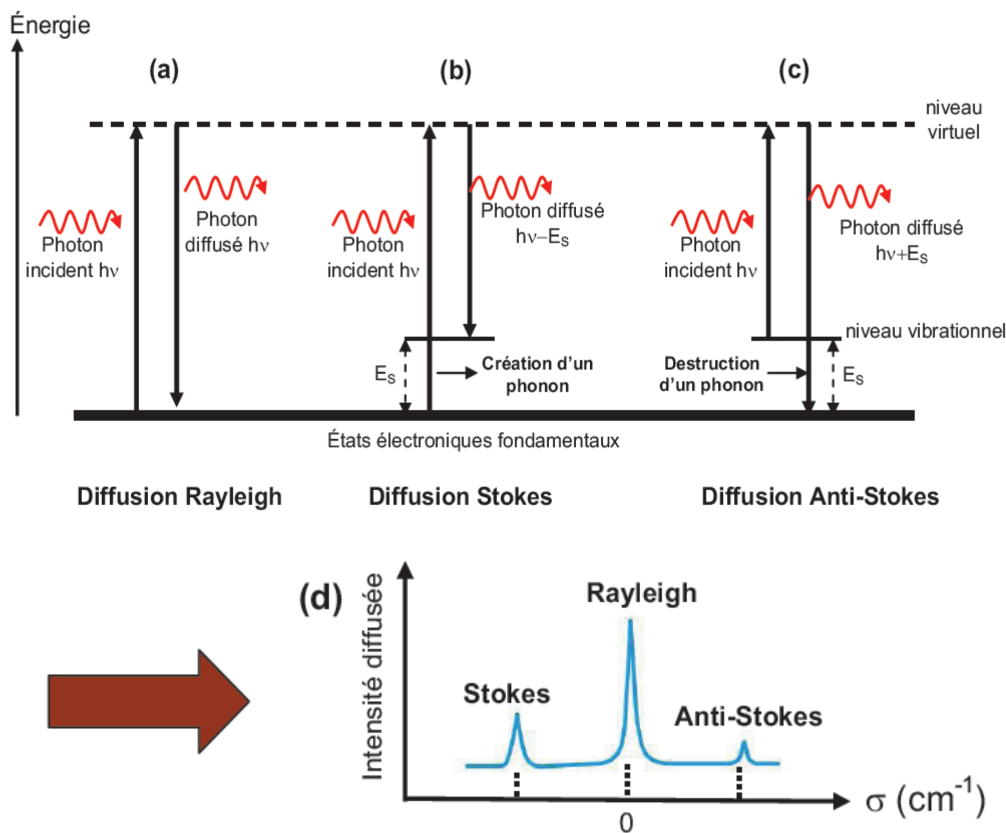

Fig. 11: Schematic diagram of Rayleigh process (a), Stokes (b) and anti-Stokes (c) and corresponding diffusion spectrum (d) [17]

The information from Raman spectrum is multiple:

- Position of rays provides information on the chemical species present in the sample.
- Mid-height width of the peaks provides information about the sample structure.
- Intensity of a peak can be related to the concentration of the species.
- Shift of peaks is function of stress and/or temperature.

2.2.3. Advantages and Disadvantages of Raman Spectroscopy

Advantages:

- It is non-destructive
- It is easy to implement and the preparation time is zero
- The nature of the samples does not count: solid, liquid or gas.
- It possible to work in "hostile" environment such high temperatures.
- It is sensitive to small structures: analysis of thin films for which diffraction methods are sometimes difficult.

Inconvenient:

- Fluorescence is more intense when it occurs but it can be avoided by changing the exciting wavelength.
- Decomposition of the samples by heating
- Photochemical reactions (decomposition of colored substances ...)
- Black body emission (by heating the sample)

2.2.4. Working Principle of Raman Spectrometer

The elements that represent Raman spectrometer are shown in the Fig. 12.

-Laser source provides stable and known frequency monochromatic radiation. There are laser in the ultraviolet (UV), visible and near infrared (NIR) depending on the nature of the sample and the purpose of analysis. For example:

UV domain: 325 nm (He-Cd)

Visible domain: 488nm (Ar^+, blue), 514 nm (Ar^+, green), 633 nm (He-Ne, red)

Near IR domain: 785nm (laser diode), 830nm (laser diode)

An interference filter or a pre-monochromator just after the laser eliminates the plasma parasitic rays in the vicinity of the exciting laser ray. The beam passes later through a polarizer placed at the entrance of the microscope fixing the incident polarization.

The Microscope focuses the incident laser spot on the sample surface via the appropriate objective, and then directs the scattered photons to the spectrometer. An analyzer used to fix the polarization diffused wave.

-As the Raman process is low intense, holographic filter is used to separate the signal of interest from the Rayleigh signal much more intense.

-The scattered photons enter in the monochromator by slit which permit to spatially locate the light. A prism, later, directs photons on a holographic grating dispersing photons according to their wavelength.

There are two types of detector on the market: CCD and InGaAs according to wavelength that we desire to analyze.

CCD detector (Charge-Coupled Device): it is a multichannel detector to simultaneously collect spatial and spectral information about the sample analyzed. Its spectral range is still between 400 nm and 1 μm.

InGaAs detector (single-channel): it is a detector, especially, for IR. Its signal/noise ratio is better than CCD detector but lower resolution.

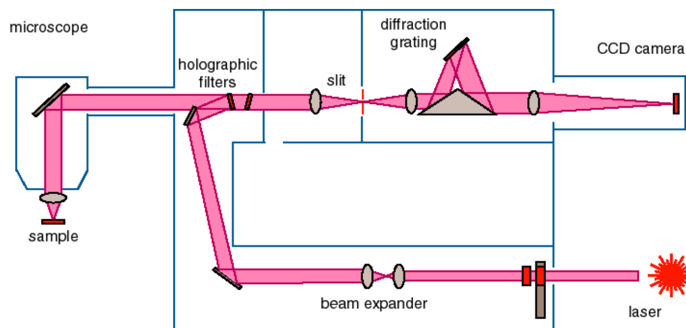

Fig. 12: Schematic representation of Raman spectrometer [18]

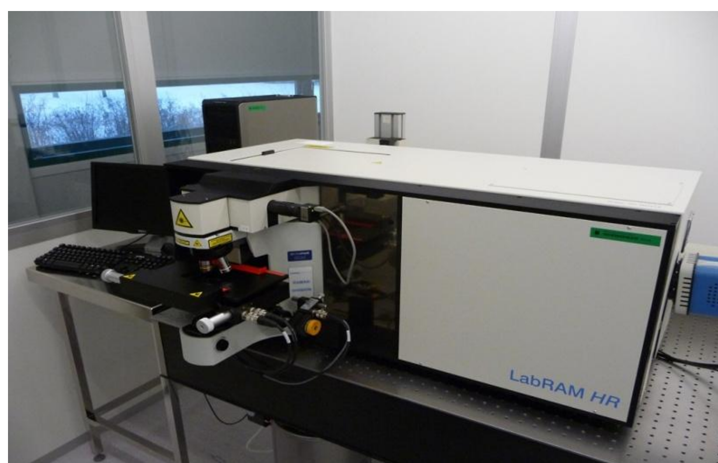

Fig. 13: Photo of UV spectrometer HR LabRaM

Diffusion Raman measurements were performed in Departamento de Fisica Aplicada-IDF, Universitat Politècnica de Valencia, España on LabRam HR UV spectrometer coupled to a Peltier-Cooled CCD camera using a helium-neon laser as excitation source of monochromatic wavelength 632.81 nm with spectral resolution of 3cm^{-1}.

Raman scattering spectra study permit to assign the observed rays to different irreducible representations provided by group theory. The vibration modes of the α-cubic phase and β-tetragonal phases of In_2S_3 are illustrated in the Fig. 14 and Table 4.

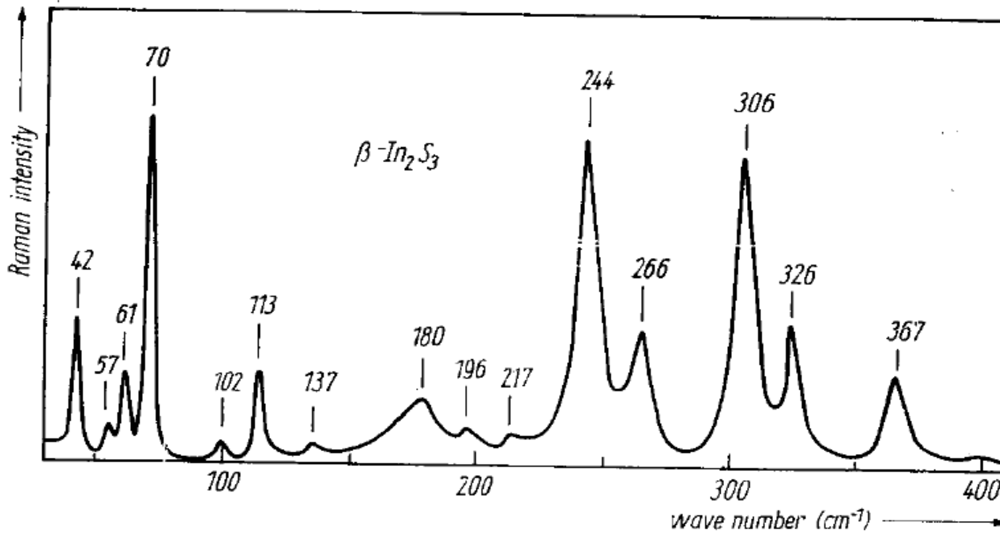

Fig. 14: Raman spectrum of β-In_2S_3 [19]

Table 4: Vibrational frequencies of α- In_2S_3 and β-In_2S_3 [19]

Vibrational frequencies (cm^{-1}) of α- and β-In_2S_3

β-In_2S_3 (Raman)	β-In_2S_3 (FIR)				α-In_2S_3 (FIR)	
	E ⊥ c		E ∥ c			
	ω_{TO}	ω_{LO}	ω_{TO}	ω_{LO}	ω_{TO}	ω_{LO}
42						
57	58	59	52	54	53	56
61						
70						
102						
113	96	111	93	108	93	96
137						
	157	159	155	157	152	156
	166	169			166	169
180						
196	197	199			200	206
	205	208				
217	219	228			212	220
	229	257	224	251	227	251
244						
266	266	281	264	279	263	274
	292	294	293	295	291	293
306						
	314	319			313	319
326	327	359	324	344	322	340
367			359	378	358	362

2.3. Scanning Electron Microscopy (SEM)

2.3.1. Introduction

Scanning Electron Microscopy is a non-destructive technique that provides surface images of practically any material at scales ranging from that of magnifier (x10) to transmission microscopy (x10^5) with a resolution of 10 nm.

SEM: - Microscopic texture, surface nature, corrosion...

- Morphology

The depth of analysis is in the order of micrometer (1µm).

The image is formed sequentially by scanning the sample surface with an electron beam and collecting either secondary electrons or backscattered electrons.

The image in secondary electrons is characterized by a very good definition until magnifications between x20 000 and x50 000 in conventional and more than > 500 000 at high resolution, with lateral resolutions limits of 10 to 20Å, according to sample, the apparatus and observation parameters. The detector mounting in the objective lens can eliminate the largest part of backscattered electrons in order to get better image of the surface, especially at low primary energy.

The backscattered electron image has a lateral resolution at best of the order of 0.1µm. The use of specialized detector (semiconductor or scintillator) brings out a contrast which is function of the atomic number (Z) of the elements present. A heavy element will give a strong signal and therefore clear zone; a small element will give a weak signal and thus dark area, a kind of mapping of atomic number.

The interaction between the electrons and the material leads to accumulations of charges at the surface. These charges are discharged to ground if the sample is conductive. On the other hand if the sample is not sufficiently conductive or insulating, the charge accumulation deflects the electron beam and causing rise in temperature at the location of the radiation, which can damage the deposit. To remedy this drawback, it is made conductive by covering it with a thin layer of carbon or gold; this is what is called metallization.

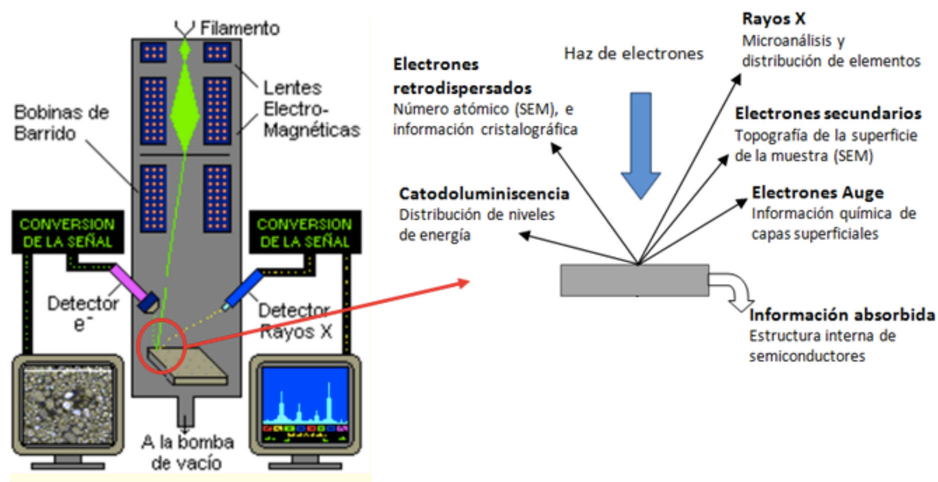

Fig. 15: SEM images formation system and the electron production scheme

Fig. 16: SEM experimental apparatus [20]

Fig. 17: Carbon metallizer for very resistive samples [21]

2.3.2. Scanning Electronic Microscope Principle (SEM)

The scanning electron microscopy comprises a primary electron beam generated by an electron canon focused by electromagnetic lenses onto the sample. The target scanned with the electron probe via deflection coils, emits signals which are received by detectors and then used to modulate the intensity of a cathode ray tube. The scanning of sample is synchronized with the electron beam.

The excitement and response of the sample are based on the radiation-matter interaction. In fact electron beam leads to different types of interactions. The primary electrons striking the

target with an energy E_p interact with atomic nuclei and are distributed either elastically (without energy loss) or inelastic (with loss of energy).

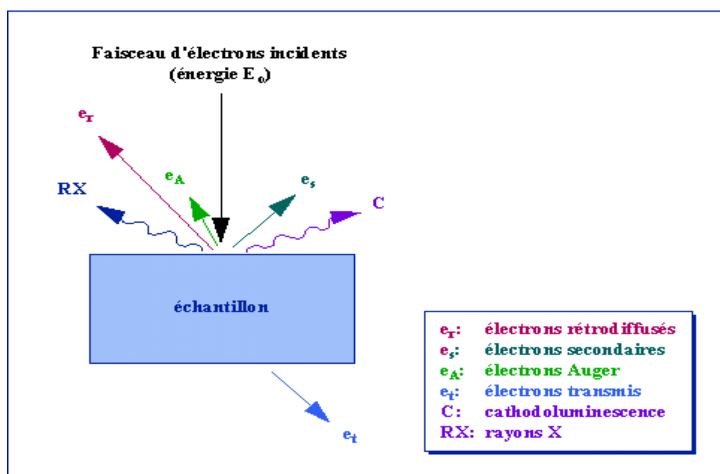

Fig. 18: Effect of electron beam on a sample

In the inelastic case, the loss of energy can be transmitted to other electrons (secondary electrons or Auger electrons) or converted into photons (X-rays, cathodoluminescence). In the case of very thin sample, electrons can be transmitted (the case of transmission electron microscopy). For an electron can leave the matter, he must earn an energy greater than his work function (limit of 0 to 50eV for real electrons). These various cases are shown in Fig. 18.

The result of all interactions is a distribution of electrons with energies ranging from 0 to Ep. Fig. 19 shows the distribution of electrons on several domains.

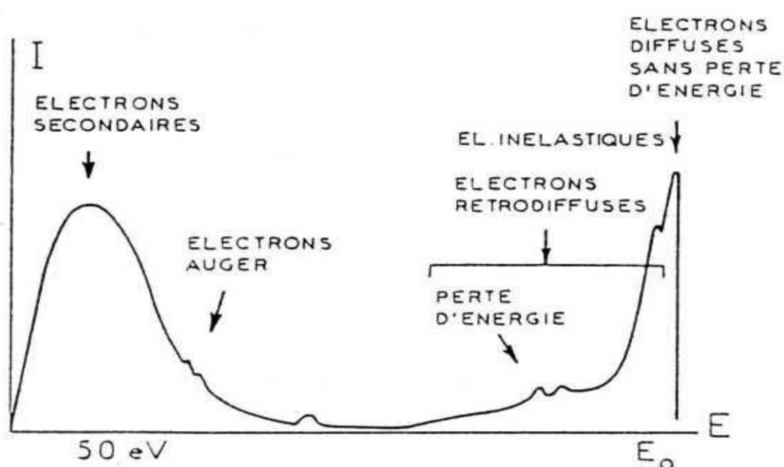

Fig. 19: Energy distribution of the emitted electrons

X-rays, which are part of the photons emitted by the sample, are the basis of Energy Dispersive X-ray Spectroscopy (EDS) analysis. It is a priori used for semi-quantitative analysis of heavy elements, the light elements, rather, emit Auger electrons.

2.3.3. Energy Dispersion X-ray Spectroscopy (EDS)

The observations of Scanning Electron Microscopy can be local, qualitative and quantitative by measuring the energy of X-rays produced by the sample. Indeed, the arrival of an incident electron into contact with an electron of heart from an atom of the sample may cause the expulsion of the latter. The atom is then excited and the vacant site may be filled by an electron from a higher energy level. This excitation is accompanied by the emission of a series of X-rays characteristic of the element. These emissions are used for the analytical study of atoms. As shown in Fig. 20, the X-ray spectrum consists of a superposition of continuous spectrum (also called Bremstrallung) and a spectrum characteristic which is represented by a series of varying intensities and discrete wavelengths rays. These lines appear with certain energies corresponding to atomic features of the studied material. The analysis of these rays permits sample identification.

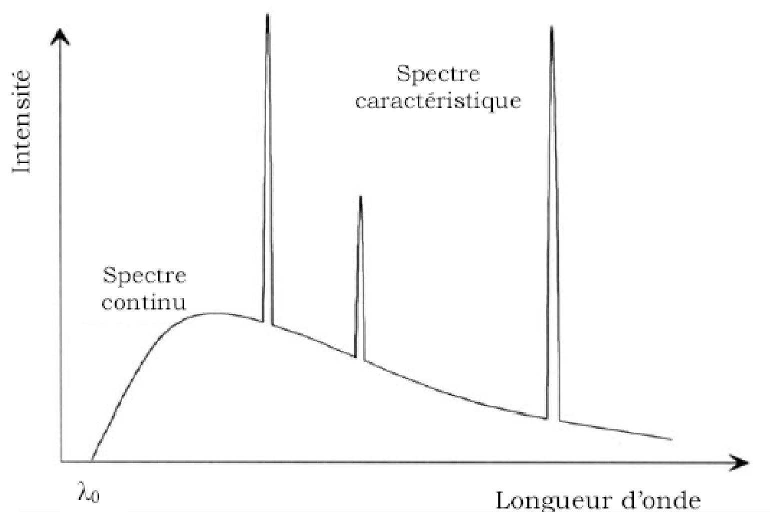

Fig. 20: Diagram of the X-ray spectrum from sample bombarded by electrons

The penetration of primary electrons in the material is accompanied by a broadening of the electron beam and progressive loss of energy. The volume of penetration is often called pear interaction.

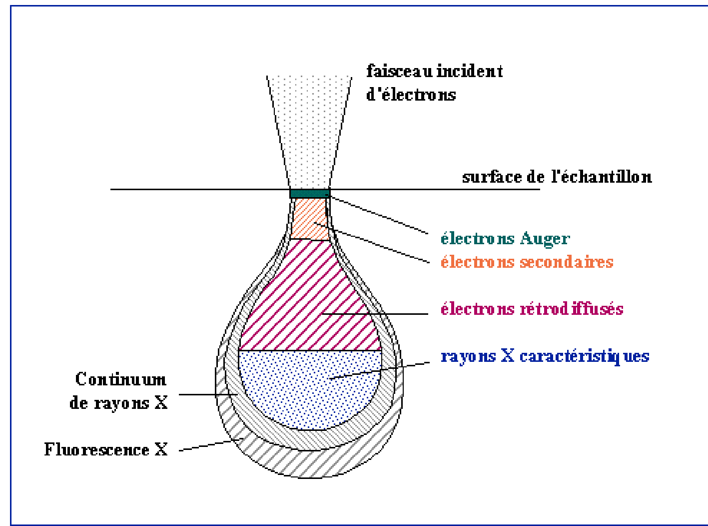

Fig. 21: Enlargement of the beam in the sample

2.4. Atomic Force Microscopy (AFM)

2.4.1. Introduction

In 1986, Binning, Quate and Gerber made a local probe microscope that can examine the morphologies of compounds both conductors and non conductors. This is the Atomic Force Microscopy (AFM). Other AFM microscope versions exist and as an example, we quote the Lateral Force Microscopy (LFM), Electric Force Microscopy (EFM) or Magnetic Force Microscopy (MFM). We will develop later the principle of Atomic Force Microscopy.

2.4.2. Device Description

The atomic force microscope is composed of three main parts: the optical head, the scanner and base. Due to the weight of the optical head, the optical detection system cannot be mounted on the piezo tube, therefore the optical head and the probe are held fixed while the sample is scanned beneath these last two. The scanner consisting of piezoelectric cylindrical tube is located in the middle of a support-ring which is fixed on the microscope base. It contains three screws serving as support for the optical head as well as for adjusting its position relative to the sample. The two screws of the scanner are operated manually while the third is controlled by a motor located in the base of the microscope. The stepper motor is controlled manually from a button on the base or automatically via the computer during the process of engagement or clearance of the tip of the surface. The base contains electronic circuits which are essential for the operation of the microscope. The LCD digital voltmeter

gives different signals depending on the position control of the DVM function (function switch).

2.4.3. Working Principle of Atomic Force Microscopy (AFM)

The working principle of Atomic Force Microscope is shown in Fig. 22. A very sharp tip used for the measurements, fixed on the end of a flexible cantilever (cantilever), arrives at the sample surface. The scanner moves the substrate under the tip in both directions x and y for scanning surfaces ranging from nm^2 to μm^2. Irregularities in height present on the sample surface induce a deflection of the cantilever. This deflection is controlled by an optical detection system located within the head of the microscope. This detection system consists of a laser beam from a diode. It reflects on the upper face of the cantilever and then reaches a photodiode which detects any variation of the incident beam, therefore any deflection of the cantilever. A servo signal is used to control vertical movement (along the z axis) of the piezoelectric during the sample scan. The piezoelectric change gives the topography of the sample surface.

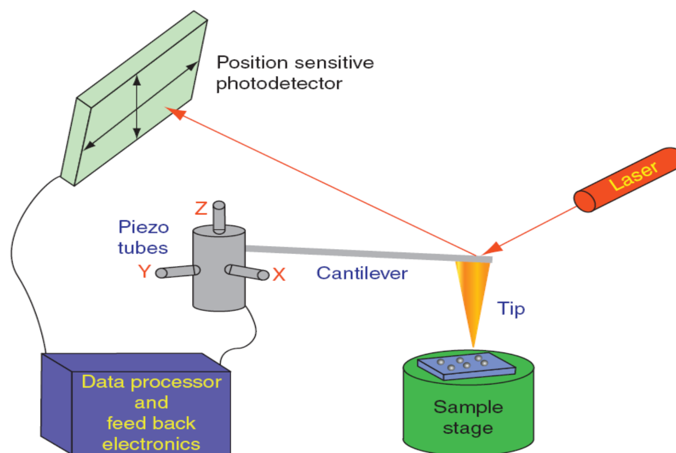

Fig. 22: Diagram of operation of the AFM [22]

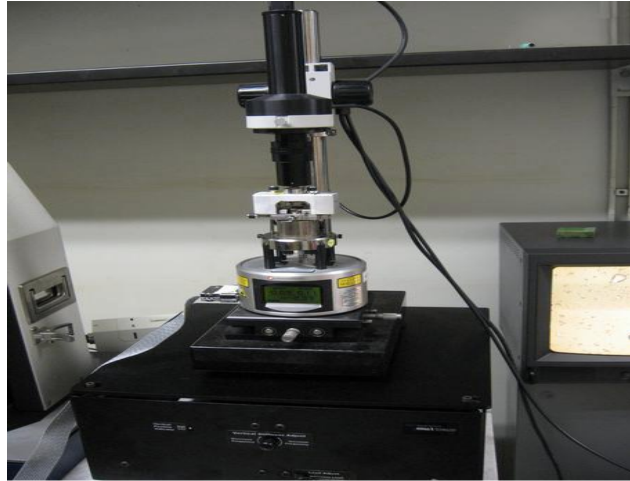

Fig. 23: Atomic force microscope, Nanoscope IIIa Veeco [23]

2.4.4. Working Mode of Atomic Force Microscope

There are two modes of working of the Atomic Force Microscope:

2.4.4.1. Contact mode operating

Atomic Force Microscope said repulsive involves short-range forces due to the interaction of the electron clouds. In this working mode, the tip remains in the presence of repulsive forces in direct contact with the surface atoms. Interaction forces due to repulsion between the electron clouds are in the order of 10^{-9} Newton. To describe the interaction forces between the tip and the surface the following potential was used:

$$U(r) = \left[\frac{-C_1}{r^{12}}\right] \quad (9)$$

r is the distance between the tip and the surface and C_1 is a constant. This is the working contact mode which relates to repulsive atomic microscope.

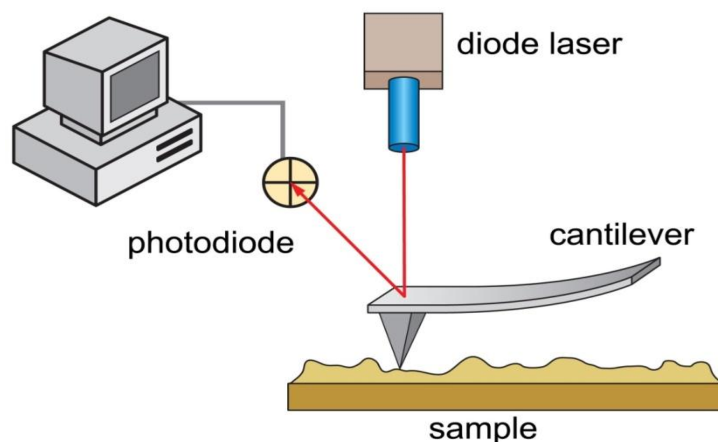

Fig. 24: Working Contact mode operation of AFM

2.4.4.2. Working Non-contact mode

Atomic Force Microscope said resonant involves the Van der Waals forces at long range. In this mode the tip is not in contact with the surface. The cantilever oscillates at its natural frequency lightly touching the substrate surface in a very short time through the tip. Brief contact between the tip and the surface causes an abrupt change in the amplitude of vibration. These changes in the magnitudes will be used to examine the morphology of the sample surface. The non-contact mode is often used for sensitive materials in order to make a visualization of the topography without destruction of sample [24]. Interaction forces are in the order of 10^{-12} Newton. In the resonant mode presented by Martin et al [25], the tip vibrates at about 50 Å above the substrate. In this interval of distance there are attractive forces that have an effect on the tip and on the frequency of the vibrating cantilever. This change in frequency regardless of the point-to-surface distance is used as control signal for the examination of the surface.

To describe, simply, the interaction tip-surface in the attractive mode, the following potential is used:

$$U(r) = \left[\frac{-C_2}{r^6}\right] \quad (10)$$

2.5. Photoluminescence (PL)

2.5.1. Introduction

The photoluminescence is a powerful optical technique for characterizing semiconductor and insulators materials. Its working principle is simple: the electrons of the sample are excited using radiation (monochromatic) and detecting the light emitted by the latter. A laser is necessary as an energy source as well as an efficient detection system. It allows, the photoluminescence, to study the configuration of the solid energy band and their levels of impurities.

One can also mention other luminescence techniques using other sources of excitations:

- Electroluminescence which is light emitted from material traversed by an electric current.
- Cathodoluminescence which results from the bombardment of the sample with an electron beam.

- Triboluminescence which is due to mechanical excitation.
- Chemiluminescence that results from chemical reaction.

2.5.2. Definition

Photoluminescence occurs when an electron in an excited state returns to the initial state by emission of photon whose energy is the difference between the energies of the excited state and the initial state. The process can be direct or indirect according to the energy of the band gap.

Photoluminescence can be used to determine the energy of the band gap since the most common transition in semiconductor is between the conduction band and valence band. In addition, the photoluminescence signals are given by the recombination of exciton (electron-hole pair), then the peak energies of free exciton of photoluminescence (emission) are lower than those of photoluminescence of the bandgap. The default bound exciton (defect-bound exciton) also has low emission energy. In fact, if excitons are bound by a deep level created by localized defect, we can observe emission levels established in the middle of the band gap. The photoluminescence is very sensitive to deep states levels [26].

2.5.3. Theory of photoluminescence

Even if the momentum h/λ (λ is the wavelength of the excitation light) is very small compared to that of the electron in the lattice h/a ("a" is lattice parameter), the absorption process of the photon must conserve the wave vector of the electron. For photon of energy hν, α(hν) absorption coefficient is also proportional to the transition probability P_{ij} from the initial state to the final state. The absorption coefficient is also proportional to the density of electrons n_i occupying the initial state and density of holes n_f occupying the final state; we must also sum over all possible pairs transition between states separated by an energy difference of hν:

$$\alpha(h\nu) = A \Sigma P_{if} n_i n_f \quad (11)$$

A is constant

Emission of radiation

- **Band to band transition**

Band to band transition occurs when the temperature of the sample exceeds that associated with the activation energy of impurities. At high temperatures this transition usually dominates the luminescence spectrum.

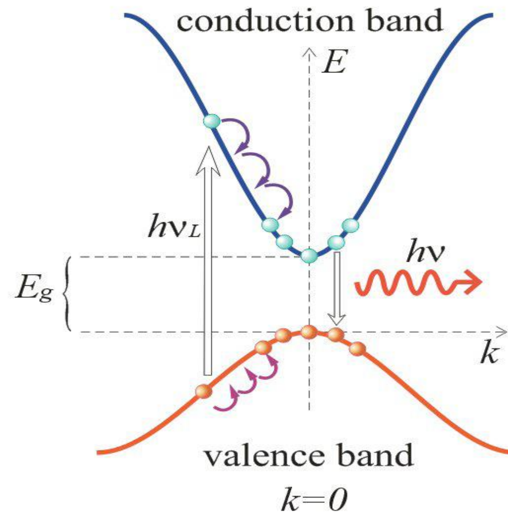

Fig. 25: Schematic diagram of the PL process in direct gap material [27]

After excitation the electron passes from the valence band to the conduction band. It quickly goes down to the bottom of it by emitting phonons (heat) and it emits a photon returning to the valence band. The emission of phonons is extremely fast and is of the order of picoseconds (10^{-12}s). Contrariwise the photon emission may take 10^{-9} to several seconds. Phosphorescent materials have longer emission time in the order of millisecond.
As the case of absorption of radiation, the conservation of the wave vector k allow to connect only states with the same wave vector k and this restriction leads to an emission coefficient of the following form:

$$\beta(h\nu) = B\left(h\nu - E_g\right)^{\frac{1}{2}} \quad (12)$$

with B is a constant,

$$B = \frac{2q^2(m_r^*)^{\frac{3}{2}}}{nch^2 m_e^*} \quad (13)$$

- **Valence band-Donor and conduction band-Acceptor transitions**

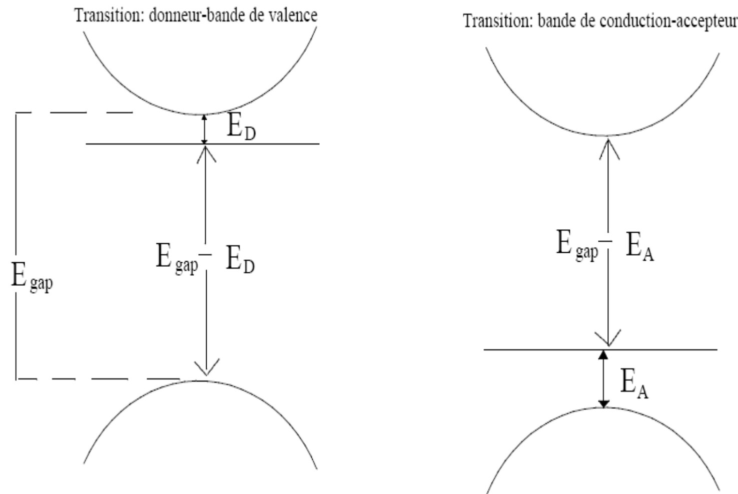

Fig. 26: Valence-band donor and Conduction band-acceptor transitions

The first transition corresponds to an electron that leaves a donor level to go to the valence band. The energy of the transition is given by:

$$E = E_g - E_D \quad (14)$$

We may also show the case where an electron leaves the conduction band to go to an acceptor level. In this case, the energy of the transition is given by:

$$E = E_g - E_A \quad (15)$$

E_D and E_A are different depending on the chemical nature of the impurity; enabling photoluminescence experiments to confirm the presence of specific type of impurity in the material.

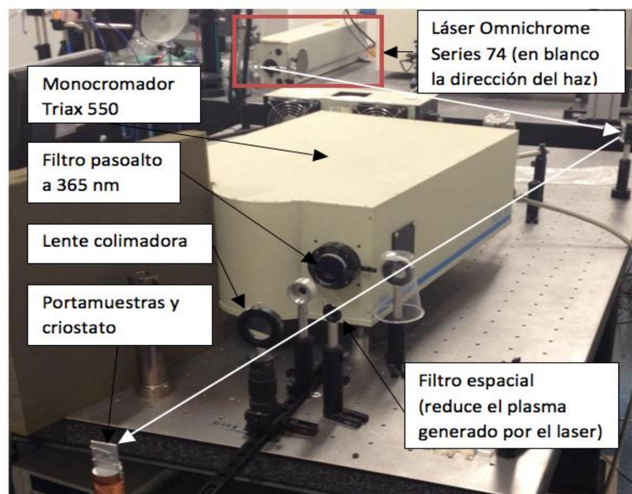

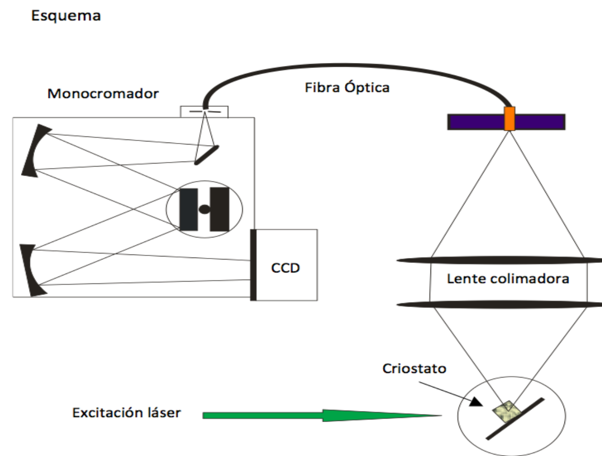

Fig. 27: Installation and schema of photoluminescence experimental apparatus schema [28]

2.6. Transmittance and Absorbance Measurement

Spectrophotometry is based on the determination of the optical properties of deposited compounds.

2.6.1. Absorbance

It is the ability of a material to absorb certain amount of light of the electromagnetic spectrum when it is excited by a light beam. This took place when the radiation energy of the incident beam is the energy required to move an electron from lower to higher permitted level (hν > Eg).

Absorbance is defined by the following equation:

$$A = Log\left(\frac{I_0}{I}\right) = -Log(T) \quad (16)$$

I is the intensity of transmitted energy

I_0 the intensity of incident energy

The laws that govern the behavior of the sample and the effect of radiation to absorb are: the Lambert and Beer's laws.

Lambert law refers to the thickness of the sample while **Beer's law** concerns the effect of the concentration of the sample on the absorption.

According to Lambert's law, when a beam of monochromatic light passes through an absorbing medium, the intensity decreases exponentially as the length of the medium increases.

$$Log\left(\frac{I_0}{I}\right) = K.L \quad (17)$$

I_0 intensity of the incident light

I intensity of transmitted light

K extinction coefficient

L thickness of the medium

According to Beer's law, when a monochromatic light beam passes through an absorbing medium, the intensity decreases exponentially with increasing concentration.

$$Log\left(\frac{I_0}{I}\right) = K'.C \quad (18)$$

By combining these two laws, we have the Beer-Lambert's law:

$$Log\left(\frac{I_0}{I}\right) = \varepsilon.C.L \quad (19)$$

ε molar coefficient or molar extinction absorption (mol^{-1})

C molar concentration (mol/l)

L length of studied medium

For a given photon energy, the absorption coefficient gives P_{if} transition probability of the electron to move from the initial state i to the final state f.

The absorption coefficient is proportional to the density of electrons occupying the initial state n_i and the hole density n_f of final state and is the sum of all possible transitions from states separated by an energy difference equal to hν = Eg.

$$A(h\nu) = A\Sigma P_{if} n_i n_f \quad (20)$$

When the semiconductor is undoped we can consider all possible transitions of conserved wave vector which means that the transition probability P_{if} is independent of the photon energy. Each initial energy state E_i is coupled to final energy state E_f where:

$$E_f = h\nu - | E_i | \quad (21)$$

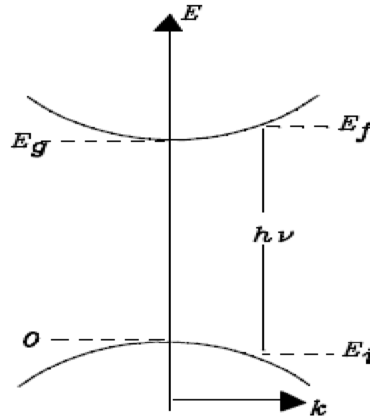

Fig. 28: Absorption Process

where the absorption coefficient is given by the following expression:

$$\alpha(h\nu) = A\left(h\nu - E_g\right)^n \quad (22)$$

$$A = \frac{q^2 (2m_r)^{3/2}}{nch^2 m_e} \quad (23)$$

m_r: reduced mass

hν: incident photon energy

Eg: bandgap energy

n is a constant and can take 1/2, 3/2 or 2 for direct permitted transition, direct not permitted transition and indirect permitted transition, respectively.

Regarding to our semiconductors we have direct transition from where the absorption coefficient is written as:

$$\alpha(h\nu) = A(h\nu - E_g)^{1/2} \quad (24)$$

2.6.2. Transmittance

The relationship between the transmitted intensities (I) and incident (I_0) is given by the following expression:

$$T = \frac{I}{I_0} \quad (25)$$

The relationship between the transmittance and the concentration is not linear, but the relationship between absorbance and concentration is linear, which is the basis of most quantitative analyzes as shown in Fig. 29.

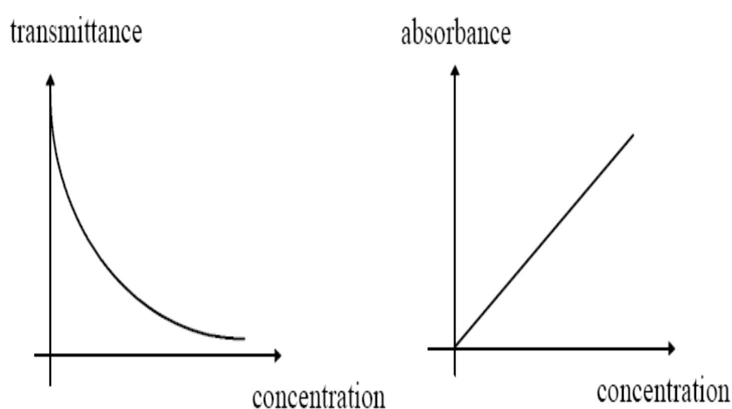

Fig. 29: Transmittance vs Concentration - Absorbance vs Concentration

2.6.3. Experimental apparatus

Fig. 30 and Fig. 31 show the description of the experimental setup used to study the transmittance of our samples.

Montaje en el laboratorio:

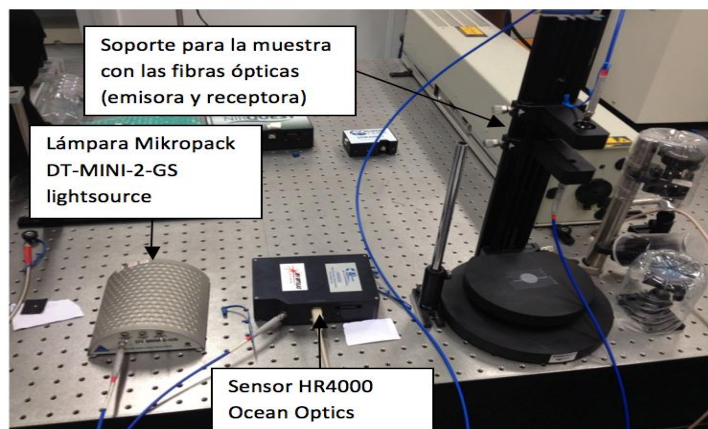

Fig. 30: Description of the experimental setup for transmittance [29]

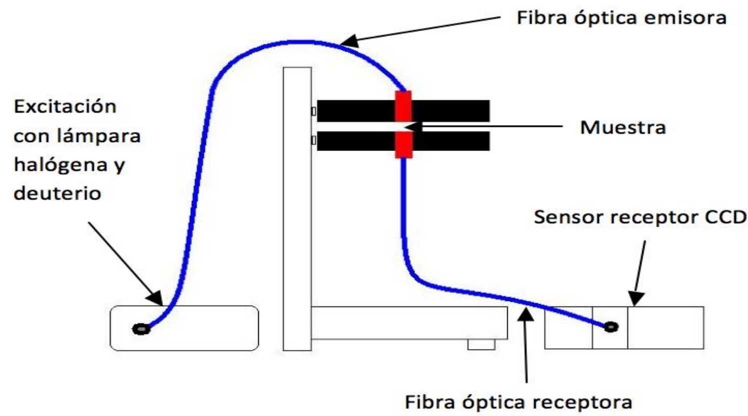

Fig. 31: Schema of the experimental setup [30]

2.7. Heat treatment

It consists of annealing the samples using a vacuum oven or in air at certain temperature and for given time to improve the crystallinity.

2.7.1. Working Principle of Oven

Fig. 32 describes the components of the furnace used for the annealing of samples.

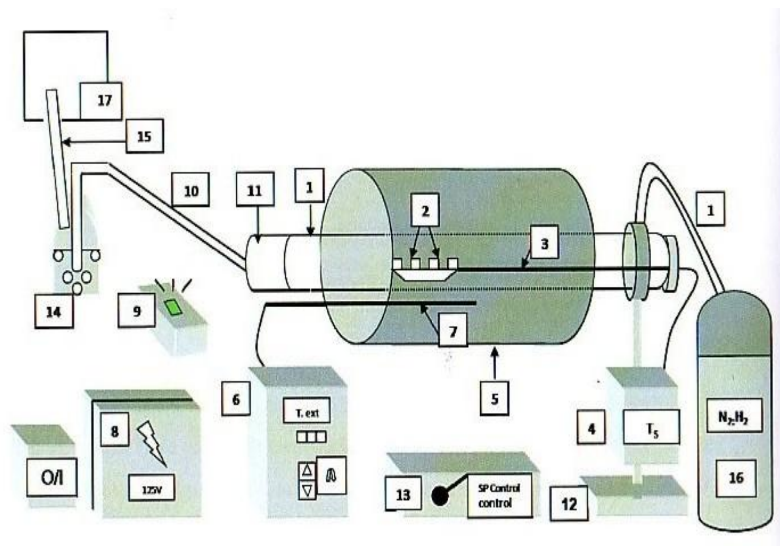

Fig. 32: Description of the constitutive elements of the annealing furnace [31]

1: Quartz tube furnace surrounded by heating resistor (used up to 1200 °C).

2: Quartz sample holder where is placed four samples maximum.

3: Thermocouple attached on the sample holder isolated by a ceramic cylinder.

4: Display unit connected to thermocouple "3" indicating the internal temperature of the furnace tube (the substrate temperature).

5: Insulator ceramic fibers surrounding the furnace.

6: Industrial controller "KS40 Philips" PID (Proportional, Integral, Derivation). Programming the rise time, stabilization and decrease of oven temperature.

7: Thermocouple (chromel/alumel) connected to the controller "KS40" in contact with the outer part of the tubular furnace.

8: 220V-125V transformer.

9: Voltage switches Watlow.

10: Tube which allows the evacuation of the gas mixture that occurs during annealing.

11: Rubber seal ensuring the sealing of the tube extremity.

12: Support for supporting the furnace.

13: Switch with two positions: -Start program

-Setting Parameters (control)

14: Water container with bubbles indicating the flow of gas within the furnace tube (with which the annealing is carried out).

15: Tube for the evacuation of the gas in the air.

16: Gas cylinder.

17: Window for gas evacuation.

The diagram in Fig. 33 shows the temperature versus annealing time where Tr is the annealing temperature of sample.

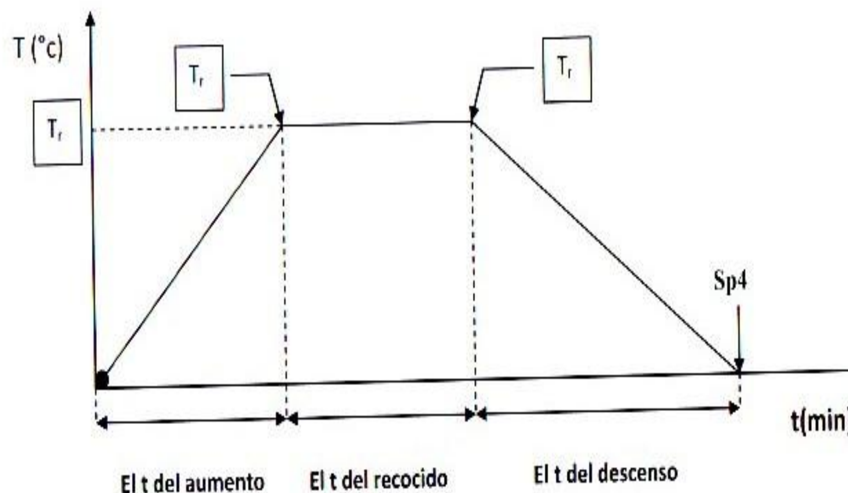

Fig. 33: Graph of temperature as function of annealing time (t) [31]

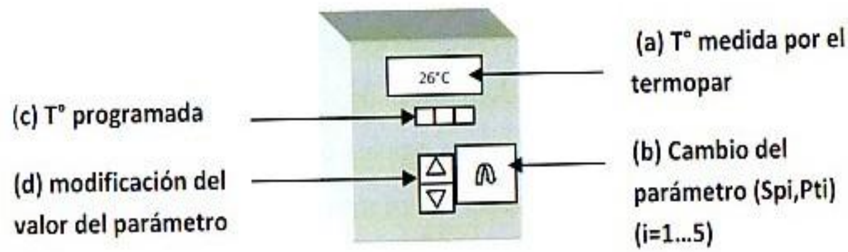

Fig. 34: The controller to adjust the parameters [31]

2.8. Four Point Probe Resistivity Measurements

2.8.1. Introduction

It's Van Der Paw, the Dutch physicist, who in 1958 gave birth to a new technique resistivity measurement. His method has the advantage of allowing the determination of resistivity arbitrarily shape sample, which have uniform and known thickness.

2.8.2. Principle of the technique of 4 points

This method is to measure the resistivity of the film if the sheet resistance is not higher than $10^7\Omega$.

It consists to inject a current of 0.1nA to 10mA through two outer probes and measuring the voltage through the inner probes allows the measurement of the substrate resistivity as shown in Fig. 35.

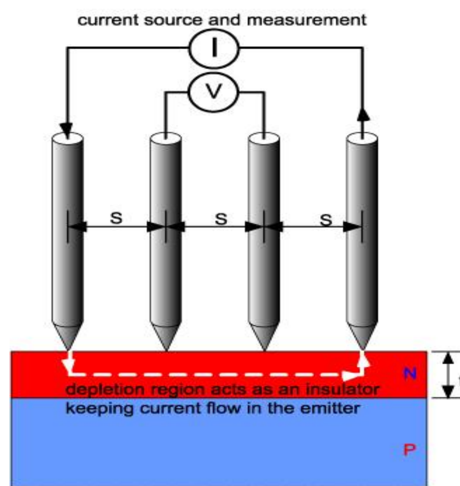

Fig. 35: Description of the method of 4 points [32]

Once the current and the voltage known, we apply the formula to the resistivity given by the manufacturer of the device.

$$\rho = 2\pi s \frac{V}{I} \quad (26)$$

when $t \gg s$

This equation is applicable for layer whose thickness (t) is very large compared to the distance between the two points of the apparatus (s).

Other hand, the resistivity of thin film is calculated using the following formula when the thickness (t) is less than a distance between 2 points of apparatus (s) [33].

$$\rho = 4.532 \frac{V}{I} . t \quad (27)$$

when $t \ll s$

where

V(V) is the difference of voltage between two points

I(A) is the injecting current

s(cm) the distance between 2 point of apparatus (given by the manufacturer s=1mm)

t(cm) the thickness of the layer

ρ(Ω.cm) the resistivity of the layer

Convenient Method for measuring 4 points

- Take measurement of V/I not too close to the sample edges
- Express Ohms measurement
- Multiply by 4.532 to get R□, note the result (still Ohms)

(The distance between centers being 1.59 mm, the thickness correction is not necessary)

- e expresses the thickness of the layer in centimeters
- Multiply R□ for e in order to obtain ρ resistivity, noting that result (in Ohm.cm)

2.9. Capacitance-Voltage measurements

2.9.1. Introduction

Mott-Schottky plot is an electrochemical technique used to determine the type, the concentration of carriers and the flat band potential of semiconductor which are very important for its characterization.

2.9.2. Semiconductor in solution

Excess of electronic charge is accumulated at the electrode surface when a conductive electrode is in contact with a liquid and the charge distribution occurs in the solution only. This is due to the fact that as the number of charged species increases, the space in which the redistribution of charges occurs shrinks [34].

The concentration of conductive species (electrons and holes) is much smaller that in the solution in the case of semiconductor electrodes. This creates a redistribution of the space charge in the semiconductor electrode at distances much larger than that in solutions, 10-100 nm [35, 36].

Redistribution in the conduction and valence band leads to potential bending at the surface:

-For n type semiconductor electrode at an open circuit, Fermi level is usually higher than the redox potential of electrolyte, and electrons are transferred from electrode to solution, producing a positive charge associated with the space charge region, causing an upward bending of band edges.

- For p-type semiconductor electrode, the opposite effect is noted; a downward bending of the band edges [37 - 38 - 35 - 36].

No bending is observed at a certain applied potential, E_{fb} called flat band potential.

The flat band potential value can be determined using Mott-Schottky plots [39-40].

The relation between $\frac{1}{C_{sc}^2}$ and the potential, where C_{sc} the semiconductor electrode capacitance is, for n-type semiconductors:

$$\frac{1}{C_{sc}^2} = \frac{2}{A^2 N_D q \varepsilon \varepsilon_0}\left(E - E_{fb} - \frac{K_B T}{q}\right) \quad (28)$$

Where ε is the dielectric constant of the semiconductors, ε_0 is the dielectric permittivity of vacuum, q is the elementary electric charge, K_B is the Boltzmann constant, N_D is the donor density, and $\frac{K_B T}{q} = 25mV$ at 25 ºC.

For a p-type semiconductor:

$$\frac{1}{C_{sc}^2} = \frac{-2}{A^2 N_A q \varepsilon \varepsilon_0}\left(E - E_{fb} + \frac{K_B T}{q}\right) \quad (29)$$

The carriers' concentration can be obtained from the gradient $\frac{dC_{sc}^{-2}}{dE}$ and the flat band potential E_{fb} with the intercept with the potential axis.

$$N_D = \frac{2}{qA^2 \varepsilon \varepsilon_0}\left(\frac{d\left(\frac{1}{C_{sc}^2}\right)}{dE}\right)^{-1} \quad (30)$$

3. Conclusion

Characterization techniques of thin films used in this research are effective tools that will allow us to study the structure and quality of layers by X-ray and Raman Spectroscopy, respectively, morphology and topography by Scanning Electron Microscopy (SEM) and Atomic Force Microscopy (AFM), respectively, photoluminescence to detect any impurities energy levels, Energy Dispersive X-ray Spectrometry (EDS) for qualitative and quantitative measurement of the elements atomic found in our samples, spectrophotometry to measure the transmittance and deduce the energy gap, four point probe method to measure semiconductors' resistivity, and finally Mott Schottky plots to determine type, carriers' concentration and flat band potential of semiconductors.

References

[1] Chamberlein R. R, Skarman J.S., J. Electrochem Soc. 113(1) (1996) 86.

[2] D. Perednis, L.J. Gauckler (2005), thin film deposition using spray pyrolysis, Journal of Electroceramics 14 103-111.

[3] Montage expérimental de Spray Pyrolysis au département de physique, Université Polytechnique de Valencia, Espagne.

[4] Pere Rocai Cabarrocas, Thèse de Doctorat, Paris VII (1988)

[5] http://fr.wikipedia.org/wiki/couche_mince.

[6] CLERET DE LANGAVANT Capucine, GOUGET Manon, LE CRANE Thomas, MERCIOL Sarah, MONFORT Laura, « les pointes liquides », VIVES Jessica (Encadrant).

[7] http://fr.wikipédia. org/wiki/Tension_superficielle

[8] http://perso.wanadoo.fr/philippe.bo euf/robert/physique/mouille.htm

[9] Phys. $3^{ième}$-Eau, Connaissances/expériences

[10] « American Institue of Physics Handbook », 2nd Ed., D. E. Gray, Ed., The Chemical Rubber Co., 1969.

[11] G. Vazquez, E. Alvarez, J.M. Navaza, Surface Tension of Alcohol +Water from 20 to 50 °C, J. Chem. Eng. Data, 40 (1995) 611-614.

[12] P. A. BERNARD, COMMENT L'ARAIGNÉE D'EAU (Ou Gerris) MARCHE-T-ELLE SUR L'EAU ?

[13] Y. Waseda, E. Matsubara and K. Shinoda, « X-Ray Diffraction Crystallography, Introduction, Examples and Solved Problems », Springer.

[14] Willeke G, Dasbach R, Sailer B, Bucher E (1992) Thin pyrite (FeS_2) films prepared by magnetron sputtering. Thin Solid Films 213:271–276

[15] Chowdhury A, Biswas B, Majumder M, Sanyal MK, Mallik B (2012) Studies on phase transformation and molecular orientation in nanostructured zinc phthalocyanine thin films annealed at different temperatures. Thin Solid Films 520:6695-6704

[16] Instituto de Diseno y Fabricacion para la Produccion Automatizada, Departamento De Fisica Aplicada, Universidad Politecnica De Valencia, Espana.

[17] Nicolas VIVET, « Elaboration et caractérisation de films minces Cr^{2+}:ZnSe nanostructurés pour la fabrication des microlasers émettant dans le moyen infrarouge », Doctorat de l'université de Caen, Août 2006.

[18] Biophy Research, Spectrsocopie Raman.

[19] K. Kambas, J. Spyridelis and M. Balkanski. » Far Infrared and Raman Optical Study of α- and β-In_2S_3 Compound ». Phys. Stat. Sol (b) 105, 291 (1981).

[20] Microscope Electronique à Balayage. Universidad Politecnica De Valencia.

[21] B. Fernandez, N. Quellard. Ingénieurs hospitalier : unité de pathologie ultrastructurale et expérimentale du CHU de Poitiers. La microscopie Electronique.

[22] S. R. Kodigala. Thin Films and Nanostructures $Cu(In_{1-x}Ga_x)Se_2$ Base Thin Films Solar Cells. Vol 35, pp. 56.

[23] Atomic Force Microscope of Universidad Politecnica De Valencia.

[24] Y. Martin. J. Appl. Phys., 61, 4723 (1987).

[25] Instruction Manual, Digital Instruments, Nanoscope III Atomic Microscope July 8, (1992) p. 23.

[26] G.D. Gilliland, Photoluminescence Spectroscopy of crystalline semiconductors, Material Science and Engineering R: Reports, Elsevier Science S.A. (1997).

[27] Umaima Elfurawi, MSci, PhD, Optical and Electronic Properties of PbS colloidal Nanocrystals, January 2012.

[298] Montage appareil de photoluminescence. Departamento de fisica applicada. Universidad politecnica de valencia.

[29] Montage expérimental- Transmittance. Département de fisica applicada-IDF, Universidad De Valencia-España.

[30] Schéma expérimental- Transmittance. Département de fisica applicada-IDF, Universidad De Valencia-España.

[31] Mustapha Sahal, Tesis Doctoral « Elaboracion y Caracterisazacion De Capas Finas De $CuInS_2$ y ZnO Intrinseco y Dopado con Al y Mg Preparadas Con Tecnicas De Bajo Coste Para Aplicaciones Fotovoltaicas », Universidad Politecnica De Valencia, 2010.

[32]http://pveducation.org/pvcdrom/characterisation/four-point-probe-resistivity measurements

[33] P. Blood and J. W. Orton, "The Electrical Characterization of semiconductors: majority carriers and electron states", Ed. N. H. March, Academic Press (1992).

[34] Andrezej Lasia, Electrochemical Impedance Spectroscopy and its Applications, 2014.

[35] 462. A.W. Bott, Curr. Sep. 17, 98 (1998)

[36] 463. K. Rajeshwar, in Encyclopedia of Electrochemistry, vol. 6, ed. by A.J. Bard, M. Stratmann, S. Licht (Wiley-VCH, Weinheim, 2002), p. 1

[37] M.E. Orazem, B. Tribollet, Electrochemical Impedance Spectroscopy (Wiley, New York, 2008)

[38] A.J. Bard, L.R. Faulkner, Electrochemical Methods. Fundamentals and Applications (Wiley, New York, 2001)

[39] W. Schottky, Z. Phys. 113, 367 (1939); 118, 539 (1942)

[40] K. Gelderman, L. Lee, S.W. Donne, J. Chem. Educ. 84, 685 (2007)

Chapter IV: Results and Discussion

A. Optimization of deposition parameters of In_2S_3 Thin Films

1. [S]/[In] Ratio Effect at Different Substrate Temperatures

1.1. Introduction

[S]/[In] ratios variation effect on the deposition of In_2S_3 thin films was studied at different substrate temperatures: 250 °C - 300 °C and 350 °C. The indium trisulfide (In_2S_3), with [S]/[In] ratios in the solution equal to 2 - 2.5 - 3 - 3.5 - 4 and 4.5, was studied. The flow rate of the nozzle is fixed at 1.5mL/min, the pressure of the compressed air at 0.7bar, the distance between the substrate and the nozzle at 30cm and the volume of the solution sprayed 10mL. The composition, morphology, structure and optical properties were studied for each substrate temperature.

1.2. Results and discussion

1.2.1. X-ray diffraction analysis

At the substrate temperature of 250 °C, we find that when [S]/[In] ratio increases from 2 to 3, the main peak (0 0 12) decreases and increases for 3.5. At low temperature, the crystallinity of In_2S_3 thin layers decreases with increasing the amount of sulfur in the initial solution until reaching [S]/[In]=3 limit. The best layers produced at this temperature are [S]/[In]= 2 and 3.5 as shown in Fig. 1. In the literature, we have found that In_2S_3 thin films produced at different ratios [S]/[In]: 3/2 - 5/2 - 8/2 - 8/1.2 has a better crystallinity for the [S]/[In] = 5/2 with (2 2 0) as main peak [1]. Moreover, thin films of In_2S_3 with [S]/[In]<2 don't have good crystallinity because the concentration of sulfur is obviously low [2].

When the temperature of the substrate increases from 250 °C to 300 °C, the main peak (0 0 12) increases with increase of sulfur concentration until the limit value of [S]/[In] 3.5. Thus, the crystallinity is improved with the increase of substrate temperature as shown in Fig. 2.

At high temperature, 350 °C, (1 0 9) peak which was low at 250 °C and 300 °C becomes more intense and for all samples. The main peak (0 0 12) increases when the concentration of sulfur in the solution increases to reach its maximum intensity at [S]/[In] = 3. We also observe the signature of the glass substrate due to the very thin layers produced at this high temperature as shown Fig. 3.

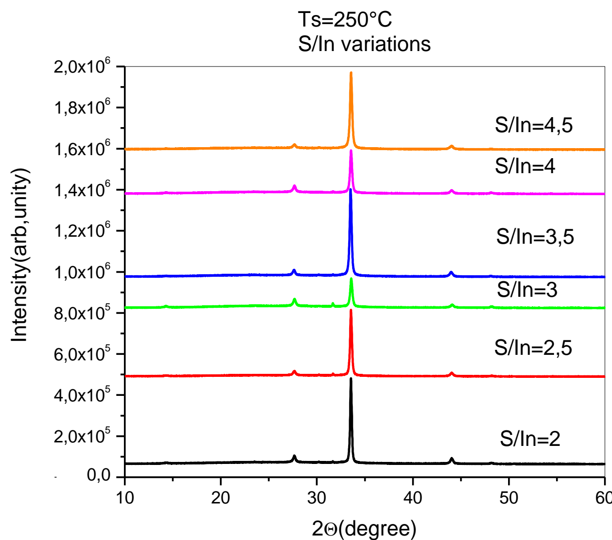

Fig. 1: X-ray diffraction spectrum of In_2S_3 at Ts = 250 °C

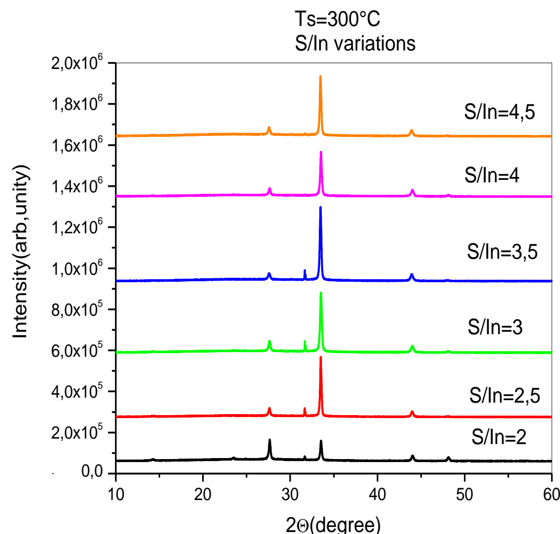

Fig. 2: X-ray diffraction spectrum of In_2S_3 at Ts = 300 °C.

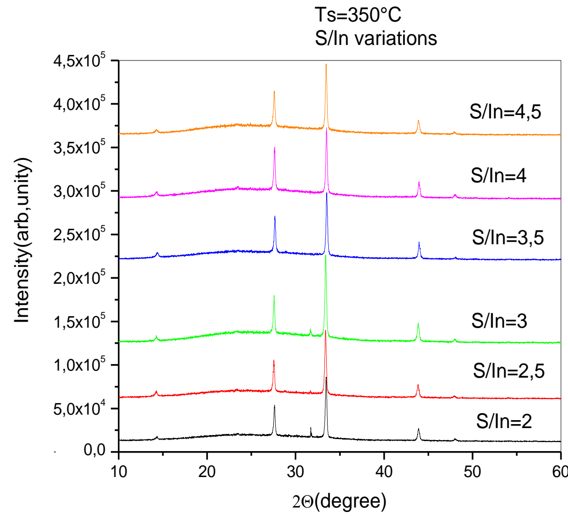

Fig. 3: X-ray diffraction spectrum In_2S_3 at Ts = 350 °C.

Crystallite size was calculated using Debye Scherrer formula of equation (6) of chapter III.

At the substrate temperature of 250 °C, the crystallite size decreases when the sulfur concentration increases from 2 to 3. When the substrate temperature increases to 300 °C, we observe an increase in crystallite size when [S]/[In] rises from 2 to 2.5. A fluctuation of crystallite size is observed and the largest size is obtained at [S]/[In] = 2.5. At high temperature, 350 °C, crystallite size decreases when the sulfur concentration increases from 2 to 3 and then reaches its maximum at 3.5 as shown in Table 1, Table 2 and Table 3.

Table 1: Crystallite Size given by Scherrer formula at Ts = 250 °C.

[S]/[In]	Sample	D (Å)
2	4	517.29
2.5	7	447.13
3	11	376.16
3.5	14	415.10
4	17	403.55
4.5	20	388.08

Table 2: Crystallite size given by Scherrer formula at Ts = 300 °C.

[S]/[In]	Sample	D (Å)
2	5	523.97
2.5	8	586.09
3	12	441.74
3.5	15	495.68
4	18	491.28
4.5	21	513.44

Table 3: Crystallite size given by Scherrer formula at Ts = 350 °C.

[S]/[In]	Sample	D (Å)
2	6	530.08
2.5	9	517.01
3	13	511.05
3.5	16	543.23
4	19	534.83
4.5	22	505.04

1.2.2. Raman Spectroscopy Analysis

For Raman spectroscopy, we have selected samples 7 - 14 and 20 prepared at 250 ℃ with $[S]/[In] = 2.5 - 3.5 - 4.5$, respectively. Raman modes observed from 100 cm^{-1} to 550 cm^{-1} confirm the β-In_2S_3 phase: Eg = 268 cm^{-1}, F2g = 329 cm^{-1}, A1g =369cm^{-1} as shown in Fig. 4.

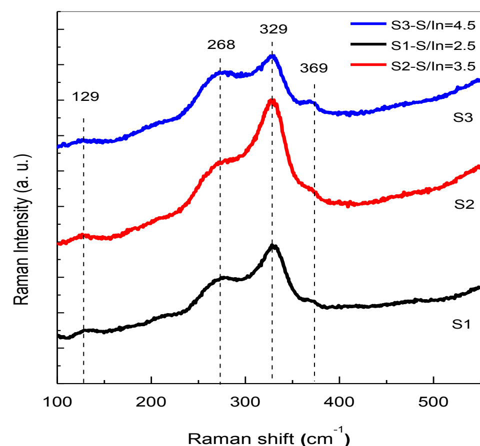

Fig. 4: Raman spectra of samples produced at Ts = 250 °C.

1.2.3. Morphological analysis by SEM

The morphology of the layers was studied using Scanning Electron Microscope (SEM). Thin layers deposited at different sulfur concentrations and at different glass substrate temperatures are dense, compact, homogeneous and practically uniform as shown in Fig. 5. Thin films synthesized at different ratios [S]/[In] = 1-2-3-4 using Chemical Spray Pyrolysis method by Xiao Zhang et al [3] have almost the same result: dense, compact and adherent well to the glass substrate films.

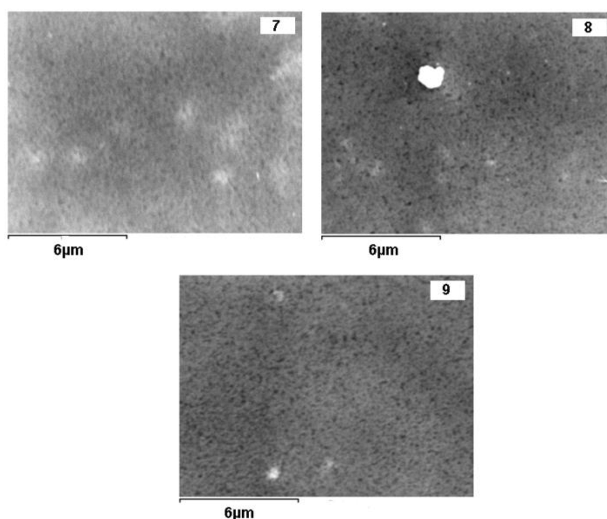

Fig. 5: SEM images of some samples at different substrate temperatures

1.2.4. EDS Analysis

The composition of thin films given by EDS reveals the presence of sulfur (S) and indium (In) in all samples with good stoichiometry. The sulfur concentration has almost no effect on the S/In ratio in the sample as shown in Table 4, Table 5 and Table 6.

Table 4: EDS of samples prepared at Ts = 250 °C.

Sample	[S]/[In]	S (%at)	In (%at)	S/In
4	2	58.74	41.26	1.42
7	2.5	58.81	41.19	1.43
11	3	59.34	40.66	1.46
14	3.5	59.24	40.76	1.45
17	4	59.44	40.56	1.47
20	4.5	59.43	40.57	1.46

Table 5: EDS of samples prepared at Ts = 300 °C

Sample	[S]/[In]	S (%at)	In (%at)	S/In
5	2	59.64	40.36	1.48
8	2.5	59.38	40.62	1.46
12	3	59.69	40.31	1.48
15	3.5	59.10	40.90	1.44
18	4	60.04	39.96	1.50
21	4.5	59.15	40.85	1.45

Table 6: EDS of samples prepared at Ts = 350 °C.

Sample	[S]/[In]	S (%at)	In (%at)	S/In
6	2	59.34	40.66	1.46
9	2.5	60.24	39.76	1.52
13	3	60.15	39.85	1.51
16	3.5	59.16	40.84	1.45
19	4	59.73	40.27	1.48
22	4.5	60.22	39.78	1.51

1.2.5. Optical Characterization

Optical characterization of our samples shows a change in transmission when the sulfur concentration increases and the substrate temperature changes. Thus at 250 °C and 300 °C, we have a transmission of about 60% which passes to 70% at high temperature, 350 °C. Moreover, a fluctuation of the gap is observed when the concentration of the sulfur and the temperature of the glass substrate vary. Fig. 6, Fig. 7, Fig. 8, Fig. 9, Fig. 10 and Fig. 11 illustrate very well the variation of the energies of the gap of samples prepared at different substrate temperatures and for various [S]/[In] ratios.

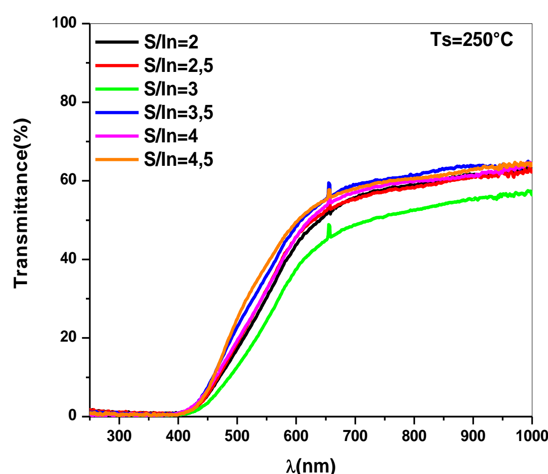

Fig. 6: Transmittance of samples prepared at Ts = 250 °C

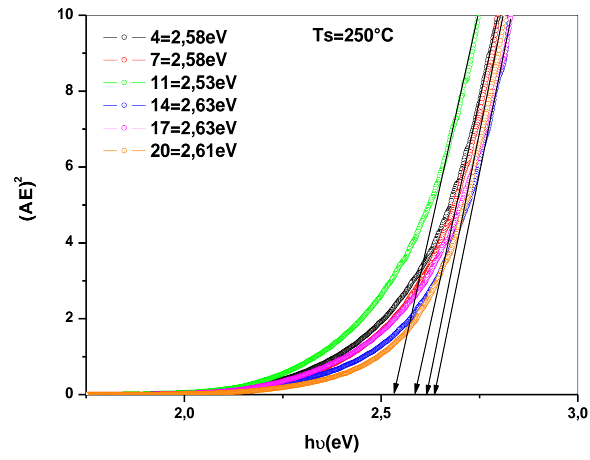

Fig. 7: Band gap energy of samples prepared at Ts = 250 °C.

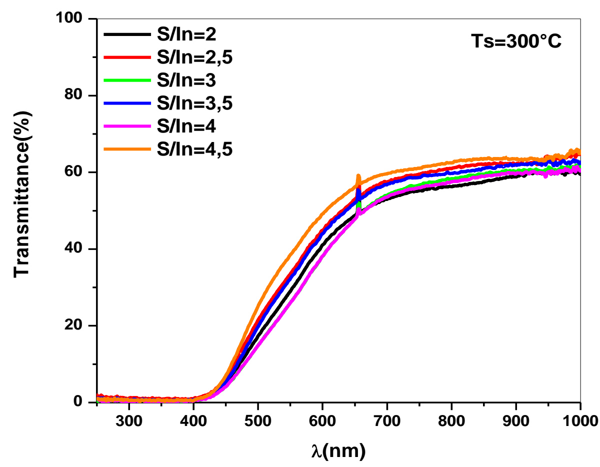

Fig. 8: Transmittance of samples prepared at Ts = 300 °C

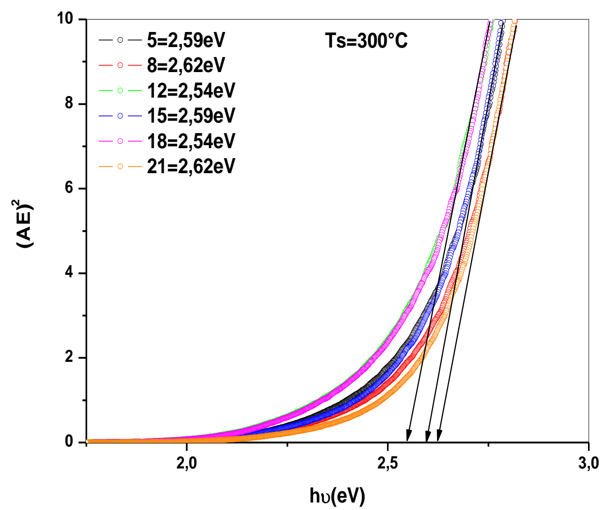

Fig. 9: Band gap energy of samples prepared at Ts = 300 °C.

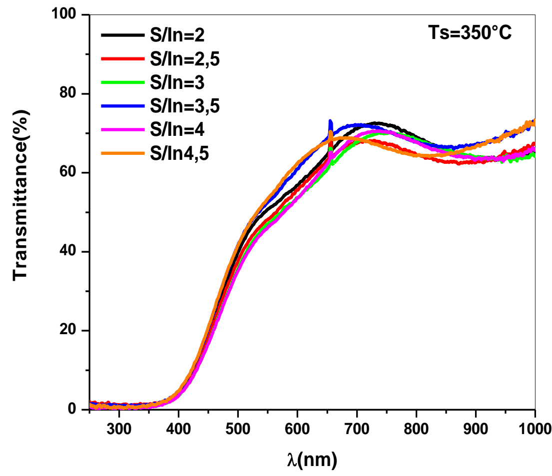

Fig. 10: Transmittance of samples prepared at Ts = 350 °C.

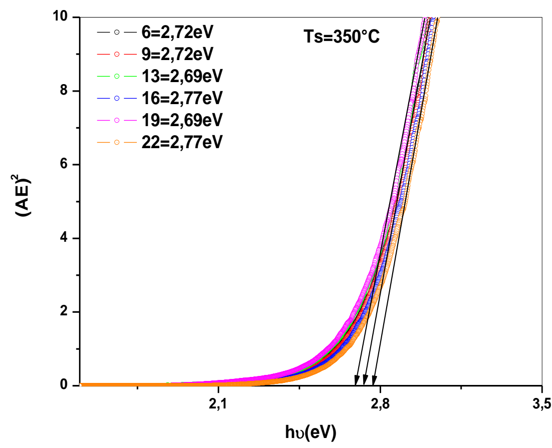

Fig. 11: Band gap energy of samples prepared at Ts = 350 °C.

Table 7: Band gap energy of samples prepared with different [S]/[In] ratios at 250 °C.

Sample	Band Gap energy (eV)
4	2.58
7	2.58
11	2.53
14	2.63
17	2.63
20	2.61

Table 8: Band gap energy of samples prepared with different [S]/[In] ratios at 300 °C.

Sample	Band Gap energy (eV)
5	2.59
8	2.62
12	2.54
15	2.59
18	2.54
21	2.62

Table 9: Band gap energy of samples prepared with different [S]/[In] ratios at 350 °C

Sample	Band Gap energy (eV)
6	2.72
9	2.72
13	2.69
16	2.77
19	2.69
22	2.77

1.3. Conclusion

β-In_2S_3 thin layers have been prepared by Chemical Spray Pyrolysis technique with different [S]/[In] ratios and at different substrate temperatures. According to the results obtained we have polycrystalline thin films with (0 0 12) as main peak which intensity decreases when [S]/[In] ratio increases from 2 to 3 at 250 °C and increases in the same ratio range at 300 °C. We also noted that (1 0 9) peak, which was low at 250 °C and 300 °C, increased in intensity at 350 °C high temperature for all ratios and all substrate temperatures. Raman spectroscopy analysis confirms β-In_2S_3 phase obtained by X-ray diffraction for some

samples elaborated at 250 °C. SEM images reveals dense, homogeneous and compact films independent of ratio and substrate temperature, and the EDS related to it reveals good stoichiometry. Samples have transmission about 60% for those elaborated at 250 °C, 300 °C and 70% for those prepared at 350 °C, independently of the ratio with band gap energies varying with the temperatures of substrates. In order to study the effect of other parameters on indium trisulphide In_2S_3 thin films, we decided to fix the ratio at [S]/[In] = 3.

2. Indium Trisulfide (In_2S_3) Elaborated at Different Substrate Temperatures

2.1. Introduction

Thin layers of In_2S_3 were prepared onto glass substrates using Chemical Spray Pyrolysis technique and using indium chloride ($InCl_3$) and thiourea ($CS(NH_2)_2$) as the indium and sulfur sources, respectively. [S]/[In] ratio of 3 at different temperatures (250 °C-300 °C-350 °C). Films before and after annealing were characterized by X-ray diffraction (XRD) for structure, Energy Dispersion Spectroscopy (EDS) for chemical element composition, Raman spectroscopy for layer quality and transmission for gap energy measurements.

2.2. Experimental conditions for preparation of In_2S_3 thin layers

2.2.1. Preparation of glass substrates

We used in this work microscope glass slides of 76x26x1mm dimension. The glass slides were cleaned by following the following procedure:

- First, they are immersed in a solution of distilled water and nitric acid (H_2O + HNO_3) for 15 minutes and rinsed with distilled water.
- Secondly, they are immersed in an ethanol solution for 15 minutes and rinsed with distilled water.
- Finally, they are immersed in an acetone solution for 15 minutes and rinsed with distilled water.

And at the end, the glass slides were dried in an oven before their use for deposition.

2.2.2. Elaboration of thin layers of indium trisulphide (In_2S_3)

Indium trisulphide (In_2S_3) is produced by the Chemical Spray Pyrolysis technique with air using a indium chloride solution (99.999% Aldrich) as a source of indium (III), thiourea (CS (NH 2) 2, ≥ 99% SIGMA-Aldrich) as a source of sulfur and air as the carrier gas. The choice of thiourea as a source of sulfur is not fortuitous because it prevents the precipitation of metal sulfides and hydroxides since it forms a complex easily with indium [4]. Bi-distilled water was chosen as solvent and the addition of alcohol (5% by volume) to the solution of 50 ml in order to reduce the surface tension of the water to allow a good adhesion of the deposit onto the glass substrate. The indium molarity was optimized at 0.026mol/l and that of sulfur was tripled with respect to that of indium in order to compensate the sulfur deficiency caused by evaporation and to have good layers of indium trisulphide.

The formation reaction of indium trisulfide (In_2S_3) is carried out by the following chemical equation:

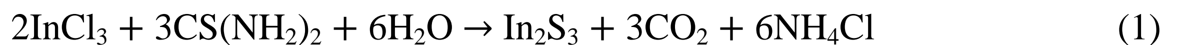

$$2InCl_3 + 3CS(NH_2)_2 + 6H_2O \rightarrow In_2S_3 + 3CO_2 + 6NH_4Cl \quad (1)$$

Table 10 summarizes all the parameters used for the preparation of thin films of indium trisulfide In_2S_3 by Chemical Spray Pyrolysis method.

Table 10: In_2S_3 films Sample deposition parameters

Sprayed solution volume	10mL
Air pressure	0.7 bar
Rate	1.5mL/mn
Nozzle-substrate distance	30cm
Substrate temperature	250°C - 300°C - 350°C
Annealing temperature	400°C-30 mn sous vide (0.02 mbar)

2.3. Results and Discussions

2.3.1. X-ray diffraction analysis

X-ray diffraction patterns shown in Fig. 12 reveal the presence of In_2S_3 film of quadratic structure with lattice parameters: a = b = 7.619Å and c = 32.329Å and (0 0 12) as preferred orientation confirmed by JSPDS (25-0390) files. The intensity of this peak increases when

the temperature of the substrate increases from 250 °C to 300 °C, enhancing the crystallinity of our films and decreases at 350 °C. This decrease can be explained by a possible evaporation of a part of the deposit at high substrate temperature. We also noted the presence of low peaks highlighted with (1 1 6) - (1 0 9) - (1 0 15) and (2 2 12). An unidentified peak at 2θ≈31.24 was demonstrated with an increase in intensity as the temperature increased from 250 °C to 300 °C as shown in Fig. 12.

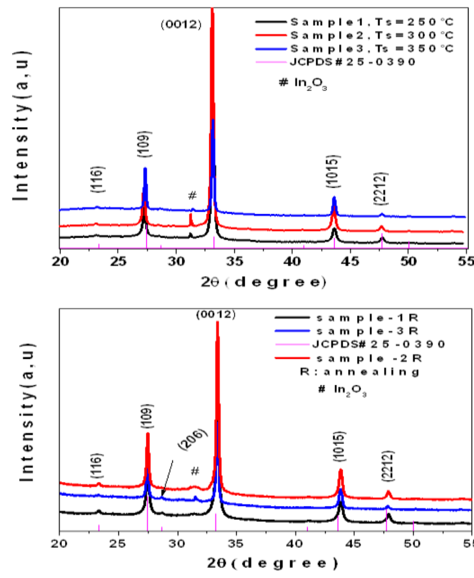

Fig. 12: X-ray diffraction spectra of samples with and without annealing

The crystallite size was calculated using the Debye -Scherrer formula and the main peak (0 0 12). An increase in size is observed, from 344 nm, 403 nm to 515 nm when the temperature of the substrate increases from 250 °C, 300 °C to 350 °C, respectively; thus confirming the improvement of the crystallinity as shown in Fig. 13.

After annealing at 400 ºC and under vacuum (0.02mbar) the diffraction peaks identified before annealing remain with (0 0 12) as preferred direction. The other secondary peaks (116), (109), (1015), and (222) exist with an additional peak (206) at 350 °C.

The unidentified peak before annealing disappears at 250 °C, decreases in intensity at 300 °C but on the other hand increases in intensity at 350 °C.

Crystallite size increases with substrate temperature but decreases with respect to those of films obtained without annealing. Thus, it is 265 nm at 250 °C, 374 nm at 300 °C and 388 nm at 350 °C as shown in Fig. 13.

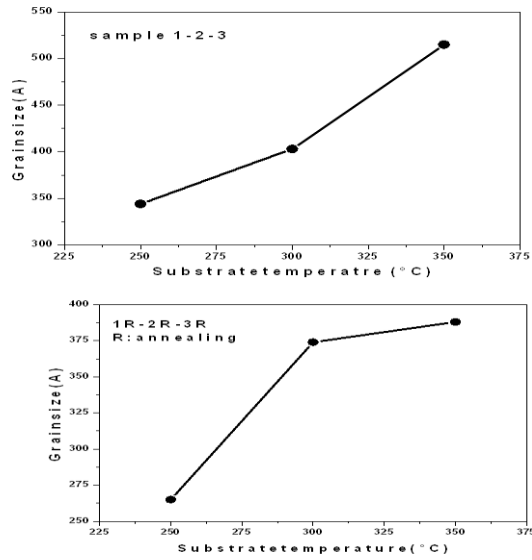

Fig. 13: Evolution of crystallite size as function of substrate temperature before and after annealing

2.3.2. Morphological analysis

Scanning Electron Microscopy (SEM) images of our samples show dense, uniform, well-covering layers that adhere well to substrates and with no cracks and voids for all substrate temperatures. Few bright white spots on the surface shown in Fig. 14 can be attributed to weakly bound β-In_2S_3 groups.

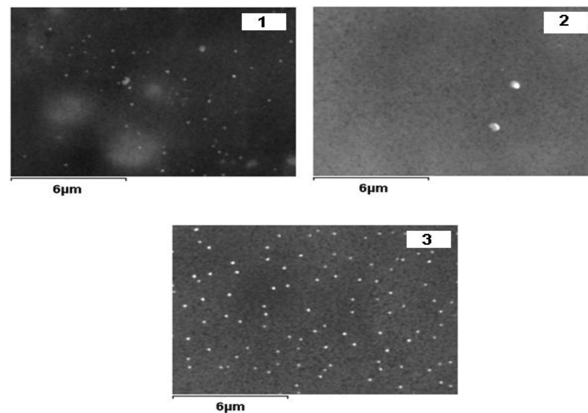

Fig. 14: SEM images of samples before annealing

After annealing at 400 °C under vacuum, SEM micrographs show layers that not practically changed in morphology with respect to the layers without treatment for the substrate temperatures 300 °C and 350 °C instead of at 250 °C we noted an evaporation of the deposited layer.

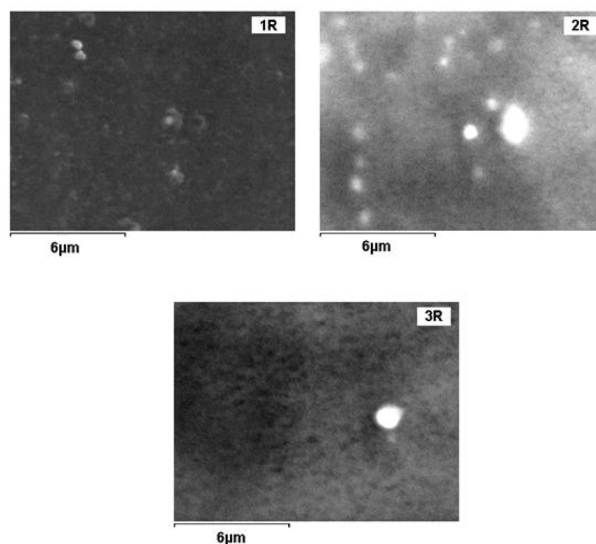

Fig. 15: SEM images of samples after annealing

2.3.3. X-ray Energy Dispersion Spectroscopy Analysis (EDS)

Chemical composition of our samples was given by EDS. These samples were carbon metalized to determine, qualitatively and quantitatively, the chemical composition. The atomic percentages of the sulfur (S) and indium (In) elements in the sample for different substrate temperatures are summarized in Table 11 that shows layers with good stoichiometry and with improvement when substrate temperature increases.

Table 11: EDS of β-In_2S_3 films without annealing

Sample	**Temperature (°C)**	**[S]/[In] (solution)**	**S (%at.)**	**In (%at.)**	**S/In (film)**
1	250	3	59.34	40.66	1.46
2	300	3	59.69	40.31	1.48
3	350	3	60.15	39.85	1.51

After annealing EDS microanalysis shows the existence of the sulfur (S) and indium (In) elements in all samples with an improvement of the stoichiometry with respect to the layers obtained without treatment at 300 °C and 350 °C and a decrease relative to the non-annealed layer at 250 °C. This decrease is probably due to the evaporation of the sulfur as revealed in Table 12.

Table 12: EDS of β-In_2S_3 films after annealing

Sample	Temperature (°C)	[S]/[In] (solution)	S (%at.)	In (%at.)	S/In (film)
1R	250	3	53.14	46.86	1.13
2R	300	3	60.39	39.61	1.52
3R	350	3	60.46	39.54	1.53

2.3.4. Optical properties

We have studied the transmittance of our samples produced at different substrate temperatures in 300−1000nm wavelength. Fig. 16 shows an increase in transmittance (70%) as substrate temperature increases. We also observe a shift of the curve towards small wavelengths when the temperature passes from 250 °C to 350 °C.

$(Ah\nu)^2$ as a function of hν graphs shows samples with band gap energies vary with the substrate temperature. When substrate temperature passes from 250 °C to 350 °C, optical gap changes from 2.47 eV to 2.74 eV. This increase of band gap energy is often interpreted as an incorporation of oxygen into the film at high temperature.

After annealing, the transmittance of the films decreases compared to that of films without annealing and the maximum transmittance obtained is 62% at 300 °C. The energies of the gap are 2.38 eV at 250 °C, 2.46 eV at 300 °C at 2.39 eV at 350 °C. It is clearly noted that the band gap energies decrease drastically with annealing at substrate temperatures 250 °C and 350 °C and it remains substantially stable at 300 °C as shown in Fig. 17.

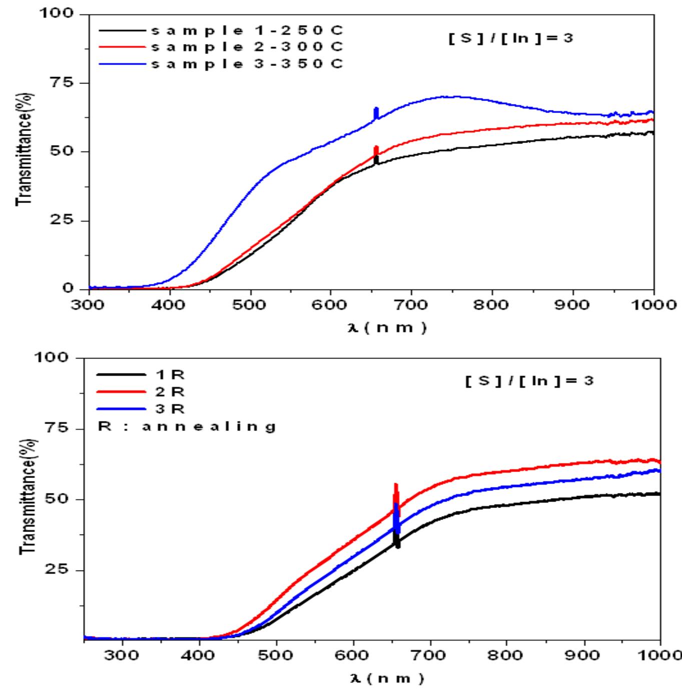

Fig. 16: Transmission of β-In_2S_3 films before and after annealing

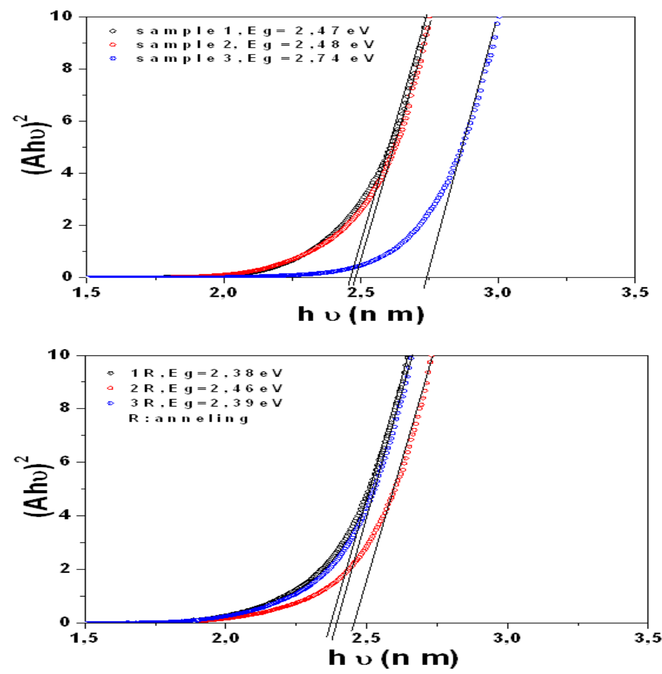

Fig. 17: Bandgap energy of β-In_2S_3 films before and after annealing

Table 13: Bandgap energy of β-In_2S_3 films before and after annealing

Sample	Band gap energy before annealing (eV)	Band gap energy after annealing (eV)
1-1R	2.47	2.38
2-2R	2.48	2.46
3-3R	2.74	2.39

2.3.5. Analysis by Photoluminescence (PL)

Photoluminescence is a non-destructive technique for determining certain impurities in a material. It is particularly suitable for detecting levels of surface impurity. The identification of the impurities is quite easy by the photoluminescence technique but the measurement of their concentration is very difficult. Photoluminescence can provide information on different types of impurities at the same time.

The photoluminescence measurements were carried out on our samples at the temperature of 8 K and with a laser of wavelength λ = 532 nm.

The analysis of photoluminescence spectrum (PL) of our samples prepared at different substrate temperatures, as shown in Fig. 18, has the appearance of Gaussian which can be characterized by three parameters: the maximum intensity (I_{PL}), the corresponding wavelength at this maximum intensity λ_{PL} and the half-width (Full Width at Half Maximum-FWHM). We observe, after annealing, two particular phenomena: the decrease of the maximum intensity of PL and the shift of the energy position of the spectrum towards the high wavelengths; from 868 nm to 920 nm for sample 3 and from 834 nm to 900 nm for sample 2. For sample 1, its intensity is low and almost negligible before and after vacuum annealing. The characteristics of these curves (maximum intensity and spectral position) vary with the structural characteristics of the sample (size, density, shape of the nano-scale grains). The decrease in both of the size and the density of grains may result in the shift of the curve towards long wavelengths and the reduction in the intensity of PL, respectively.

The peaks observed at positions 807 nm, 854 nm, 879 nm correspond to a sulphur deficit-valence band transition, sulfur deficit and interstitial indium atom, respectively. The peaks 967nm and 1040nm are not identified. These positions do not correspond to the peaks found

in the literature for In/S = 0.72 and measured at a temperature of 15°K that are at 568nm and 663nm positions, respectively corresponding to the transitions $V_S \rightarrow V_{In}$ and $I_{ni} \rightarrow O_{VS}$ [5].

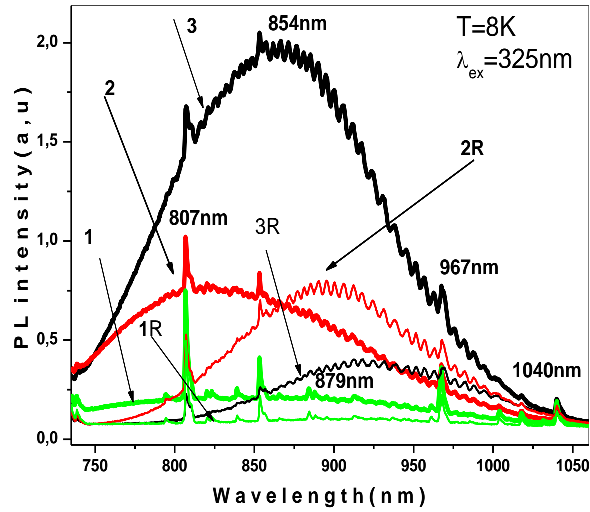

Fig. 18: PL spectrum of β-In_2S_3 films before and after annealing

2.3.6. Raman Spectroscopy Analysis

Raman spectroscopy is a non-destructive and relatively fast technique for determining the phase and quality of our samples.

For sample 2 and sample 3, we observed a dominant Raman vibration mode F2g at 325cm^{-1} while for sample 1 the dominant mode is at the position 332cm^{-1}.

After annealing at 400 °C under vacuum, the vibration modes of our samples become more prominent, illustrating an improvement in crystallinity and we have identified four modes for all samples which are F2g at 180 cm^{-1}, Eg at 270 cm, F2g at 325 cm^{-1} and A1g at 370 cm^{-1} and that correspond well to the vibration modes encountered in the literature for the indium trisulfide compound (In_2S_3) [6] as shown in Fig. 19

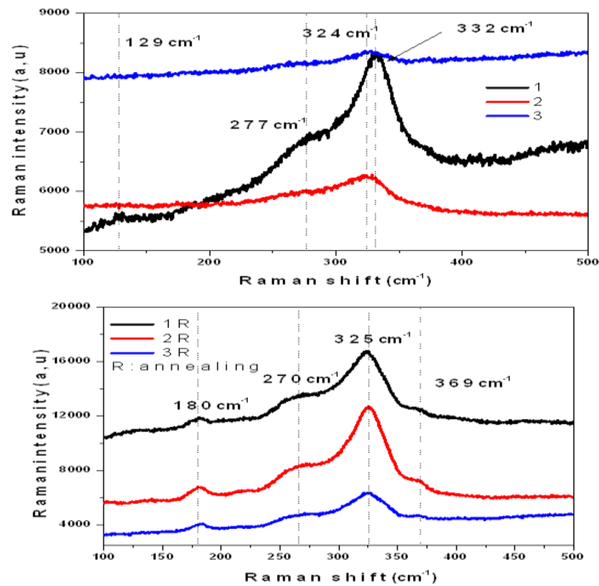

Fig. 19: Raman spectrum of β-In_2S_3 films before and after annealing

2.4. Conclusion

Thin layers of indium sulphide (In_2S_3) are deposited on glass substrates by Chemical Spray Pyrolysis method at different temperatures: 250 °C - 300 °C and 350 °C and are characterized. X-ray diffraction shows well-crystallized layers with (0 0 12) as preferential orientation perpendicular to the surface of the glass substrate. The composition of layers given by EDS shows films with good stoichiometry after vacuum annealing. Raman spectroscopy confirms the presence of β-In_2S_3 phase with more pronounced modes after vacuum annealing. Bandgap energy measurements reveal large band gap energy of β-In_2S_3 films that drastically decrease after annealing at Ts = 250 °C and Ts = 350 °C and stable gap energy at Ts = 300 °C.

3. β-In_2S_3 deposited by Chemical Spray Pyrolysis method from Bi-Distilled Water Solvent and Alcohol Solvent

3.1. Introduction

In this chapter, we have prepared indium sulfide (β-In_2S_3) thin films by Chemical Spray Pyrolysis method using distilled water solvent and distilled water solvent with alcohol (isopropyl 5% of the total volume of 50 mL). We used X-ray diffraction (XRD) to characterize the structure, Scanning Electron Microscopy (SEM) and the Atomic Force Microscopy (AFM) for the morphology and topography, Energy Dispersive X-ray

Spectroscopy (EDS) associated to SEM for qualitative and quantitative analysis of films' elements and finally spectrophotometer for the determination of bandgap energy.

3.2. Experimental details

Thin layers were prepared using Indium Chloride, Thiourea, bi-distilled water and alcohol (isopropyl) as precursors with 0.026M of In, [S]/[In] = 3 and an amount of alcohol of 5% with respect to the total volume of the solution of 50 ml. Temperatures of the glass substrates were varied: 250 °C - 277 °C-300 °C-330 °C and 350 °C.

We used glass substrates of dimension 76mm x 26mm x 1.1mm. These substrates are first rinsed in a solution of hydrochloric acid and distilled water for 15 minutes, followed by acetone solution for 15 minutes and finally in ethanol solution for 15 minutes followed by dried before use.

Deposition parameters used in spray pyrolysis are summarized in Table 14.

Table 14: Sample deposition parameters

Spray solution volume	5mL
Carrier gas pressure	0.7 bar
Spray deposition rate	1.5mL/mn
Nozzle-to-Substrate distance	30cm
Substrate temperature	250 °C - 277 °C - 300 °C - 330 °C - 350 °C

3.3. Results and Discussions

3.3.1. X-ray diffraction analysis

Fig. 20 and Fig. 21 show that X-ray diffraction analysis of the samples reveals polycrystalline thin films with (0 0 12) as main peak [7] which increases in intensity when the substrate temperature rises from 250 °C to 300 °C. We also note other peaks at 14.17 ° - 22.30 ° - 27.54 ° - 43.96 ° and 48.06 ° corresponding to (103), (107), (116), (109), and (1 0 15), respectively for aqueous solution confirming β-In_2S_3 phase (JCPDS # 25-0390). The same peaks are observed with a shift towards large angles except the peak (107) which is absent in samples prepared with alcoholic solution.

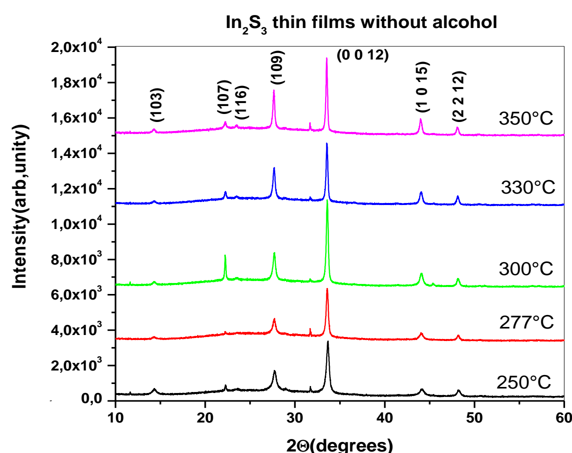

Fig. 20: XRD spectrum β-In_2S_3 thin films prepared with aqueous solution

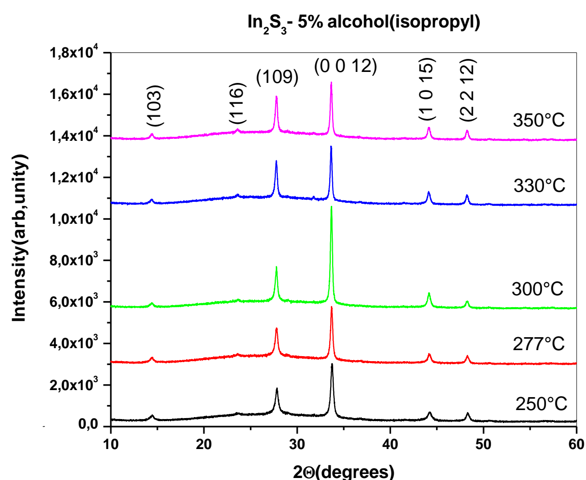

Fig. 21: XRD spectrum β-In_2S_3 thin films prepared with alcoholic solution

Crystallite size of different samples was determined from the X-ray diffraction spectra using Scherrer formula and (0 0 12) main peak.

In Table 15 and Table 16, for samples synthesized with aqueous solution as for those elaborated with alcoholic solution, we note an increase of crystallite size when the temperature of the substrate increases with almost equal sizes in both cases.

Table 15: Crystallite size of β-In_2S_3 films obtained by aqueous solution

Samples	Crystallite size (nm)
W1	28.66
W2	31.95
W3	38.08
W4	39.54
W5	46.09

Table 16: Crystallite size of β-In_2S_3 films obtained by alcoholic solution

Samples	Crystallite size (nm)
A1	26.80
A2	34.62
A3	36.09
A4	37.57
A5	35.96

3.3.2. Morphological analysis by SEM

SEM is used to study the morphology of indium sulphide thin films at different substrate temperatures and solvents. We note from SEM images, homogeneous, dense, well-cover surface of the substrate of In_2S_3 films with cracks on thin layers prepared from aqueous solution in addition of aggregates while those made with alcoholic solution are smooth and no aggregate is observed. We also notice very fine grains for indium trisulphide (In_2S_3) layers made with alcoholic solution because the use of alcohol favors the formation of small grains because of its low surface tension compared to simple distilled water [8] as shown in Fig. 22 and Fig. 23.

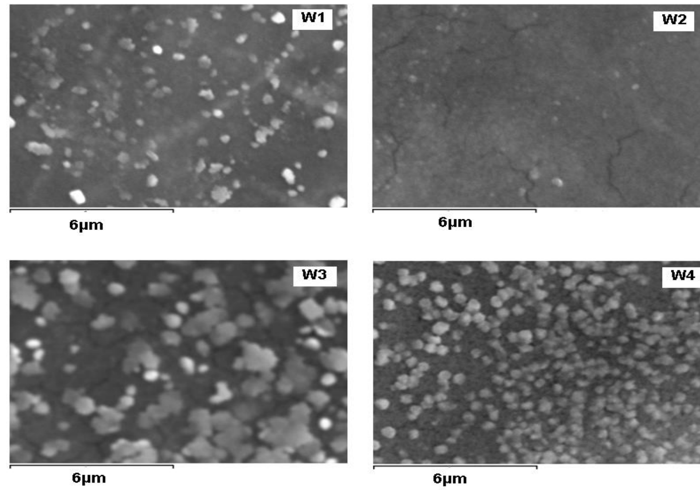

Fig. 22: SEM micrograph of β-In_2S_3 thin films prepared from aqueous solution

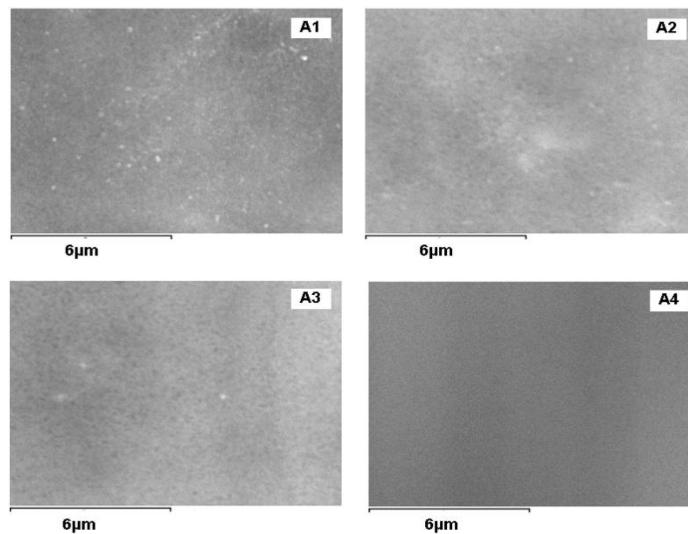

Fig. 23: SEM micrograph of β-In_2S_3 thin films prepared from alcoholic solution

3.3.3. Topographic analysis by AFM

We used AFM in addition to SEM to characterize the topography of In_2S_3 thin films prepared by Chemical Spray Pyrolysis method. The 2D images are recorded for a general view of the film surfaces and to determine, quantitatively, roughness and grain size. AFM photographs of In_2S_3 prepared from various solvents and at different substrate temperatures analyzed over an area of 1µm×1µm are given in Fig. 24 and Fig. 25. The films are typically rough due to incoherent segregation on the surface of layers.

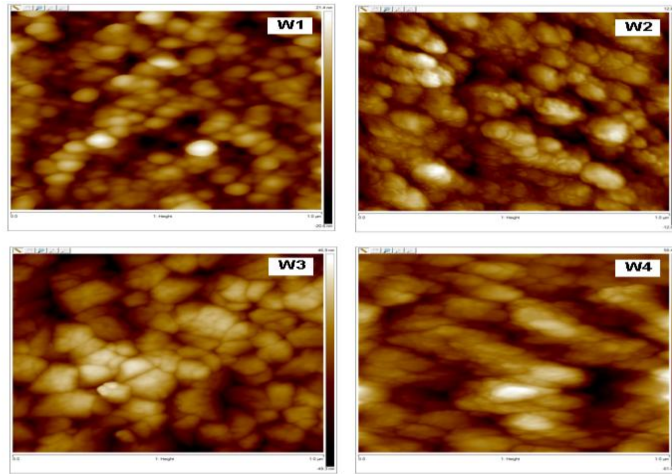

Fig. 24: 2D image of β-In_2S_3 thin films produced from bi-distilled water solvent

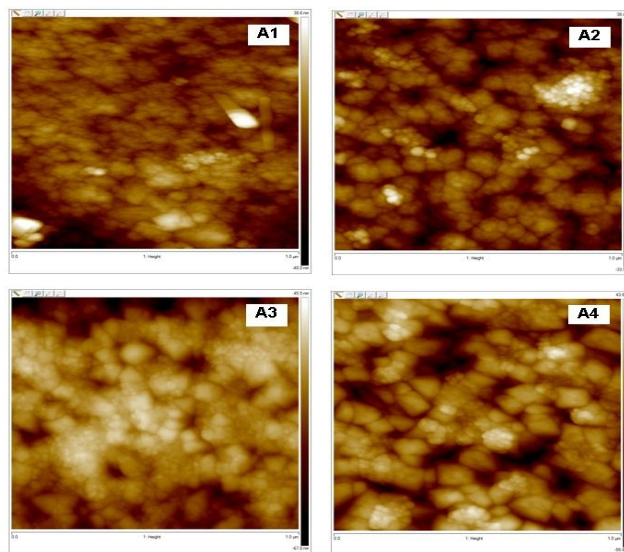

Fig. 25: 2D image of β-In_2S_3 thin films produced from alcoholic solvent

The roughness and grain size summarized in Table 17 and Table 18 show that the layers made from an aqueous solution have almost the same roughness as those prepared from alcoholic solvent and we note a variation of grains size with solvent used and temperature of the substrate. The grain size is larger for films prepared without addition of alcohol than by those prepared with an alcoholic solution. Moreover, we also note that the grain size measured from AFM technique is larger than crystallite measured from Debye Scherrer formula due to the fact that a grain is formed by several crystallites.

Table 17: Roughness and Grain size of β-In_2S_3 layers obtained from aqueous solution

Sample	Roughness (nm)	Grains size (nm)
W1	7.26	79.71
W2	6.37	82.58
W3	11.60	130.45
W4	33.00	117.03
W5	12.30	223.84

Table 18: Roughness and Grain size of the β-In_2S_3 layers obtained from aqueous solution with alcohol

Sample	Roughness (nm)	Grains size (nm)
A1	6.86	66.17
A2	7.05	73.29
A3	12.20	69.96
A4	11.00	92.66
A5	7.38	59.41

3.3.4. Energy Dispersion X-ray Spectroscopy analysis (EDS)

It is a tool for quantitative and qualitative measurements of elements present in samples after their preparation. The X-ray microanalysis of In_2S_3 thin films revealed the presence of sulfur (S) and indium (In) elements. The atomic concentrations of In and S are given in Table 19 and Table 20. All the samples produced have good stoichiometry, which means that the amount of alcohol added does not influence the atomic concentration in films.

Table 19: EDS composition of β-In_2S_3 thin films prepared with bi-distilled water solvent

Sample	S(%at)	In(%at)	S/In
W1	59.70	40.30	1.48
W2	58.95	41.05	1.44
W3	57.60	42.40	1.36
W4	59.25	40.75	1.45
W5	60.42	39.58	1.52

Table 20: EDS composition of β-In_2S_3 thin films prepared with alcoholic solvent (5%)

Sample	S(%at)	In(%at)	S/In
A1	59.32	40.68	1.46
A2	59.09	40.91	1.44
A3	58.78	41.22	1.43
A4	58.94	41.06	1.44
A5	59.27	40.73	1.46

3.3.5. Optical Properties of In_2S_3 Thin Films

Yvon-Jobin HR 460 UV-VIS-Infrared spectrophotometer permits to carry out optical transmission measurements in a wavelength range between 250 nm and 1000 nm. Transmission spectra of thin films deposited from bi-distilled water solvent and bi-distilled water in which alcohol was added and at different substrate temperatures showed transmittance between 56% and 66% for films prepared with bi-distilled water solvent and transmittance between 67% and 80% for those prepared from alcoholic solvent. Then, the addition of alcohol has an influence on the transmittance of In_2S_3 layers as shown in Fig. 26 and Fig. 27.

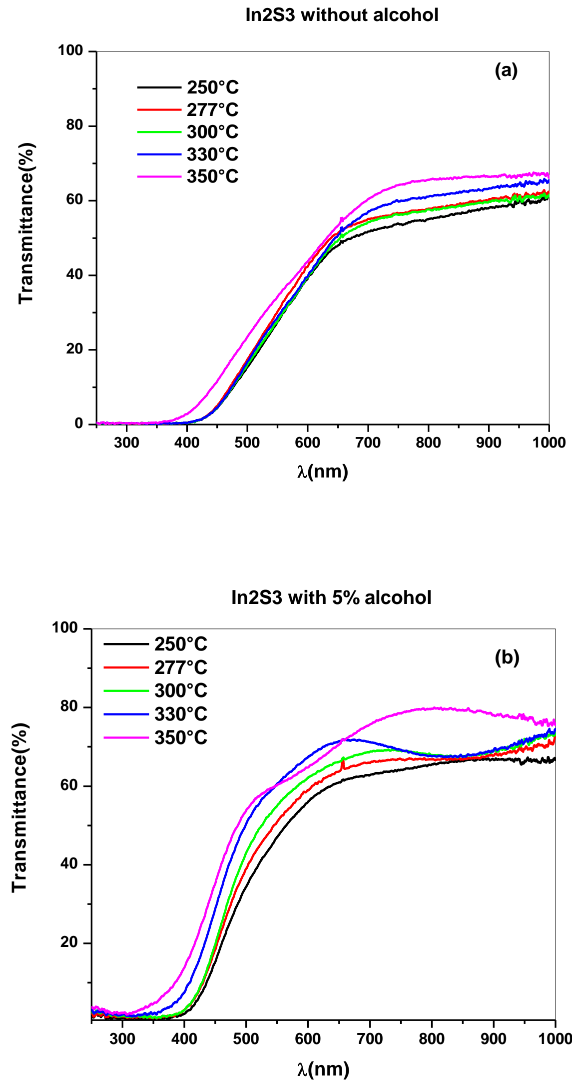

Fig. 26: Transmittance spectrum of β-In_2S_3 thin films prepared with bi-distilled water solvent (a) and alcoholic solvent (b)

The figure shows curves of $(Ah\nu)^2 = f(h\nu)$ relative to thin layers studied. The extrapolation of $(Ah\nu)^2 = 0$ leads to band gap energies values between 2.54eV and 2.81eV for layers prepared from bi-distilled water solvent and band gap energies values between 2.70eV and 2.89eV for those prepared from alcoholic solvent; which is very different to band gap energies obtained by M. Calixto-Rodriguez et al. Al [9] and Kim et al. [10] who also used an alcoholic solution and obtained band gap energies around 2.2eV and 2.2-2.4 eV, respectively. On the other hand, K. Otto et al [11] obtained band gap energy of 2.95eV with films prepared using Chemical Spray Pyrolysis technique at substrate temperature of 230 °C and [In]/[S]=1/6 ratio. The increase in bandgap value observed for alcoholic solvent is probably due to the small thickness of samples that we did not have the opportunity to

measure. On the other hand, we also note an increase in the band gap energy with the increase of the substrate temperature for films prepared from alcoholic solvent and a stability of the energy of band gap energy for those prepared from bi-distilled water solvent from 250 °C to 330 °C as shown in Fig. 27.

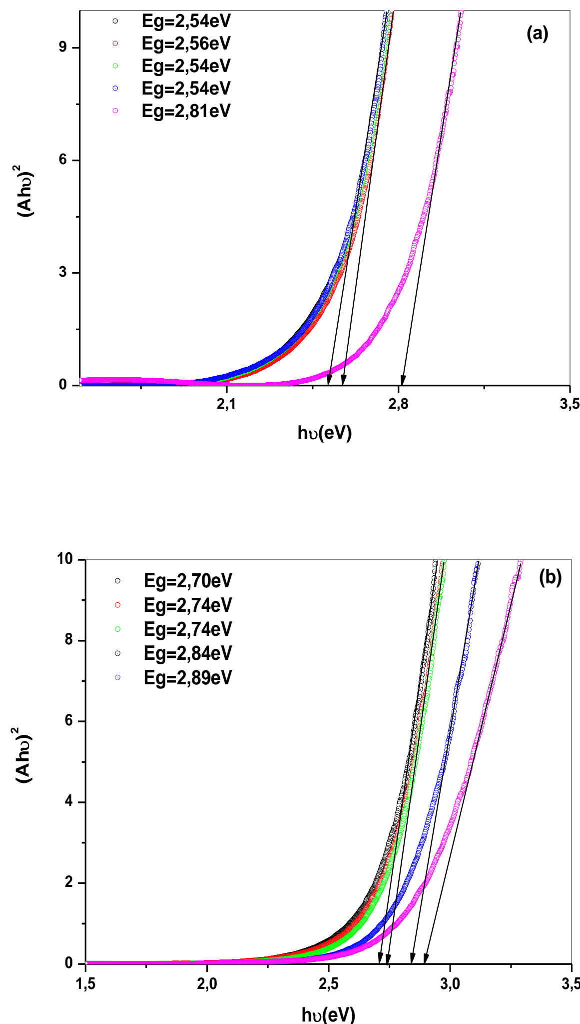

Fig. 27: Bandgap energy of β-In_2S_3 films prepared from bi-distilled water solvent (a) and alcoholic solvent (b)

3.4. Conclusion

β-In_2S_3 thin films are prepared by Chemical Spray Pyrolysis using $InCl_3$ and Thiourea as the source of indium and sulfur, respectively. Distilled water and alcohol are also used as well as different substrate temperatures. The X-ray diffraction spectrum shows polycrystalline films with (0 0 12) as the main peak which reaches a maximum intensity at 300 °C for two solvents. We also note (1 0 7) peak only in samples elaborated without alcohol. SEM images

show homogeneous, dense, compact layers which adhere well to the substrate and without void for thin films prepared with 5% alcohol, while for those prepared with bi-distilled water some cracks are highlighted. Topographic analysis confirms the SEM results and shows that layers have almost same roughness independently of the solvent but with larger grain sizes for alcohol-free layers. Finally, the bandgap energies of our samples prepared with alcohol are greater than those produced without alcohol. This is probably due to the size of the small grains observed with alcoholic solvent.

In order to obtain β-In_2S_3 thin layers prepared by Chemical Spray Pyrolysis technique, polycrystalline, homogeneous, dense, compact, which adhere well to the glass surface substrate and without crack, with good stoichiometry, acceptable roughness and high bandgap energy in order to recover part of the solar spectrum in the small wavelengths a certain quantity of alcohol in the initial solution has to be added in order to reduce the surface tension of the water and to use substrate temperature of 300 °C with [S]/[In]=3.

B. Optimization of Deposition Parameters of SnS Thin Films

1. Effect of [S]/[Sn] ratios

1.1. Experimental details

Tin monosulfide (SnS) thin films were prepared onto glass substrate from aqueous solution containing tin (II) chloride dihydrate ($SnCl_2.2H_2O$), thiourea ($CS(NH_2)_2$) (≥99%) and alcohol (10% in volume) to reduce the surface tension of water. The concentration of tin chloride was fixed at 0.02M and the [S]/[In] ratio was varied from 1 to 4 in step of 1. The substrate temperature was fixed at 300 °C. The volume sprayed was 5 mL, the spray rate 1.5 mL/min, the air compressed pressure 0.7 bar and the distance between the glass substrate and nozzle was kept to 25 cm.

Glass substrates were washed in ultrasonic bath of acetone for 15 minutes, rinsed with distilled water following by washed in a bath of ethanol for 15 minutes and rinsed with distilled water before dried and used for spray.

1.2. Results and Discussion

1.2.1. X-ray diffraction

SnS thin films with different [S]/[Sn] ratios were prepared by Chemical Spray Pyrolysis technique and XRD spectra are presented in Fig. 28. All films are SnS polycrystalline with orthorhombic structure and preferential orientation along (111) at [S]/[Sn]=1 while when the ratios increase from 2 to 4, the main peak becomes (101) and the (111) peaks decreases. We noted also others peaks like (021) and (141) for all ratios.

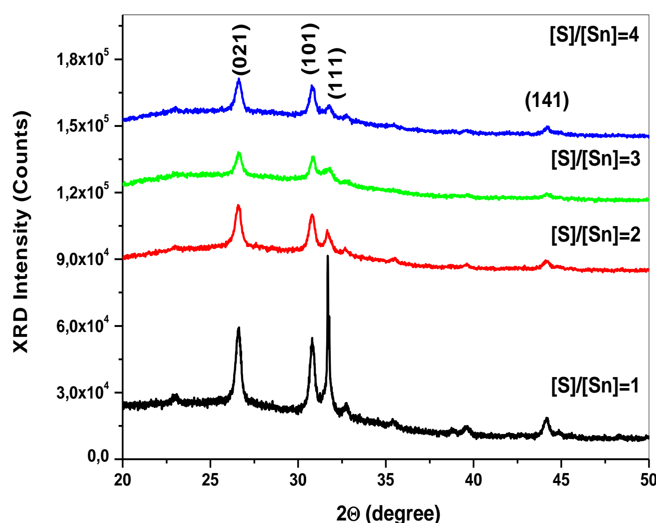

Fig. 28: X-ray diffraction patterns of SnS thin films with different ratios.

The variation of crystallite size with various [S]/[Sn] ratios was investigated using the Debye-Scherrer formula from (111) for [S]/[Sn]=1 and from (101) for [S]/[Sn] varied from 2 to 4 diffraction line. It is worth to notice that crystallites decrease when [S]/[Sn] ratios increase from 1 to 4. Table 21 shows the variation of crystallites size with the variation of [S]/[Sn] ratio.

Table 21: Crystallite size of SnS thin films with different [Sn]/[S] ratios

[S]/[Sn] ratio	**D (Å)**
[S]/[Sn] = 1	88.2
[S]/[Sn] = 2	36.7
[S]/[Sn] = 3	30.5
[S]/[Sn] = 4	27.0

1.2.2. Raman Spectroscopy

Raman spectroscopy is very important tool for studying semiconductor films structure and was used to determine second phase like SnS_2, Sn_2S_3, SnO or SnO_2 in our films. Raman spectra of SnS thin films recorded in the range of 80-350cm^{-1} are shown in Fig. 29. Raman modes located at 88, 107, 170 and 193 cm^{-1} confirm that only SnS phase is present in our films and any other secondary phases were observed [12-13].

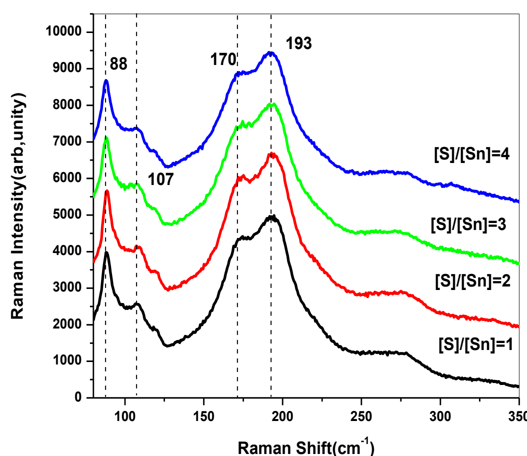

Fig. 29: Raman spectroscopy analysis spectra of SnS prepared with different [S]/[Sn] ratios.

1.2.3. Surface Morphology measured by SEM

SEM is one of the predominant techniques to survey the surface of the films. Fig. 30 shows SEM micrographs of SnS thin films deposited with various ratios at fixed substrate temperature of 300 ºC. SEM images revealed well covered films onto glass substrate with rounded uniform grains size for all ratios and size flake-like particles but those deposited with [S]/[Sn]=2 seems smaller that others ratios and the same film was denser and more compact compared to others. It is possible that the difference in morphology is caused by the effect of different concentrations of sulphur.

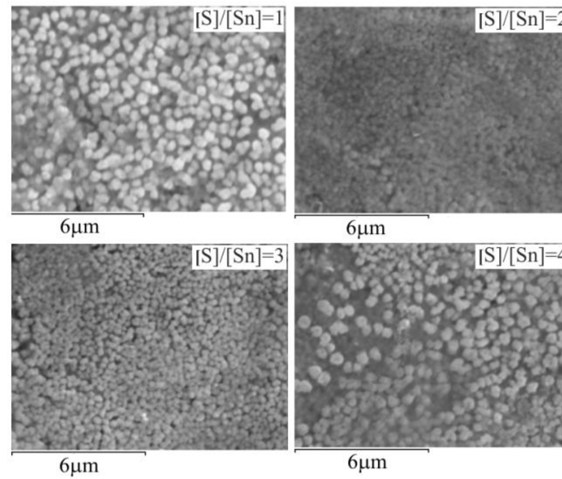

Fig. 30: SEM images of SnS films deposited with different [S]/[Sn] ratios.

1.2.4. Surface Topography measured by AFM

AFM is a technique for analyzing in order to achieve a direct insight into surface topography features of films. It was used to study the evolution and the developpement of the morphological state of the sprayed SnS thin films as a function of thiourea concentration in [S]/[Sn] ratio. It gives grain size and roughness of thin films. It is clear seen that the topography of our films changes with the variation of thiourea concentration in the initial solution. We notice that all films are rough with film prepared with [S]/[Sn] ratio of 1 the most rougher with 45nm and it has also the larger grain size evaluate at 247.35 nm than others films. When [S]/[Sn] ratio increase from 2 to 4, ones noted that the roughness increases from 20.20 to 26.60 nm and grain size increases significantly at the same time from 127.5nm to 222.2 nm. The reason is that the films deposited at low [S]/[Sn] ratio shows densely and compact films but while when the concentration of sulphur increases the coalescence and large grains increase grains boundaries which were the cause of the increase of the roughness. Table 22 shows the variation of crystallites size with the variation of [S]/[Sn] ratio.

Table 22: Roughness and Grain size of SnS thin films prepared with different [Sn]/[S] ratios

[S]/[Sn] Ratio	Roughness (nm)	Grain size (nm)
[S]/[Sn] = 1	45.0	247.4
[S]/[Sn] = 2	20.2	127.5
[S]/[Sn] = 3	20.9	162.4
[S]/[Sn] = 4	26.6	222.2

Fig. 31 shows two-dimensional AFM images of SnS thin films prepared with different [S]/[Sn] ratios. The difference between grain size given by AFM and crystallites size given by XRD is explained by the fact that a grain was formed by several crystallites.

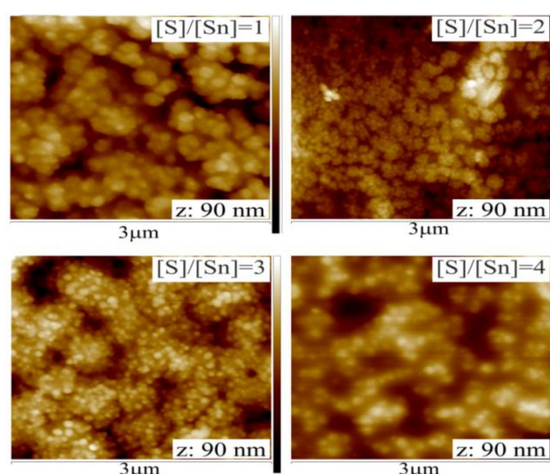

Fig. 31: Two-dimensional images of SnS thin films prepared with various [S]/[Sn] ratios.

1.2.5. Energy Dispersive Spectroscopy Analysis (EDS)

The Energy Dispersive X-ray Spectroscopy (EDS) is a powerful technique to analyze the chemical composition of samples based of X-ray emitted by the atoms of elements in the sample. From the Table 23 we noted that all films contain only tin and sulphur and when the ratio increases the stoichiometry improved and best S/Sn ratio in films was obtained for [S]/[Sn]=3 and [S]/[Sn]=4 in the solution, which indicates that the composition of films depend on the amount of sulphur in the initial composition of the solution.

Table 23: Composition of SnS thin films obtained from EDS analysis.

[S]/[Sn] Ratio	% S	% Sn	S/Sn
[S]/[Sn] = 1	42.26	57.74	0.73
[S]/[Sn] = 2	47.60	52.40	0.91
[S]/[Sn] = 3	50.14	49.86	1.00
[S]/[Sn] = 4	50.39	49.61	1.01

1.2.6. Optical properties

Fig. 32 shows the optical transmission spectra of SnS thin films with various ratios in the wavelength region of 500-1000nm. In the wavelength between 500 to 650 nm transmittance, all films exhibited very low transmittance which was close to 0% and the transmittance increases rapidly after 650 nm. The higher transmittance observed was 43%. The low transmittance in the visible region shows clearly that SnS thin films are absorber layers.

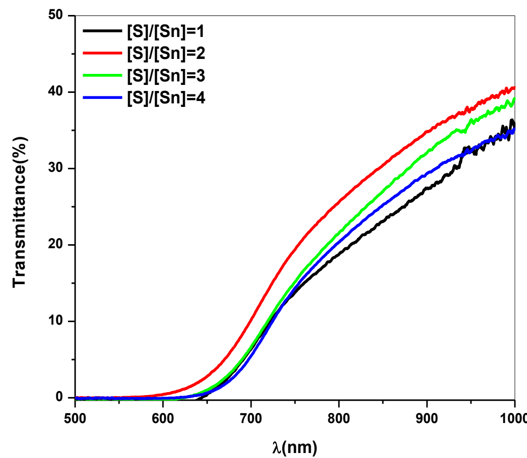

Fig. 32: Transmittance of SnS thin films prepared with different [S]/[Sn] ratios.

The band gap energy for SnS thin films were obtained from optical transmission data plotting $(Ah\nu)^2$ versus hν at various [S]/[Sn] ratios where A is the absorbance and hν is the photon energy, as shown in Fig. 33. When the [S]/[Sn] ratio varied from 2 to 4 we noted a decrease of the band gap energy from 1.83 eV to 1.77 eV which was higher than the gap

energy of pure SnS-1.3eV. Table 24 displays the optical band-gap values for SnS films synthesized from different [Sn]/[S] ratios.

Table 24: Optical band gap of SnS thin films prepared with various [Sn]/[S] ratios.

[S]/[Sn] Ratio	Eg (eV)
[S]/[Sn] = 1	1.77
[S]/[Sn] = 2	1.83
[S]/[Sn] = 3	1.79
[S]/[Sn] = 4	1.77

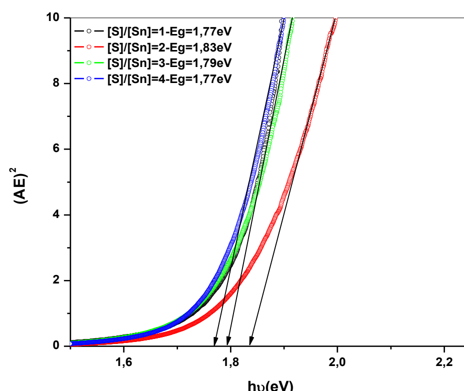

Fig. 33: Plot of $(Ah\nu)^2$ versus photon energy of SnS thin films prepared with different [S]/[Sn] ratios.

The increase of the band gap energies of our samples, compared to pure SnS thin film which has a band gap of 1.3eV [14], is due to the incorporation of oxygen into samples. Assuming that the variation of band gap energy of $SnS_{1-x}O_x$ increases linearly with the augmentation of oxygen content. One plot a calibration curb in order to determine the amount of oxygen contended in our samples by considering as limit values band gap energies 1.3eV for SnS layer and 2.7eV (in N_2 atmosphere annealing) and 3.4eV (in O_2 atmosphere annealing) for SnO layer [15]. According to Fig. 34 the percentage of oxygen contained in SnS layers is around 23±1% and 33±2% using 3.4eV and 2.7eV as band gap energies reference of SnO, respectively.

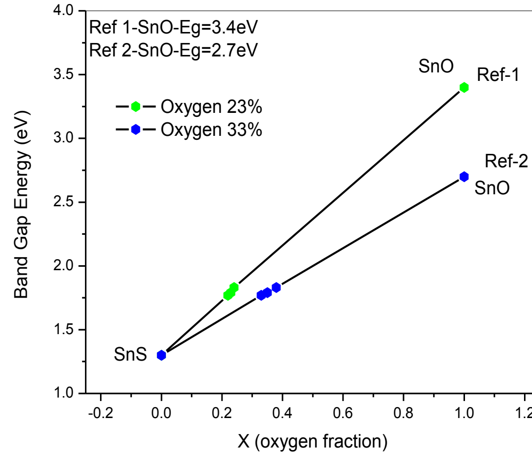

Fig. 34: Energy band-gap versus oxygen (O_2) content in SnS thin films prepared with different [S]/[Sn] ratios.

1.3. Conclusion

Tin mono-sulfide (SnS) thin films have been deposited onto simple glass substrate by Chemical Spray Pyrolysis. All deposited films are identified to be SnS polycrystalline with orthorhombic structure and with (111) as preferential peak for ratio equal to one while when the ratio increases from 2 to 4 the main peak becomes (101) and the (111) peak decreases. Raman modes confirm the presence of SnS phase without any additional parasite phases such SnS_2, Sn_2S_3, SnO or SnO_2. SEM images revealed rounded grain for all ratios and EDS analysis shows an improvement of the stoichiometry with the increase of ratio. AFM studies revealed that SnS thin film with [Sn]/[S] ratio equals to 1 has larger grains and higher mean roughness. The transmission in the visible region of all films was found to be very low showing the absorber character of SnS films. We noted that the band gap energies of SnS thin films prepared by Chemical Spray Pyrolysis decrease when the [Sn]/[S] ratios increase from [S]/[Sn]=1 and 4.

2. Effect of substrate temperature

2.1. Experimental Details

Tin monosulfide (SnS) thin films were prepared onto glass substrate from an aqueous solution containing tin (II) chloride dihydrate ($SnCl_2{\cdot}2H_2O$), thiourea ($CS(NH_2)_2$) (≥99%) and alcohol (10% in volume) to reduce the surface tension. The concentration of tin chloride

was fixed at 0.104M and the [S]/[In] ratio was 1. The substrate temperature varied: 250°C, 300°C, 350º, 400ºC and 450ºC. The volume sprayed was 5mL, the spray rate 1.5 ml/min, the air compressed pressure 0.7 bar and the distance between the glass substrate and nozzle was kept at 25 cm.

2.2. Results and Discussion

2.2.1. X-ray diffraction (XRD) analysis

Fig. 35a shows the XRD spectra of SnS thin films sprayed at various substrate temperatures, i.e. 250 ºC, 300 ºC, 350 ºC, 400 ºC and 450 ºC, respectively. From 250 ºC to 450 ºC the XRD peaks matched SnS orthorhombic phase (JCPDS#39-0354) well. XRD peaks were located at 26.10, 30.47, 31.53, 39.05, and 44.74 degrees, corresponding to diffraction between the following crystallographic planes: (021), (101), (111), (131) and (141), respectively. The highest intensity observed for the (111) diffraction peak at 31.53° is the preferential crystallographic direction for all temperatures except for films prepared at 300 ºC in which the (101) peak dominates. Apart from the SnS peaks, one additional peak corresponding to the Sn_2S_3 phase was observed in the XRD spectra for films deposited at 450 ºC. This peak is due to the re-evaporation of SnS and tin from the substrate surface as vapor [16]. Sn_2S_3 is a compound made of SnS and SnS_2 which means that some Sn (IV) ions are present. This may happen if part of Sn (II) dismutates into Sn (0) and Sn (IV) to produce Sn_2S_3 as a secondary phase [17, 18]. It is noteworthy to notice that at 400 ºC and 450 ºC, the (101) peak tends to vanish and simultaneously an increase of the (111) main peak is observed. A decrease of other indexed peaks at all temperatures below 400 ºC was also observed.

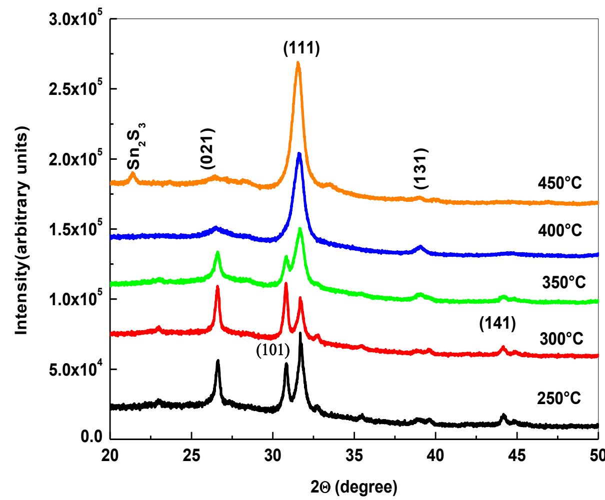

Fig. 35a: X-ray diffraction spectra of SnS films deposited at different substrate temperatures.

Fig. 35b shows a detail of the XRD pattern around the (021), (101) and (111) peaks. It is noteworthy that the (111) peak at 400 °C and 450 °C is clearly the overlap of (101) and (111) observed at substrate temperatures between 250 °C and 350 °C.

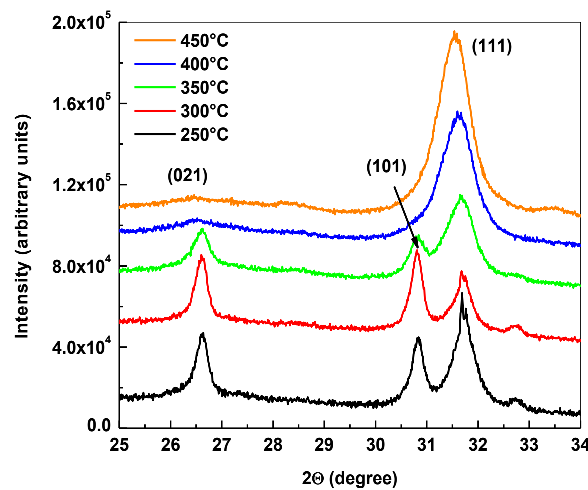

Fig. 35b: Detail of the X-ray diffraction spectra of SnS thin films clearly showing the (111) peak.

The lattice plane index (h k l), interplanar distance d_{hkl} and lattice parameters have the following relationship for orthorhombic crystal of equation (5) in chapter III.

Using XRD data, we calculated the lattice parameters (a, b and c) of SnS thin films. The evaluated lattice parameters of the SnS films are listed in Table 25. Lattice parameters are in good agreement with the standard orthorhombic SnS pattern JCPDS#39-0354.

The variation of the crystallite size with substrate temperature was investigated using the Debye-Scherrer formula equation (6) in chapter III using the (111) and (101) diffraction lines after deconvolution of wide (111) peaks at 400 °C and 450 °C

Table 25 shows the crystallite sizes calculated from the Scherrer's equation for (101) and (111) diffraction peaks. The trend is the higher the temperature the smaller the crystallite size and the higher the intensity. When the temperature increases two competitive phenomena take place simultaneously: one is the increase of the crystallite size and the other one is the enlargement of the nucleation centers, which might result in an increase of the density of crystallites and then in an increase of the intensity of the diffraction peaks. In this case the second phenomenon is likely to dominate and as a result a higher density of smaller crystallites is produced when the temperature increases.

Table 25: Crystallites' size and lattice parameters of SnS thin films deposited at various substrate temperatures.

Ts (°C)	Crystallite size (nm)	Lattice parameters (Å)		
		a	b	c
250	23.5	4.18	11.18	4.03
300	20.9	4.17	11.26	4.01
350	13.6	4.34	10.45	3.97
400	11.5	4.22	11.28	3.92
450	11.6	4.19	11.32	4.04
Standard-039-0354	-	4.32	11.19	3.98

2.2.2. Raman Spectroscopy Analysis

Raman spectroscopy is a powerful tool to analyze the phase and structure of SnS thin films. Raman spectra were analyzed to confirm the SnS phase and to identify the presence of the other phases as well. Raman spectra of SnS thin films deposited at different substrate

temperatures recorded in the range 80-350 cm^{-1} are shown in Fig. 9. Raman spectroscopy reported modes for SnS at 94 cm^{-1}, 193 cm^{-1}, 218 cm^{-1}, 225 cm^{-1} assigned to Ag, and 88 cm^{-1}, 170 cm^{-1}, 178 cm^{-1} belonging to B2g, and for Sn_2S_3 with a mode at 307 cm^{-1} [19-20]. The Raman mode at 307 cm^{-1} confirms the presence of the Sn_2S_3 phase for films deposited at 450 ºC, which is in good agreement with the XRD spectra in Fig. 36, in which the presence of the Sn_2S_3 for films deposited at 450 ºC and no Raman mode corresponding to SnS_2 was observed. Otherwise, Raman spectra also confirm that the SnS phase is obtained in all samples prepared at different temperatures. Therefore, both Raman and X-ray diffraction results were complimentary.

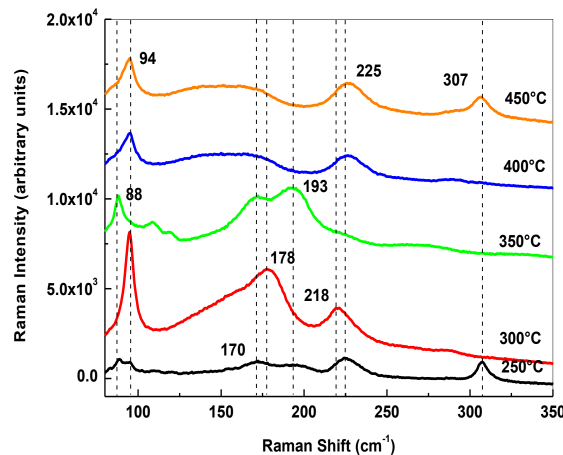

Fig. 36: Raman spectra of SnS thin films deposited at different substrate temperatures.

2.2.3. Scanning Electron Microscopy analysis

An electron beam is used to scan the surface of films in the Scanning Electron Microscope by applying a typical acceleration voltage of 20 kV. Scanning Electron Microscopy characterization was carried out on all samples and representative micrographs are shown in Fig. 37. SEM studies revealed that SnS thin films deposited from 250 ºC to 350 ºC substrate temperatures were well covered and strongly adherent to the glass surface with the formation of agglomerations of small grains probably due to the segregation of excess tin. At 400 ºC and 450 ºC SnS thin films were homogeneous, dense, pinholes free and more compact than films sprayed at lower temperatures. At lower temperatures (below 400 ºC), SnS grains had a spherical shape, being almost uniform and some voids between them were observed. At higher temperatures (at 400 ºC and 450 ºC), the grainy surface structure disappeared and

films were denser and more compact.

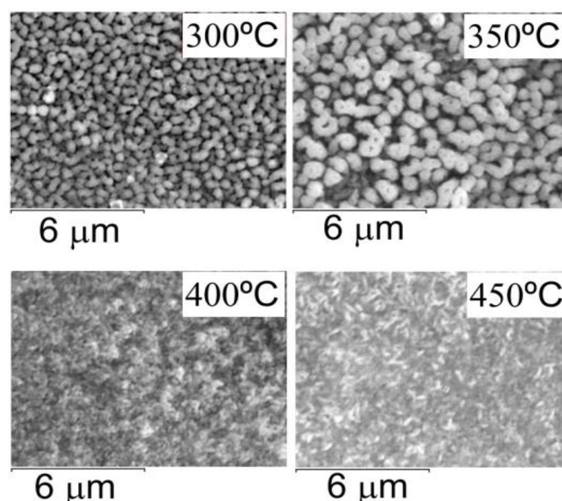

Fig. 37: SEM images of SnS thin films deposited at different substrate temperatures.

2.2.4. Atomic Force Microscopy analysis

The surface topography of SnS films grown at different substrate temperatures was examined by Atomic Force Microscopy and 2D pictures scanning in an area of 3μm×3μm and a scale bar in the height of 70 nm are shown in Fig. 38. When the substrate temperature increased from 350 ºC to 450 ºC, the film surface roughness decreased from 24.7 nm to 16.6 nm probably due to the suppression of the segregation of tin on the surface. Films deposited at 350 ºC were the roughest (24.7 nm) and had the largest grain size (252 nm), while films prepared at 450 ºC had the lowest roughness (16.6 nm) and the smallest grain size (148 nm). Roughness and grain size for all samples are shown in Table 6. Furthermore, when the substrate temperature increased from 350 to 450 °C, the void fraction over the surface decreased, resulting in a reduction of the roughness (Table 26). Therefore, the film surfaces were smoother compared to films prepared at 250 and 300 °C. The difference between the crystallite size given by Scherrer's equation and the grain size given by AFM is due to the fact that a grain is an agglomeration of several crystallites.

Taken into account the data provided by XRD and AFM measurements, the increase of substrate temperature results in the formation of a larger number of crystallites but with smaller sizes. This effect can be related to the generation of a higher density of nucleation centers with the temperature resulting in a higher density of crystallites but with smaller

sizes.

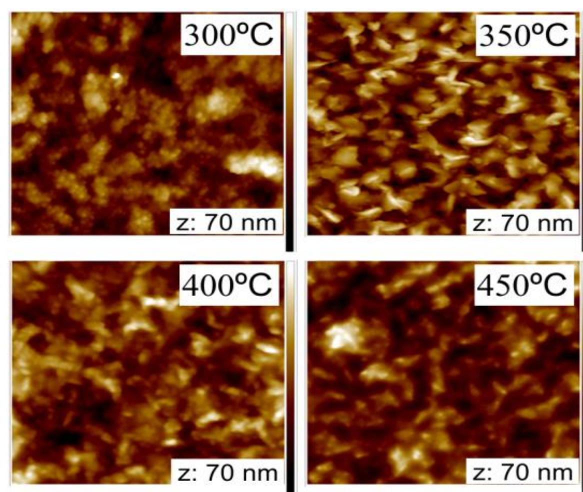

Fig. 38: AFM micrographs of SnS thin films deposited at different substrate temperatures.

Table 26: Roughness and grain size of SnS thin films prepared at various substrate temperatures.

Ts (ºC)	Roughness (nm)	Grain size (nm)
250	20.6	174
300	17.3	219
350	24.7	252
400	21.5	177
450	16.6	148

2.2.5. Energy-Dispersive X-ray Spectroscopy measurements

Energy-dispersive X-ray spectroscopy is a powerful technique to analyze the chemical composition of the sample, being based on X-ray emitted by the atoms in the sample. The molar ratios shown in Table 27 indicate that all films contain only sulfur and tin. The proportion of S and Sn in SnS thin films revealed that when the substrate temperature increased from 250 ºC to 350 ºC, all the ratios indicated an excess of tin, but when the substrate temperature was 400 ºC and 450 ºC, respectively, a drastic decrease in the amount of tin was observed, leading to S/Sn close to unity confirming the XRD results. Therefore,

according to the EDS results the stoichiometry deviation can be attributed to the excess of tin.

Table 27: Composition of SnS thin films deposited onto glass substrate obtained by EDS at different temperatures.

Ts (ºC)	%Sn	%S	S/Sn
250	56.4	43.6	0.77
300	56.1	43.9	0.78
350	55.3	44.7	0.81
400	53.3	46.7	0.88
450	52.6	47.4	0.90

2.2.6. Electrical measurements

Resistivity of the samples was obtained by the four-probe technique. Table 28 displays the thickness, sheet resistance and resistivity of all samples in relation to the substrate temperature. A decrease in the resistivity of films was observed when the substrate temperature rose from 250 to 450 °C, being is correlated with the decrease of film thicknesses. The lowest thickness (576 nm) and resistivity (60 Ω·cm) were obtained for film prepared at the highest temperature, 450 °C.

Table 28: Thickness and Resistivity measurements of SnS thin films deposited onto glass substrate at different temperatures.

Temperature (ºC)	Thickness (nm)	R□ (Ω)	ρ (Ω·cm)
250	1530	1.13×10^7	1695
300	1350	0.90×10^7	1215
350	1090	0.81×10^7	883
400	912	0.58×10^7	529
450	576	1.04×10^6	60

2.2.7. Optical analysis

The optical transmittance of SnS thin films deposited by CSP onto simple glass taken in the range of 500 -1000 nm is displayed in Fig. 39. We noted a low transmittance at low substrate temperature of 250 ºC and an increase of the transmittance from 300 ºC to 450 ºC due to the decrease of thickness when the substrate temperature increased from 250 to 450 °C. We also noted, particularly, that films prepared at a substrate temperature in the range of 350 to 450 ºC had the same transmittance variation. For all films, the transmittance starts above 800 nm, as characteristic for SnS absorber layer.

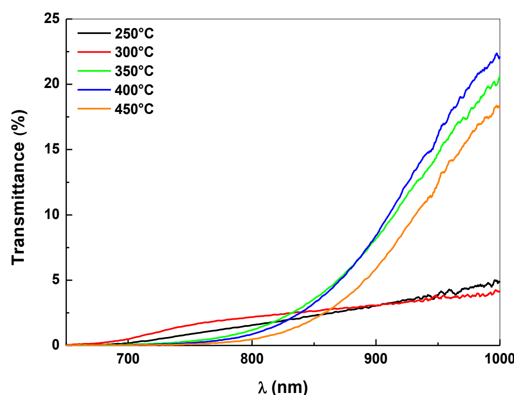

Fig. 39: Optical transmission spectra of SnS thin films deposited with different substrate temperatures

The bandgap energies of SnS thin films were obtained from optical transmission data plotting $(Ah\nu)^2$ versus hν at various temperatures, where A is the absorbance and hν is the photon energy. The calculated optical bandgap for every sample appears in the legend of Fig. 40. At lower temperatures, 250 ºC and 300 ºC, suitable bandgap energy between 1.70 eV to 1.74 eV was calculated, while at a higher substrate temperature, in the range of 350 to 450 ºC, the gap energy decreased from 1.50 eV (the ideal bandgap energy) to 1.46 eV. The change in preferred film orientation from (010) to (111) planes can be correlated to the change in the optical gap energy of SnS thin films; the optical bandgap of SnS changed from 1.74 to 1.46 eV when the substrate temperature increased from 300 to 450 °C, respectively, where the parallel plane was replaced by a plane perpendicular to the surface.

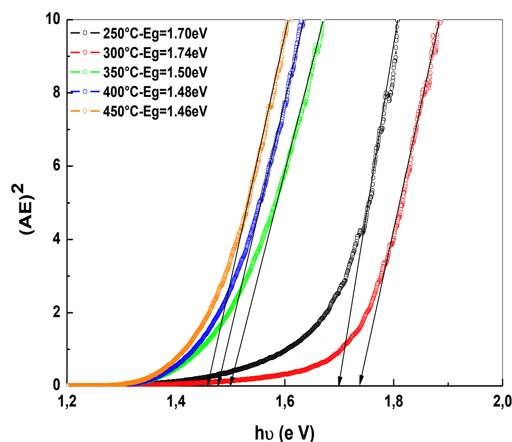

Fig. 40: Plot of $(Ah\nu)^2$ vs. the photon energy (hν) of SnS thin films prepared with different substrate temperatures

2.3. Conclusion

Tin monosulfide (SnS) thin films were deposited by CSP technique using $SnCl_2{\cdot}2H_2O$ and $CS(NH_2)_2$ as precursors of tin (II) and sulfur, respectively. All films were polycrystalline and crystallized in the SnS orthorhombic phase, with (111) as main peak. No SnS_2 Raman mode was observed, while Sn_2S_3 modes were detected, thus confirming the XRD results. In addition, two SnS modes were observed in all samples. The SnS films showed a granular morphology between 250 ºC and 350 ºC, while at 400 ºC and 450 ºC, films became denser and more compact. According to Energy-dispersive X-ray spectroscopy (EDS) results, films with improved stoichiometry could be achieved with higher substrate temperatures, and AFM micrographs showed films with a greater roughness and relatively big grain size. The optical energy bandgap and electrical resistivity were found to decrease with the increase of the substrate temperature achieving a minimum of 1.46 eV and 60 Ω·cm at 450 ºC, respectively.

Polycrystalline SnS films with good stoichiometry, denser and compact morphology and suitable gap energy of 1.46-1.50 eV were obtained by the CSP inexpensive technique and also using abundant elements (Sn and S), making SnS to be a promising candidate to substitute the $CuInS_2$ absorber layer in solar cells thin films technology.

The results obtained herein emphasize that the influence of substrate temperatures on the physical and chemical properties of SnS films pyrolysised is crucial in order to produce suitable SnS films, which have to be deposited at temperatures from 350−450 ºC.

3. Effect of substrate nature

3.1. Experimental

For the preparation of SnS thin films by CSP, we used an aqueous solution containing Tin (II) chloride dihydrate ($SnCl_2.2H_2O$), thiourea ($CS(NH_2)_2$), and alcohol (10 vol%) to reduce the surface tension of water. The utilization of Sn (II) rather than Sn (IV) was to mitigate possible contamination by Sn_2S_3 and SnS_2 phases [21]. The concentration of tin chloride was fixed at 0.104 M and the [S]/[Sn] ratio was 1. The substrate temperature was kept to 350 °C. A volume of 5 mL was spayed at a rate of 1.5 mL/min. The air compressed pressure was 0.7 bar and the distance between the substrate and the nozzle was 25 cm.

3.2. Results and Discussion

3.2.1. XRD analysis

XRD is an effective method to investigate crystalline properties of a synthesized material. XRD spectra of SnS thin films deposited by CSP onto pure glass, ITO-, and Mo-coated glass substrates shown in Fig. 41 revealed a unique XRD peak located at 31.788, which corresponds to the preferential crystallographic direction oriented along (111) planes for all samples without any additional parasite phase like SnS_2, Sn_2S_3, or SnO_2. Thin film deposited on glass substrate showed only one sharp peak, whereas for films deposited onto ITO- and Mo-coated glasses other peaks corresponding to ITO and Mo were visible. The observed diffraction peak for SnS matches well with SnS Herzenbergite orthorhombic structure phase and is in good agreement with the standard data (Ref. JCPDS card, PDF#39–0354). The intensity of (111) diffraction peak is higher in film deposited onto bare glass substrate than in films deposited onto ITO- or Mo-coated glass substrates indicating that film deposited on glass has a minimum potential energy of the nuclei on the surface of the glass substrate leading to the enhanced crystallite size [22]. The variation of crystallites size with the substrate nature was also evaluated using Scherrer's formula of equation (6) in chapter III from (111) diffraction line.

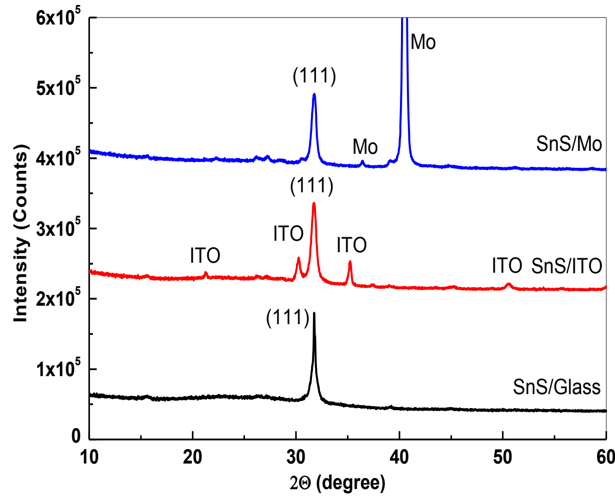

Fig. 41: XRD spectra of SnS thin films deposited onto various substrates

Table 29 displays the crystallite size (D), microstrain (ε) (equation (7) of chapter III) and dislocation density (δ) (equation (8) of chapter III) for SnS thin films deposited onto different substrates. It is noteworthy that film prepared onto glass has larger crystallite size compared to others because its crystallinity is better than that of films deposited onto ITO and Mo-coated glass.

The microstrain and dislocation variation were correlated to the grains size with the change of the substrate nature. The smaller values of microstrain and dislocation density of film deposited onto simple glass substrate indicated a densely packed structure with minimum defects, good crystallinity, and high quality of SnS/Glass films compared to others.

Table 29: Grains size of SnS thin films deposited at various substrates

Sample	D (Å)	ε (10^{-3})	δ (10^{7} lines m^{-2})
SnS/Glass	459	0.75	2.17
SnS/ITO	160	2.16	6.25
SnS/Mo	183	1.89	4.46

3.2.2. Raman spectroscopy analysis

Raman analysis was also used, as it is a highly sensitive tool to analyze the structural and compositional changes of thin films [23]. The orthorhombic structure has 24 vibrational modes represented at the center of Brillouin zone by the following irreducible representation:

$$\Gamma = 4Ag + 2B1g + 4B2g + 2B3g + 2Au + 4B1u + 2B2u + 4B3u \quad (2)$$

For SnS, 21 optical phonon modes were detected of which 12 were Raman active modes (4Ag, 2B1g, 4B2g and 2B3g) [24].

Fig. 42 shows the Raman spectra of SnS/Glass, SnS/ITO and SnS/Mo films analyzed within the range 30-300 cm^{-1}. It was observed that Raman spectra for all samples were similar with only small variations in the intensity of the Raman signal. The modes detected in our study are located at 47, 65, 94, 160, 186 and 219 cm^{-1}, all-corresponding to SnS single crystal modes [25] without any contamination of secondary phases. Modes located at 94, 186 and 219 cm^{-1} are assigned to Ag modes while 47, 163 cm^{-1} are attributed to B3g mode and 65 is attributed to B2g or B1g modes. The modes obtained were the same that these observed by H. R. Chandrasekhar et al. [25]. The modes obtained confirm the results obtained by the XRD analysis.

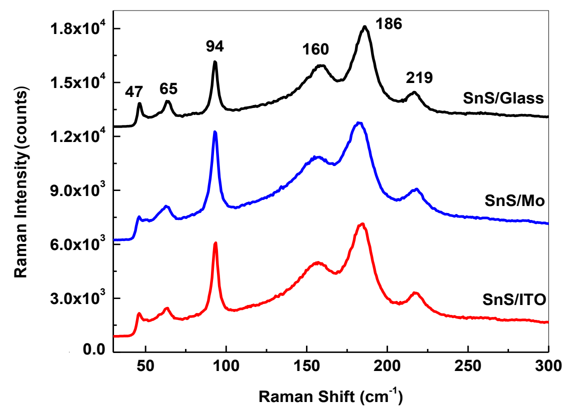

Fig. 42: Raman spectra of SnS thin films deposited onto pure glass, ITO and Mo-coated glass substrate at 350 °C.

3.2.3. Scanning Electron Microscopy (SEM) analysis and EDS measurements

FESEM was used to analyze the surface morphology of SnS thin films deposited onto various substrates.

Fig. 43 shows that all films were formed by cornflake-like particles, homogeneous, with a uniform surface and good adhesion to substrates. Substrates are well covered and no pinholes

were observed. Films deposited onto ITO and Mo-coated glasses were denser and more compact than those deposited on bare glass. N. Revathi et al. found the same result using PVD technique to grow SnS onto different surfaces [26].

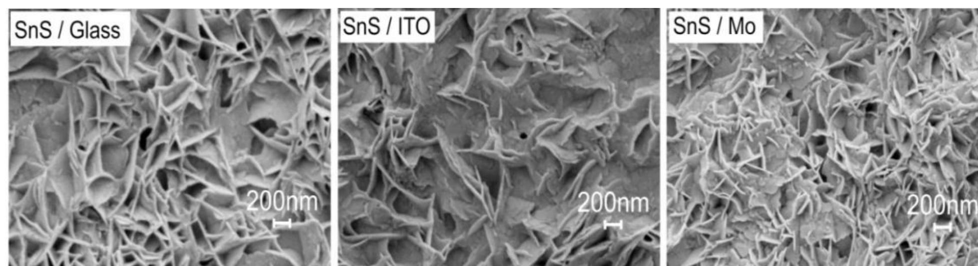

Fig. 43**:** FESEM images of SnS films deposited on different substrates.

The composition of sprayed SnS thin films was estimated by Energy Dispersive X-ray Spectroscopy (EDS). The EDS spectra revealed the presence of sulfur and tin in all films. Films deposited onto bare glass substrates were nearly stoichiometric, whereas films deposited onto ITO had a little excess of tin coming certainly from the ITO substrate. An excess of tin was also detected in films deposited onto Mo-coated glass substrates. The atomic percentages of these elements are shown in Table 30. Non-stoichiometric SnS may be due to either Sn^{2+} vacancies or excess tin atoms generating deep acceptor states with activation energy in wide range between 0.22 and 0.45 eV depending on the deposition technique [27-28-29-30].

Concerning Mo substrates, the sulfur deficiency can be explained by a combination of two causes; a) the evaporation of sulfur due to the substrate temperature (350 °C), and b) the thermal activation of the diffusion process of sulfur into the molybdenum (Mo) layer [31]. The last process takes place without leading to the formation of individual compound phases, as revealed by XRD analysis and confirmed by Raman results.

Table 30: Composition of SnS thin films deposited at various substrates obtained from EDS analysis.

Samples	Sn (%)	S (%)	Sn/S
SnS/Glass	50.5	49.5	1.02
SnS/ITO	53.8	46.2	1.15
SnS/Mo	60.0	40.0	1.50

3.2.4. Atomic Force Microscopy (AFM) Analysis

Fig. 44 shows AFM images of films prepared by Chemical Spray Pyrolysis technique onto pure glass, ITO and Mo-coated glass. The scan area surface was 7µm×7µm. The images agreed well with the FESEM images and confirmed that films were formed by cornflake-like particles. This morphology was observed in all samples with more compact film on Mo-coated substrate.

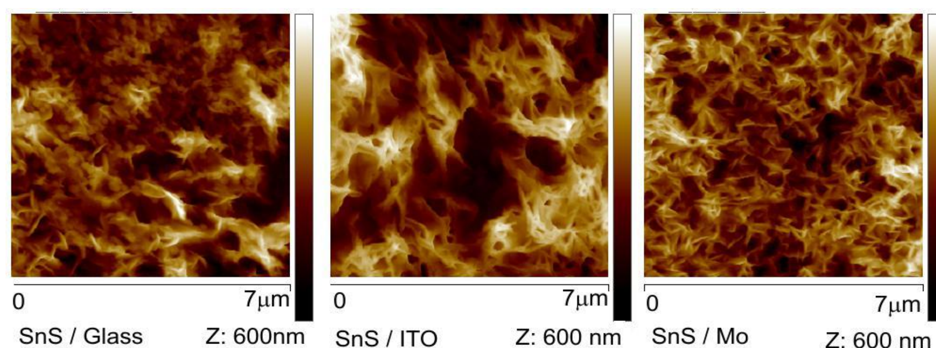

Fig. 44**:** AFM micrographs of samples SnS thin films deposited onto different substrates.

The grain size and the RMS (Root-Mean-Square) surface roughness values are reported in Table 31. The films deposited onto glass had large grains and high surface roughness. It can be explained by the fact that the improvement of crystallinity due to the coalescence of small grains to form large ones increases grain boundaries and then increases the roughness.

The difference between crystallites size calculated from Scherrer equation and grains size gives by AFM analysis is explained by the fact that Scherrer's formula gives the size of crystallites while AFM analysis gives grains size. However, one grain (as seen by AFM) contains several crystallites (as detected by XRD).

Table 31: Roughness and grains size of SnS thin films sprayed onto various substrates

Samples	Roughness (nm)	Grain size (nm)
SnS/Glass	89	286
SnS/ITO	138	175
SnS/Mo	77	234

3.2.5. Optical analysis

The optical properties of SnS thin films deposited onto different substrates: simple glass, ITO and Mo-coated glass were studied by measuring the transmittance across the full UV-Vis-IR range wavelength of 300-1000nm. We noted a transmittance of 24% and 29% for films deposited onto pure glass and ITO, respectively. The low transmittance in the visible region clearly showed that SnS thin films are absorber layers.

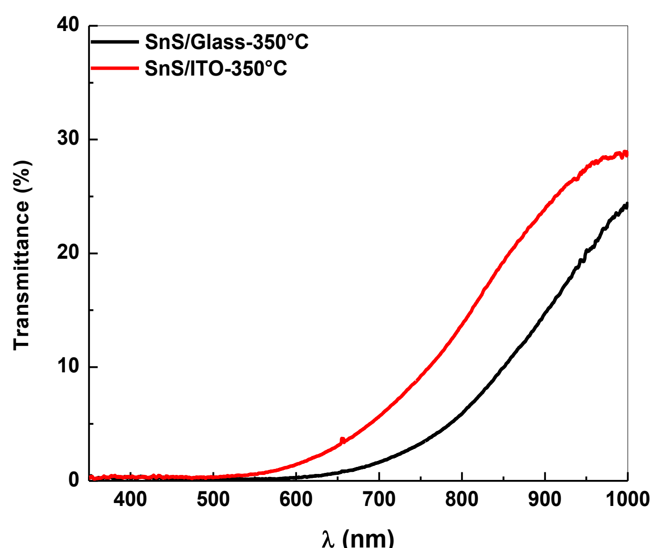

Fig. 45: Transmittance spectra of SnS films onto different substrates.

The band gap energy can be obtained from strapolating the straight line of $(\alpha h\nu)^2$ vs $h\nu$ plot where α is the absorption coefficient for a direct-transition semiconductor material, h the Planck constant and ν the frequency of the incident photon. The Eg values were found to be 1.64 eV and 1.82 eV for samples deposited onto pure glass and ITO-coated glass, respectively. These band gap values are larger than the theoretical estimation for the SnS

band gap; it is likely due to the contamination with oxygen during the Spray Pyrolysis deposition which is performed in air.

In order to estimate the band gap in SnS films deposited onto Mo-coated substrates we have measured the reflectance and then apply the Kubelka-Munk function to obtain the absorbance. A band gap value of 1.74 eV, obtained by extrapolating $(\alpha h\nu)^2$ versus hν, was found for SnS films deposited in Mo substrates. This value yields between the values found for ITO and glass substrates. The reason for the higher band gap value obtained for films deposited in ITO substrates with respect to the other substrates studied here is related to the higher diffusion of oxygen from the ITO substrates to the SnS layer, as was already reported in In_2S_3 films sprayed on ITO substrates [32].

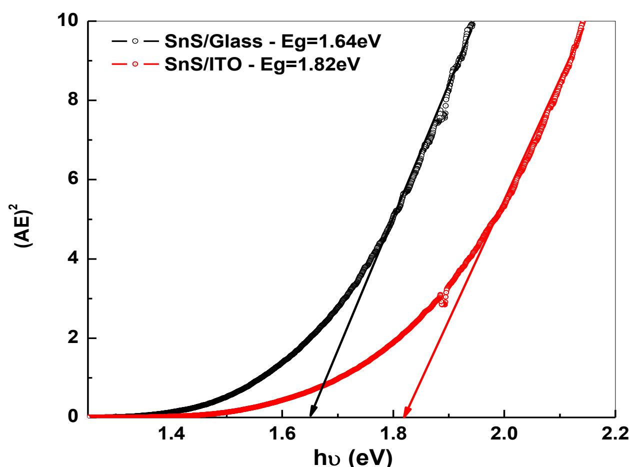

Fig. 46**:** Plot of $(\alpha h\nu)^2$ vs photon energy of SnS thin films sprayed onto different substrates.

3.3. Conclusion

In this work, we presented the synthesis of SnS thin films by Chemical Spray Pyrolysis onto various surface substrates such as bare glass, ITO and Mo-coated glass. XRD analysis revealed that sprayed SnS films only present a diffraction peak corresponding to (111) planes. This result is independent of the substrate used and means that SnS films grow following the preferential direction (111). Raman spectroscopy confirmed the XRD results with modes according to the SnS orthorhombic structure without any parasite phase for all samples. FESEM images show films made of cornflake-like particles. EDS analysis revealed

the presence of sulfur and tin in all films with a near stoichiometric ratio for films deposited onto glass and an excess of sulfur in films deposited onto ITO and Mo coated glass. Films deposited onto glass have larger grains and high roughness. The direct band gap energy was estimated to be 1.64 and 1.82 eV for films deposited onto simple glass and ITO-coated glass. These films have great potential for the use in photovoltaic devices.

The SnS thin film prepared onto glass substrate showed better crystallinity, good morphology, band gap energy near the ideal value and then is then suitable for the solar absorber in solar cell devices using CSP as experimental technique for their elaboration.

C. Effect of doping on physical and chemical properties of SnS thin films

1. Introduction

SnS thin films deposited by Chemical Spray Pyrolysis were doped with silver (Ag), aluminum (Al), iron (Fe) and indium (In) in order to enhance physico-chemical properties.

Techniques like XRD, SEM, AFM, photoluminescence, Four probe method, Mott-Schottky plots and Spectrophotometer were used to characterize films structure, morphology and topography, resistivity, semiconductors type and band gap energies, respectively.

2. SnS thin films doped with silver (Ag^{+})

2.1. Experimental details

For the preparation of SnS thin films by Chemical Spray Pyrolysis we used aqueous solution containing tin (II) chloride dihydrate ($SnCl_2.2H_2O$), thiourea ($CS(NH_2)_2$), silver nitrate ($AgNO_3$) at different percentages: 0%-3%-5%-7%-10% and alcohol (10% in volume) to reduce the surface tension of water. The concentration of tin chloride was fixed at 0.104 M and the [S]/[Sn] ratio was 1. A volume of 5 mL was sprayed for each film at a spray rate of 1.5 mL/min and at a pressure of 0.7 bar. The substrate temperature was kept to 350 °C and the distance between the substrate and the nozzle was set at 25 cm.

2.2. Results and discussions

2.2.1. X-ray diffraction (XRD) analysis

The XRD spectra shown in Fig. 47 indicated that the SnS thin films doped with silver were all polycrystalline with (111) as main peak and all SnS-peaks were assigned to SnS orthorhombic structure of Herzenbergite (Ref.JCPDS card, PDF#39-0354). Others peaks like (110), (120), (021), (101) and (131) were also detected. The crystallinity of films was influenced by the silver dopant and was enhanced with the increasing of Ag-percentage in the solution from 3% to 10%. This improvement of crystallinity was probably due to the new nucleation sites creation from the silver dopant [33]. The Ag atoms, probably, occupy both substitutional and interstitial positions in the SnS films lattice. We noted also two peaks; one located at 28.55° and due to a secondary phase of Ag_8SnS_3 and a second peak at 44.78° associated to Ag aggregates resulting from Ag atoms that are not incorporated into the SnS lattice. Peimin Lua et al. found the same result [34].

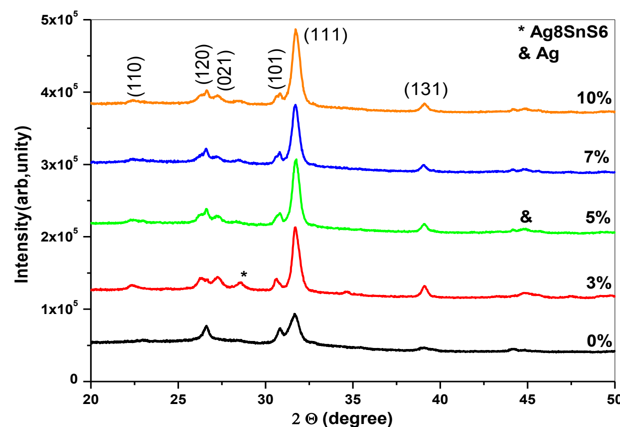

Fig. 47: XRD spectra of SnS thin films doped with various Ag ratio

Variation of crystallites size with Ag-doping percentage was also evaluated using Scherrer's formula of equation (6) of chapter III from (111) diffraction line.

The micro-structural parameters like crystallites size, strain and dislocation density have been calculated and are shown in Table 32. The small values of strain suggest that crystallization degree is better for the Ag doped SnS films with lower amount of defects.

Table 32: Grains size, microstrain, dislocation and lattice parameters of SnS deposited with various silver ratios

Samples	Grain Size (Å)	ε (10^{-3})	δ (10^{15} lines.m^{-2})	Lattice parameters (Å)		
				a	b	c
SnS undoped	136	1.97	5.40	-	-	-
SnS-Ag-3%	181	1.74	3.05	4.21	11.30	4.01
SnS-Ag-5%	186	1.92	2.89	4.26	11.25	4.02
SnS-Ag-7%	181	1.97	3.05	4.17	11.32	4.04
SnS-Ag-10%	174	2.05	3.30	4.21	11.29	4.03

The large crystallites size, low strain and dislocation density of film deposited with 5% of Ag-doping element show a good crystallinity of this sample. Adequate crystallites size can play an important role in solar cell reducing scattering of charge carriers by grain boundaries.

2.2.2. Scanning Electron Microscopy (SEM) analysis

The EDS was used to determine the composition of samples. It was seen that the composition of silver present in films was low but increased slightly with the percentage of silver adding in the initial solution. The small amount of Ag in our samples may be due, not to the low dissolution of $AgNO_3$ in the initial solution but to the detection limit of EDS technique. The best stoichiometric films were obtained for films doped with 5% and 10%.

Table 33: Composition of SnS thin films doped with Silver given by EDS

Samples	%S	%Sn	%Ag	S/Sn
undoped	45.00	55.00	0.00	0.82
SnS:Ag-3%	46.98	52.47	0.56	0.90
SnS:Ag-5%	49.44	50.01	0.64	0.98
SnS:Ag-7%	48.05	51.31	0.64	0.94
SnS:Ag-10%	48.85	50.45	0.70	0.97

The morphology of films doped was different from the undoped one because they were more compact and denser than the spherical grains in the undoped film. The doped films are lessened under the influence of Ag dopant ions and substitute to “vermicelli” like shape grains. Ag-doped SnS films are uniform and crack-free contrary to the SnS undoped film

which has some empty spaces between the grains. When the concentration of Ag increases the morphology of films had almost the same for all films and so the silver doping element has no effect beyond 3% of Ag-doping percentage. It might be explained by the fact that the amount of silver in the thin films was relatively low.

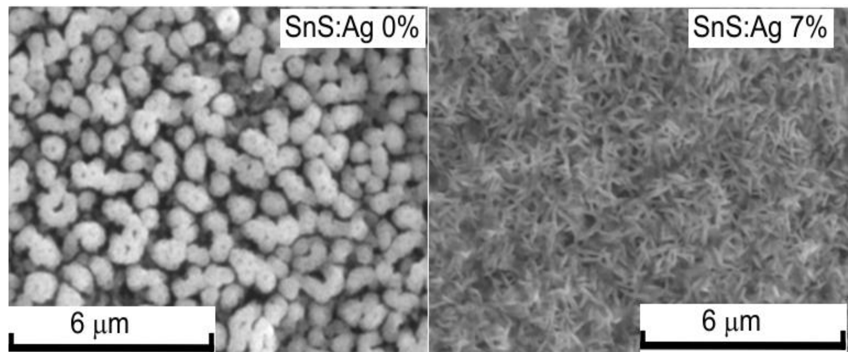

Fig. 48: SEM images of SnS thin films doped with Ag at various percentages

We note also that when the Ag-doping percentage increases in the solution, the grains size given by AFM increases from 114nm at 3% to 199nm at 10% and at the same time the roughness fluctuates. The difference between dimension of grains size given by AFM and crystallites given by XRD is due to the fact that a grain is an agglomeration of several crystallites.

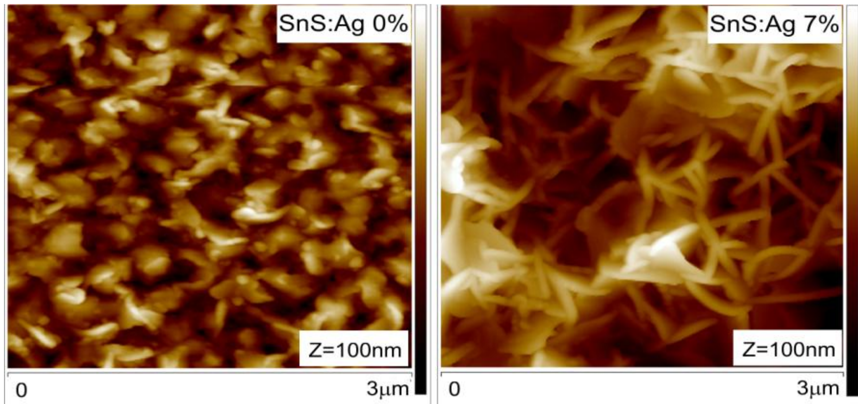

Fig. 49: AFM images of SnS thin films doped with Ag at various percentages

Table 34: Grain size and Roughness SnS thin films doped with Silver-Ag

Samples	Roughness (nm)	Grain size (nm)
undoped	24	180
SnS:Ag-3%	68	114
SnS:Ag-5%	55	122
SnS:Ag-7%	96	186
SnS:Ag-10%	63	199

2.2.3. Electrical properties

Table 35 shows the results of electrical measurements of SnS thin films doped with silver. It was noted that the introduction of 3% of silver increased the resistivity three times compared to undoped film creating a more resistive layer. And when the percentage of dopant element increases from 5% to 10%, resistivity decreases from 297.8 to 108.5 Ω.cm due to the substitution of tin (Sn) by silver (Ag) creating acceptor states in film structure.

Table 35: Resistivity, Density carriers N_A and Flat-band potential V_{fb} of SnS thin films doped with Silver-Ag at various percentages

Samples	Resistivity (Ω.cm)	N_A (cm^{-3})	V_{fb} (V)
SnS undoped	155.20	4.68×10^{18}	0.15
SnS-3%	476.42	3.08×10^{17}	0.04
SnS-5%	297.81	5.19×10^{17}	-0.07
SnS-7%	128.95	2.09×10^{17}	-0.01
SnS-10%	108.50	1.56×10^{18}	0.21

2.2.4. Electrochemical analysis: Mott-Schottky Plots

Capacitance measurements can be used to evaluate the characteristics of SnS thin films doped with silver (Ag^+). C−V measurements, which are most common capacitance measurements, can be used to estimate the carrier's density (N_A) and the type of semiconductors using the equations (29) and (30) of chapter III.

To analyze the SnS thin films semiconductors properties doped with Silver (Ag) at various percentages the electrochemical impedance measurements conducted in three electrodes configuration using 0.1 M of Na_2SO_4 aqueous solution electrolyte in the range of potential from −0.5 V to +0.3 V were used in this study. The Mott-Schottky plots obtained at the frequency of 1357 Hz in dark have been done. FRA software was used to exploit the data. All curves exhibit negative slope revealing p-type semiconductors for all films. The flat-band potentials estimated from the extrapolation of the Mott-Schottky plots are given relative to Ag/AgCl reference electrode. Table 35 shows the carriers density and the flat-band potential of films at different percentages. The carrier density of film decreases from 4.68×10^{18} cm^{-3} to 2.04×10^{17} cm^{-3} when the Ag-doping percentage increases from 0% to 7%, respectively.

Lower majority carriers could be due probably to the presence of traps (deep levels closer to the middle of the band gap) in the band gap that reduce the majority charge carriers by promoting recombination in the space charge region. When the doping concentration increases the flat band potential (V_{fb}) was negative (at 5% and 7% of A-doping) and space charge became broadened as a result there is an increase of recombination of charge carriers and a diminution of hole density carrier N_A. This diminution of hole carrier density may be due to: recombination in the space charge layer [35], hole trapping at surface defects [36] and hole accumulation at the surface due to poor charge transfer kinetics [37].

The carrier concentration value of $SnS:Ag^+$ and the ITO ($6.28x10^{20}$ cm^{-3}) substrate are different and this mean that there exist the opposite charged interface states at the interface [38].

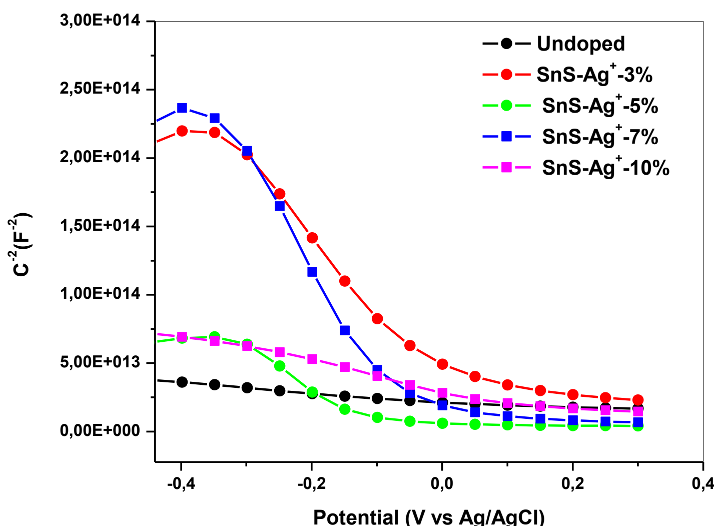

Fig. 50: $1/C^2$ vs bias voltage for SnS thin films doped with Ag at various percentages

2.2.5. Optical properties

Fig. 51 shows the optical properties, transmittance T versus λ and Fig. 52 depicts band gap energy measurement of SnS thin films doped with silver at various percentages. The band gap energy increases from 1.46 eV to 1.66 eV corresponding to films doped with 5%-Ag and 10%-Ag, respectively. This variation of band gap proved that silver doping element had effect in the optical properties of SnS thin films.

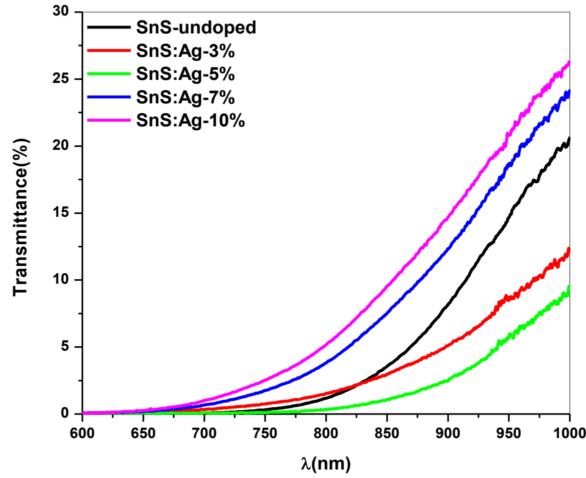

Fig. 51: Optical transmittance spectra of SnS thin film doped with Silver

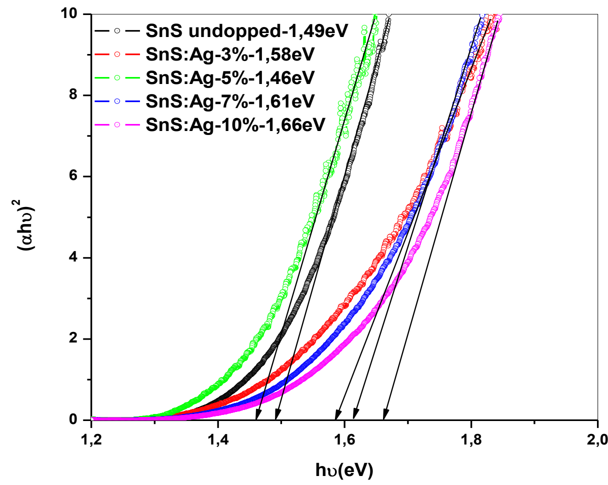

Fig. 52: Plot of $(\alpha h\nu)^2$ against photon energy (hν) of SnS thin films doped with silver at various percentages

Table 36: Band gap energy of SnS thin films doped with Silver-Ag

Samples	Band gap energy (eV)
Undoped	1.49
SnS-3%-Ag	1.58
SnS-5%-Ag	1.46
SnS-7%-Ag	1.61
SnS-10%-Ag	1.66

2.3. Conclusion

SnS thin films doped with silver (Ag) with different concentrations were successfully synthesized from aqueous solution using Chemical Spray Pyrolysis method at 350°C substrate temperature. All films are shown polycrystalline with (111) as main peak with an improvement of crystallinity when Ag-dopant element increases in the solution. One also noted Ag_8SnS_6 and Ag as secondary phases at 3% and 5%, respectively. SEM and AFM analysis show that Ag doping element has no effect in the morphology and the topography of films doped from 3% to 10% but reveal different morphology between undoped and doped films. EDS highlights an increase of Ag in films when the amount of Ag increases in the solution with S/Sn≈0.98 near to 1 at 5% of Ag doping percentage. Electrical and energy band gap measurement show a decrease of resistivity with Ag percentage increasing with a lower value of 108 Ω.cm at 10% and a low energy of 1.46 eV at 5%, respectively. Mott-Schottky plots allow highlighting p-type semiconductors for all films with variation of carrier's concentration.

For having p-type SnS thin films with enhancement of crystallinity, good morphology, stoichiometric, relatively low resistivity and acceptable band gap energy, one must use a percentage of 5% of silver to dope tin sulfide prepared by Chemical Spray Pyrolysis technique.

3. SnS thin films doped with aluminum (Al^{3+})

3.1. Experimental details

For the preparation of SnS thin films by Chemical Spray Pyrolysis we used an aqueous solution containing tin (II), chloride dihydrate ($SnCl_2.2H_2O$), thiourea ($CS(NH_2)_2$), aluminum chloride ($AlCl_3$) at different percentages: 0%-3%-5%-7%-10% and alcohol (5mL) to reduce the surface tension of water. The concentration of tin chloride was fixed at 0.104 M with an [S]/[Sn] ratio of 1. The substrate temperature was kept at 350°C, the sprayed volume at 5 mL, the spray rate at 1.5 ml/min, air pressure was 0.7 bar and the distance between the substrate and the nozzle was 25 cm.

3.2. Results and Discussion

3.2.1. X-ray diffraction (XRD) analysis

Fig. 53 shows the XRD patterns of SnS thin films doped with various percentages of aluminum (Al^{3+}). Polycrystalline films, having (111) as their main peak for all samples and no parasite secondary phase, was revealed by XRD analysis. All SnS-peaks were assigned to a SnS orthorhombic Herzenbergite (JCPDS#00-39-354) structure. Also, aluminum doping enhanced crystallinity of the films and intensified the (101) peak reaching its highest intensity at 10%: when the percentage increased, crystallinity of the main (111) peak improved from 3% to 7% and decreased when reaching 10%, which may be explained by new aluminum atoms filling the interstitial sites which were previously unoccupied. New growth centers were probably created when the percentage of dopant increased above 7% [39]. At 10%, saturation was attained and the crystallinity of the film was broken.

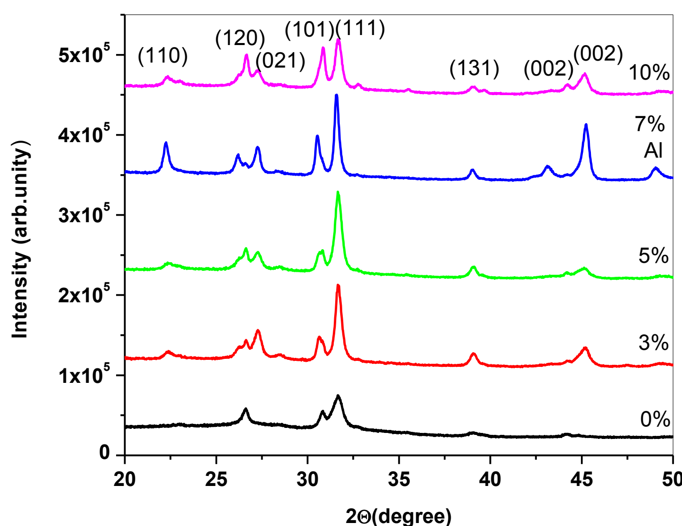

Fig. 53: XRD spectra of SnS thin films doped at various Al ratios

The variation of the crystallite size in relation to aluminum doping was evaluated applying Scherrer's formula to the (111) diffraction line. The microstrain (ε) was calculated using the and the dislocation density (δ) was calculated applying Williamson and Smallman's formula. The crystallite size, D, obtained from this equation (6) of chapter III corresponds to the mean minimum dimension of a coherent diffraction domain.

Table 37 shows the increase of the crystallite size with Al-doping from 136 Å to 308 Å corresponding to 0% and 7% films, respectively, confirming the enhancement of the

crystallinity of the films. The microstructure and dislocation density (δ) were correlated to the crystallite size with the percentage of Al doping. Small values of dislocation and microstructure, 1.05 10^{15} lines.m^{-2} and 1.17 10^{-3} at 7% Al-doping, indicated a minimum defects and a densely packed structure, good crystallinity and a high quality of the corresponding sample compared to others. Lattice parameters are in good agreement with standard sample (JCPDS#039-0354).

Table 37: Grains size, microstrain and dislocation of SnS thin films deposited at various Al percentages

Samples	**Crystallite size (Å)**	**ε(10^{-3})**	**δ (10^{15} lines.m^{-2})**	**Lattice parameters(Å)**		
				a	b	c
SnS-undoped	136	1.97	5.40	4.34	10.45	3.97
SnS-3%	181	1.99	3.05	4.25	11.28	4.00
SnS-5%	186	2.30	2.89	4.16	11.28	4.02
SnS-7%	308	1.17	1.05	4.27	11.23	4.00
SnS-10%	169	2.13	3.50	4.11	11.48	3.98
Standard-JCPDS# 39-0354	-	-	-	4.32	11.19	3.98

3.2.2. Surface Morphology and Composition Analysis

Surface morphology plays an important role in photovoltaic devices. The effect of aluminum doping on the surface morphology of samples was clear when reaching 10% with the corresponding film covered well the substrate surface and was denser than other films without any hole and crack. It is apparent from the electron micrograph that the change in morphology is strongly dependent on the Al compositions in films. From 3% to 7%, films have a fishnet-like morphology with numerous holes. The undoped film showed well covered glass substrate with rounded uniform grains size. Then, the morphology of SnS:Al thin films depended on dopant concentration as seen in Fig. 54.

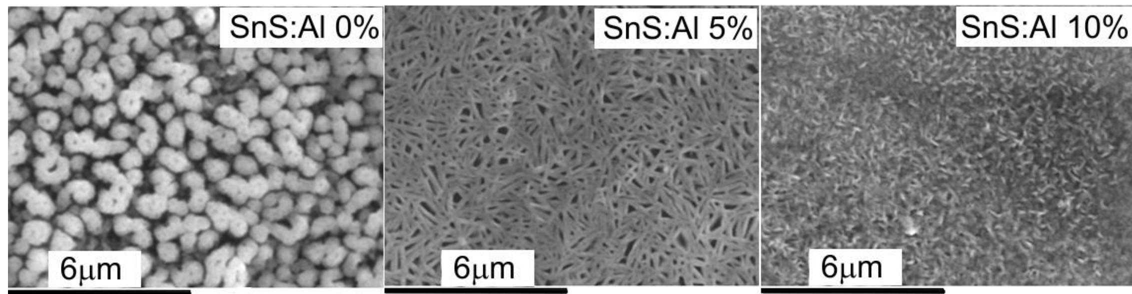

Fig. 54: SEM images of SnS thin films doped at various Al percentages

Table 38 shows the composition of Al-doped SnS films. The composition analysis determined by Energy Dispersive X-ray Spectroscopy (EDS) showed the presence of tin (Sn), sulfur (S) and aluminum (Al) and showed an increase of the atomic percentage of aluminum when the percentage of doping increased in the initial solution, and at the same time, the atomic percentage of tin decreased due probably due to the substitution of Sn by Al. We noted also that the presence Al in the films revealed that the atomic percent of Sn in Al-doped SnS is lesser than in undoped SnS film which may be due to the substitution of Sn by Al atoms.

Table 38: Composition of SnS thin films doped with various ratios of Aluminum

Samples	%S	%Sn	%Al	S/Sn
SnS undoped	45.00	55.00	0.00	0.82
SnS:3%	47.10	50.53	2.38	0.93
SnS:5%	47.23	50.00	2.77	0.94
SnS:7%	46.44	49.62	3.95	0.94
SnS:10%	47.49	48.08	4.43	0.99

Fig. 55 shows AFM images of a scanning area of 3μmx3μm for the SnS:Al. The display surface had a mean roughness value decreasing from 68nm to 33nm when the Al-doping increased from 3% to 10%; an increase of the grain size was shown in Table 39 and was observed in the same range, probably due to the coalescence of small grains to form big ones with the reduction of grain boundaries. This result is in contradiction to the common interpretation relation between roughness and grain size which states that roughness increased with grain size and the reduction of grain boundaries. However, this common result is supposed to be valid in the case of spherical like-grain and not in the case of elongated grain shape.

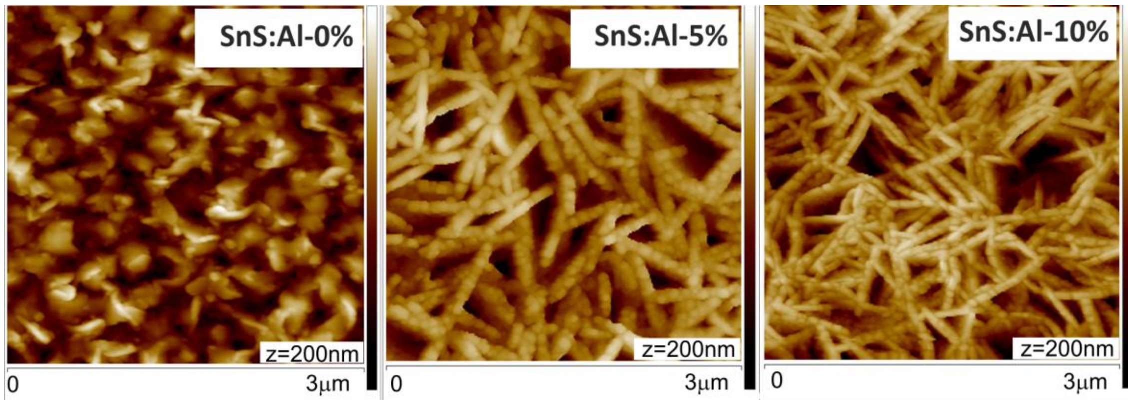

Fig. 55: AFM images of Al-doped SnS thin films at various percentages

Table 39: Grain size and roughness of Al-doped SnS thin films

Samples	Roughness (nm)	Grain size (nm)
SnS undoped	24	180
SnS:3%	68	94
SnS:5%	56	104
SnS:7%	48	138
SnS:10%	33	176

3.2.3. Electrical Properties

Table 40 shows the variation of resistivity with the variation of the Al-doping percentage in the solution. It was noted that the resistivity decreased from 789.89 to 171.30 Ω.cm when the aluminum doping ratio increased from 3% to 10%. The decrease of resistivity can be assigned to an increase of acceptor states in the SnS structure [40], helping to increase hole carrier concentration in the valence band and leads to low resistivity at room temperature [41]. Even if, resistivity decreases, its value remains high probably due to the presence of grain boundaries and holes as seen in the SEM images. The low resistivity value of undoped film was due to the excess of tin (Sn) in the sample.

Table 40: Resistivity of SnS thin films doped with Aluminum at various percentages

Samples	Resistivity(Ω.cm)
SnS undoped	155.20
SnS-3%	769.86
SnS-5%	498.75
SnS-7%	189.39
SnS-10%	171.30

3.2.4. Mott-Schottky Plots

In order to study the carrier density and the type of semiconductor, a Mott-Schottky plot was used. A conventional three-electrode cell was used for the electrochemical test. A silver/silver chloride electrode (Ag/AgCl) was used as reference electrode and a platinum ring was used as a counter electrode. The measure of capacitance (C) of the interface between the SnS film and the electrolyte (Na_2SO_4) is described by the equations (29) and (30) of chapter III.

N_A is calculated from the slope and its sign provides the character of the carrier type, using the equation (30) of chapter III.

Generally, the semiconducting properties of most of compounds depend on their non-stoichiometry and are related to the presence of intrinsic defects such vacancies and interstitials. Fig. 56 shows density carriers and flat-band potential of Al-doped SnS thin films obtained from the Mott-Schottky equation. Mott-Schottky plots showing that all films are p-type semiconductors and majority density carriers (hole) increased gradually from 2.90 $x10^{17}$ to 4.97 $x10^{18}$ cm^{-1} when the Al-doping increased from 3% to 10%. But the decrease of the concentration of carriers from 3.72 $x10^{18}$ cm^{-1} to 2.90 $x10^{17}$ when Al-doping increased from 0% and 3% was probably due to the existence of traps near to the space charge region leading to recombinations. Table 41 shows that the flat-band potential decreases from 0.390V to 0.10V when the Al-doping increases from 0% to 7%, respectively. All flat band potential are positive and electrons are attracted towards space charge region, hence this region decreases and it leads to the increase of recombination of charge carrier leading to the diminution of carriers' density of doped films compared to undoped sample with an increase tendency when percentage of doping element increases.

It has been generally considered that the formation of n-type tin sulphide is very difficult because of self compensation effects due to tin (Sn) vacancies. Adding donor ion (Al^{3+}) compensates native acceptors (V_{Sn}) but not enough to change the conductivity type of our material from p-type to n-type.

Electron from donors will recombine with holes on the native acceptors (Sn) in order to compensate some carrier concentration in the SnS doped Al films as result the diminution of carrier concentration given by the Mott-Schottky analysis. When the percentage of doping is so high (10%), the carriers concentration increases because the native acceptors can't compensate it so enough.

Otherwise, the increase of carrier concentration was correlated to the decrease of resistivity shown above.

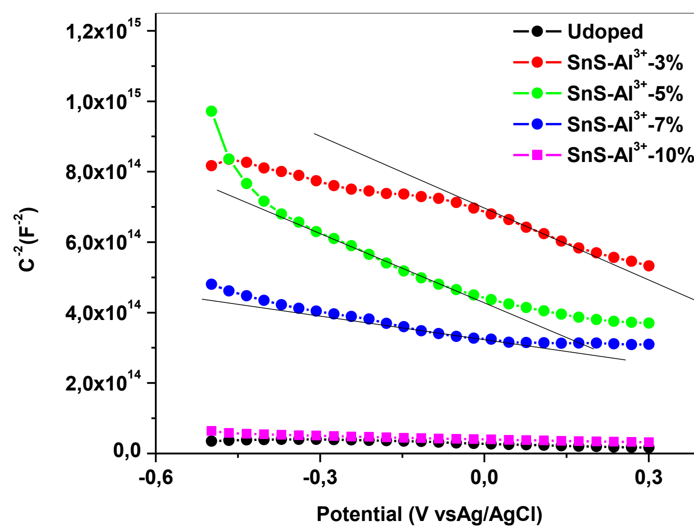

Fig. 56: Mott-Schottky plots of Al-doped SnS thin films percentages

Table 41: Density carriers N_A and flat-band potential V_{fb} of SnS thin films doped with Al

Samples	**N_A (cm^{-3})**	**V_{fb} (V)**
SnS undoped	3.72×10^{18}	0.39
SnS-3%	2.90×10^{17}	0.32
SnS-5%	3.00×10^{17}	0.20
SnS-7%	6.28×10^{17}	0.10
SnS-10%	4.97×10^{18}	0.41

3.2.5. Optical Properties

Optical transmission of SnS thin films doped with Al deposited onto glass substrates with various percentages is shown in Fig. 57. The transmittance of all films is low, probably due, to the thickness of our material with an average transmittance in the range of 15%-40% and in the visible region, the transmission is zero.

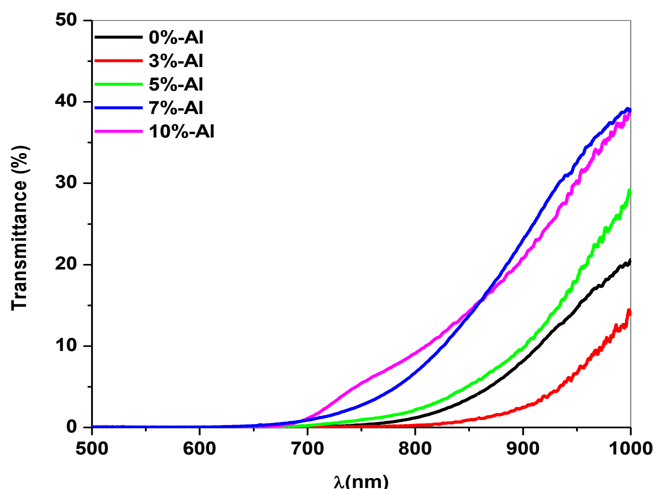

Fig. 57: Optical transmittance spectra of Al-doped SnS thin films

Energy band gap values are estimated from the plot (αhν) versus hν by extrapolating the straight line portion of the graph in the absorption regime, where α is the absorption coefficient and hν the photon energy. The results are shown in Fig. 58. In Table 42, it can be noted that band-gap energy of our samples increases as the lattice parameters decrease.

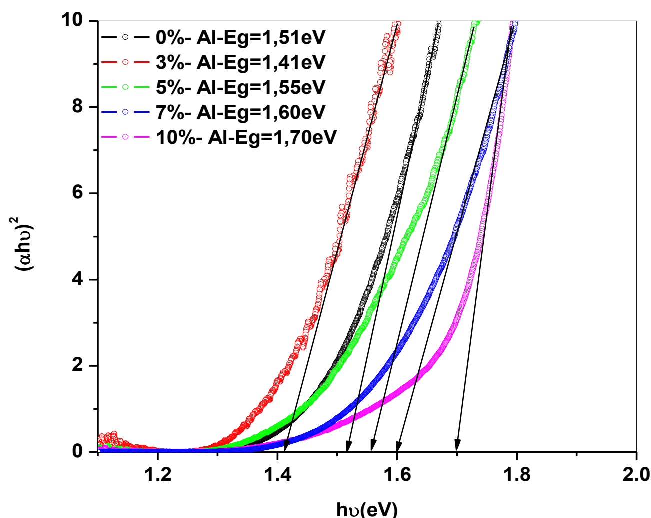

Fig. 58: Plot of $(\alpha h\nu)^2$ against photon energy (hν) of Al-doped SnS thin films at various percentages

Table 42: Bandgap energy of SnS thin films doped with Silver-Al

Samples	Band gap energy (eV)
SnS undoped	1.51
SnS-3%	1.41
SnS-5%	1.55
SnS-7%	1.60
SnS-10%	1.70

3.3. Conclusion

Orthorhombic SnS thin films doped with aluminum (Al) were successfully prepared by the Chemical Spray Pyrolysis technique with enhancement of crystallinity when Al doping increased in the initial solution. SEM analysis revealed a fishnet-like morphology with numerous holes for samples doped from 3% to 7% and a denser and well covered film at 10%. EDS showed improvement of stoichiometry with an increase of the Al atomic percentage in films when the Al concentration increased in the solution. A relatively low resistivity of 171.30 Ω.cm is found for films doped at 10%. The energy bandgap, given by Tauc's law, showed an increase of the bandgap energy when the Al-concentration increased in the solution. All films are p-type with a decrease of majority carrier density (hole).

Finally, it can be affirmed that suitable SnS-Al thin films can be deposited by CSP with good crystallinity, morphology, relatively low resistivity and reasonable band gap energy for the absorber layer, using an Al doping percentage of 10% of Aluminum is suitable, for optoelectronic or photovoltaic applications.

4. SnS thin films doped with iron (Fe^{2+})

4.1. Experimental Procedure

For the preparation of SnS thin films with Chemical Spray Pyrolysis we used aqueous solution containing tin (II) chloride dihydrate ($SnCl_2.2H_2O$), thiourea ($CS(NH_2)_2$), Iron Chloride ($FeCl_2$) at different percentages: 0%-3%-5%-7% and alcohol (10% in volume) to

reduce the surface tension of water. The concentration of tin chloride was fixed at 0.104 M and the [S]/[Sn] ratio was 1. The substrate temperature was kept to 350°C, the sprayed volume at 5 mL, the spray rate at 1.5 mL/min, the air compressed pressure 0.7 bar and the distance between the substrate and the nozzle 25 cm.

4.2. Results and Discussion

4.2.1. X-ray diffraction (XRD) analysis

Fig. 59 shows XRD analysis of SnS thin films doped with iron (Fe) at different percentages. All films have polycrystalline structure, crystallized in the Herzenbergite orthorhombic phase (JCPDS#39-354) with orientation along the (111) as main peak for all samples. Others peaks like (120), (002) and (112) were also detected. One noted also, when Fe-doping element increased in the solution, the decrease of the main peak intensity, attesting the incorporation of Fe-atoms in the SnS structure. Otherwise, $SnFe_2S_4$ phase was also noted in the films explained the decreasing of (111) intensity.

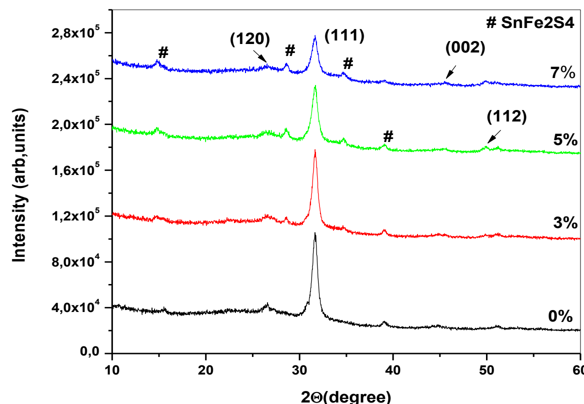

Fig. 59: XRD spectra of SnS thin films doped with various Fe concentrations

The crystallite size of layers was evaluated using the Debye-Scherrer formula. It can be seen clearly in Table 43 that crystallite size decreased with the decreasing of (111) intensity when the Fe percentage increased in the initial solution. This can be explained by an increase of grain boundaries and/or the presence of the secondary phase, $SnFe_2S_4$, in the samples.

Table 43: Crystallite size of SnS Thin Films deposited at various Fe percentages

Samples	Crystallite Size (nm)
SnS:Fe^{2+}-0%	13.0
SnS:Fe^{2+}-3%	13.1
SnS:Fe^{2+}-5%	11.3
SnS:Fe^{2+}-7%	12.2

4.2.2. Morphological properties and Microanalysis

To investigate the surface morphology and the surface topography, SEM and AFM were used respectively. As it can be seen in Fig. 60, at low level of doping percentage (3%) the surface morphology of undoped and SnS:Fe-3% were not different while when the concentration of Fe increased in the initial solution from 5% to 7%, the morphology changed and became more compact, denser without pinholes and cracks. From Fig. 61, one shows the AFM pictures scanning in an area of 3µmx3µm. It confirmed uniform films, well-covered with small grain uniformly distributed over the substrate surface proving the reliability of AFM to provide SEM images. The decrease of the grain size and the roughness shown in Table 44 are correlated with the result obtained by SEM and XRD analysis confirming the Fe-doping effect in the SnS thin films. For the element composition of films, EDS revealed the presence of tin (Sn), sulphur (S) and iron (Fe) in all samples as shown in Table 45. The increase of Fe in the solution enhanced the S/Sn ratio in the sample from 0.85 to 0.92 corresponding to 3% and 7%, respectively and we noted also the diminution of Sn concentration in the films due to the increase of iron doping element. The deficit of sulphur noted into films was due probably by the evaporation of sulphur due to the high substrate temperature used for the deposition-350 °C.

Table 44: Grain size and roughness of SnS thin films doped with Fe

Samples	Grain Size(nm)	Roughness(nm)
SnS:Fe^{2+}-0%	180	24
SnS:Fe^{2+}-3%	158	38
SnS:Fe^{2+}-5%	138	28
SnS:Fe^{2+}-7%	130	14

Table 45: Composition of SnS thin films doped with various ratios of Fe

Samples	%S	%Sn	%Fe	S/Sn
SnS:Fe^{2+}-0%	50.53	49.47	0	1.02
SnS:Fe^{2+}-3%	45.03	52.78	2.19	0.85
SnS:Fe^{2+}-5%	45.38	51.46	3.17	0.88
SnS:Fe^{2+}-7%	45.84	49.49	4.68	0.92

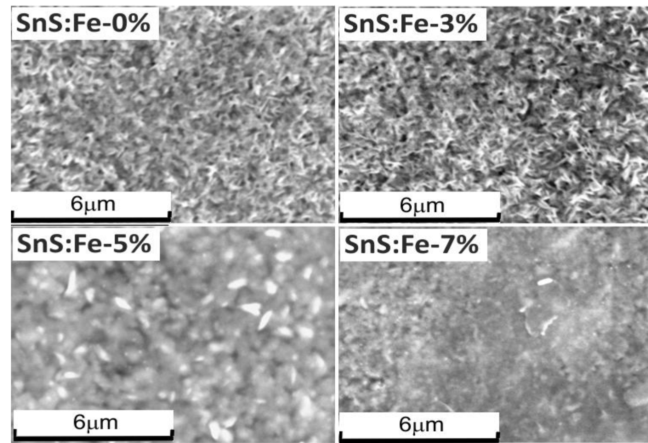

Fig. 60: SEM images of SnS thin films doped with Fe at various percentages

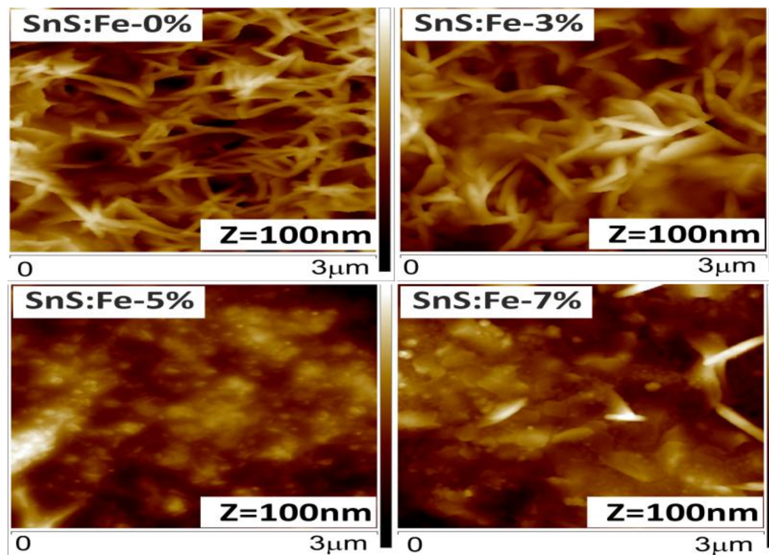

Fig. 61: AFM images of SnS thin films doped with Fe at various percentages

4.2.3. Optical properties

Fig. 62 shows the transmission of SnS doped with Fe and deposited at different concentrations of iron by Spray Pyrolysis in the range of 400-1000nm. The dopant element improved the transmittance which passed from 24% at 0% to 48% at 7%. The low

transmittance in the visible region was due to the thickness of the films and/or the absorber character of tin sulphide semiconductor.

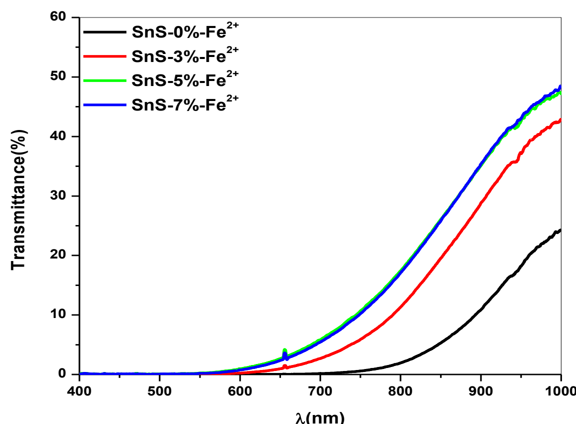

Fig. 62: Optical transmittance spectra of SnS thin film doped with Iron-Fe at various percentages

To investigate the effect of Fe dopant on the SnS thin films, the energy band gap was measured from transmittance spectra using the following equation (22) chapter III where α is absorbance, A constant, hν photon energy, Eg band gap energy and n=2 for direct transition which we have considered in this paper. The linear nature of plot at the absorption edge confirms that SnS was a semiconductor with direct band gap. The band gaps of the films have been calculated using Tauc's plot by plotting $(\alpha h\nu)^2$ versus photon energy hν as shown in Fig. 63 and by extrapolating the linear portion of the absorption edge to find the intercept with energy axis $(\alpha h\nu)^2=0$ of on hν. The shift of band gap energy towards high energy from 1.50eV to 1.77eV proves that Fe^{2+} doping-element has an effect in optical properties of our samples by substituting the tin (Sn^{2+}) atom in the SnS film structure.

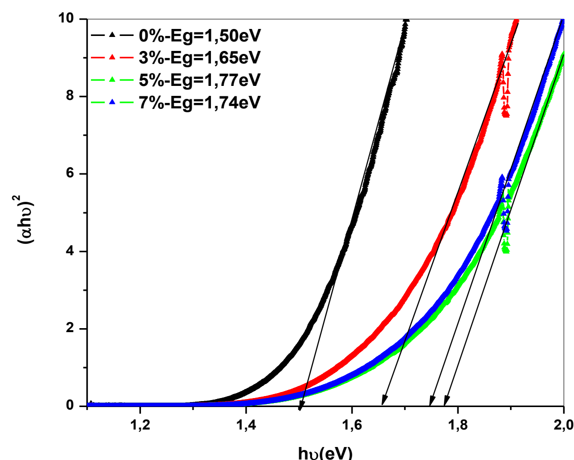

Fig. 63: Plot of $(\alpha h\nu)^2$ against photon energy (hν) of SnS thin films doped with Iron-Fe at various percentages

Table 46: Band gap energy of SnS thin films doped with Iron-Fe

Samples	**Band gap energy (eV)**
$SnS:Fe^{2+}$-0%	1.50
$SnS:Fe^{2+}$-3%	1.65
$SnS:Fe^{2+}$-5%	1.77
$SnS:Fe^{2+}$-7%	1.74

4.2.4. Electrical properties

Table 47 shows the electrical properties of undoped and doped SnS thin films with Fe. The undoped film has a resistivity of 211.05Ω.cm. When the Fe is incorporated in the structure of the SnS films we noted an increase of the resistivity from 211.05 to 362.78 Ω.cm corresponding to 0% and 7%, respectively. This augmentation of the resistivity can be explained probably by the presence of $SnFe_2S_4$ secondary phase detected by the XRD analysis.

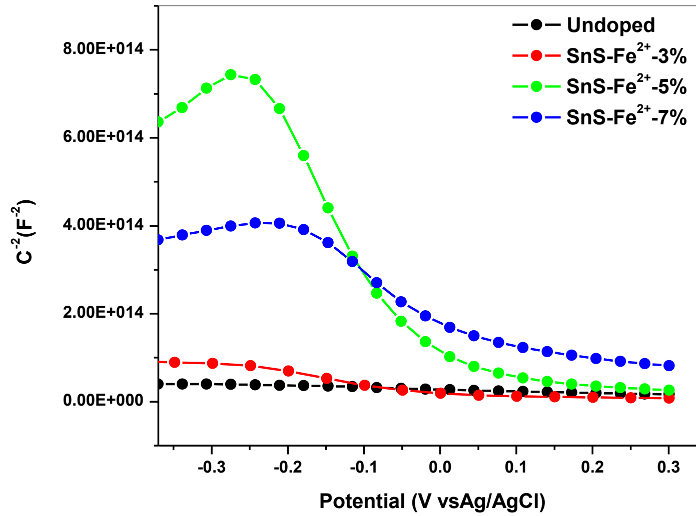

Fig. 64: $1/C^2$ vs bias voltage for SnS thin films doped with Fe at various percentages

4.2.5. Electrochemical analysis: Mott-Schottky plots

A conventional three-electrode cell was used for electrochemical tests. The cell was equipped with platinum counter electrode and silver/silver chloride electrode (Ag/AgCl) as reference electrode. The experiments was carried out at ambient temperature using 0.1 M of Na_2SO_4 as blocking electrolyte and applied potential from -0.5 V to +0.3 V.

All curves exhibit the negative slope characteristic for p-type semiconductors and the slope of the curves can be used to calculate the donor density. Table 48 shows the N_A concentration of carriers with a decrease of density carrier from 3.72 10^{18} to 5.77 10^{16} and flat-band potential from 0.39V to 0.04V corresponding to 0% and 5%, respectively for both when the percentage of Fe-doping increase in the solution. This diminution of carriers' density can be explained by deep level state in the band gap of SnS doped with Fe promoting recombination not only in the charge space region but also in the SnS film and then the diminution of majority charge carriers (holes). The donor sulfur vacancies (V_S) defects have a donor-like characteristic (D_S^{2+}) in *p*-type material, i.e. compensate the intentional doping of SnS film with Fe. This is why the holes concentration (N_A) decrease when the percentage of Fe doping increase up to 5%.

Table 47: SnS thin films doped with Fe at various percentages

Samples	Resistivity (Ω.cm)
$SnS:Fe^{2+}$-0%	211.05
$SnS:Fe^{2+}$-3%	345.70
$SnS:Fe^{2+}$-5%	322.81
$SnS:Fe^{2+}$-7%	362.78

Table 48: Carriers' density and the flat-band potential of SnS thin films doped with Fe at different percentages

Samples	N_A (cm^{-3})	V_{fb} (V)
$SnS:Fe^{2+}$-0%	3.72×10^{18}	0.39
$SnS:Fe^{2+}$-3%	6.41×10^{17}	0.05
$SnS:Fe^{2+}$-5%	5.77×10^{16}	0.04
$SnS:Fe^{2+}$-7%	1.24×10^{17}	0.08

4.3. Conclusion

SnS thin films doped with Fe with different concentrations were prepared and the effects of Fe-doping on the structural, morphological and topological, electrical and optical properties were studied. The XRD results show polycrystalline film with (111) as preferrential orientation. The presence of $SnFe_2S_4$ secondary phase was detected and so, explained the decrease of (111) main peak when the percentage of Fe increased in the solution. SEM and AFM images show same morphology and topography for undoped and 3%-Fe doped films but from 5% to 7%, films became denser and more compact than before. Microanalysis revealed the presence of tin (Sn), sulfur (S) and iron (Fe) in films with an enhancement of stoichiometry with augmentation of Fe in the films and energy band gap increased with the doping element from 1.50eV to 1.77eV at 0% and 5%, respectively. The electrical properties given by four-probe technique show an increase of resistivity with Fe-doping due probably to the presence of secondary phase and Mott-Schottky plots revealed p-type semiconductors for all films.

Finally we can notice that the concentration of Fe can affect the physical and chemical properties of p-type SnS thin films and it was preferable to dope SnS films with low

concentration (≤3%) in order to modify slightly the physical and chemical properties and avoid secondary phase which increased the resistivity.

5. SnS thin films doped with indium (In^{3+})

5.1. Thin film preparation

The SnS films were prepared using aqueous solution containing tin (II) chloride dehydrate ($SnCl_2 \cdot 2H_2O$), thiourea ($SC(NH_2)_2$). Indium chloride ($InCl_3$) was directly added to the solution at different concentrations. To avoid growth of Sn_2S_3 and SnS_2 phases, Sn (II) instead of Sn (IV) was used [21]. Thin films were grown on the glass substrate keeping the constant substrate temperature of 350°C. To obtain clean and stain-free substrates, an ultrasonic bath was used and substrates were immersed for 15 minutes in acetone solution bath, rinsed with distilled water, immersed in an ethanol bath solution, rinsed with distilled water before drying and before use for deposition.

5.2. Results and Discussion

5.2.1. X-ray diffraction (XRD) analysis

To investigate the crystalline properties of synthesized films XRD measurements were made. The diffraction spectra of all four SnS thin films are presented in Fig. 65.

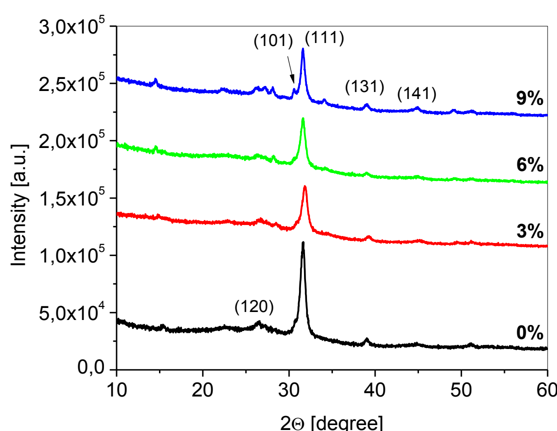

Fig. 65: XRD spectra of SnS thin films doped with In at various concentration

All films are polycrystalline and XRD peaks are in good agreement with standard data for SnS orthorhombic phase (JCPDS #39-0354) with (111) as the preferential crystallographic direction. The peaks are broad which indicates high disorder in the material as well as point

into small crystallite sizes. The intensity of the (111) main peak decreases with increased amount of In. The crystallite size of SnS thin film doped with indium for the main (111) XRD peak can be calculated using Scherrer formula of equation 6 (Chapter III). Calculated crystallite sizes are presented in Table 49. Size of crystallites in investigated samples is in the range 116 Å – 125 Å and does not depend significantly on the amount of indium supplied during growth.

5.2.2. Atomic Force Microscopy Analysis

Fig. 66 shows AFM images of investigated SnS thin films. The scan area was 8 μm x 8 μm with 512 x 512 resolution. Films have irregular structure with longitudinal type of grains, which was already observed in spray pyrolyzed SnS thin films [42]. The average grain size and the average roughness height are presented in Table 49. The presence of indium during growth generally increases the mean grain size from around 38 nm to around 60 nm as well as the roughness of the film. However, there is no further increase of grain size when more indium is added. The average grain size is also larger than the average crystallite size obtained from XRD. This might be a result of different physical meaning of calculated size parameters between XRD and AFM analysis. Scherrer equation gives the minimum crystallite size and the analysis of AFM provides the mean grain size. Taking into account that the grains are clearly longitudinal we might expect higher average grain size then the minimum crystallite width. The second reason might be the fact that the grains might actually consist of few smaller crystallites undistinguishable by AFM analysis.

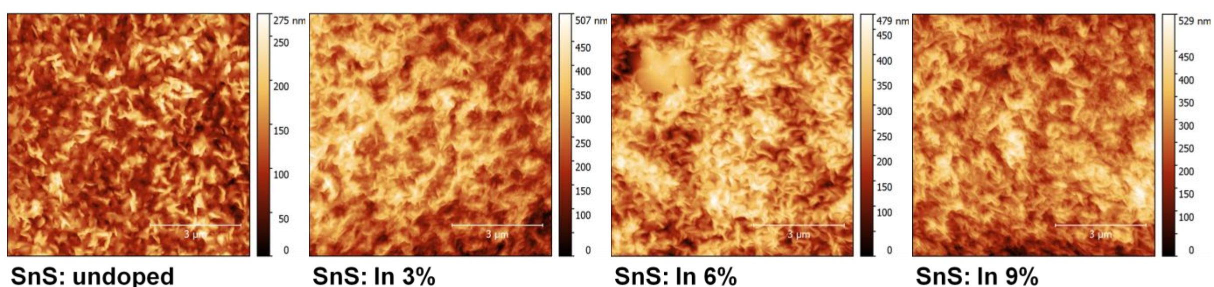

Fig. 66: AFM images of SnS thin films doped with In with different concentration

Table 49. Crystallites size calculated from XRD spectra and Grain size calculated from AFM of SnS thin films doped with In.

Sample	Crystallite size (Å)	Mean Grain size (nm)	Mean Roughness height (nm)
SnS: undoped	125	37.7 ± 3.8	155 ± 27
SnS: In 3 %	116	61,0 ± 9.2	193 ± 25
SnS: In 6 %	125	62.6 ± 6.8	196 ± 20
SnS: In 9 %	119	58.6 ± 6.5	203 ± 38

5.2.3. Optical Absorption

Fig. 67 presents a plot, which allows identifying a direct transition. As we were unable to precisely determine the thickness of the layers, the absorption coefficient (α) is replaced here by total absorption (A).

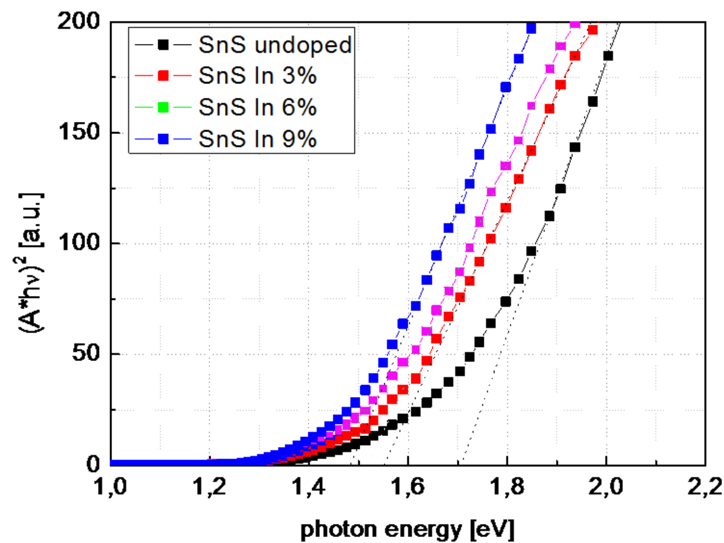

Fig. 67: Plot of $(Ah\nu)^2$ versus photon energy hν of SnS thin films with different In concentration.

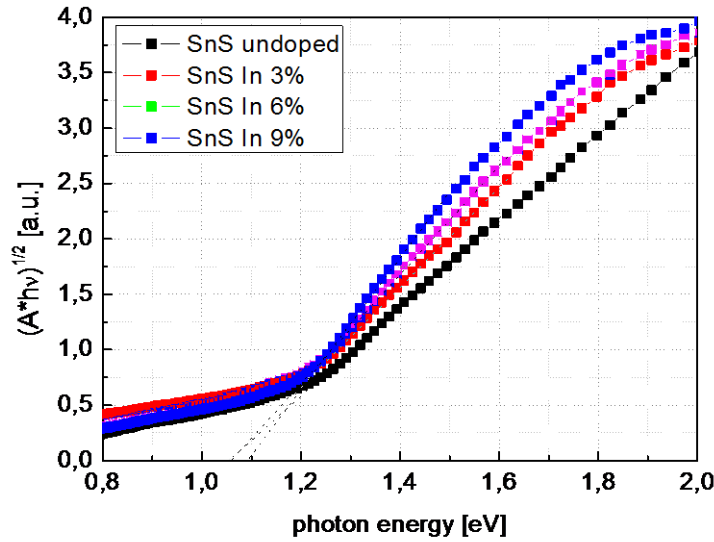

Fig. 68: Plot of $(Ah\nu)^{1/2}$ versus photon energy hν of SnS thin films with different In concentration.

The direct bandgap energies depend on the In concentration in the sprayed solution and decrease from 1.71 eV in case of undoped film to 1.48 eV for the film prepared with 9% concentration of In (Table 50). This is consistent with the available data on SnS thin films which mostly reports it as a direct bandgap semiconductor with bandgap energies around 1.5 eV [42, 43, 44]. This effect has already been observed [43] and explained by effective bandgap narrowing due to increased shallow acceptor concentration and formation of a defect intermediate energy band close to the valence band. However, this effect starts to be significant when carrier concentrations approach atomic concentrations and was observed i.e. in heavily doped ZnO [45]. This is not the case of investigated SnS samples, as their conductivity did not indicate such high carrier concentrations. The other reason of the lower bandgap in the In doped SnS might be at least twofold. The band structure of the material can change with addition of In and this will directly change the bandgap energy. However, the XRD data shows the same crystal structure of the material in all the samples. This implies no significant changes also in the band structure. The second reason might be related to the fact that the films were made in a non-vacuum process making incorporation of oxygen possible. It has been previously observed that the presence of oxygen widens the bandgap of the SnS [46]. The In might reduce incorporation of the oxygen atoms resulting in the lower bandgap of the SnS. It can be noted that the fitting was made here for the energies above 1.6 eV. The $(Ah\nu)^{1/2}$ vs hν plot and a fitting made for lower energies reveals an

indirect transition of around 1.05 eV independent on In concentration (Fig. 68). It agrees well with the theoretical calculations of the SnS band structure, which indicates indirect bandgap energy of 1.07 eV [47].

Table 50. Direct and Indirect band gap energies of SnS thin films with different In concentration

[In]/[Sn] ratio (%)	Direct transition energy (eV)	Indirect transition energy (eV)
0	1.71 ± 0.13	1.05 ± 0.03
3	1.55 ± 0.09	1.04 ± 0.03
6	1.52 ± 0.11	1.06 ± 0.04
9	1.48 ± 0.09	1.09 ± 0.04

5.2.4. Photoluminescence

Photoluminescence is a widely used method to study defects in semiconductors by analysis of radiative recombination processes. Fig. 69a shows a PL spectrum of an undoped SnS thin film measured at 10 K. The spectrum is a superposition of two radiative processes, labeled on the Fig. 69a as (1) and (2). Fittings made with two Gaussian distributions give energies of observed radiative processes around E_A=1.1 eV and E_B=1.24 eV. The In doping does not change the shape of the PL spectrum significantly (Fig. 69b). A 20 meV shift is observed in the sample with 9% of indium but in other cases, the change was negligible. There is also a change in the low energy part but looking at all the samples, these changes did not follow any systematic trend.

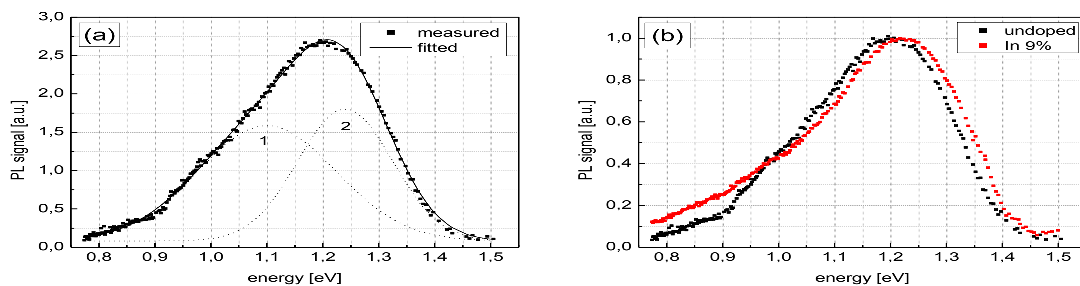

Fig. 69: (a) A Photoluminescence spectrum of an undoped SnS thin film measured at 10K. Fitting with two Gaussian functions (1 and 2) is included on the graph. (b) Comparison of PL spectra for an undoped SnS layer and SnS layer prepared with 9% of indium in the solution. The spectra are normalized to unity for the clarity.

The luminescence intensity I_{PL} follows a power law dependence on the excitation intensity I_{ex}:

$$I_{PL} = A * I_{ex}^{\gamma} \tag{3}$$

where A and γ are constants. It has been found that the type of the transition can be identified by the value of γ parameter with γ<1 indicating a donor to acceptor transition, γ=1 - free to bound transitions and 1<γ<2 - the exciton-like transitions [48]. Fig. 70 shows a PL intensity dependence on the excitation power. Fitting with a power law dependence (Equation 3) give the parameter γ=0.54 ± 0.08 which points into donor to acceptor (DA) transitions.

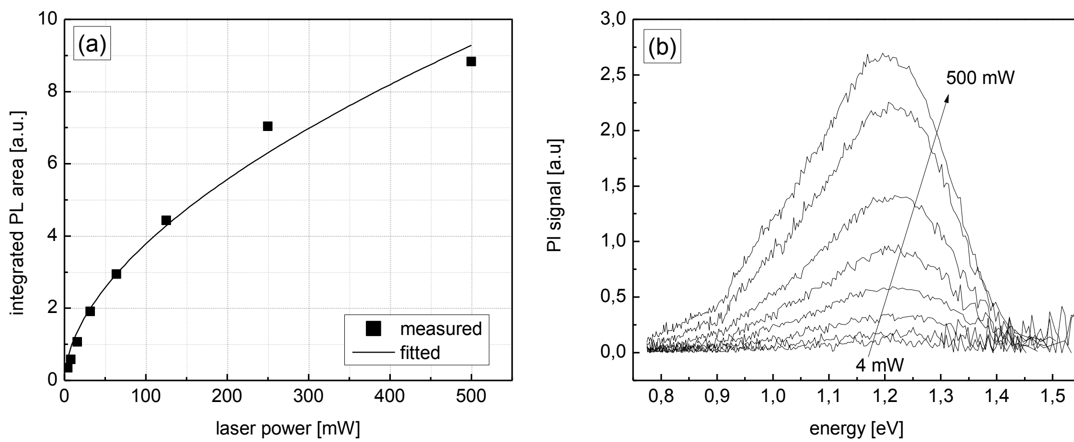

Fig. 70: (a) Integrated area of Pl spectra measured at 10 K as a function of laser power. Fitting was made with power law dependence (Equation 3) and is included on the graph. (b) Complete PL spectra in the 4 mW – 500 mW laser power range.

To determine defect thermal activation energies temperature dependent measurements were performed. With increased temperature, the process of thermal emission from a defect level to the nearest band becomes more probable than the recombination and the intensity of PL decreases. The activation energy of a defect can be then calculated from quenching of the PL signal according to [49]:

$$PL \propto \frac{1}{1 + T^{3/2} \sum_{i=1} a_i e^{-eE_{ai}/k_B T}} \tag{4}$$

where a_i is constant including a capture cross-section, E_{ai} is a thermal activation energy of a defect and k_B is a Boltzmann constant. The quenching of two identified DA transitions is shown on the Fig. 71 together with the PL spectra at different temperatures.

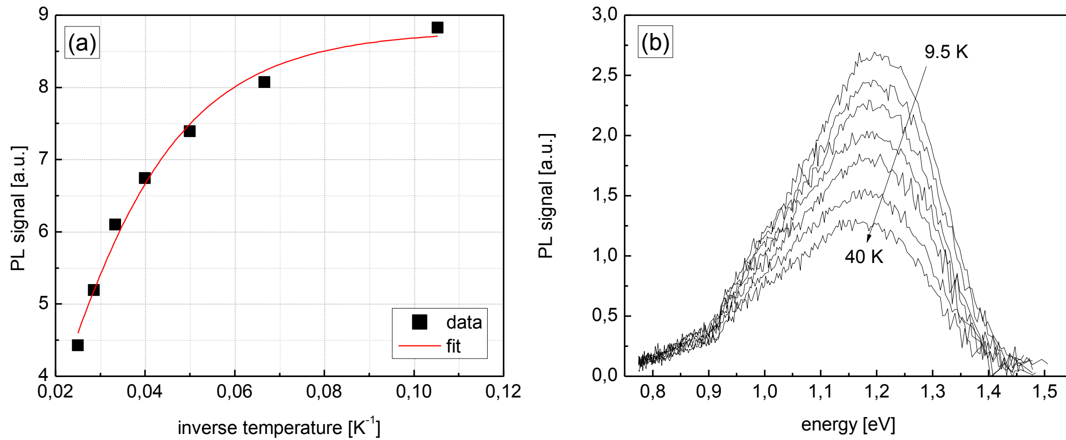

Fig. 71: (a) Quenching of PL intensity for two observed donor acceptor transitions with increasing temperature. Fittings made using Equation (4) are included on the graph. (b) Complete PL spectra recorded in 9.5 K – 40 K temperature range.

Fittings made using Equation (4) gave in both cases one thermal activation energy, which is the activation energy of a shallower defect taking part in the donor-acceptor recombination process. We have obtained the following values of $E_{a1}= 85\pm11$ meV and $E_{a2}= 93\pm13$ meV. Taking into account the quality of the PL spectra and the quality of the fit itself, we conclude that in both transitions one of the defect levels taking part in the recombination process is the same and have thermal activation energy of 89 ± 12 meV. The second defect must introduce in both cases a deep level because the sum of the activation energy and the transition energies is much lower than the bandgap value.

5.2.5. Conductivity Measurements

Applicability of a material as an absorber in a solar cell requires not only good optical properties but also appropriate electrical conductivity. Fig. 72 presents the electrical conductivity dependence on temperature of all investigated films. In temperatures above 200 K, the conductivity is thermally activated and follows exponential dependence on (1/T). Thus the linear fitting to logarithm of conductivity versus (1/T) provides an activation energy (E_{act}) of conductivity, which in case of a p-type semiconductor is an energy distance

from acceptor level (E_A) and the valence band $E_{act}=E_V-E_A$. The undoped SnS had activation energy of 164±2 meV and it does not change significantly except the case of sample with 9% of In concentration where value of 145±2 meV was obtained. Additionally slightly lower (160±2 meV) activation energy in layer with 6% In concentration may point into decreasing dependence of activation energy on In concentration. Taking into account the fact that the energy of a direct bandgap depends on the amount of indium in the solution this might mean that the energy position of the acceptor level responsible for the conductivity also changes when In is introduced.

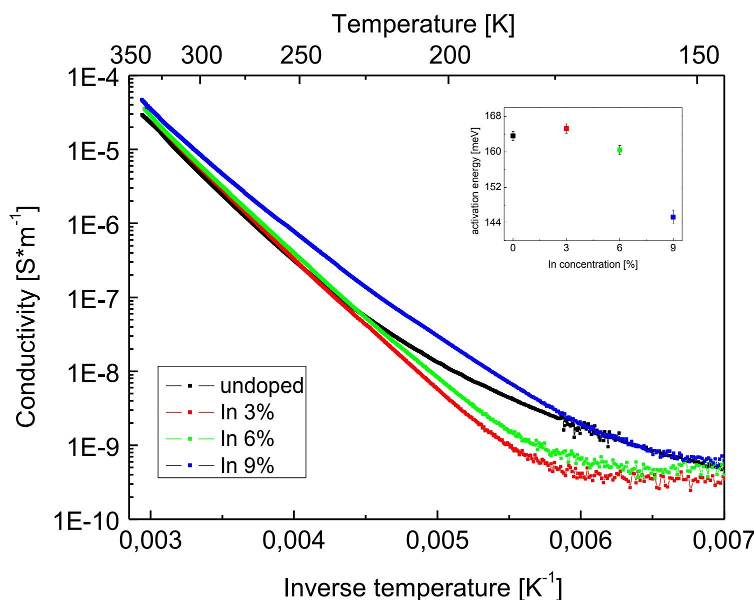

Fig. 72: Electrical conductivity dependence on temperature for investigated series of thin films. The linear fittings were made in the same 250 K – 330 K temperature range for all the samples, providing activation energies included on the inset.

The conductivity at room temperature increases with increased amount of indium by factor of 1.78 between undoped SnS film and one doped with 9% of In. This might be a result of decreased activation energy. The observable decrease of activation energies should by itself give an increase of conductivity by factor of 2.1 ± 0.4.

5.3. Conclusion

We presented the opto-electrical study of In doped SnS thin films made by Spray Pyrolysis. XRD analysis revealed orthorhombic structure with (111) dominant peak. AFM imaging show that films consist of longitudinal grains. The In doping slightly increase the roughness

of the surface as well as the average size of the grains while the crystallite size remains constant. The material has an indirect bandgap with energy around 1.05 eV independent on In concentration. However, the absorption is dominated by the direct transition with energies decreasing with increased amount of indium from 1.71 eV to 1.48 eV. The PL study revealed two donor to acceptor transitions independent on the In concentration. In both transitions, one of defect levels taking part in recombination process is common characterized by thermal activation energy of around 90 meV. However, our study did not allow us to judge whether the defect is a donor or an acceptor. The conductivity measurements show thermally activated conductivity with activation energies inversely dependent on In concentration in the 145 meV – 162 meV range. This decrease of activation energy results directly in higher conductivity of investigated thin films.

D. CdS, ZnO and ZnO:Al Thin Films

1. Introduction

In order to fabricate SnS thin films based solar cells, thin films like cadmium sulphide (CdS), zinc oxide (ZnO) and zinc oxide doped with aluminum (ZnO:Al) are prepared by Chemical Spray Pyrolysis and characterized by techniques like XRD for the structure, SEM and AFM for the morphology and topography, respectively, four probe method pour the electrical properties and spectrophotometer for the measurement of band gap energy

2. CdS Thin Films

2.1. Structural Investigation of CdS Thin Films

A CdS thin film was deposited onto glass substrate by Chemical Spray Pyrolysis technique. XRD analysis revealed polycristalline film with peaks at 24.95°, 26.59°, 28.22°, 36.55°, 43.84°, 47.86° and 52.05° corresponding to (100), (002), (101), (102), (110), (103) and (112), respectively as shown in Fig. 73. No secondary phase was detected. The average size of crystallite size is 12.7nm.

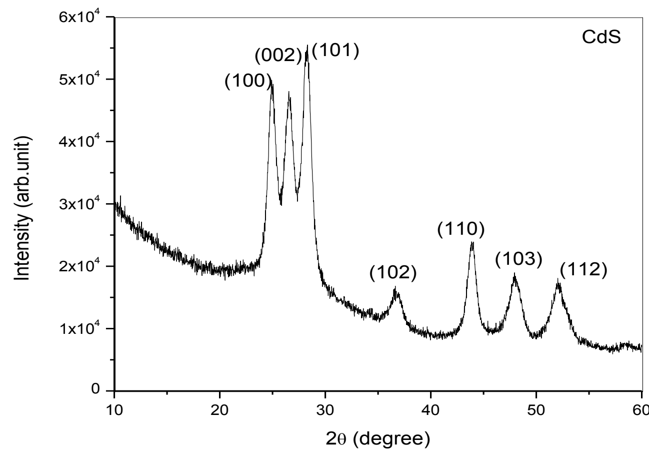

Fig. 73: XRD spectrum of CdS thin film

2.2. Morphology and Microanalysis of CdS Thin Films

Surface morphology of CdS thin film was analyzed using FESEM. A uniform, well-covered, dense film without pinholes and cracks with small grain was shown in Fig. 74.

According to EDS microanalysis attached to FESEM, cadmium and sulfur was detected with 51.66% at of Cd and 48.34% at of S with a stoichiometric ratio of $Cd/S \approx 1.06$.

Topography of the surface in 2D of AFM analysis measured in an area of 3µmx3µm confirms FESEM analysis as shown in Fig. 75. We noted a grain size of 236 nm and an RMS roughness of 36 nm.

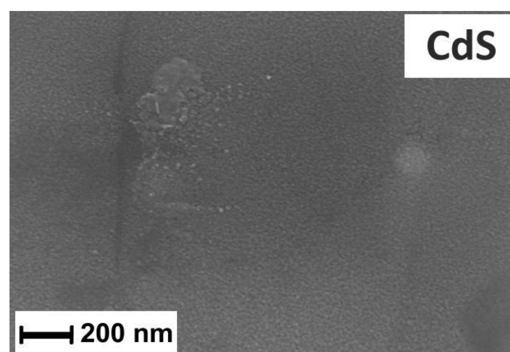

Fig. 74: FESEM image of CdS thin film

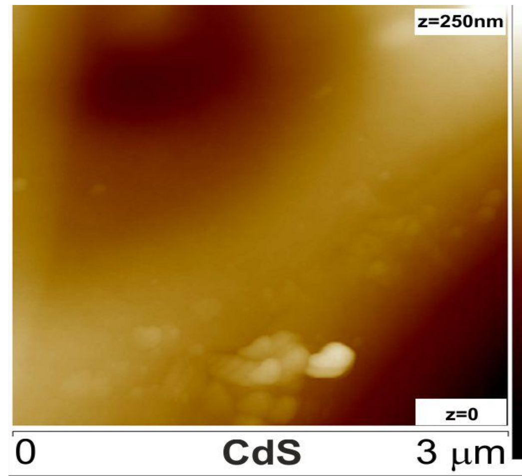

Fig. 75: AFM image of CdS thin film

2.3. Electrical analysis of CdS Thin Films

Electrical characterization of CdS thin film was done using four probe technique measurements. We noted relatively high resistivity of 419Ω.cm due probably to existence of grain boundaries and inhomogeneities of the film.

2.4. Optical property of CdS Thin Film

CdS thin film optical property was evaluated using spectrophotometer. Fig. 76. Revealed a transmittance of around 50% and $(Ah\nu)^2 = f(h\nu)$ plot showed an energy band gap of 2.46eV which is consistent with the value found in the literature.

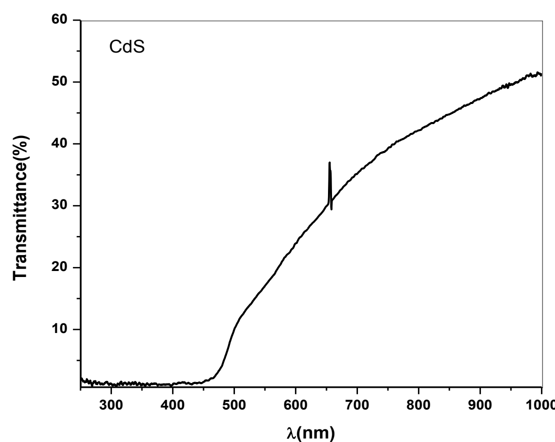

Fig. 76: Transmittance of CdS thin film

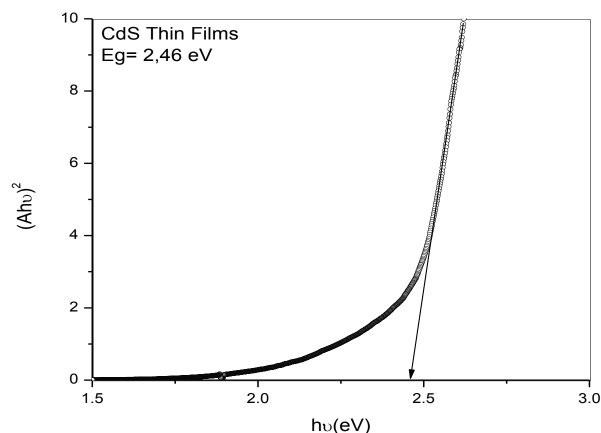

Fig. 77: Band gap energy of CdS thin film

3. ZnO Thin Films

3.1. Structural Investigation of ZnO Thin Films

Polycristalline hexagonal (Wurtzite) structure of ZnO thin film was deposited onto glass substrate using Chemical Spray Pyrolysis technique. Fig.78. revealed peaks at 31.67°, 34.25°, 36.08° and 47.32° corresponding to (100), (002), (101) and (102), respectively without any secondary phase. No preferential orientation is also detected between (100), (002) and (101) peaks. The average size of crystallite size is 14.4nm.

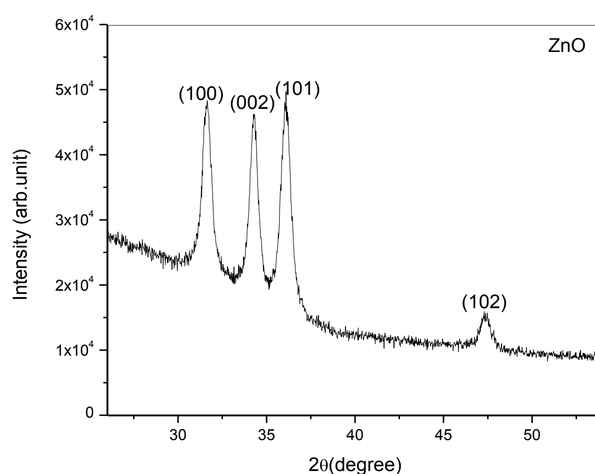

Fig. 78: XRD spectrum of ZnO thin film

3.2. Morphology and Microanalysis of ZnO Thin Films

ZnO thin film deposited was well-covered and dense with wedge like structure as revealed in Fig.79. Composition of the film given by EDS attached to FESEM showed 51.71% of O and 48.29% of Zn with Zn/O ratio of 0.93.

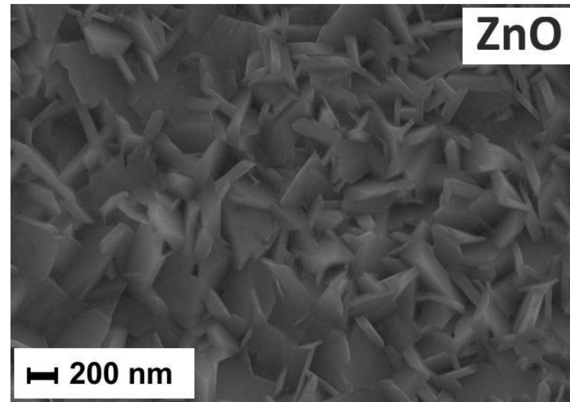

Fig. 79: FESEM image of ZnO thin film

The AFM analysis confirms FESEM result and showed film with a grain size of 143nm and a roughness of 52nm as shown in Fig. 80.

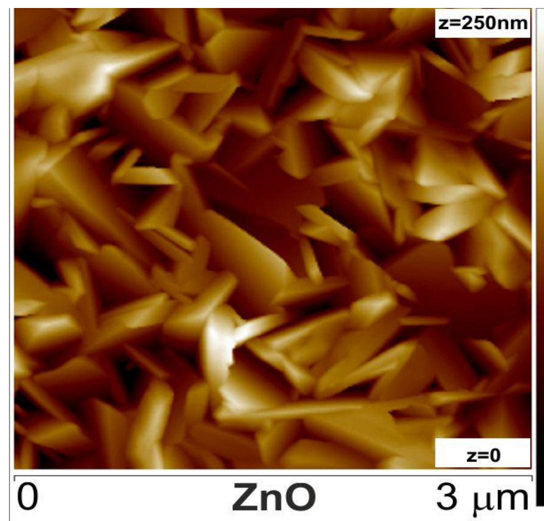

Fig. 80: AFM image of ZnO thin film

3.3. Electrical analysis of ZnO Thin Films

A resistivity of 711Ω.cm was observed using four probe method measurements. The high value of this resistivity can be explained by the wedge like structure of the film which cannot allow an easy passage of current.

3.4. Optical property of ZnO Thin Film

Fig. 81 showed a transmittance of ZnO thin film of around 75% in the UV-Vis-IR range. The band gap energy given by the $(Ah\nu)^2 = f(h\nu)$ plot was 3.20eV which is consistent with values founded in the ZnO-literature.

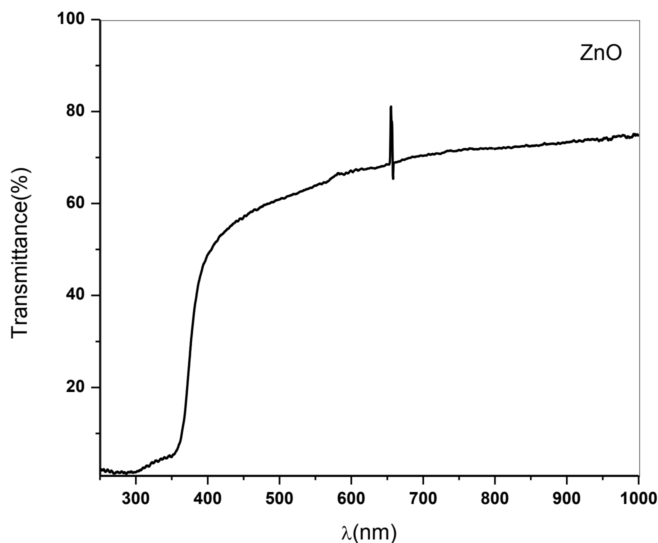

Fig. 81: Transmittance of ZnO thin film

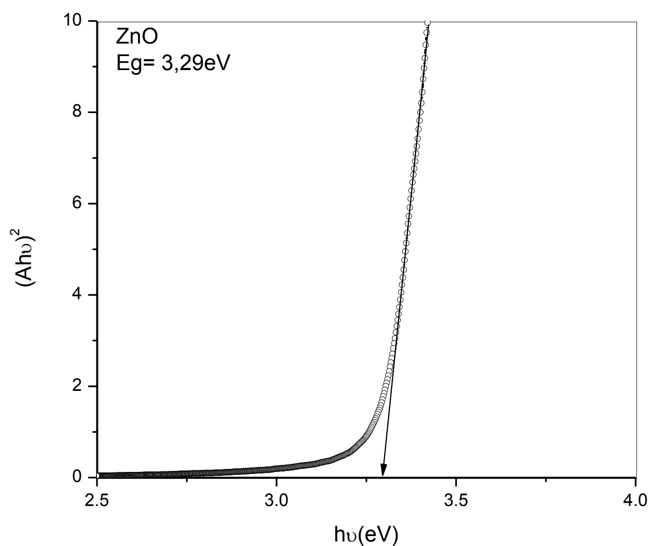

Fig. 82: Band gap energy of ZnO thin film

4. ZnO:Al Thin Films

4.1. Structural Investigation of ZnO-Al doped Thin Films

Fig. 83 shows XRD pattern of ZnO-doped with Al deposited by Chemical Spray Pyrolysis onto glass substrate. Polycristalline weak peaks were observed corresponding to (100), (002), (101), (102), and (110) with (002) as main peak without secondary phase. The signature of the glass substrate was clear revealing the low thickness of the film. The average size of crystallite is 14.8nm

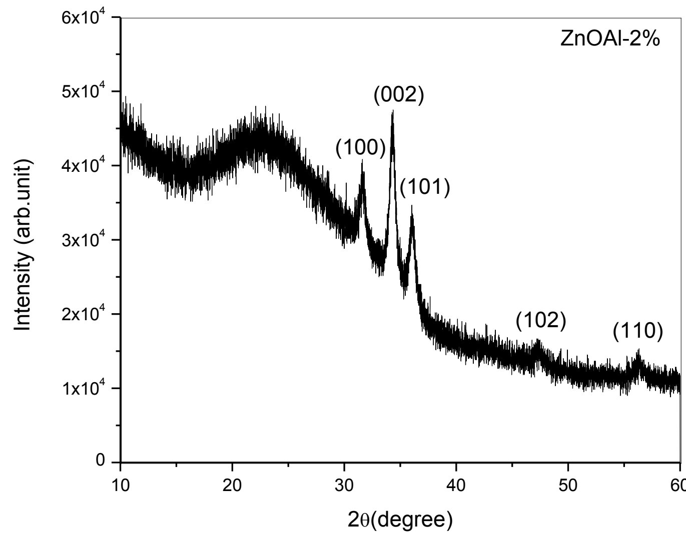

Fig. 83: XRD spectrum of ZnO-Al doped thin film

4.2. Morphology and Microanalysis of ZnO-Al doped Thin Films

Fig. 84 show FESEM image of ZnO: Al thin film. Film was well-covered, dense without crack and pinholes with small grain size. EDS analysis gave the composition of film with 50.48% at of O, 48.59% at of Zn and 0.93% of Al with Zn/O of 0.96, near to stoichiometry.

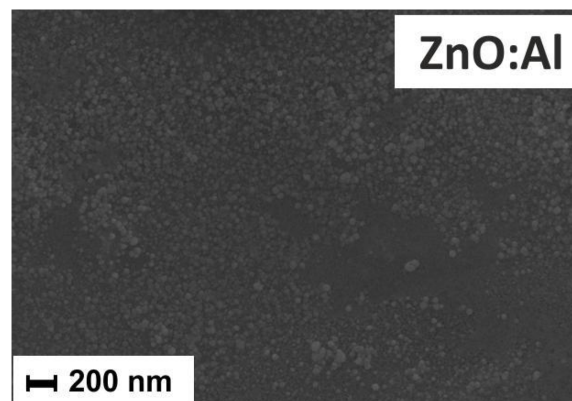

Fig. 84: FESEM image of ZnO-Al doped thin film

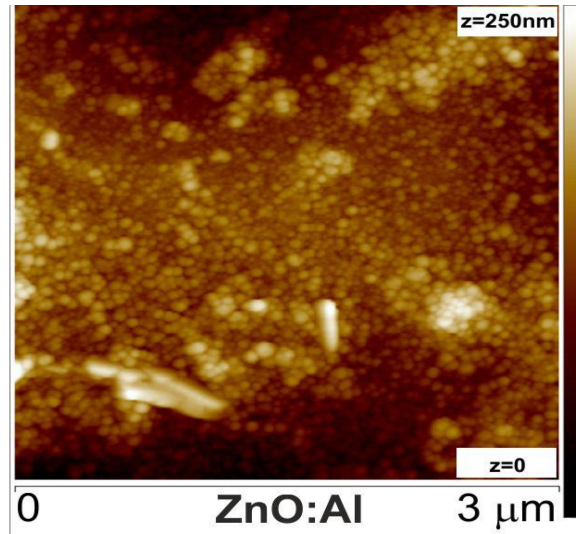

Fig. 85: AFM image of ZnO-Al doped thin film

AFM picture showed in Fig.85 confirmed FESEM morphology and revealed a grain size of 114nm and a roughness of 26nm.

4.3. Electrical analysis of ZnO-Al doped Thin Films

ZnO thin film doped by Al electrical resistivity was evaluated by four probe method measurements and a value of 681Ω.cm was obtained which was lower that undoped one. This relatively high value of the resistivity was due probably to the existence of grain boundaries in the film.

4.4. Optical property of ZnO-Al doped Thin Film

The transmittance of ZnO doped by Al spectrum was shown in Fig. 86 with $> 70\%$ of intensity. Band gap energy measurement revealed 3.31eV after doping in Fig. 87. The increase of band gap energy can be explained by Burstein-Moss effect.

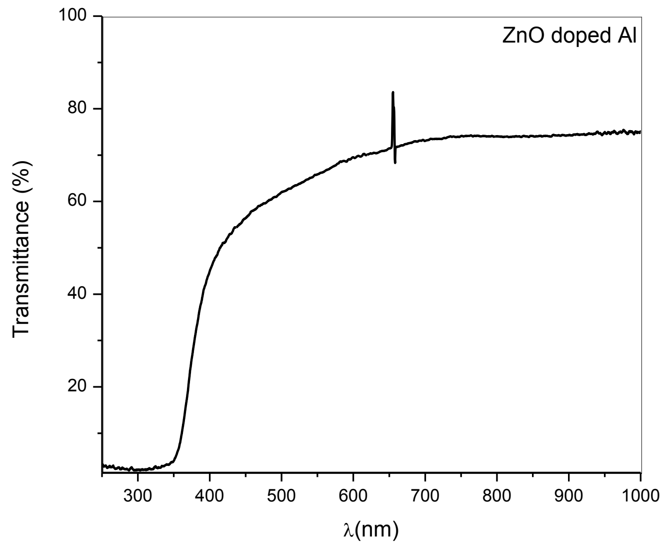

Fig. 86: Transmittance of ZnO-Al doped thin film

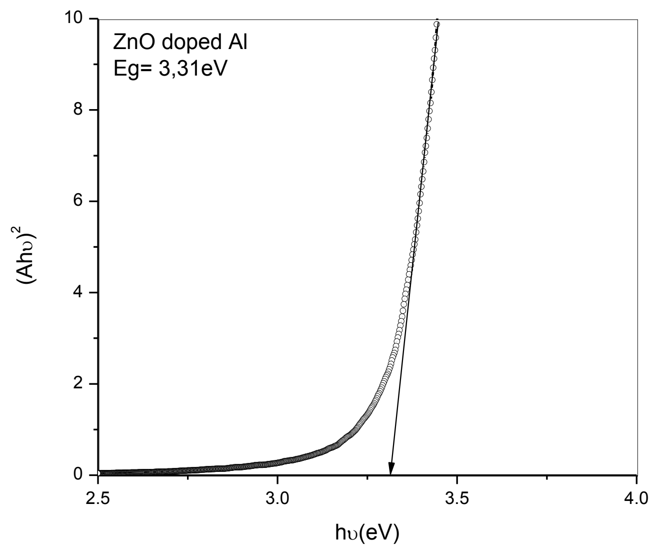

Fig. 87: Band gap energy of ZnO-Al doped thin film

5. Conclusion

CdS, ZnO and Al doped ZnO thin films were well deposited onto glass substrate using Chemical Spray Pyrolysis technique. All films are polycristalline, uniform, dense, well-covered, homogeneous and have good adherence on the glass substrate. We noted also high resistivity of ZnO and ZnO-Al due, probably to the existence of grain boundaries in

corresponding films. They had band gap energies corresponding to those found in the literature.

References

[1] Tina Sebastian Ph.D « Automation of Chemical Spray Pyrolysis Unit and Fabrication of Sprayed $CuInS_2/In_2S_3$ Solar Cell ». August 2009.

[2] Teny Theresa John, S. Bini, Y. Kashiwaba, et al. Semicond. Sci Technol, Vol. 18(2003), p.491-500.

[3] X. Zhang, H. Wang, J. Xu, L. Yang and M. Ren. « Effect of different S/In ratio on properties of In_2S_3 films prepared by ultrasonic spray pyrolysis method ». Key Engineering Materials Vols. 474-476 (2011) pp 998-1001.

[4] M. Ortega – Lopez and A. Morales- Acevedo, Thin Solid Films 330 (1998) 96.

[5] R. Jayakrishnan. « Defect analysis of semiconductor thin films for photovoltaic applications using photoluminescence and photoconductivity ». April 2008.

[6] H. Spasevska, C. C. Kitts, C. Ancora and G. Ruani, "Optimised In_2S_3 thin films deposited by spray pyrolysis," Hindawi Publishing Corporation, International Journal of Photoenergy, Vol 2012, pp. 1−7, January 2012.

[7] K. Otto, A. Katerski, O Volobujeva, A. Mere and M. Krunks, Indium sulfide thin films deposited by chemical spray of aqueous and alcoholic solutions. Energy Procedia 3 (2011) 63-69.

[8] P.S. Patil, Versatility of chemical spray pyrolysis technique, Materials Chemistry and Physics 59 (1999) 185-198.

[9] M. Calixto-Rodriguez, A. Tiburcio-Silver, A. Ortiz, A. Sanchez-Juarez, Optoelectronical properties of indium sulfide thin films prepared by spray pyrolysis for photovoltaic applications, Thin Solid Films 480–481 (2005) 133-137.

[10] W.-T. Kim, C.-D. Kim, Optical energy gaps of β-In_2S_3 thin films grown by spray pyrolysis, J. Appl. Phys. 60 (1986) 2631-2633.

[11] K. Otto, A. Katerski, A. Mere, O. Volobujeva, M. Krunks, Spray pyrolysis deposition of indium sulphide thin films, Thin Solid Films 519 (2011) 3055–3060.

[12] H. R. Chandrasekhar, R. G. Humphreys, U. Zwick and M. Cardona, Infrared and Raman spectra of the IV-VI compounds SnS and SnSe, Phys. Rev. B. 15 (1977) 2177-2183.

[13] J. Malaquias, P.A. Fernandes, P.M.P. Salome, A.F. da Cunha, Assessment of the potential of tin sulphide thin films prepared by sulphurizationof precursors as cell absorbers, Thin Solid Films 519 (2011) 7416-7420.

[14] N. R. Mathews, H. B. M. Anaya, M. A. Cortes-Jacome, C. Angeles-Chavez, J. A. Toledo-Antonio, Tin sulfide thin films by pulse electrodeposition:structural, morphological, and optical properties, J. Electrochem Soc. 157 (2010) H337 - H341.

[15] R. Sivaramasubramaniam, M. R. Muhamad, S. Radhakrishna, Optical Properties of Annealed Tin (II) Oxide in Different Ambients, Phys. Status Silidi (a) 136 (1993) 215-222.

[16] M. Vasudeva Reddy, G. Sreedevi, C. Park, R.W. Miles, and K.T. Ramakrishna Reddy, Curr. Appl. Phys. 15, 588 (2015).

[17] A. Molenaar, Extended Abstracts, vol. 84-2, Pennington, N.J., 634 (1984).

[18] S. López, S. Granados, and A. Ortiz, Semicond. Sci. Technol. 11, 433 (1996).

[19] H.R. Chandrasekhar, R.G. Humphreys, U. Zwick, and M. Cardona, Phys. Rev. B 15, 2177 (1977).

[20] S. Cheng and G. Conibeer, Thin Solid Films 520, 837 (2011).

[21] Hibbert TG, Mahon MF, Molloy KC, Price LS, Parkin IP (2001) Deposition of tin sulfide thin films from novel, volatile (fluoroalkythiolato) tin (IV) precursors. J Mater Chem 11:469-473.

[22] Reddy NK, Ramesh K, Ganesan R, Reddy K, Gunasekhar KR, Gopal E (2006) Synthesis and characterization of co-evaporated tin sulphide thin films. Appl Phys A 83:133–138.

[23] Deepa KG, Vijayakumar KP, Kartha CS (2012) Lattice vibrations of sequentially evaporated CuInSe2 by Raman microspectrometry. Mat Sci Semicond Proc 15:120-124.

[24] Nikolic PM, Lj Miljkovic P, Mihajlovic Lavrencic B (1977) Splitting and coupling of lattice modes in the layer compound SnS. J Phys C 10:L289-L292.

[25] Chandrasekhar HR, Humphreys RG, Zwick U, Cardona M (1977) Infrared and Raman of IV-IV compounds SnS and SnSe. Phys Rev B 15:2177-2183.

[26] Revathi N, Bereznev S, Iljina J, Safonova M, Mellikov E, Volobujeva O (2013) PVD grown SnS thin films onto different substrate surfaces. J Mater Sci: Mater Electron 24:4739-4744.

[27] Wang Y, Gong H, Fan BH, Hu GX (2010) Photovoltaic behavior of nanocrystalline SnS/TiO2. J Phys Chem C 114:3256–3259.

[28] Tanusevski A, Poelman D (2003) Optical and photoconductive properties of SnS thin films prepared by electron beam evaporation. Sol Energy Mater Sol Cells 80:297-303.

[29] Sajeesh TH, Poornima N, Kartha CS, Vijayakumar KP (2010) Unveiling the defect levels in SnS thin films for photovoltaic applications using photoluminescence technique. Phys Status Solidi A 207:1934–1939.

[30] Sinsermsuksakul P, Heo J, Noh W, Hock AS, Gordon RG (2011) Atomic layer deposition of tin monosulfide thin films. Adv Energy Mater 1:116-125.

[31] Bashkirov Simon A, Lazenka Vera V, Gremenok Valery F, Bente Klaus (2011) Microstructure of SnS thin films obtained by hot wall vacuum deposition method. J Adv Microsc Res 6:153-158.

[32] Sall T, Mari Soucase B, Mollar M, Hartitti B, Fahoume M (2015) Chemical spray pyrolysis of β-In_2S_3 thin films deposited at different temperatures. J Phys Chem Solids 76:100-104.

[33] F. Paraguay D, J. Morales, W. Estrada L, E. Andrade, M. Miki-Yoshida, Influence of Al, In, Cu, Fe and Sn dopants in the microstructure of zinc oxide thin films obtained by spray pyrolysis, Thin Solid Films. 366 (2000) 16–27.

[34] P. Lu, H. Jia, S. Cheng, Optical and Electrical Properties of SnS: Ag Films as Solar Cell Absorbers, Adv. Mat. Res. 60-61 (2009) 11-15.

[35] J. Reichman, The current–voltage characteristics of semiconductor-electrolyte junction photovoltaic cells. Appl. Phys. Lett. 36 (1980) 574-577.

[36] L.M. Peter, J. Li, R. Peat, Surface recombination at semiconductor electrodes. 1. Transient and steady-state photocurrents. J. Electroanal. Chem. 165 (1984) 29–40.

[37] R. Memming, Semiconductor Electrochemistry. Wiley, New York (2000).

[38] W. Suzhen, D. Zanhong, D. Weiwei, S. Jingzhen, F. Xiaodong, Fabrication and electrical properties of p-$CuAlO_2$/(n-, p-)Si heterojunctions, J. Semicond. 35 (2014) 043001-1-043001-5.

[39] F. Paraguay D, J. Morales, W. Estrada L, E. Andrade, M. Miki-Yoshida, "Influence of Al, In, Cu, Fe and Sn dopants in the microstructure of zinc oxide thin films obtained by spray pyrolysis", Thin Solid Films, Volume 366, Issues 1-2, 1 May 2000, pp. 16-27.

[40] K. Santhos hKumar, A. Gowri Manohari, S. Dhanapandian, T. Mahalingam, "Physical properties of spray pyrolyzed Ag-doped SnS thin films for opto-electronic applications, Materials Letters, Volume 131, 15 September 2014, pp. 167-170.

[41] Shuai Zhang, Shuying Cheng, "Thermally evaporated SnS:Cu thin films for solar cells", Micro & Nano Letters, IET, Volume: 6, Issue: 7, 2011, pp.559-562.

[42] T. Sall, M. Mollar and B. Marí, Substrate influences on the properties of SnS thin films deposited by chemical spray pyrolysis technique for photovoltaic applications, J. Mater. Sci. 51 (2016), p. 7607, doi:10.1007/s10853-016-0039-9.

[43] K. S. Kumar, C. Manoharan, S. Dhanapandian, A.G. Manohari, T. Mahalingam, Effect of indium incorporation on properties of SnS thin films prepared by spray pyrolysis, Optik - International Journal for Light and Electron Optics 125, 15 (2014), pp. 3996-4000, doi:/10.1016/j.ijleo.2014.01.144.

[44] J.A. Andrade-Arvizu, M. Courel-Piedrahita, O. Vigil-Galán, SnS-based thin film solar cells: perspectives over the last 25 years, J. Mater. Sci. Mater. Electron. 26 (2015), p. 4541

[45] C. E. Kim et al., Effect of carrier concentration on optical bandgap shift in ZnO: Ga thin films, Thin Solid Films 518 (2010), pp. 6304-6307

[46] T. Sall, B. Marí Soucase, M. Mollar, B. Hartiti, M. Fahoume, Chemical spray pyrolysis of β-In_2S_3 thin films deposited at different temperatures, J Phys Chem Solids 76 (2015), pp. 100–104.

[47] J. Vidal, S. Lany, M. d'Avezac, A. Zunger, A. Zakutayev, J. Francis, J. Tate, Band-structure, optical properties, and defect physics of the photovoltaic semiconductor SnS, App. Phys. Lett. 100, 032104 (2012), doi:/10.1063/1.3675880

[48] J. I. Pankove, Optical Processes in Semiconductors (Dover Publications, New York, 1975).

[49] H. Shibata, Jpn. J. Appl. Phys. 37 (1997), p. 550.

Chapter V: SnS-based Solar Cells

1. Introduction

SnS- based solar cells samples were deposited onto FTO substrate using Chemical Spray pyrolysis as deposition technique and J-V characteristics curves upon illumination of heterojunction for characterization.

2. Experimental Procedure

SnS, In_2S_3, CdS, ZnO and ZnO doped with Al were deposited using Chemical Spray Pyrolysis and parameters in the Table.

Table 1: Deposition parameters on films using in solar cells

Thin Films	Volume Sprayed (mL)	Substrate Temperature (°C)	Nozzle-Substrate Distance (cm)	Ambient air pression (bar)	Spray rate (mL/min)
SnS	10	350	25	0.7	1.5
In_2S_3	5	300	25	0.7	1.5
CdS	5	300	25	0.7	1.5
ZnO	3	400	25	0.7	1.5
ZnO:Al	5	400	25	0.7	1.5

3. J-V characteristics of Cells

J-V characteristics of cells were measured using Science tech Power Supply Model SCI 200. Cells were illuminated using Xenon lamp with an intensity of $100mW/cm^2$ through the FTO substrate side.

The distance between the cell and the source is 6 cm.

General Purpose Electrochemical System (GPES) software was used for the recording and processing of data.

Active areas of 1x1cm were studied for all cells under dark and illumination ($100mW/cm^2$) and an alloy of Cu, Sn and Al is used as metallic contact.

4. Result and Discussion

The J-V characteristics of FTO/CdS/SnS, FTO/In_2S_3/SnS, FTO/ZnO:Al/SnS, FTO/ZnO/CdS/SnS and FTO/ZnO:Al/CdS/SnS heterojunction was studied and electrical parameters were summarized in the Table.

Table 2: Cell parameters of different samples

Samples	Jsc (mA/cm^2)	Voc (V)	FF (%)	Rs (Ω)	Rsh (Ω)	η (%)
FTO/CdS/SnS	1.45	0.23	29.7	$1.34\ 10^{2}$	$2.04\ 10^{2}$	$9.8\ 10^{-4}$
FTO/ZnO/CdS/SnS	0.55	0.73	36.8	$6.59\ 10^{2}$	$2.84\ 10^{3}$	$1.48\ 10^{-3}$
FTO/ZnO:Al/CdS/SnS	1.60	0.28	26.2	$1.53\ 10^{2}$	$2.00\ 10^{2}$	$1.17\ 10^{-3}$
FTO/ZnO :Al/SnS	$3.31\ 10^{-4}$	0.79	56.9	$7.40\ 10^{5}$	$8.06\ 10^{6}$	$1.48\ 10^{-6}$
FTO/In_2S_3/SnS	0.34	0.48	66.1	$2.65\ 10^{3}$	$14.08\ 10^{3}$	$1.08\ 10^{-3}$

Fig. 1, Fig. 2, Fig. 3, Fig. 4 and Fig.5 shows the current-voltage (J-V) characteristics of FTO/CdS/SnS, FTO/ZnO/CdS/SnS, FTO/ZnO:Al/CdS/SnS, FTO/ZnO:Al/SnS and FTO/In_2S_3/SnS configurations under illumination, respectively. The efficiency was found to increase slightly when ZnO thin film was introduced in the FTO/CdS/SnS cell configuration from $9.8\ 10^{-4}$ % to $1.48\ 10^{-3}$ % due probably to the reduction of lattice mismatch between ZnO and SnS which caused the most of time intermediate trap states at the SnS/ZnO interface; we also noticed a net increase of V_{oc}. We noted also a very low efficiency in FTO/ZnO:Al/SnS configuration with a very low J_{sc} due probably to the recombination at the junction. The crystallinity, morphology surface and grains boundaries were also factors limiting the efficiency of solar cells. In addition, we can say that factors limiting to obtain high efficiency were heterojunction band discontinuity leading to low V_{oc}, short diffusion length of minority carriers due to grain boundaries leading to low J_{sc} and a weak fill factor, among others. The low values of efficiencies can also due to high values of series resistances as shown in Table 2.

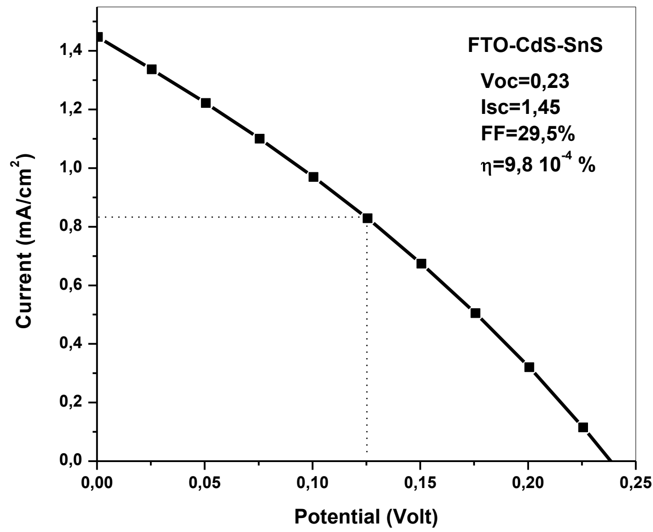

Fig. 1: J-V characteristics of FTO/CdS/SnS

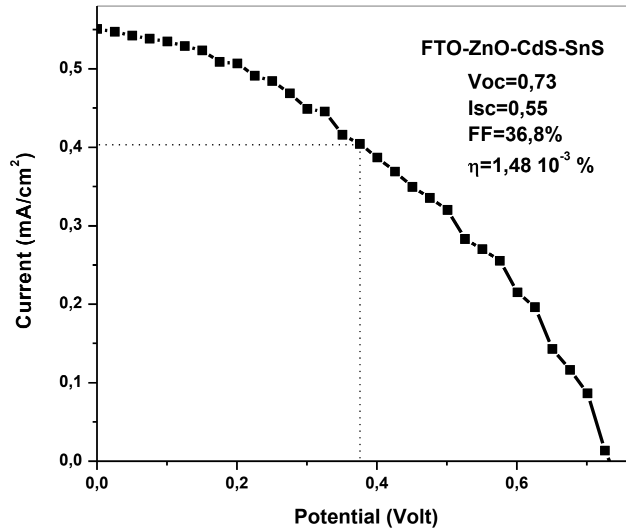

Fig. 2: J-V characteristic of FTO/ZnO/CdS/SnS

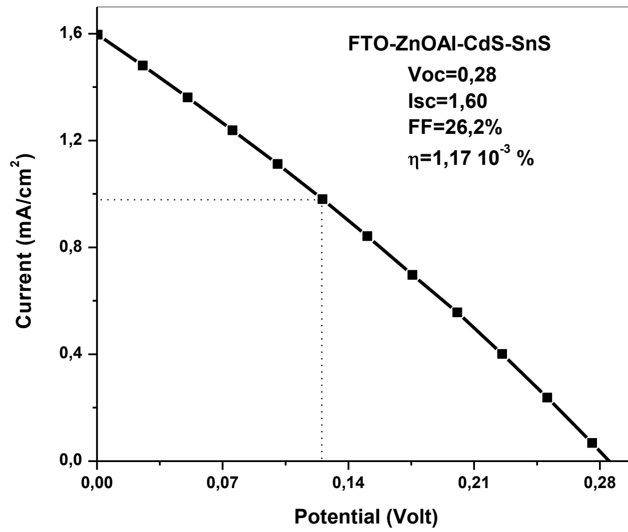

Fig. 3: J-V characteristic of FTO/ZnO:Al/CdS/SnS

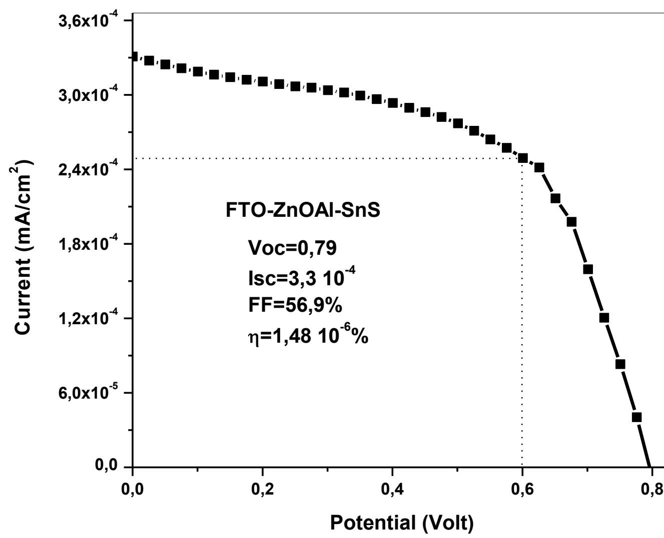

Fig. 4: J-V characteristic of FTO/ZnO:Al/SnS

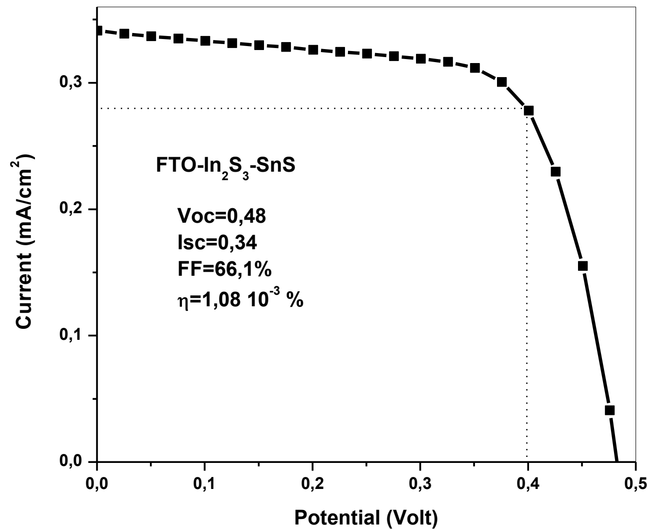

Fig. 5: J-V characteristic of FTO/In_2S_3/SnS

5. Conclusion

We noted that SnS-based solar cells were well fabricated using low cost Chemical Spray Pyrolysis technique. The J-V measures revealed that all configurations had low efficiency due, probably, to recombination at junctions, grain boundaries that limited photogenerated carriers, etc..We also noticed a slight increase of efficiency in FTO/CdS/SnS configuration when ZnO window layer was introduced, from 9.8 10^{-4} % to 1.48 10^{-3} %, due certainly to the reduction of mismatch between SnS/ZnO interface.

Chapter VI: General Conclusion

General Conclusion

SnS and β-In_2S_3 thin films have been prepared onto glass substrate using Chemical Spray Pyrolysis technique. The structural, morphological, topographical, electrical, and optical were carried out using various techniques like XRD, FE(SEM), AFM, spectrophotometer, photoluminescence and Mott-Schottky measurements in order to determine physico-chemical features of films. The most noticeable results are summarized as follows.

1. β-In_2S_3 Thin Films

a. Effect of the [S]/[In] ratio on the properties of In_2S_3 thin films

Based on the results obtained for the In_2S_3 thin layers prepared by Chemical Spray Pyrolysis at different [S]/[In] ratios, layers are polycrystalline with (0 0 12) as main peak regardless of substrate ratio and temperature. We also note that this main peak decreases when [S]/[In] ratio increases from 2 to 3 for the substrate temperature 250 °C but increases in the same ratio range for the substrate temperature of 300 °C. The (109) peak which is low at 250 °C and 300 °C increases in intensity at high temperature of the substrate (350 °C) and this for all ratios. Raman spectroscopy confirms the presence of the β-In_2S_3 phase obtained by XRD for few samples analyzed and elaborated at 250 °C. SEM images show dense, compact and homogeneous samples independently of [S]/[In] ratio and substrate temperature, and the EDS reveals good stoichiometry. The samples prepared at low temperature of substrate, 250 °C and 300 °C, have transmission around 60% whereas at high temperature, 350 °C, the transmission increases significantly to 70% independently of the [S]/[In] ratio with bandgap energies that vary with temperature.

b. In_2S_3 thin layers deposited by Chemical Spray Pyrolysis at different substrate temperatures

In_2S_3 thin films are deposited by Spray Pyrolysis technique onto glass substrates at different temperatures (250 °C - 300 °C - 350 °C). X-ray diffraction shows well-crystallized layers with (0 0 12) as preferred direction perpendicular to the plane which contains the surface of the glass substrate. The composition of the layers given by EDS shows films with good stoichiometry after vacuum annealing. Raman analysis confirms the presence of β-In_2S_3 phase with well-prominent modes after vacuum annealing. The band gap energies decrease after annealing for the substrate temperatures of 250 °C and 350 °C but remain stable at 300 °C. Hence, the temperature of 300 °C is considered to be the most suitable temperature to study the effects of the other deposition parameters other than the temperature of the substrate.

c. β-In_2S_3 thin films deposited by Chemical Spray Pyrolysis method from Bi-Distilled Water Solvent and Alcohol Solvent

In this part, In_2S_3 thin films are prepared with and without alcohol in the solvent of bi-distilled water. X-ray diffraction analysis shows polycrystalline films in both cases with (0 0 12) as main peak which reaches its maximum intensity at the substrate temperature of 300 °C, thus illustrating the improvement in crystallinity. We also note (107) peak only in samples prepared without alcohol. SEM images reveal dense, homogeneous and compact thin films that adhere well to the glass substrate and no vacuum is observed in In_2S_3 thin films prepared with 5% alcohol, while for those prepared with double distilled water, we observe some cracks. AFM micrographs show that films have roughly the same roughness independently of the solvent used but with larger grain sizes for films synthesized without alcohol. Optical analyzes show that the samples prepared with alcohol have transmission which extends between 67% and 80% depending on the substrate temperature, whereas those prepared without alcohol have transmission that extends between 56% and 66%. The band gap energies of films prepared with alcohol are greater than those prepared without alcohol. So, we can say that thin layers of β-In_2S_3 prepared by the Chemical Spray Pyrolysis technique with alcohol have better physico-chemical properties than those elaborated with bi-distilled water solvent.

2. SnS Thin Films

a. Optimization of Deposition Parameters of SnS Thin Films

SnS thin films deposited by Chemical Spray Pyrolysis technique onto glass substrate with [S]/[Sn]= 1 at 350 °C were polycristalline with (111) as main peak. Raman modes confirm the presence of SnS phase without any additional secondary phases like SnS_2, Sn_2S_3, SnO or SnO_2. SEM analysis revealed well-covered, denser, compact, adhesive and stable films and EDS attached to SEM, depicted the presence of sulfur (S) and tin (Sn) in all films with stoichiometric ratio. AFM analysis emphasized films with larger grains and high roughness. Suitable band gap energy between 1.46 and 1.50eV were obtained, making SnS to be a promising candidate to substitute $CuInS_2$ absorber layer in solar cells thin films technology.

b. Effect of doping on the physical and chemical properties of SnS thin films

SnS thin films doped by silver (Ag^+), aluminum (Al^{3+}), iron (Fe^{2+}) and indium (In^{3+}) were deposited onto glass substrates using Chemical Spray Pyrolysis technique and films were characterized using various analytical techniques.

-SnS thin films doped with Silver (Ag^+)

All films were polycristalline with (111) as preferential orientation and an enhancement of crystallinity with Ag doping concentration. Ag_8SnS_6 and Ag as secondary phases were, also highlighted by XRD.

More compact and denser films with "vermicelli" like shape were obtained after doping and a ratio of S/Sn≈0.98 at 5% given by EDS confirms the improvement of stoichiometry with silver doping. P-type semiconductors, variation of carrier concentration with lower value of resistivity of 108 Ω.cm at 10% and lower band gap energy of 1.46eV at 5% were highlighted by Mott-Schottky and spectrophotometer measurements, respectively.

-SnS thin films doped with Aluminum (Al^{3+})

Improvement of crystallinity of SnS thin films doped with aluminum was revealed by XRD analysis. Compact and denser films were obtained at 10% Al-doping while from 3% to 7%,

films showed fishnet-like morphology with scores of holes. EDS highlighted improvement of stoichiometry with Al-doping, $S/Sn \approx 0.99$.

Relatively low resistivity of 171.30 Ω.cm at 10% and an increase of bandgap energies were revealed by Mott-Schottky and spectrophotometer measurements, respectively.

-SnS thin films doped with Iron (Fe^{2+})

XRD results showed polycristalline films with (111) as main peak decreasing with Fe-doping explaining the presence of $SnFe_2S_4$ secondary phase. Well-covered, compact and denser films were observed for films from 5% to 7% Fe-doping and EDS revealed the presence of sulfur, tin and iron with improvement of stoichiometry.

Band gap energies increased from 1.50 to 1.77eV corresponding to 0% and 5%, respectively were highlighted by spectrophotometer measurements while Mott-Schottky one showed an increase of resistivity due to the presence of secondary phase.

In the light of this study, we can affirm that, for preparing good solar cell with high efficiency and with low cost technique, SnS thin films can be deposited onto glass substrate using Chemical Spray Pyrolysis technique.

-SnS thin films doped with Indium (In^{3+})

In this work we presented the opto-electrical study of In doped SnS thin films made by spray pyrolysis. XRD analysis revealed orthorhombic structure with (111) dominant peak. AFM imaging show that films consist of longitudinal grains. The In doping slightly increase the roughness of the surface as well as the average size of the grains while the crystallite size remains constant. The material has an indirect bandgap with energy around 1.05 eV independent on In concentration. However, the absorption is dominated by the direct transition with energies decreasing with increased amount of indium from 1.71 eV to 1.48 eV. The PL study revealed two donor to acceptor transitions independent on the In concentration. In both transitions, one of defect levels taking part in recombination process is common characterized by thermal activation energy of around 90 meV. However, our study did not allow us to judge whether the defect is a donor or an acceptor. The conductivity

measurements show thermally activated conductivity with activation energies inversely dependent on In concentration in the 145 meV – 162 meV range. This decrease of activation energy results directly in higher conductivity of investigated thin films.

3. SnS-based Solar Cells

SnS-based solar cells with various configurations were deposited successfully onto FTO substrate using Chemical Spray Pyrolysis technique and using ZnO, ZnO doped with Al, CdS and In_2S_3 thin films as windows and buffer layers in order to measure J-V characteristics.

In the light of measures, we found that efficiencies of all configurations were very low due probably to recombination at junctions, grain boundaries in films surfaces, etc… We noted also an increase of efficiency when ZnO window layer was introduced in FTO/CdS/SnS configuration from 9.8 10^{-4} % to 1.48 10^{-3} %.

4. Scope for the future work

We propose to fabricate SnS-based solar cells as an absorber layer and In_2S_3 as a buffer layer in order to compare the results obtained with those of the standard CdS buffer layer: **Glass/Mo/p-SnS/n-In_2S_3/i-ZnO/ ZnO:Al/Metal.**

CONFERENCES AND PUBLICATIONS

- "Elaboration and characterization of In_2S_3 thin films by Spray Pyrolysis with [S]/[In]=3 ratio"

  Thierno Sall, B. Hartitti, B. Mari, M. Miquel, L. Laanab and M. Fahoume
  International Renewable and Sustainable Energy Conference (IRSEC) 2013, IEEE pp.58−62.

- "Synthesis by Chemical Spray Pyrolysis and characterization of In_2S_3 with different [S]/[In] ratios"

  Thierno Sall, A. Nafidi, B. M. Soucase, M. Mollar, B. Hartitti and M. Fahoume
  Journal of Semiconductors, Vol 35, N° 6, June 2014

- "Chemical Spray Pyrolysis of β-In_2S_3 Thin Films deposited at different temperatures"

  Thierno Sall, Bernabé Marí Soucase, Miguel Mollar, Bouchaib Hartitti, Mounir Fahoume.
  Journal of Physics and Chemistry of Solids, Vol 76, N°, August 2014.

- "β-In_2S_3 Thin Films doped by Tin (Sn^{4+}) and deposited by Chemical Spray Pyrolysis technique for photovoltaic applications"

  Thierno Sall, Bernabé Mari Soucase, Miguel Mollar, Mounir Fahoume
  International Renewable and Sustainable Energy Conference (IRSEC) 2014, IEEE pp.667 − 671.

- "Substrate influences on the properties of SnS thin films deposited by Chemical Spray Pyrolysis technique for photovoltaic applications"

  Thierno Sall, Miguel. Mollar and Bernabé. Mari. Journal of Materials Science. May 2016.

- "SnS thin films prepared by Chemical Spray Pyrolysis at different substrate temperatures for photovoltaic applications"

Thierno Sall, Bernabe Mari Soucase, Miguel Mollar, and Juan Angel Sans, Journal of Electronic Materials, March 2017 Volume 46, Issue 3, pp.1714-1719

- "Opto-electrical characterisation of In-doped SnS thin films for photovoltaic applications"

  A. Urbaniak, M. Pawłowski, M. Marzantowicz, ***Thierno Sall***, B.Marí, Thin Solid Films 636 (2017) 158−163.

- "Tin-mono-sulfide (SnS) thin films prepared by chemical spray pyrolysis with different [S]/[Sn] ratios"

  Thierno Sall, Miguel Mollar, and Bernabé Marí
  Optical and Quantum Electronics, Vol 49, N 11, November 2017, 49:386